ELASTIC-PLASTIC FRACTURE MECHANICS ANALYSIS OF A TUBULAR T-JOINT IN OFFSHORE STRUCTURES

by
Zhen-Zhong Du

Submitted to the University of Glasgow
for the degree of
Doctor of Philosophy

July, 1989

ProQuest LLC.
789 East Eisenhower Parkway
P.O. Box 1346
Ann Arbor, MI 48106 – 1346

Abstract

A tubular welded T-joint containing a series of semi-elliptical cracks of increasing depth located near the chord-brace intersection under both elastic and elastic-plastic conditions, has been analysed using shell elements with the cracks modelled by line springs. The same problem has also been modelled with 20 noded bricks allowing the stress intensity factor and J integral to be determined by virtual crack extension. The direction of crack growth has been determined both using off-axis virtual crack extension, and solutions for kinked cracks, to determine the orientation which maximise either the strain energy release rate or the mode I stress intensity factor. The calculated crack path agrees with reported experiments. The stress intensity factors for straight and curved cracks in simple welded joints have been compared in terms of their effective depth. Finally, the stress field in single edge bars under mixed mode elastic-plastic loading condition relevant to tubular joints has been analysed, and the size requirement for J dominance is discussed.

Acknowledgments

I gratefully thank my supervisor Professor John. W. Hancock for all his help and support during this research. His advice and guidance throughout this work were invaluable. I particularly want to thank him for his patience and kindness during the writing of this thesis.

Thanks are due to Professor B.F. Scott, Head of the Department of Mechanical Engineering for providing the equipment and facilities in the Engineering Laboratory. I am also glad to be able to acknowledge the financial support of the British Council and the Government of the People's Republic of China.

I also wish to acknowledge helpful discussion with Professor D.M. Parks in M.I.T., Professor F.M Burdekin in U.M.I.S.T. and Professor W.D. Dover in U.C.L..

Thanks to Mr. L. Williams in University of Manchester Region Computer Center and the System Managers in the C.A.E. Centre of the Department of Mechanical Engineering in the University of Glasgow for help in using the computer facilities and Mr. A. Torry for technical assistance in performing experiments.

Thanks are also due to Mr. C.W. Hodgson for part of the 3D mesh generation and all my friends in Mechanical Engineering who made my research enjoyable.

I also acknowledge Mr. Aaghakouchaak for using two of his diagrams. (Fig.1.1 and Fig.1.3)

Finally, I would like to express my gratitude to my mother, sisters, brothers and my wife for their love.

Notation

a	crack length
a'	curved crack length
b	uncracked ligament length
c	compliance, or "critical" or a material constant in the Paris law or "correction" if used as a subscript
e	subscript or superscript denoting on edge cracked bar
eff	subscript for "effective"
f	dimensionless coefficient
f_N, f_M	stress intensity factor calibrations
{f}	vector of prescribed nodal loads
g	strain energy release rate for kinked crack
hot	subscript for hot spot stress
k	stress intensity factor for kinked crack
m	dimensionless coefficient
max	subscript for "maximum"
min	subscript for "minimum"
n	subscript for strain hardening rate or a material constant in the Paris law
p	superscript for plate or subscript for plastic or potential energy
q_i	generalised line spring displacement
r	plastic zone size or subscript for reference
s	subscript for "stress" and surface
t	thickness for the brace of tubular joints or subscript for crack tip
u	displacement in x direction
v	displacement in y direction
w	displacement in z direction, or work, or weight function or

	superscript for welded joint
x	coordinate along a part through crack
y	subscript for yield
∞	superscript denoting far field variables
+, -	superscript for top and bottom limit along the discontinuity
A	area
B	thickness of a three point bend specimen
C	crack length for semi-elliptical crack
C_c	locally defined correction factor
[C]	line spring compliance matrix
E	Young's modulus
F	force
F(a)	function for reference stress intensity factor
G	energy release rate or crack driving force
G(a)	function for crack length
H(a,x)	weight function
J	J-integral
K	stress intensity factor
[K]	a matrix, particularly the global stiffness matrix
M	membrane moment/thickness or correction factor for stress intensity factor
N	membrane force/thickness or number of cycle
P	pressure
P_0	limit load
[P]	compliance for single edge cracked bar
Q_i	generalised line spring force
R	crack resistance
S	stress range
SCF	stress concentration factor

SIF	stress intensity factor
[S]	stiffness
T	Thickness of cracked bar or thickness of the chord of tubular joints
U	energy
W	width or strain energy density
X	coordinate along surface crack
α	a material constant
σ	stress
θ,	rotation of line spring or angle of kinked at a crack tip
δ	crack opening displacement or displacement of line spring
ε	strain
υ	Poisson's ratio
τ,α,β	geometric parameters of tubular joints
ρ	distance from a point in a plane crack to the crack front
γ_e	surface energy per unit area
γ_p	plastic work

Figure Captions

Tracey(71)

Fig.2.10. The non-dimensional function d_n against n and σ_y/E after Sailor (72)

Fig.2.11 The non-dimensional function d_n against n and σ_y/E after Shih(70)

Fig.2.12 The perfectly plastic slip-line fields for cracked bend bar, center cracked panel,and a double edge notched specimen

Fig.2.13 The kinematics of crack tip opening in terms of generalised load point displacements

Fig.2.14 The side view of a deeply cracked specimen

Fig.3.1 The geometry of the tubular welded T joint.

Fig.3.2 A schematic Illustration the connection of bricks, shells and transition elements

Fig3.3 a) A fifteen noded transition element made by degenerating a twenty noded brick element.

b) A twenty noded brick element.

c) A twelve noded transition element made by degenerating a twenty noded brick element

d) An eighteen noded transition element made by degenerating a twenty noded brick element

e) A schematic cross section through the weld, illustrating the brick elements,the transition elements, the shell elements and the crack

Fig 3.4 a) A finite element mesh using shell elements and line springs for axial loading case

b) A finite element mesh using shell and brick elements for axial loading case.

Fig.3.5 A finite element mesh using shell for the out-plane bending

Fig.5.10 A comparison of the non-dimensionalised maximum k_I ($k_I/\sigma\sqrt{a}$) between a central slant cracked bar and a central normal cracked bar under tension

Fig.5.11 A comparison of the non-dimensionalised maximum k_I ($k_I/\sigma\sqrt{a}$) between T-plate joint with a normal crack and a T-plate joint with a curved crack

Fig.5.12 Non-dimensionalised maximum k_I ($k_I/\sigma\sqrt{a}$) for a kinked crack and non-dimensionalised K_I ($K_I/\sigma\sqrt{a}$) for the normal main crack in a T plate joint as a function of a/T

Fig.6.1 The non-dimensionalised maximum k_I ($k_I/\sigma\sqrt{a}$) for the 3 dimensional brick model as a function of the angle, a/T=0.2, a/c=0.1

Fig.6.2. The non-dimensionalised maximum k_I ($k_I/\sigma\sqrt{a}$) for the 3 dimensional brick model as a function of the angle, a/T=0.6, a/c=0.3

Fig.6.3 The non-dimensionalised maximum k_I ($k_I/\sigma\sqrt{a}$) for the 3 dimensional brick model as a function of the angle, a/T=0.9,a/c=0.45

Fig.6.4 The non-dimensionalised maximum k_I ($k_I/\sigma\sqrt{a}$) for the shell model as a function of the angle, a/T=0.2, a/c=0.1

Fig.6.5. The non-dimensionalised maximum k_I ($k_I/\sigma\sqrt{a}$) for the shell model as a function of the angle,a/T=0.6, a/c=0.3

Fig.6.6. The non-dimensionalised maximum k_I ($k_I/\sigma\sqrt{a}$) for the shell model as a function of the angle,a/T=0.9, a/c=0.45

Fig.6.7. The non-dimensionalised g ($E'g/\sigma^2 a$)for the 3 dimensional bricks model with as a function of the angle, a/T=0.2, a/c=0.1

Fig.6.8. The non-dimensionalised g ($E'g/\sigma^2a$) for the 3 dimensional bricks model with as a function of the angle,a/T=0.6, a/c=0.3

Fig.6.9. The non-dimensionalised g ($E'g/\sigma^2a$) for the 3 dimensional bricks model with as a function of the angle,a/T=0.9, a/c=0.45

Fig.6.10 The predicted crack path and the experimental observation of Noordhoek et al.(52)

Fig.6.11 A comparison between the non-dimensionalised maximum k_I ($k/\sigma_h\sqrt{T}$) obtained numerically and the experimental data K_{exp} ($K_{exp}/\sigma_h\sqrt{T}$) for axial loading

Fig.6.12 A comparison between the non-dimensionalised effective stress intensity factor K ($E'G/\sigma^2a$) and the non-dimensionalised maximum k_I ($k_I/\sigma\sqrt{a}$) for normal cracks

Fig.7.1 The geometry of a edge cracked bar

Fig.7.2 The mesh of a single edge cracked bar loaded by force

Fig.7.3 The mesh of a single edge cracked bar under three point bending

Fig.7.4 A comparison of the non-dimensionalised $J=E'J/\sigma_n{}^2a$ for the present finite element calculation and the data of Kumar et al. (79) for a bar under axial loading

Fig.7.5 A comparison of the non-dimensionalised $J=E'J/\sigma_n{}^2a$ for the present finite element calculation and the data of Kumar et al. (79) for a bar under three point bending

Fig.7.6 A comparison of the non-dimensionalised $J=E'J/\sigma_y{}^2a$ at the deepest point of a semi-elliptical crack in a tubular T-joint under axial loading for the elastic material,the strain

hardening material and the light strain hardening material when a/T=0.9,a/c=0.45

Fig.7.7 A comparison of the non-dimensionalised $J=E'J/\sigma_y{}^2a$ at the deepest point of a semi-elliptical crack in a tubular T-joint under axial loading for the elastic material,the strain hardening material and the light strain hardening material when a/T=0.6,a/c=0.3

Fig.7.8 A comparison of the non-dimensionalised $J=E'J/\sigma_y{}^2a$ at the deepest point of a semi-elliptical crack in a tubular T-joint under axial loading for the elastic material,the strain hardening material and the light strain hardening material when a/T=0.2,a/c=0.1

Fig.7.9 The relationship between the non-dimensionalised applied force P/σ_yA, and the non-dimensionalised load point displacement v/T, where A is the section area of the brace and T is the thickness of the chord when n=3 and n=13 for a/T=0.9 a/c=0.45

Fig.7.10 The relationship between the non-dimensionalised applied force P/σ_yA, and the non-dimensionalised load point displacement v/T, where A is the section area of the brace and T is the thickness of the chord when n=3 and n=13 for a/T=0.6 a/c=0.3

Fig.7.11 The relationship between the non-dimensionalised applied force P/σ_yA, and the non-dimensionalised load point displacement v/T, where A is the section area of the brace and T is the thickness of the chord when n=3 and n=13 for a/T=0.2 a/c=0.1

Fig.7.12 A comparison of the non-dimensionalised $J=E'J/\sigma_y{}^2a$ at the

Fig.7.22 The ratio of bending moment to force times the ligament length as a function of a/T

Fig.8.1 A schematic illustration of a straight crack extends in a non-planar fashion along a plane inclined to the original crack plane by an angle.

Fig.8.2 a) A single edge cracked bar subject to asymmetric three point bending

b) Mesh of a single edge cracked bar subject to asymmetric three point bending

Fig.8.3 Maximum circumferential tensile stress normalised by the yield stress as a function of distance from the crack tip normalised by J/σ_y for asymmetric three point bending

Fig.8.4 Illustration of plastic zone for asymmetric three point bending

Fig.8.5 Mesh of a single edge cracked bar

Fig.8.6 Maximum circumferential tensile stress normalised by the yield stress as a function of distance from the crack tip normalised by J/σ_y for single edge cracked bar.

Fig.8.7 Mesh of a single edge slant cracked bar

Fig.8.8 Illustration of plastic zone for single edge slant cracked bar

Fig.8.9 Maximum circumferential tensile stress normalised by the yield stress as a function of distance from the crack tip normalised by J/σ_y for single edge slant cracked bar.

Fig.8.10 A finite element mesh for boundary layer formulation

Fig.8.11 Maximum circumferential tensile stress normalised by the HRR field as a function of T stress normalised by the

yield stress for boundary layer formulation.

Fig.8.12 Illustration of plastic zone obtained from boundary layer formulation solution

Table Captions

Table 3.1 The number and type of element as well as the number of degrees of freedom of the system for both shell model and 3D brick model

Table 3.2 A comparison of the non-dimensionalised $K_I=K_I/\sigma\sqrt{\pi a}$ and $K_{II}=K_{II}/\sigma\sqrt{\pi a}$ from current finite element calculations and the data given by Wilson (99)

Table 3.3 A comparison of the non-dimensionalised $K_I=K_I/\sigma\sqrt{a}$ and $K_{II}=K_{II}/\sigma\sqrt{a}$ at the deepest point of the semi-elliptical crack from the line-spring and brick element calculations under axial loading

Table 4.1 C_{ij} as a function of the angle for the kink crack derived by Bilby et al. (105)

Table 4.2 A comparison of the crack growth angle predicted using maximum g and maximum k_I theory with experimental data for the asymmetric specimens (x=3T)

Table 7.1 A dimensionless quantity $f^{p'}= J^p/\alpha\sigma_y\varepsilon_y a(P/P_0)^{n+1}$ as a function of a/T and n

Introduction

The integrity of many offshore structures is critically dependent on the behaviour of tubular welded joints. In the marine environment, fatigue is a major problem and is the most common cause of structural failure. The traditional approach to design against fatigue is based on S/N curves in conjunction with stress concentration factors. However, routine inspection reveals that structures may contain crack like defects introduced during manufacture. Alternatively cracks may develop early in the operational life, so that much of the life is occupied by fatigue crack growth. In this situation, design and maintenance is based on fatigue crack growth, as the traditional approach does not give any information on the relative contributions of crack initiation and crack growth.

The emergence of fracture mechanics has made the analysis of fatigue crack growth in offshore structures possible. The characterising parameter which relates crack growth rate to the applied stress is the stress intensity factor. The stress intensity factor provides a one parameter characterisation of the stress field ahead of a sharp crack and the energy available for propagation. Stress intensity factors of cracks in tubular joints can be obtained by analytical, numerical and experimental methods. However, full scale laboratory experiments are expensive and inconvenient for analysing the very wide range of crack shapes found in joints although they elucidate the essential features of the problem. In contrast, numerical methods provide potentially flexible and efficient techniques for determining the stress intensity factors of tubular joints subject to a wide range of loading systems .In this context, both weight functions and finite element methods have played an important role.

Two finite element techniques have been developed in the present work: a

virtual crack extension method involving solid brick elements, and line-springs in conjunction with shell elements. A comparison of the two approaches indicates that, former requires a large amount of computer memory and execution time, while the latter however has the virtue of simplicity and the consequential saving in computing time, but does not allow such detailed modelling.

Cracks in tubular joints are frequently found to follow complex paths. The prediction of the crack growth direction in such joints is thus an important problem, as fatigue analyses involve integrating the fatigue crack growth rates to chord penetration. The crack length and consequent fatigue life depend on the crack path through the chord. The direction of crack propagation has therefore been examined numerically by maximising the potential energy release rate, or the mode I stress intensity factor component under mixed mode loading. In order to verify the numerical calculations, a series of experiments were undertaken to verify the numerical models. Since modelling curved cracks in tubular joints is geometrically difficult, an alternative method has been proposed to simplify the problem, by establishing a relationship between the stress intensity factors for straight normal cracks and slant or curved cracks. This approach has been verified by comparing numerical results with well documented calculations on simple two dimensional cracked bars to give confidence for predictions in three dimensional structures.

Although developments in linear elastic fracture mechanics provide a powerful technique for assessing the integrity of cracked structures, LEFM analysis may be invalidated by the extent of plastic deformation, due to overloads in storm conditions. Elastic-Plastic Fracture Mechanics however provides more soundly based assessment of fracture behaviour in these conditions. In this case the appropriate characterising parameter is the J

integral.

To assess the response of defects in offshore structures under elastic-plastic conditions, a three dimensional tubular welded T-joint has been analysed by finite element methods for two strain hardening rates. However, as three dimensional elastic-plastic problems are demanding, both in terms of computer storage and cpu time, the extent to which the crack tip field could be modelled was necessarily limited. To assess the accuracy of the solutions bench-marking calculations which had the same crack tip element configuration and material response as the tubular welded joint were undertaken. In addition, non-linear line springs were used to calculate the fracture parameters under elastic-plastic conditions. The results have been compared with those obtained using detailed brick finite elements, and the application of the line spring method to model offshore structures has been verified for both elastic and elastic-plastic conditions.

Finally, the stress ahead of the crack tip under plane strain mixed mode loading conditions, relevant to tubular joints has been analysed. This has been studied by performing a series of numerical analysis on edge cracked bars subject to mixed mode loadings with varying ratios of mode II to mode I components. The full field finite element solutions have been compared with boundary layer formulations under small scale yielding conditions and with the mixed mode HRR field. The size requirement for J dominance of defects in tubular joints under elastic-plastic condition is then discussed.

CHAPTER 1. Linear Elastic Fracture Mechanics

Section 1.1 Stress Concentration Factors in Tubular Joints

Tubular joints are the most frequently occurring structural detail in jacket type steel offshore structures. The behaviour of tubular joints is of primary importance to the integrity of offshore steel jacket structures. The intersections of tubular members may be cast or welded. They may be planar or multi-planar and of simple or complex forms as shown schematically in Fig.1.1. The most common types of tubular T joints are made by welding one end of the vertical tubular (brace) onto the outside surface of other tubular member, which is known as the chord. This causes changes in cross section as well as complicated junctions between components. These discontinuities produce locally high stresses in which the ratio of peak stress to the applied stress is known as the stress concentration factor (SCF), which is used to limit the local stress on the material in relation to its yield or fatigue strength. For some joints, the SCF can produce a maximum stress at the intersection of the brace and the chord as high as twenty times the applied stress and aggravate the fatigue of tubular joints. The maximum stress can arise from three main causes; the basic structural response of the joint to the applied load producing nominal stresses, the need to maintain compatibility between the tubes, producing geometric stresses and highly localised deformations of the tube wall causing notch stresses.

Nominal stresses arise due to the tubes' behaviour as beams, and may be calculated by frame analysis of the structure. In contrast, the geometric stresses result from the difference in deformation between the chord and brace under load and can be appropriately analysed by regarding the tubes as thin walled shells whose thickness is very much less than their diameter.

In these circumstances stress analysis can be carried out on the assumption that the stress distribution is linear through the thin wall of the tube. Notch stresses however arise because of the finite thickness of the tube wall and the details of the geometry of the weldments, such as the weld angle and radius. The determination of notch stresses demands detailed modelling of the weld profile which is difficult to achieve due to the variety of weld details. An alternative, is to assess the hot spot stress which combines the response of nominal stresses and geometric stresses. This is defined as the maximum principal stress obtained by extrapolating the stresses along the tube to the weld toe avoiding the influence of the notch stresses. This procedure is illustrated in Fig.1.2 following the guidance notes of the U.K. Department of Energy (1). This stress is often used in fatigue calculations. The hot spot SCF, is defined as the ratio of the hot spot stress to the maximum nominal stress in the brace. A number of parametric studies using different methods of stress analysis have been carried out and parametric equations have been derived for hot spot SCF's in simple tubular joints. Of these equations, the sets in the most general use are due to Wordsworth and Smedley (2), based on the results of acrylic model tests; and Kuang et al. (3) and Gibstein (4) derived from a series of finite element analysis of tubular joints. These equations can be used to calculate the hot spot SCF's in three basic modes of loading (Fig.1.3); axial, out of plane bending (OPB) and in plane bending (IPB). As the hot spot stress excludes the notch stress due to the weld, hot spot stress concentration factors are only functions of the non-dimensional geometrical parameters (α, β, γ, τ, ζ) defined in Fig.1.4. As an illustration the following equations are presented following Kuang et al. (3).

$$SCF_{hot}=1.177(\gamma)^{0.808}e^{-1.2\beta^3}\tau^{1.333}(\alpha/2)^{0.057}$$

(Axial Loading)

$$SCF_{hot}=0.41(2\gamma)^{0.6}\beta^{3}\tau^{0.86}$$

(In-Plane Bending)

$$SCF_{hot}=0.465(2\gamma)^{1.014}\beta^{0.787}\tau^{0.889}$$

(Out-Plane Bending) $(0.3\leq\beta\leq0.55)$

$$SCF_{hot}=0.199(2\gamma)^{1.014}\beta^{-0.619}\tau^{0.889}$$

(Out-Plane Bending) $(0.5\leq\beta\leq0.75)$ Eqn.(1-1)

There are two basic approaches to the fatigue life assessment of tubular joints, the first method is described as the S-N approach and relies on an empirically derived relationship between the applied stress range and the number of cycles to failure. The second is based on linear elastic fracture mechanics and considers the crack growth rate at each stage in its propagation.

To predict fatigue life by the S-N approach, a linear fatigue damage model is used in conjunction with the relevant S-N curve. A S-N curve recommended by the U.K. Department of Energy Guidance Notes (1) is given in Fig.1.5 for joints in air or seawater where adequate protection against corrosion is provided. This curve is based on a total of 64 T, X and K joint test results and is recommended for joints having a chord thickness of 32mm. To assess the fatigue life of a tubular joint under random loading, several points, which include the saddle point or crown point around the periphery of a tubular joint are usually considered. The joint life includes the following three parts: N_1 is the number of stress cycles when the first visible crack appears; N_2 is the number of stress cycles to the penetration of the chord wall and N_3 is the number of stress cycles when the test stopped due to loss of stiffness. For a tubular joint under variable amplitude loading, each stress cycle will have an associated stress range.

If the ith stress cycle with stress range ΔS_i, and increment of damage equal to $1/N_i$ occurs, fatigue failure occurs as soon as the linear cumulative damage of the cycles in the variable amplitude loading sequence has achieved a critical value, that is,

$$\sum_{\substack{\text{all} \\ \text{cycle}}} \frac{n_i}{N_i} = D_S \qquad \text{Eqn.(1-2)}$$

Here, n_i is the number of cycles in the stress ranges ΔS_i which occur in the design life of the structure. N_i is the corresponding number of cycles to failure under constant amplitude loading obtained from the relevant S-N curve, and D_S is the damage summation failure limit, which is often taken as unity. The S-N approach however does not give any information about the extent of crack growth.

An alternative approach based on linear elastic fracture mechanics has therefore been increasingly used by the offshore industry. Linear elastic fracture mechanics (henceforth LEFM), is concerned with failure under largely elastic conditions, with the object of maintaining the integrity of structures, by establishing a relationship between the crack size and the fatigue crack growth rate or the failure stress. The principal objective is to determine the crack size that can be tolerated under service loading conditions. In practice this might involve determining how long it takes the minimum detectable crack to grow under fatigue loading to the critical size at which failure occurs. To address these questions, the material properties which relate the fracture stress or the fatigue crack growth rate to the applied stress system must be determined. When the structure is largely elastic, this relation is established by the concept of a stress intensity factor.

SECTION 1.2. The Stress Intensity Factor

When crack like flaws are present, stress concentration factors can not be used as the SCF for a sharp crack is infinite.(5). To illustrate this, consider an infinite plate under uniform tension with a central crack of length 2a as shown in Fig.1.6. The stress field was described by Westergaard (5) as an asymptotic infinite series about the crack tip:

$$\sigma_{yy}=\sigma\sqrt{(\pi a)}\cos(\theta/2)(1+\sin(\theta/2)\sin(3\theta/2))/\sqrt{(2\pi r)}+\text{term of order } r^0$$
$$\sigma_{xx}=\sigma\sqrt{(\pi a)}\cos(\theta/2)(1-\sin(\theta/2)\sin(3\theta/2))/\sqrt{(2\pi r)}+\text{term of order } r^0$$
$$\sigma_{xy}=\sigma\sqrt{(\pi a)}\cos(\theta/2)\sin(\theta/2)\cos(3\theta/2))/\sqrt{(2\pi r)}+\text{term of order } r^0$$

Eqn.(1-3)

where r,θ are the polar coordinates of a point with respect to the crack tip and σ is the remotely applied uni-axial stress.

If r<<a, the leading term in the expansion dominates the stress and strain field near the crack tip. In terms of principal stresses, the leading term of eqn.1-3 can be expressed as :

$$\sigma_1=\sigma\sqrt{(\pi a)}\cos(\theta/2)(1+\sin(\theta/2))/\sqrt{(2\pi r)}$$
$$\sigma_2=\sigma\sqrt{(\pi a)}\cos(\theta/2)(1-\sin(\theta/2))/\sqrt{(2\pi r)} \qquad \text{Eqn.(1-4)}$$

σ_3 is either 0 in plane stress or $\upsilon(\sigma_1+\sigma_2)$ in plane strain.
Consequently these equations adopt the general form

$$\sigma_{ij}=\sigma\sqrt{(\pi a)}f(\theta)/\sqrt{(2\pi r)} \qquad \text{Eqn.(1-5)}$$

where f(θ) are the appropriate universal functions of angle θ

From equation (1-5), it is clear that the stress components and corresponding stress concentration factors are infinite at the crack tip for cracks of all crack depths. Therefore, the stress concentration factor can not characterise the elastic stress field at a crack tip as it predicts no effect of crack length on the failure stress. As a result, some other parameter must be used.

For the specific case of an infinite plate under uniform tension, $\sigma\sqrt{(\pi a)}$ is defined as the stress intensity factor, denoted K. However, in general the stress intensity factor K can be expressed in the form:

$$K=f(a,t)\sigma\sqrt{(\pi a)} \qquad \text{Eqn.(1-6)}$$

where f(a,t) is a function of the geometry of the cracked body, crack size and loading conditions. Thus Eqn.1-5 can be written in the form

$$\sigma_{ij}=Kf(\theta)/\sqrt{(2\pi r)} \qquad \text{Eqn.(1-7)}$$

Since the applied stress system may involve tensile, in plane, or out of plane shear components, three corresponding stress intensity factors exist, which are known as mode I, K_I (the opening mode), mode II, K_{II} (the sliding mode) and mode III, K_{III}(the tearing mode) as illustrated in Fig1.7. In practice, mode I is usually the dominant mode and consequently most attention has been paid to this component.

The critical stress intensity factor for crack extension K_c depends on the specimen's thickness and material properties (6). But beyond a certain thickness, K_c becomes asymptotic, to a minimum value which is independent of the thickness and is a material property denoted K_{Ic}, the plane strain fracture toughness as shown in Fig.1.8. This can be explained in

terms of a constraint effect. Irwin (7) derived a purely empirical equation describing the effect of thickness on K_c,

$$K_c=K_{Ic}\sqrt{[1+1.4/B^2(K_{Ic}/\sigma_y)^4]} \qquad \text{Eqn.(1-8)}$$

In elastic conditions, for thick plates, $K_{Ic} << \sqrt{B}\sigma_y$,

$$K_c=K_{Ic} \qquad \text{Eqn.(1-9)}$$

When K_c becomes equal to K_{Ic}, the crack starts to extend, possibly in an unstable manner, and as a result, structures are designed to operate under conditions such that K is less than K_{Ic}.

SECTION 1.3. The Relation Between the Energy Approach and the Stress Intensity Factor

In 1920, Griffith (8) was the first to examine the energy balance in a body which contained a crack. He considered an infinite plate of unit thickness which contained a central through crack of length 2a under a remotely applied uniform tensile stress shown in Fig.1.6. The total elastic energy U of the cracked plate may be written as:

$$U=U_0+U_a+U_\gamma U_F \qquad \text{Eqn.(1-10)}$$

where U_0 is the elastic energy of the loaded uncracked plate; U_γ is the change in the surface energy caused by creating the the crack surfaces; Ua is the change in the elastic strain energy caused by introducing a crack in the plate; U_F is the work performed by external forces in this geometry. As

the crack deforms into an ellipse, the crack flank displacements can be given as:(6)

$$u=2\sigma\sqrt{(a^2-x^2)}/E' \qquad \text{Eqn.(1-11)}$$

Thus the change in elastic strain energy due to introducing a crack is:

$$U_a=\int_0^a \sigma u dx=\int_0^a \sigma^2 2\sqrt{(a^2-x^2)}\ /E'dx=\pi\sigma^2a^2/E' \qquad \text{Eqn.(1-12)}$$

where E' equals E in plane stress, and $E/(1-\upsilon^2)$ in plane strain. The total surface energy U_γ is equal to the product of the surface energy per unit area γ_e and the area of the crack per unit thickness.

$$U_\gamma=2(2a\gamma_e) \qquad \text{Eqn.(1-13)}$$

When the elastic energy release due to an increment of crack growth, da, as shown in Fig.1.9, outweighs the demand for surface energy for the same crack growth, then the crack extension is energetically favourable as illustrated on Fig.1.10.

Under fixed displacement conditions, no external work, U_F, is done and the energetically favourable condition for crack extension is obtained by setting dU/da equal to zero in eqn.(1-10)

$$\frac{d(\frac{-\pi\sigma^2a^2}{E'}+4a\gamma_e)}{da}=0 \qquad \text{Eqn. (1-14)}$$

$$\pi\sigma^2 a/E' = 2\gamma_e \qquad \text{Eqn. (1-15)}$$

The left hand side of this equation is called the strain or potential energy release rate, G and represents the elastic energy per unit crack surface area, available for infinitesimal crack extension. The right hand side of equation represents the surface energy increase that would occur owing to infinitesimal crack extension and is called the crack resistance, R.

However, the Griffith theory is restricted to ideally brittle materials in which there is no plasticity at the crack tip. In 1944 Irwin (9) showed that Eqn.1-15 could be modified, and applied to both perfectly brittle materials and materials that exhibit plastic deformation. The modification recognised that a material's resistance to crack extension is equal to the sum of the elastic surface energy, and the plastic work γ_p. Consequently, Eqn.1-15 was modified to

$$\pi\sigma^2 a/E' = 2(\gamma_e+\gamma_p) \qquad \text{Eqn.(1-16)}$$

For most materials $\gamma_p >> \gamma_e$, and the resistance to crack extension is mainly plastic work and the surface energy then can be neglected.

From the above discussion, it is clear that the energy approach is equivalent to the stress intensity factor approach (9) in which fracture occurs where a critical stress distribution ahead of crack tip is reached. The material property governing fracture may therefore be stated as a critical stress intensity factor K_c or equivalently a critical strain energy release rate G_c. For tensile loading, the relation between K_c and G_c (or K and G) in linear elastic fracture mechanics is :

$$G_c = K_c^2/E' \qquad \text{Eqn.(1-17)}$$

As a result, the energy balance and elastic stress field approach are directly equivalent.

SECTION 1.4,The Validity of Linear Elastic Fracture Mechanics

Linear elastic fracture mechanics is limited by the requirement for the body to be largely elastic, even though localised plasticity may occur in a small region at the crack tip. The validity of linear elastic fracture mechanics is determined by the size of the crack tip plastic zone. Using the Von Mises yield criterion, the plastic zone r_y can be estimated as follows. Yielding occurs when

$$(\sigma_1-\sigma_2)^2+(\sigma_2-\sigma_3)^2+(\sigma_3-\sigma_1)^2=2\sigma_{eff}^2 \qquad \text{Eqn.(1-18)}$$

when the effective stress σ_{eff} equals the uniaxial yield stress σ_y
Recalling Eqn.(1-4) , in plane stress conditions, the radius of the plastic zone r_y is

$$r_y= 1/2\pi(K_I/\sigma_y)^2\text{Cos}^2(\theta/2)(1+\text{Sin}^2(\theta/2)) \qquad \text{Eqn. (1-19)}$$

Straight ahead of the crack, $\theta=0$ and Eqn.1-19 can be reduced to

$$r_y=1/2\pi(K_I/\sigma_y)^2 \qquad \text{Eqn.(1-20)}$$

For plane strain with Poisson's ratio $\upsilon=1/3$, the plastic zone size is

$$r_y= 3/4\pi(K_I/\sigma_y)^2\,(2/9\text{Cos}^2(\theta/2)\ +3/2\text{Sin}^2\theta) \qquad \text{Eqn.(1-21)}$$

When $\theta=0$, Eqn.1-21 can be reduced to

$$r_y = 1/6\pi \, (K_I/\sigma_y)^2 \qquad \text{Eqn.(1-22)}$$

From these expressions it is clear that the plastic zone size in plane strain is smaller than that in plane stress. This arises because under plane strain conditions there is a much higher hydrostatic component of the stress system which does not produce yielding.

Valid LEFM is ensured if the specimen dimensions are large compared to the plastic zone size r_y. In other words, the smallest relevant length such as the crack length, ligament or thickness must be large compared to the plastic zone size (10). The necessary size requirements given by the ASTM (10) are

$$a \geq 2.5(K_{Ic}/\sigma_y)^2$$
$$B \geq 2.5(K_{Ic}/\sigma_y)^2$$
$$W \geq 5.0(K_{Ic}/\sigma_y)^2 \qquad \text{Eqn.(1-23)}$$

Where σ_y is the yield stress and the dimensions a,B,W are illustrated in Fig1.11

Section 1.5, Methods for Determining Stress Intensity Factors

1.5.1 General form for Stress Intensity Factors

There are many methods of determining the stress intensity factors, including experimental; theoretical and finite element methods. Some of these are particularly suitable for assessing the stress intensity factors of tubular joints, and emphasis has been put on these methods. The most important geometry is the semi-elliptical surface crack as this is the most

common form of crack found in engineering structures. Such cracks are often called part through cracks as opposed to through crack problems which being two dimensional are simpler and are thus discussed first.

The stress intensity factor for through cracks takes the form:

$$K=f(a/t)\sigma\sqrt{(\pi a)} \qquad \text{Eqn.(1-24)}$$

f(a/t) is a non-dimensional function of the geometry of the cracked body. As an example, it is appropriate to consider some simple geometries with through cracks. For a finite width plate with an edge crack under uniaxial tensile stress (Fig.1.12), the stress intensity factor can be given by: (11)

$$K_I=\sigma\sqrt{(\pi a)}(1.12-0.23(a/t)+10.6(a/t)^2-21.7(a/t)^3+30.4(a/t)^4) \qquad \text{Eqn.(1-25)}$$

where σ is the applied stress.

For the same geometry under pure bending (12) (Fig.1.13)

$$K_I=6M\sqrt{\pi a/t^2}(1.12-1.39(a/t)+7.32(a/t)^2-13.1(a/t)^3+14.0(a/t)^4). \qquad \text{Eqn.(1-26)}$$

where M is the bending moment.

In addition for the same geometry (12) under the three point bending configuration shown in Fig.1.14

$$K_I=6M\sqrt{\pi a/t^2}(1.11-1.55(a/t)+7.71(a/t)^2-13.5(a/t)^3+14.2(a/t)^4). \qquad \text{Eqn.(1-27)}$$

where L/t=4 and M=LP/2, P is the applied load and L is the distance between

the two constrained points. When L/t=2 and M=LP/2

$$K_I=6M\sqrt{\pi a/t^2}(1.09-1.73(a/t)+8.20(a/t)^2-14.2(a/t)^3+14.6(a/t)^4)$$

Eqn.(1-28)

For semi-elliptical, or part through cracks, the stress intensity factors may be written in a form suggested by Irwin (13)

$$K=M_S M_t M_p \sigma\sqrt{(\pi a)}/\phi_0 \qquad \text{Eqn.(1-29)}$$

Where Ms , Mt, Mp and ϕ_0 are non-dimensional correction factors.

M_S is a correction to allow for the effect of a free surface at the mouth of the crack, which depends on the ratio of crack depth to width and varies with position around the crack front. Paris and Sih (14) suggest the free surface correction to be

$$M_S=1+0.12(1-a/c) \qquad \text{Eqn.(1-30)}$$

Later this correction factor has been studied in detail by Smith (15), who gives

$$M_S=f(\alpha)[(a/c)^2\mathrm{Cos}\phi+\mathrm{Sin}\phi]^{1/4}[1.1/f(a)-(1.1/f(\alpha)-1)a/c].$$

Eqn.(1-31)

where α defines the position around the crack mouth corresponding to the crack front position ϕ shown in Fig.1.15, and $f(\alpha)$ is a correction factor. The form of the solution can best be summarised by plotting M_S values against a/2c as illustrated in Fig.(1.16).

M_t is a correction factor which allows for the presence of a free surface ahead of the crack, which depends both on the crack depth to plate thickness ratio and the crack front shape. Kobayashi and Smith(16) obtained the approximate values of M_t shown in Fig.1.17.

Mp is a correction factor which allows for crack tip plasticity, this depends on the size of the crack and the size of crack plastic zone. It is relatively unimportant and can be ignored unless a/B is large and the value of a/2c is small. ϕ_0 is the complete elliptical integral defined as:

$$\phi_0 = \int_0^{\pi/2} [1-(1-a^2/c^2)\sin^2\phi]^{1/2} d\phi \qquad \text{Eqn.(1-32)}$$

As most service cracks originate at a stress concentrations, such as a weld toe, it is necessary to assess the influence that the stress concentrations have on the stress intensity factor. One approach would be to assume that K was simply magnified by the stress concentration factor, SCF, regardless of the crack depth. However, the effective value of the SCF, near the crack tip, decreases as the crack propagates away from the stress concentration, so that this approach leads to an overestimation of K. Recently, Hayes (17) and Burdekin (18) have provided stress intensity factor solutions for cracks in the regions of stress concentration and which are directly relevant to the current problem of a crack at the toe of a fillet weld. In their studies, Hayes and Burdekin introduced a factor M_K which varies according to the ratio of the crack depth to the thickness of the wall, as a magnification factor for the influence of the stress concentration on the stress intensity factor.

From the above discussion, it is clear that the determination of the stress intensity factors is essentially a problem of determining the appropriate correction factors for through-thickness and part-through (semi-elliptical)

cracks.

1.5.2 Experimental Methods

1.5.2.1 Compliance Method

The most direct approach to determining stress intensity factors is to assess the stress and strain near the crack tip, but this method has the difficulty of requiring detailed modelling. It is therefore often more convenient to evaluate stress intensity factors by obtaining the compliance C, which is simply equal to v/P, where P is the applied force and v is the corresponding displacement as illustrated in Fig.1.18. The change in the potential energy of the system as the crack increases by an infinitesimal amount da is given by the potential energy release rate G.

$$GBda=d(U_F-U_a) \qquad \text{Eqn.(1-33)}$$

By substituting

$$U_a=Pv/2 \qquad \text{Eqn.(1-34)}$$

and

$$U_F=Pv \qquad \text{Eqn.(1-35)}$$

and v=PC into Eqn.1-33, the following relation between the stress intensity factor and compliance was obtained by Irwin: (9)

$$K_I^2=GE'=\frac{P^2E'}{2B}\frac{\partial C}{\partial a} \qquad \text{Eqn.(1-36)}$$

This equation gives an explicit relation between the crack extension force G and the compliance C. Thus if the compliance can be obtained as a function of crack length, as shown in Fig.1.19, K_I may be calculated using Eqn.1-36. A well known example of this technique is the double cantilever beam specimen shown in Fig.1.20.

The displacement v in the load line of the DCB specimen is given by

$$v=\frac{2Pa^3}{3EI}=\frac{8Pa^3}{EBh^3} \qquad \text{Eqn.(1-37)}$$

Since

$$C=v/P \qquad \text{Eqn.(1-38)}$$

$$C=8a^3/EBh^3 \qquad \text{Eqn.(1-39)}$$

and

$$dC/da=24a^2/EBh^3 \qquad \text{Eqn.(1-40)}$$

From equation 1-36, one obtains

$$K_I^2=GE'=\frac{E'P^2}{B}\frac{dC}{da}=\frac{12E'P^2a^2}{EB^2h^3} \qquad \text{Eqn.(1-41)}$$

for plane stress

$$K_I=\frac{2\sqrt{3}Pa}{Bh^{3/2}}$$ Eqn.(1-42)

while for plane strain

$$K_I=\frac{2\sqrt{3}Pa}{Bh^{3/2}(1-\upsilon^2)}$$ Eqn.(1-43)

1.5.2.2 Experimental Technique using Fatigue

This approach is based on the relation between the stress intensity factor and the rate of crack growth under cyclic loading conditions. A model which has met with considerable success and still remains simple is the well known Paris relationship:

$$da/dN=c(\Delta K)^n$$ Eqn.(1-44)

Here, da/dN is the rate of crack propagation, which represents an increment of crack length per fatigue cycle dN. ΔK is the stress intensity range, c and n are experimentally determined constants which depend on the material, and the environmental conditions. By performing a fatigue test on a standard specimen whose stress intensity factor is already known, Dover et al (19) obtained the material parameters c and n for a typical offshore steel denoted BS4360 50D which is used to make tubular joints. To obtain stress intensity factors for tubular joints, the problem is to measure crack growth rates in tubular joints. To do this, Dover and co-workers (20) have performed a series of fatigue tests on tubular joints using the A.C.

potential drop technique to monitor the crack length. In this technique an alternating current is applied through leads at the specimen ends, probes are located each side of the crack to measure the potential drop across the crack as it grows. The potential difference between the two probes can be related to the crack length provided a suitable calibration curve is available. As a result, the stress intensity factors for tubular joints were obtained from full scale experiments. Some values of stress intensity factors non-dimensionalised with respect to applied stress and the crack depth for various tubular joints, as determined by this procedure, are plotted as a function of a/T in Fig.1.21. However, due to the variety of tubular joints, direct measurements of the stress intensity factor in full scale tests is inconvenient and expensive. An alternative is therefore to use numerical methods.

1.5.3 Stiffness Derivative Finite Element Technique

The principle of the stiffness derivative or virtual crack extension technique lies in the relation between the crack tip stress field as characterised by the stress intensity factor and the potential energy release rate. The direct approach to this problem would necessitate determining the change in stiffness or potential energy by undertaking solutions for cracks with incremental different lengths. This technique was used by Brown, Hancock and Green (21) for through cracks in tubular joints. This procedure is however very inefficient, and a more elegant and efficient technique for calculating the change in potential energy as the crack undergoes infinitesimal extension has been developed by Parks (22), who introduced the stiffness derivative finite element technique. Subsequently a closely related approached was developed by Hellen (23), who aptly named the technique 'virtual crack extension'. Recently, this method has been

developed by Delorenzi (24) and Delorenzi and Shih (25), and has been used to derive the energy release rate for a general 3-dimensional crack configuration not from a finite element, but from a continuum mechanics viewpoint. Here, however, an account of the virtual crack extension method is given following Parks (22)

Suppose that a finite element analysis has been performed on a given planar linear elastic body of unit thickness containing a crack, a set of equations relate the stiffness, displacement and nodal load as described by Zienkiewicz (26)

$$[K]\{v\}=\{f\} \qquad \text{Eqn.(1-45)}$$

where [K] is the master stiffness matrix, $\{f\}$ is the vector of prescribed nodal loads and v are the nodal displacements. Now consider a small virtual increment Δa in crack length with no change in external mechanical loading, then following Zienkiewicz (26), the potential energy U_p of the model can be represented as

$$U_p=0.5\{v\}^T[K]\{v\}-\{v\}^T\{f\} \qquad \text{Eqn.(1-46)}$$

where the superscript 'T' denotes a transpose. The energy release rate G is obtained from the rate of change of potential energy U_p with respect to crack length at constant load

$$\frac{\partial U_p}{\partial a} = \frac{\partial [v]^T}{\partial a} [[K][v]-[f]] \; -0.5[v]^T \frac{\partial [K]}{\partial a}[v] \; +[v]^T \frac{\partial [f]}{\partial a} \qquad \text{Eqn.(1-47)}$$

Now,[K] is symmetric and the vector in the square brackets is zero, so for

plane strain

$$\frac{\partial U_P}{\partial a} = \frac{K_I^2(1-\upsilon^2)}{E} = -0.5[v]^T \frac{\partial [K]}{\partial a}[v] + [v]^T \frac{\partial [f]}{\partial a} \qquad \text{Eqn.(1-48)}$$

The matrix $\partial[K]/\partial a$ represents the change in the master stiffness matrix per unit crack advance. In the mesh shown in Fig. 1.22, there are two contours 1 and 2 around the crack tip. If all nodes on or within a contour 1 were displaced by only a very small amount Δa in the x-direction, while all the other nodes remain in their original position, the master stiffness matrix [K] depends on only individual elements. The geometry, displacement function and materials properties remain unchanged in the regions interior to 1 and exterior to 2, and so only the band of elements between the contours is related to $\partial[K]/\partial a$, if the number of element between the contour 1 and 2 is N_c, one has

$$\partial[K]/\partial a = \sum_{i=1}^{N_c} \partial[K_i]/\partial a \qquad \text{Eqn.(1-49)}$$

and $\partial[K_i]/\partial a$ may be approximated by simple forward finite difference as

$$\frac{\partial [K_i]}{\partial a} = \frac{\Delta [K_i]}{\Delta a} = \frac{[K_i]_{a+\Delta a} - [K_i]_a}{\Delta a} \qquad \text{Eqn.(1-50)}$$

where $[K_i]_a$ is the stiffness of an inter-contour element, calculated with its initial nodal coordinates and $[K_i]_{a+\Delta a}$ is the elements' stiffness calculated with the x-coordinates of each of its nodes lying on contour 1 incremented

by Δa. If the loading is due to forces outside the crack tip element, then $\partial f/\partial a=0$, and the final term of Eqn (1-48) can be dropped, reducing (Eqn.1-48) to

$$\frac{K_I^2(1-\upsilon^2)}{E} = -0.5[v]^T \frac{\partial[K]}{\partial a} [v] \qquad \text{Eqn.(1-51)}$$

This method can be extended to non-planar crack configurations as well, in which case, in Eqn.1-49 would be the number of the element within the outer contour 2 rather than just the band of elements between contour 1 and 2, since the stiffness of all elements within contour 2 varies with crack advance. In practice this method has proved to be very accurate (23) and has the advantage that its implementation does not require a second solution for a slightly different crack length, nor does it require special crack tip elements and rather coarser finite element meshes can be used which enhances the possibility of three dimensional analysis. Moreover Parks (27) has extended the validity of this method to nonlinear elastic and elastic /plastic materials.

1.5.4 Weight Functions

Weight functions were introduced by Bueckner (28,29), and later developed by Parks (30), who noted that any linear elastic crack problem can be reduced by superposition to that of an uncracked body plus that of the cracked body loaded by surface tractions present on the interface of the loaded but uncracked body. The principle of superposition is illustrated in Fig.1.23. Initially, consider a plane with a straight edge crack of length "a" on the axis oX. A finite surface stress σ is applied on both sides of the

crack surface at coordinate x shown in Fig.1.24. Using the solution for the stress intensity factor of a single edge cracked bar with a surface stress σ located at 'x', K can be written in the form

$$K=\sigma H(x,a) \qquad \text{Eqn.(1-52)}$$

where H(a,x) is only a function of the geometry of the cracked configuration in a symmetric planar body. This concept can be extended to the creation of a stress free crack surface by the application of appropriate face stress $\sigma(x)$ shown in Fig.1.25. The stress intensity factor can then be expressed in the form

$$K_I=\int_0^a \sigma(x)H(a,x)dx \qquad \text{Eqn.(1-53)}$$

Here $\sigma(x)$ is the stress distribution perpendicular to the crack surface in the uncracked component. Bueckner (28,29) and Rice (31) pointed out that weight functions could easily be determined if the displacement field $v_r(a,x)$ was obtained and stress intensity factors K_r as function of crack length were known

$$H=H(a,x)=\frac{E'}{K_r}\frac{\partial v_r(a,x)}{\partial a} \qquad \text{Eqn.(1-54)}$$

As an example, Petroski and Achenbach (32) proposed the following expression as an approximation for $v_r(a,x)$ for the cracked pressure vessel shown in Fig.1.26.

$$v_r(a,x)=\frac{\sigma_0[4F(a)\sqrt{(a)}\ \sqrt{(a-x)}+G(a)\ \frac{(a-x)^{3/2}}{\sqrt{a}}]}{H\sqrt{2}}$$

Eqn.(1-55)

Here r is the polar coordinates of a point with respect to the crack tip, and the reference stress intensity factor K_r is given by

$$K_r=\sigma_0\sqrt{(\pi a)}F(a)$$

Eqn.(1-56)

and σ_0 is a stress parameter of the reference stress field $\sigma_r(x)$. It is convenient to set $\sigma_r(x)=\sigma_0$=constant. The unknown function G(a) in equation (1-55) has to be determined using the requirement for self-consistency in equation (1-53), putting $K=K_r$

$$\sigma(x)=\sigma_r(x)$$

Eqn.(1-57)

This leads to

$$G(a)=\frac{5\pi}{\sqrt{2}a^2}\int_0^a[F(a)]^2da-\frac{20}{3}F(a)$$

Eqn.(1-58)

For $\sigma_r(x)=\sigma_0$=constant

Another way of obtaining the reference stress intensity factor (33) or the reference crack opening displacement is to use finite element calculations. Only the displacement at the crack mouth v_{max} is required from the finite element calculations, while for the X-dependence of the crack opening displacement, one has

$$v_r(x,a)=v_{max}(a)(1-x/a)^{1/2} \qquad \text{Eqn.(1-59)}$$

Weight functions are very efficient for calculating stress intensity factors in two dimensional problems. Once the weight function is known, the calculation of K is reduced to a simple integral and requires only the calculation of the stress along the crack line in the uncracked body. This method may be extended to the general three dimensional case (28) as:

$$K_I=\frac{E'}{K_r}\int_{crack}\sigma(a,s)\frac{\partial u}{\partial a}ds \qquad \text{Eqn.(1-60)}$$

However in this case the method is rather less convenient because of the requirement for a reference solution for K_r and an associated displacement field.

In order to evaluate the stress intensity factors of semi-elliptical surface cracks in tubular joints, two different techniques using weight functions are presented. The first method is to estimate the stress intensity factors of embedded irregular cracks using a form of generalised weight function known as the O-integral (34) to which correction factors for surface cracks have been introduced. The second method is a technique which uses weight functions for cracks in two dimensional bodies to calculate SIFs, for surface cracks.

1.5.4.1 O-Integral Technique

Oore and Burns (34) applied the weight function method to calculate the stress intensity factor of an irregular flat crack embedded in an infinite solid subject to an arbitrary normal stress field. At a specific point Q'

shown in Fig.1.27 on the crack front, the stress intensity factor is expressed an integral calculated on both crack surfaces, having area A,

$$K_{Q'}=\iint_A w(x,y)\sigma_Z(x,y)dA \qquad \text{Eqn. (1-61)}$$

Here, both the weight function w and the internal stress σ_Z are two dimensional variables. After studying the weight function for a circular embedded crack; a semi-infinite straight crack front in an infinite solid (34); and a circular ligament in an infinite cracked solid (35); Oore and Burns (36) proposed a general form of weight function at point Q' where a point load is applied at point Q as

$$W_{QQ'}=\frac{\sqrt{2}}{\pi l_{QQ'}^2\left[\int_s \frac{ds}{\rho^2}\right]^{1/2}} \qquad \text{Eqn.(1-62)}$$

Here, $l_{QQ'}$ is the distance between Q and Q' and ρ is the distance from the point load at Q to the center of the element of crack front ds.

In order to evaluate stress intensity factors of surface cracks, Oore and Burns (36) later introduced a correction factor C_c for embedded cracks. It was assumed that the ratio of the stress intensity factor at a point on the surface crack to the stress intensity factor at a corresponding point of the embedded crack is a constant (C_c) which is dependent on geometry but not on loading. This assumption enables the stress intensity factor for surface cracks to be evaluated. Burdekin et al. (37) and Dover et al. (38) have used the O-integral weight function method to calculate the stress intensity factors for plate joints and tubular joints. In comparison with the experimental results, the stress intensity factor at the deepest point of

the crack, the results were in broad agreement for the intermediate range of the crack depth, however the results usually under predicted the stress intensity factors for cracks of depth greater than half of tubular wall thickness. The disagreement is most significant for low a/c ratios, and has been regarded as the effect of bending stress. Recently, some modified correction factors correcting this problem have been introduced by Desjardins et al.(39). However these correction factors are dependent on the loading mode.

1.5.4.2 Nui and Glinka Weight Function

Recently, Niu and Glinka (40) have derived a weight function which allows the stress intensity factor to be calculated at the deepest point of a semi-elliptical surface crack in a tee-butt weld. They also derived the stress distribution for a range of geometries by performing the stress analysis of the uncracked joints. Initially Niu and Glinka (40) derived a weight function for flat plates, and a weight function, which was a function of weld angle and weld radius for an edge crack in a T-butt welded joint. Then they assumed that:

$$K_s^w = \frac{K_e^w}{K_e^p} K_s^p \qquad \text{Eqn.(1-63)}$$

here, K^w_s is the stress intensity factor for a surface crack in a welded joint, K^p_s is the stress intensity factor for a surface crack in a plate subjected to the same stress distribution, K^w_e is the stress intensity factor for an edge crack in a welded joint and K^p_e is the stress intensity

factor for an edge crack in a plate subjected to the same stress distribution.

Using this assumption, they found that the effect on the stress intensity factor of the weld angle was much larger than of the weld radius (41), agreeing with finite element results by Bell et al. (42).

1.5.5 The Line Spring Technique

The line spring method is an efficient computational technique proposed by Rice and Levy (43) as a simplified method for analysing surface cracks in plate and shell-type geometries. The simplicity of the model lies in the way in which a three dimensional crack analysis problem can be reduced to a quasi 2-D, shell problem which is economical in computing time. Recently this technique has received considerable attention (44,45,46,47), and the results obtained have been found to be in good agreement with complete 3-D solutions. For example Parks (45) and Desvaux(48) found agreement of better than 3% between line spring calculations and a full three dimensional solution (49) at the deepest point of the crack with an aspect ratio of 0.2 in a flat plate, while calculations on simple cylinders containing cracks with an aspect ratio of 0.33 gave agreement to within 2%.

The line-spring concept of Rice and Levy (43) is illustrated in Fig.1.28 which shows a surface crack of length 2c and variable depth a(x) in plate or shell of thickness t. A two dimensional idealisation of the configuration is shown in Fig.1.28; in which a part through surface crack is idealised as a through wall crack of length 2c with a series of one dimensional springs across the crack faces. The plate is loaded remotely by a membrane force N^{∞} and a bending moment M^{∞} per unit length. Because of the uncracked ligament, there are non-zero membrane forces N(x) and bending moments

M(x) transmitted across the crack faces. If $\Delta(x)$ and $\theta(x)$ represent the relative displacement and rotation of the plate mid-surface across the crack faces, respectively, these displacements and rotations are related to the plate mid-surface displacements $v_X(x,y)$,$v_Y(x,y)$ and $v_Z(x,y)$ by:

$$\Delta(x)=v_y^{+}(x,0)-v_y^{-}(x,0) \qquad \text{Eqn.(1-64)}$$

$$\theta(x)=\partial v_z^{-}(x,0)/\partial y-\partial v_z^{+}(x,0)/\partial y \qquad \text{Eqn.(1-65)}$$

where + and - signs refer to top and bottom limits along the discontinuity in Fig1.28. Note also that $\Delta(x)$ and $\theta(x)$ are work conjugate displacements to N(x) and M(x), respectively. Line spring modelling relates these local force and moments to $\Delta(x)$ and $\theta(x)$ at each point along the cut in following manner:

$$\begin{bmatrix}\Delta(x)\\ \theta(x)\end{bmatrix}=\begin{bmatrix}c(x)_{11} & c(x)_{12}\\ c(x)_{21} & c(x)_{22}\end{bmatrix}\begin{bmatrix}N(x)\\ M(x)\end{bmatrix} \qquad \text{Eqn.(1-66)}$$

or, equivalently

$$\begin{bmatrix}N(x)\\ M(x)\end{bmatrix}=\begin{bmatrix}s(x)_{11} & s(x)_{12}\\ s(x)_{21} & s(x)_{22}\end{bmatrix}\begin{bmatrix}\Delta(x)\\ \theta(x)\end{bmatrix} \qquad \text{Eqn.(1-67)}$$

where C and $S=C^{-1}$ are the local elastic compliance and stiffness matrices, respectively.

In order to implement the line spring element, determination of the local compliance [C(x)] is required. This is obtained by modelling each spring as a

plane strain edge cracked plate specimen of width t and crack depth a subject to an axial force N and a bending moment M per unit thickness. If Δ_c and θ_c are the load-point displacement and rotation in the single edge cracked plate due to the crack then, the following relationship can be defined for elastic conditions:

$$\begin{bmatrix} \Delta_c \\ \theta_c \end{bmatrix} = \begin{bmatrix} P_{11} & P_{12} \\ P_{21} & P_{22} \end{bmatrix} \begin{bmatrix} N \\ M \end{bmatrix} \qquad \text{Eqn.(1-68)}$$

Here the matrix P is obtained from the stress intensity factor solution for an edge cracked plane strain bar following procedures outlined in reference (43) or by directly using the elastic solutions for Δ_c and θ_c developed by Kumar and Lee (50). The line spring method assumes that C=P and consequently $S=P^{-1}$.

In a line spring analysis of a surface crack problem, the springs are placed across a through-crack in an appropriate finite element shell model. The resulting set of equations are solved for $\Delta(x)$ and $\theta(x)$. N(x) and M(x) are in turn calculated and the local stress intensity factor $K_I(x)$ derived from the relationship

$$K_I(x) = \sqrt{(\pi a(x))}\left[f_1\left(\frac{a(x)}{t}\right)\frac{N(x)}{t} + f_2\left(\frac{a(x)}{t}\right)\frac{6M(x)}{t^2}\right] \qquad \text{Eqn.(1-69)}$$

where f_1 and f_2 are dimensionless functions of crack depth to thickness ratio which can obtained by referring to a single edge plane strain bar under tension or bending respectively.This basic technique has been extended by Desvaux. (48) to incorporate Mode 2 and Mode 3 loadings.

This method has been used by Huang and Hancock (51), to model semi-elliptical cracks in a tubular welded T-joint. This is a complex problem using conventional fracture mechanics methods, as the crack originates at a site of stress concentration. They considered a tubular welded T joint with a semi-elliptical crack located at the chord and brace intersection under tension, in-plane bending and out plane bending. The crack was located at a position representative of the weld toe at the chord side of the chord and brace intersection. This was chosen to be one brace wall thickness from the centre line intersection. For shallow cracks, the notch stress due to the weld detail has a significant effect on the stress intensity factor, and shell elements can not take account of this effect. Thus, the unmodified line spring method is not appropriate for shallow cracks at stress concentrations. However for deeper cracks in which the ratio of the crack depth to the chord thickness (a/T) is larger than 0.2, the effect of the notch stress on the stress intensity factor decreases, and good agreement was obtained between their results and the experimental results (20) in the range $0.2<a/T<0.8$. However, when $a/T>0.8$, their finite element result gives significantly lower values than the experimental results. This is most likely due to the fact the crack path is no longer normal to the chord wall but adopts a curved path under the chord-brace intersection (52). In the present work, this problem has been addressed using either maximum strain energy release rate or k_I component theory, and the details are given in Chapters 4 ,5 and 6.

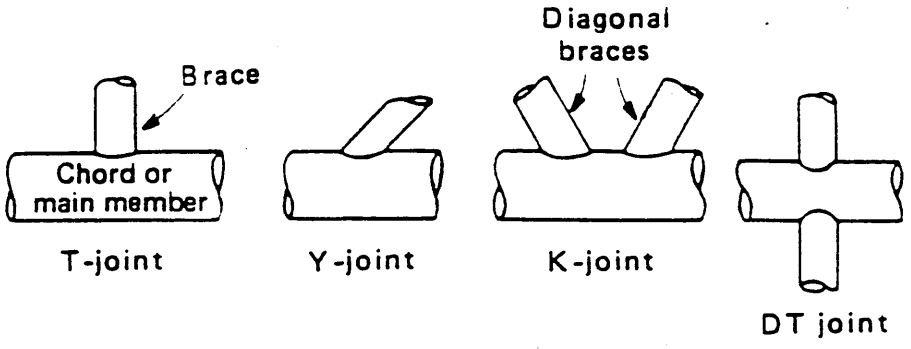

a) Simple joints

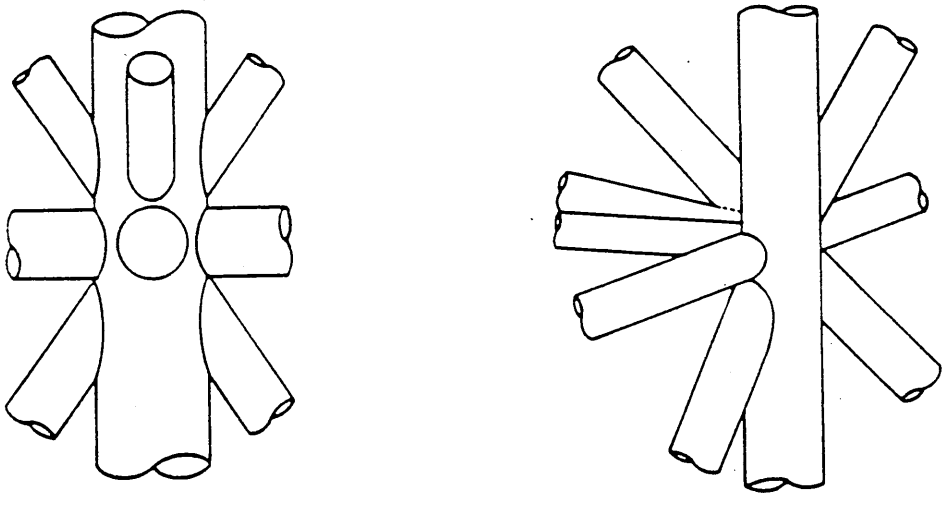

b) Multiplanar joint

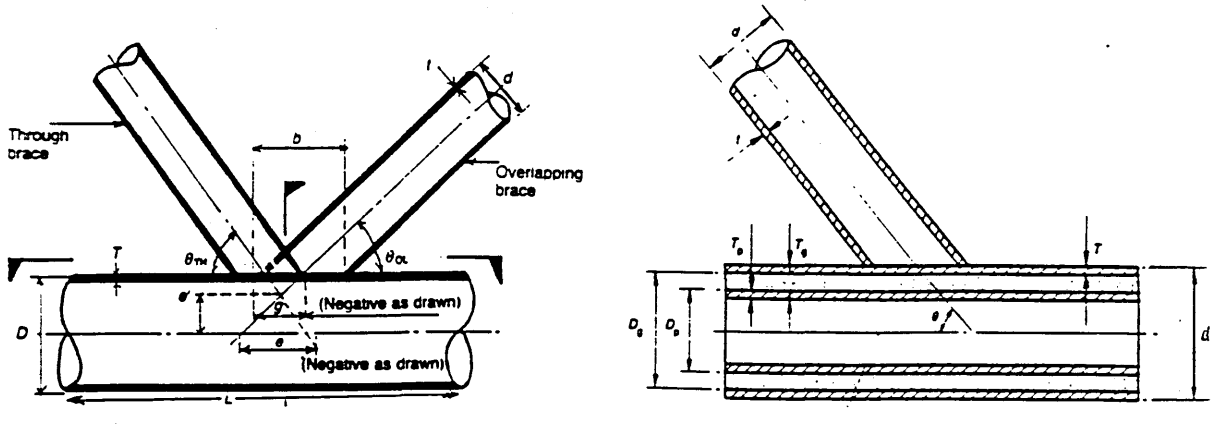

c) Overlapped joint

d) Composite joint

FIG.1.1 Schematic illustration of planar and multi-planar tubular joints

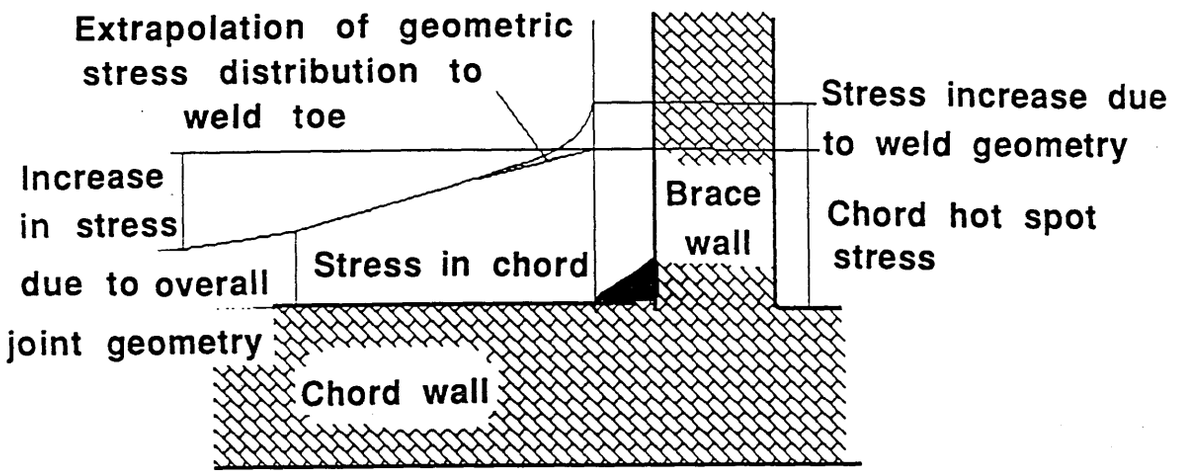

FIG.1.2 An illustration of the hot spot stress following the guidance notes of the U.K. energy department (1)

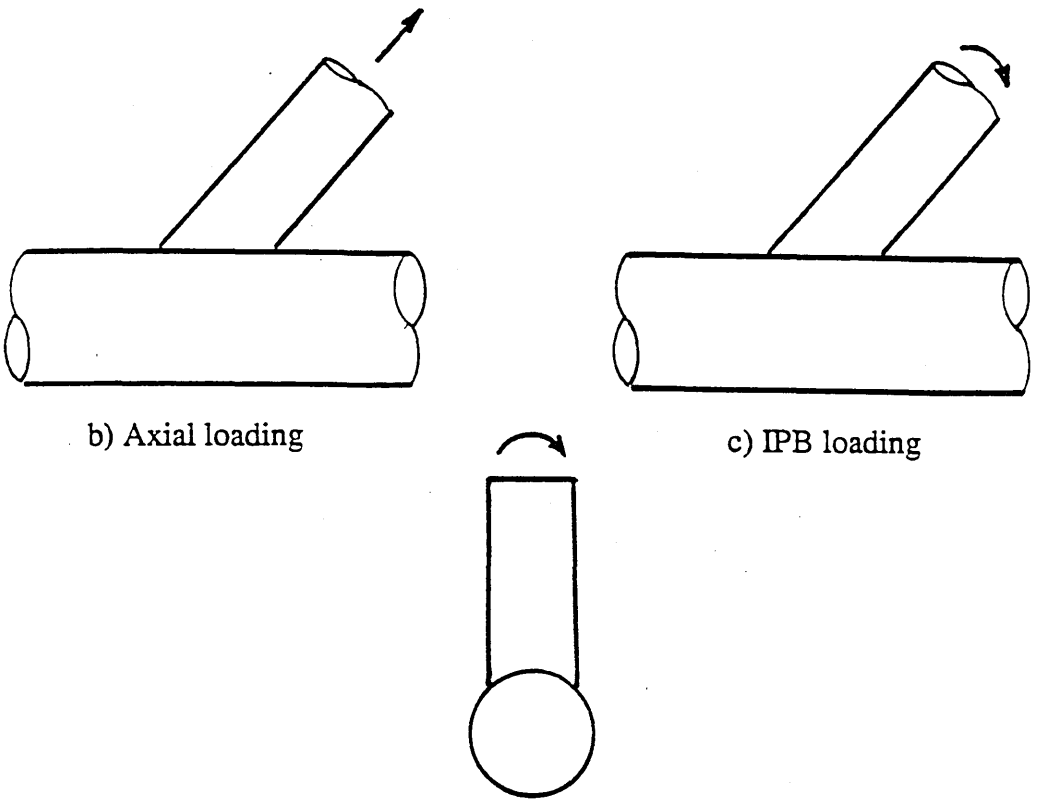

FIG.1.3 **Three basic modes of loading for tubular joints**

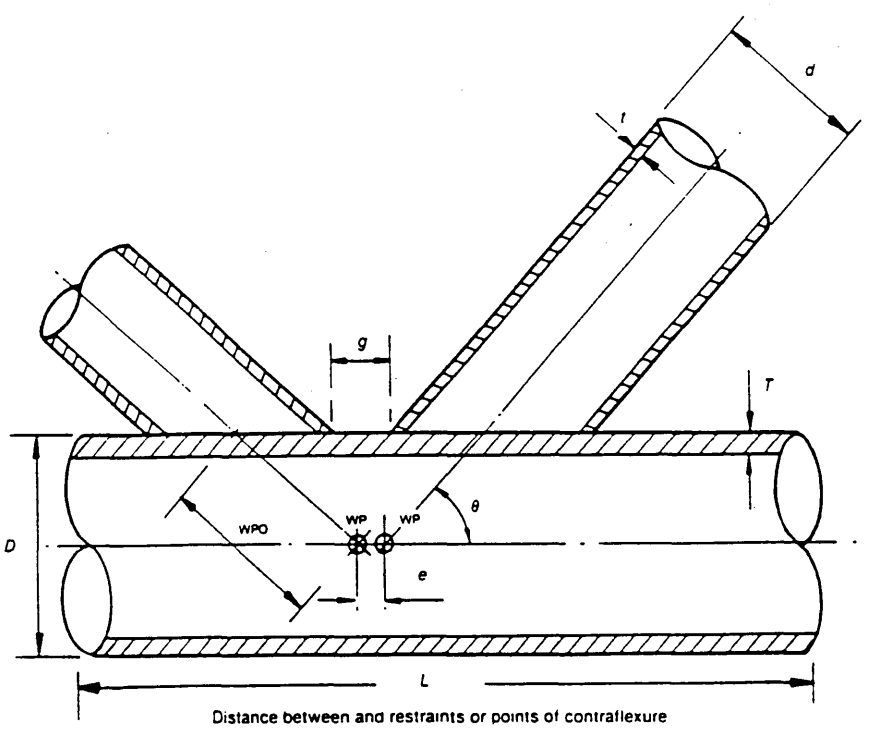

Geometric ratios: $\alpha = \frac{2L}{D}$ $\beta = \frac{d}{D}$ $\gamma = \frac{D}{2T}$ $\tau = \frac{t}{T}$ $\zeta = \frac{g}{D}$

FIG.1.4 **An Illustration of the non-dimensional parameters τ,β and γ used in the stress concentration factors calculations**

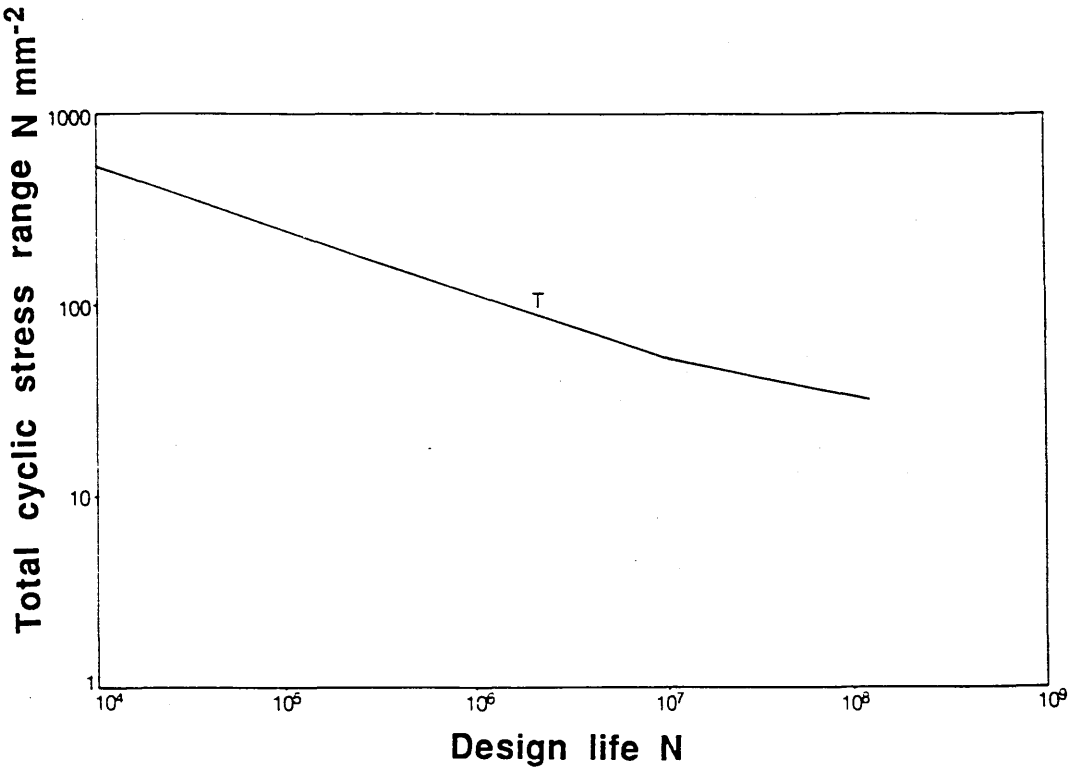

FIG.1.5 A schematic illustration of a S-N curve recommended by U.K.Department Energy (1)

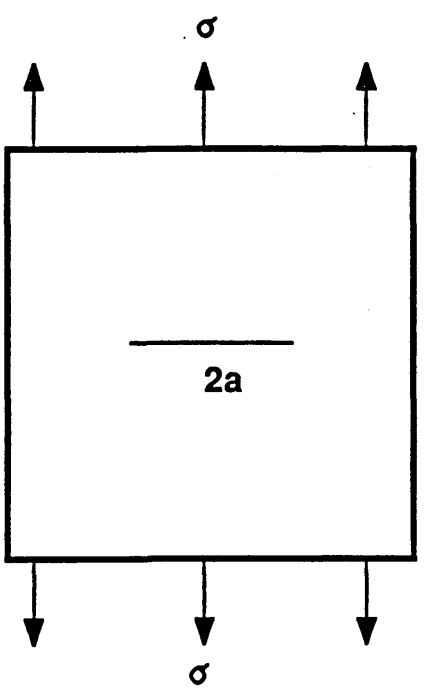

FIG.1.6 An infinite plate under uniform tension with a central crack of length 2a

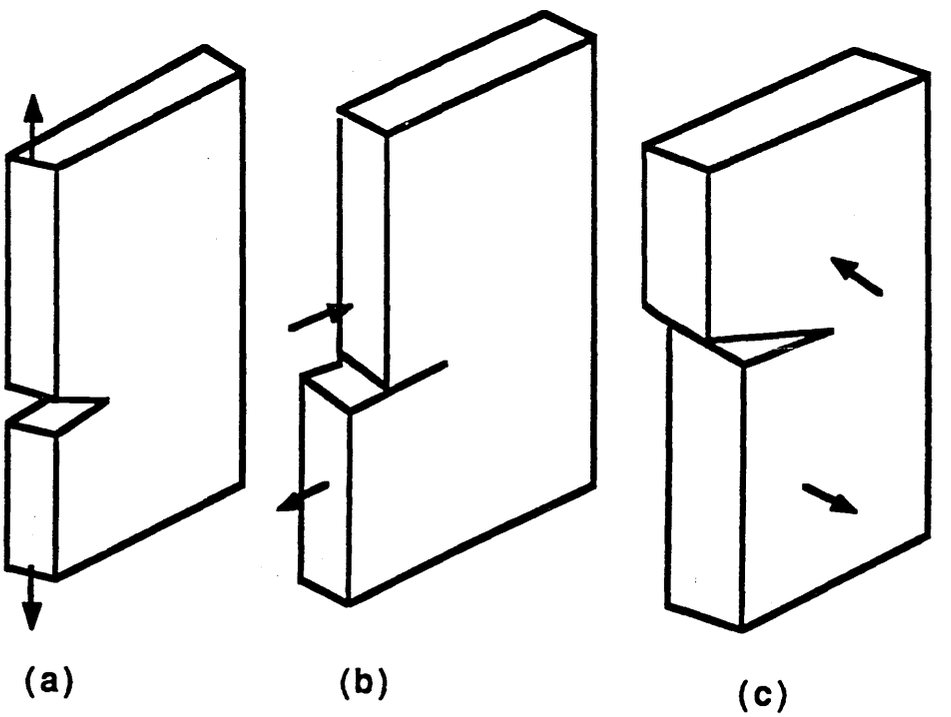

FIG.1.7 Basic modes of crack surface displacement

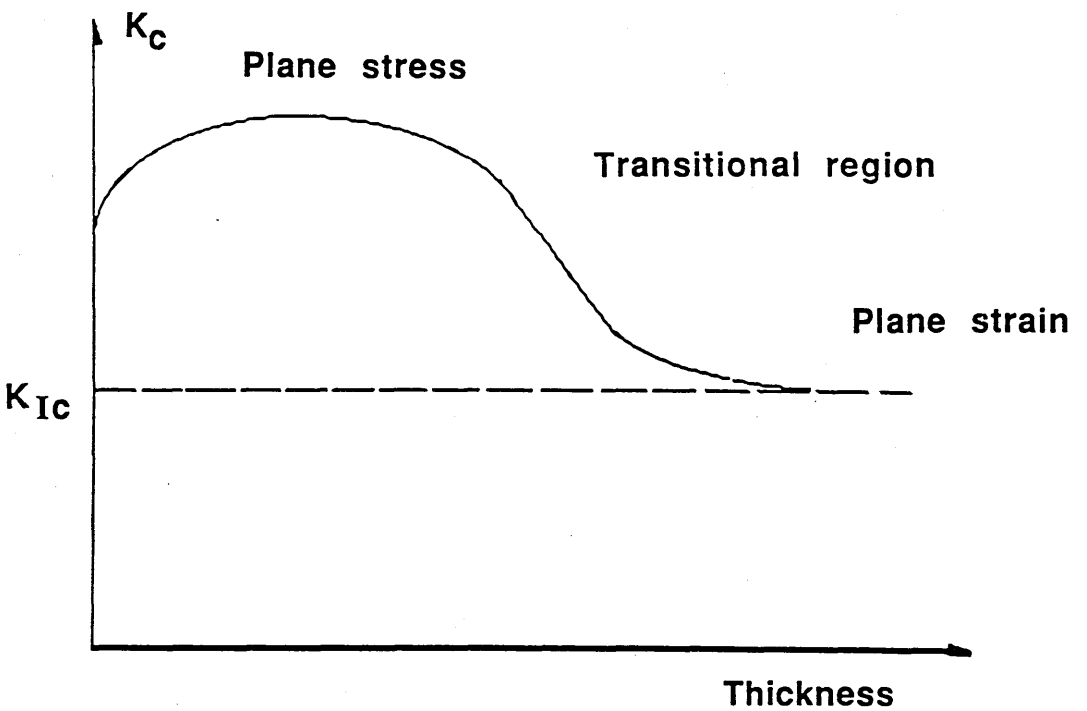

FIG.1.8 The critical stress intensity K_C as a function of the thickness after Irwin et al.(7)

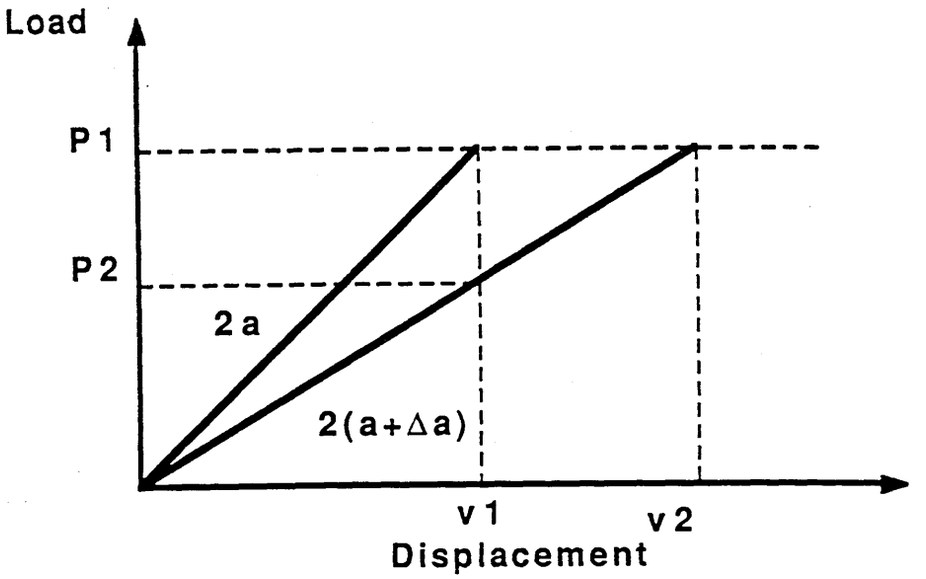

FIG.1.9 The elastic energy release due to an increment of crack growth da

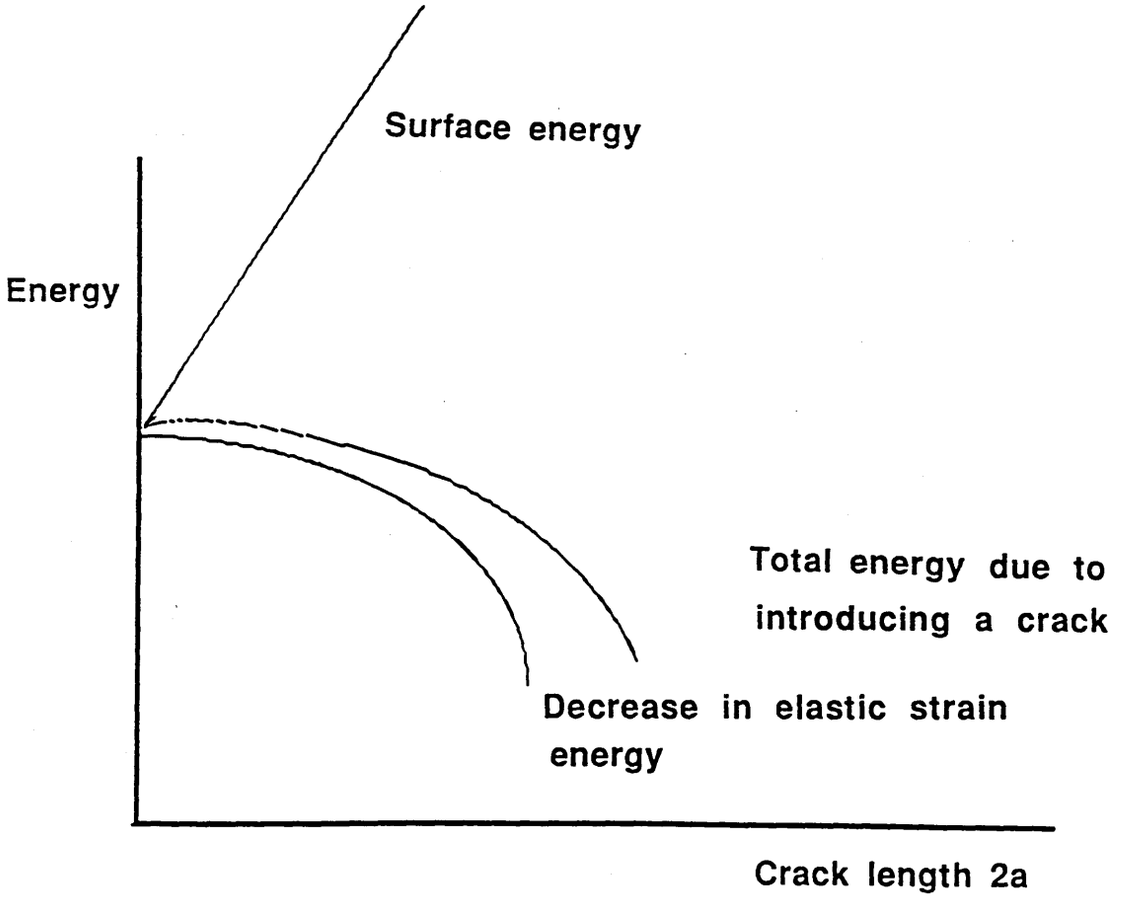

FIG.1.10 The variation of energy in a cracked body

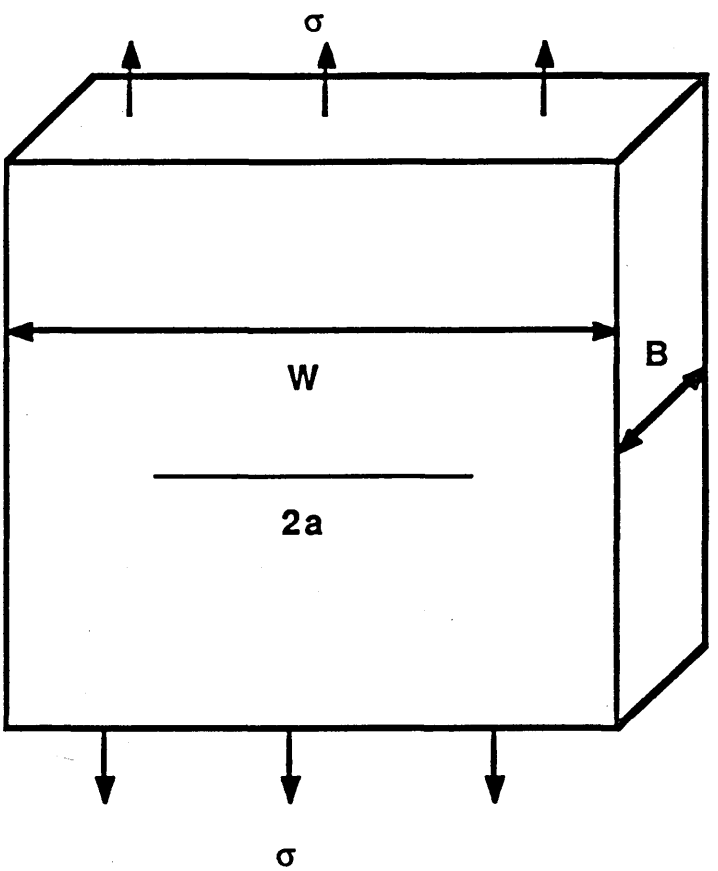

FIG.1.11 The specimen dimension requirements for plane strain fracture toughness testing

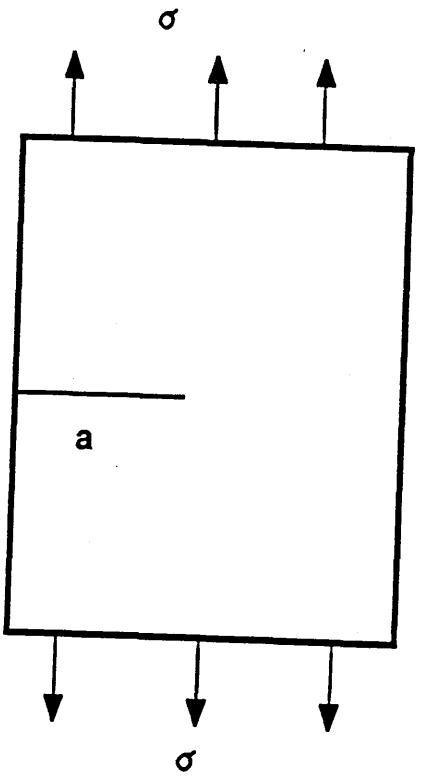

FIG.1.12 A finite width with edge cracked bar under uniaxial tensile stress

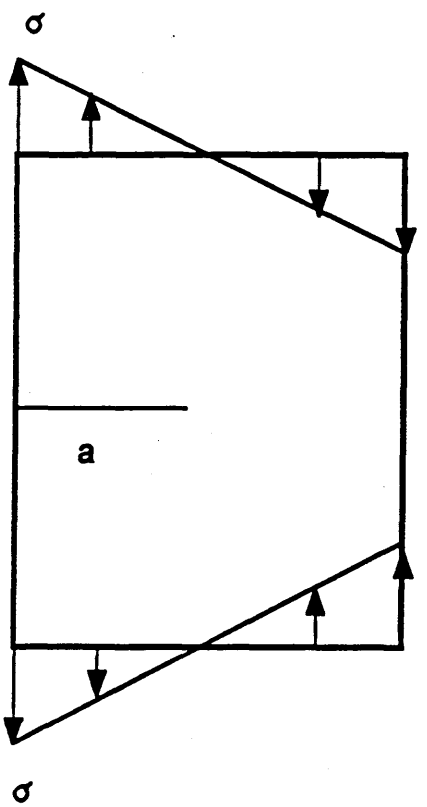

FIG.1.13 A finite width with edge cracked bar under pure bending

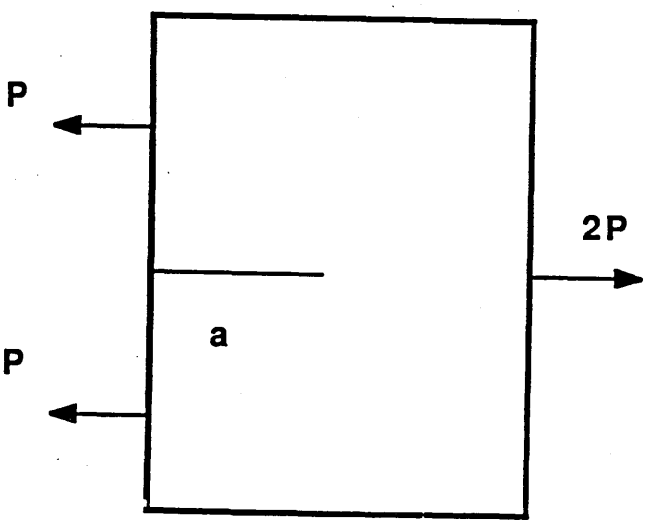

FIG.1.14 A finite width with edge cracked bar under three point bending

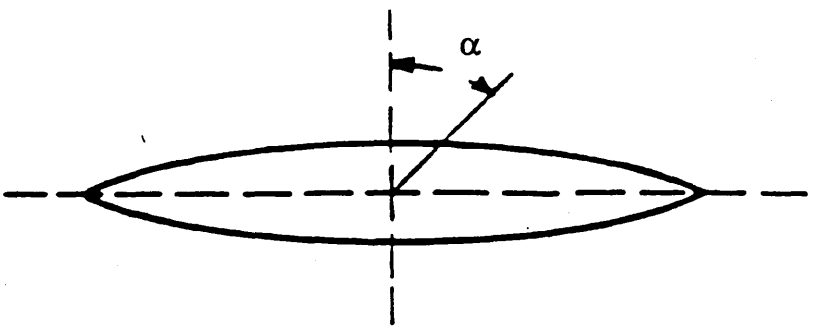

Mouth of crack

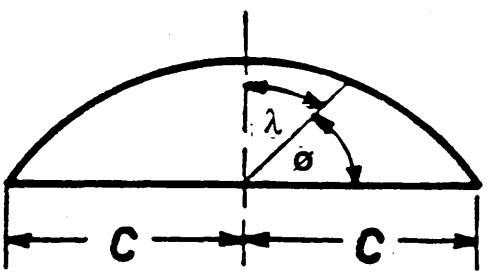

Plane of crack

FIG.1.15 A schematic illustration of a semi-elliptical surface crack in a plate

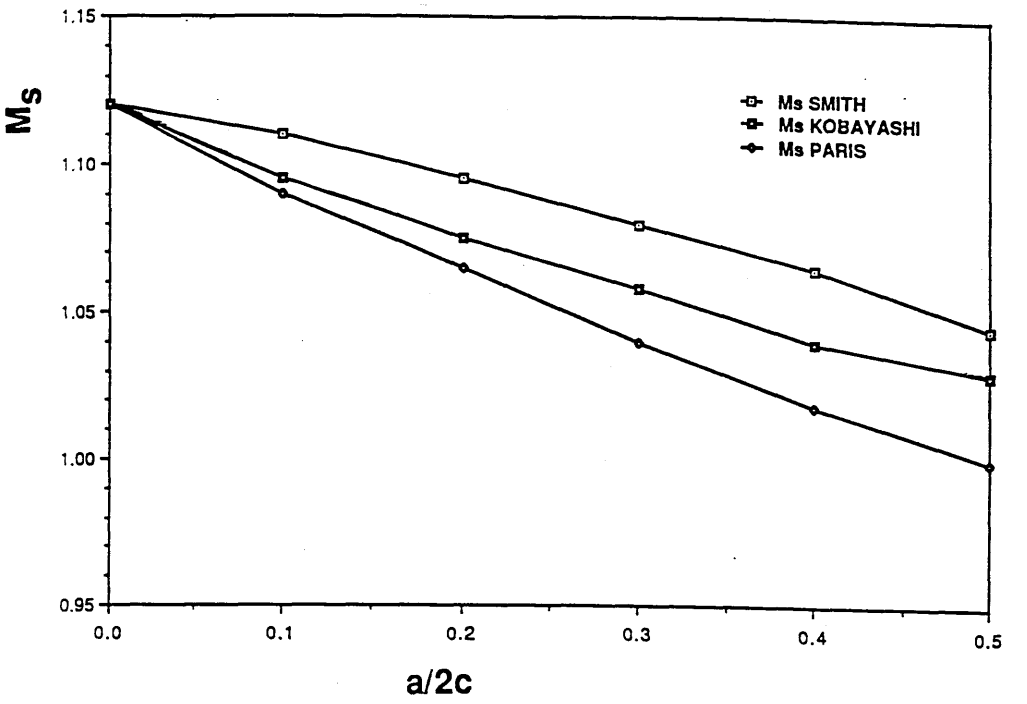

FIG.1.16 The surface correction factor M_S value versus a/2c

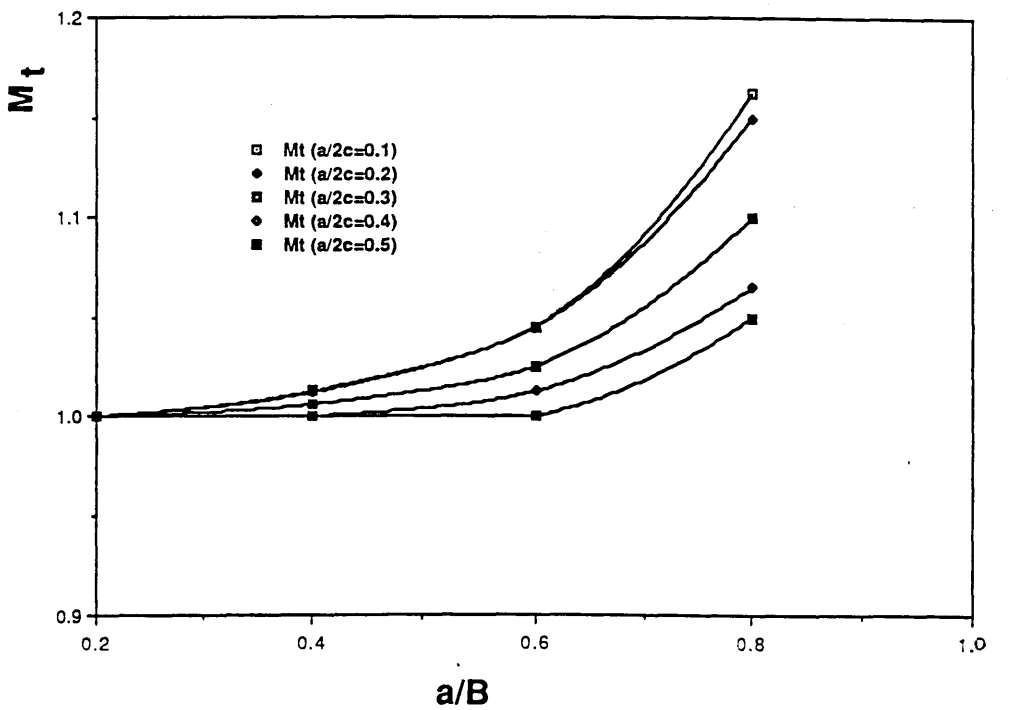

FIG.1.17 The thickness correction factor M_t value versus a/B

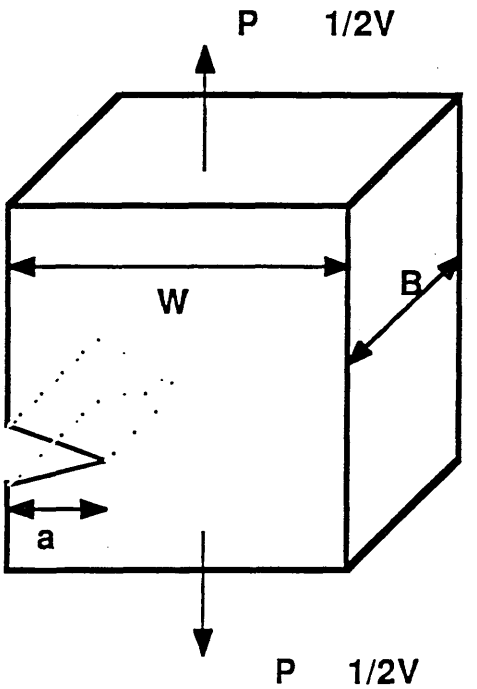

FIG.1.18 An edge notched bar subjected to tension

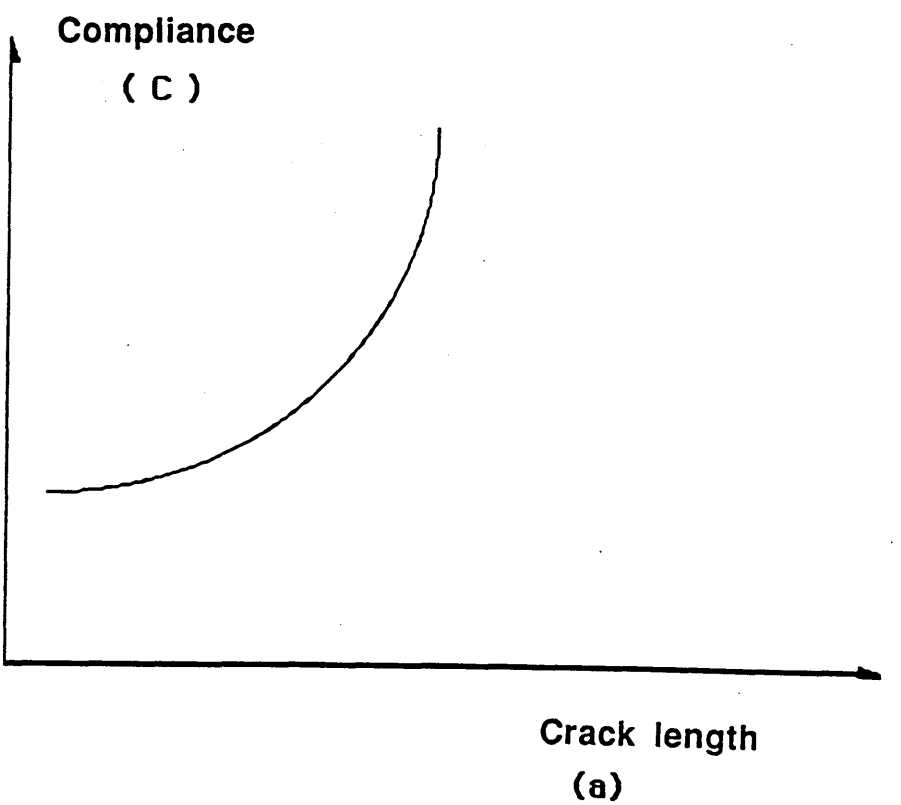

FIG.1.19 The compliance as a function of crack length

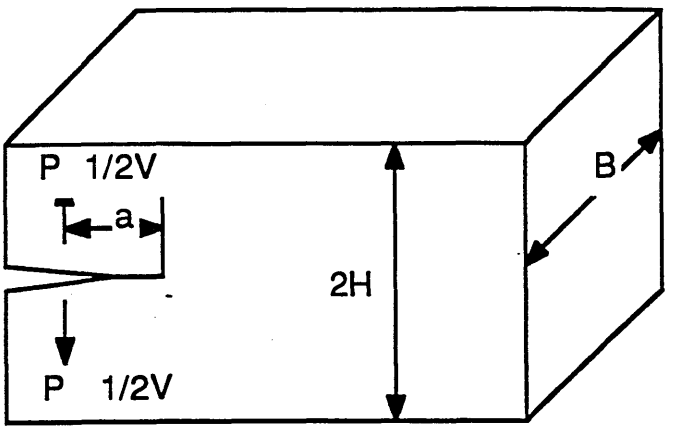

FIG.1.20 A double cantilever beam specimen

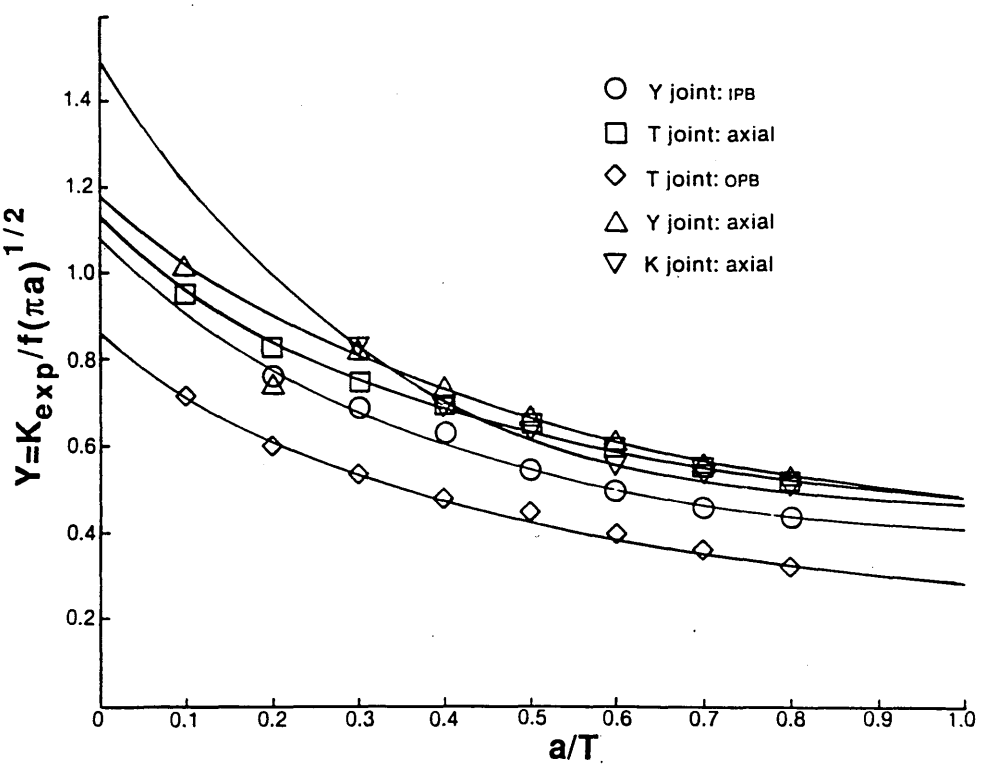

FIG.1.21 Stress intensity factors non-dimensionalised with respect to the applied stress and crack depth ($K/\sigma_n\sqrt{\pi a}$) as a function of crack depth (a/T) for tubular joint given by Dover et al.(20)

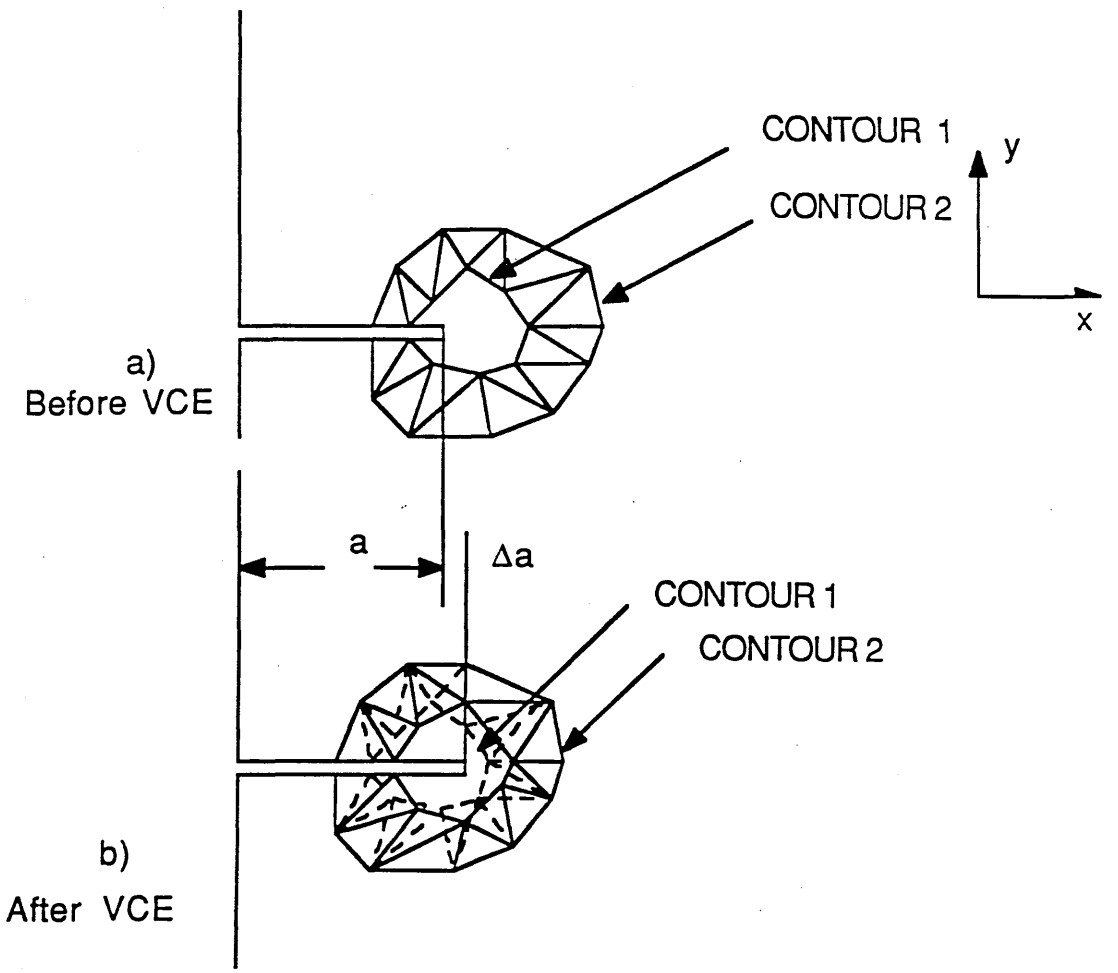

FIG.1.22 Virtual crack extension after Parks(22)

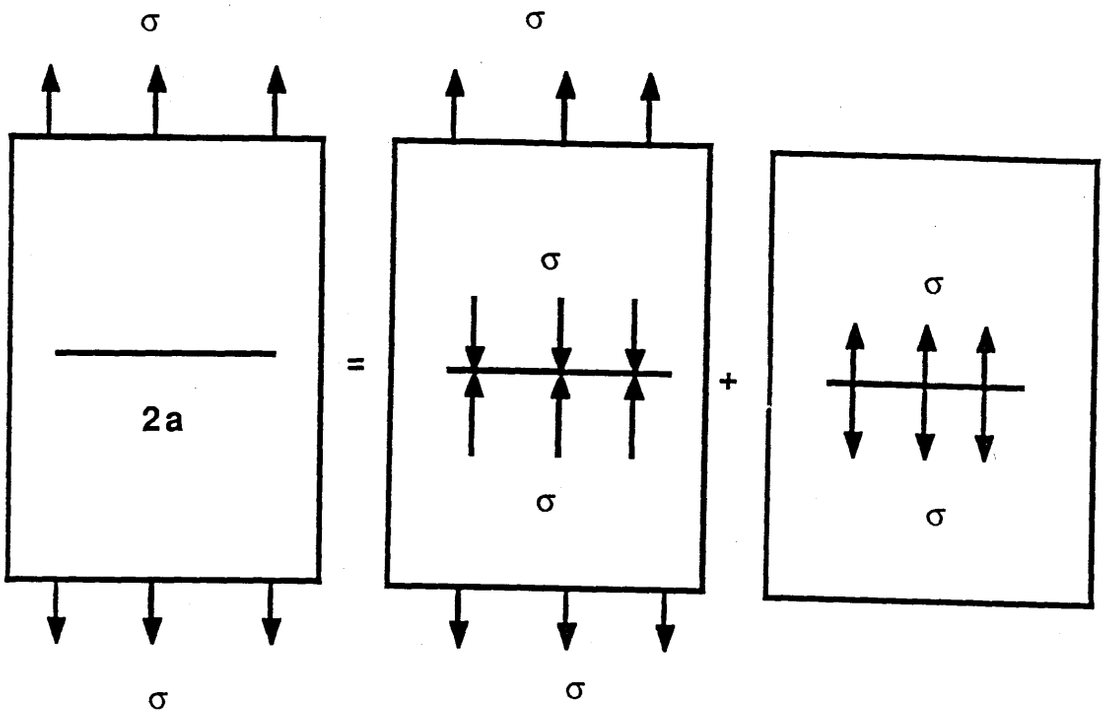

FIG.1.23 The principle of Weight Function

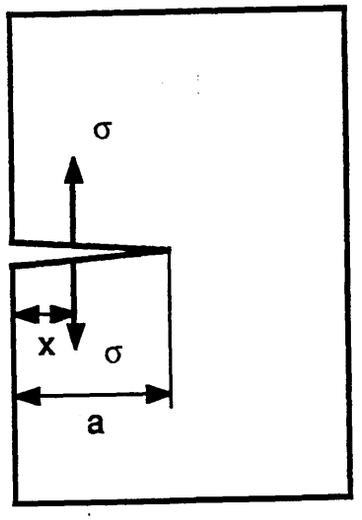

FIG.1.24 A single edge cracked bar subjected to a finite surface load σ

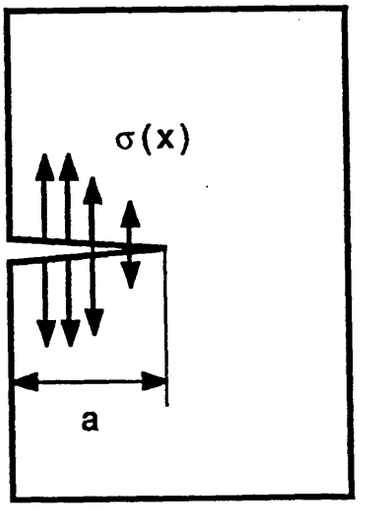

FIG.1.25 A single edge cracked bar subjected to a face load σ(x)

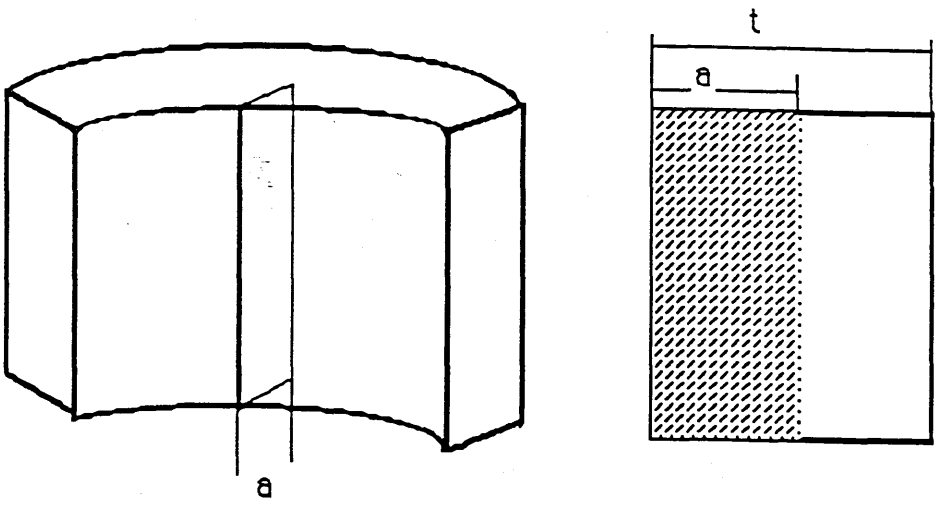

FIG.1.26 A pressure vessel with a through crack

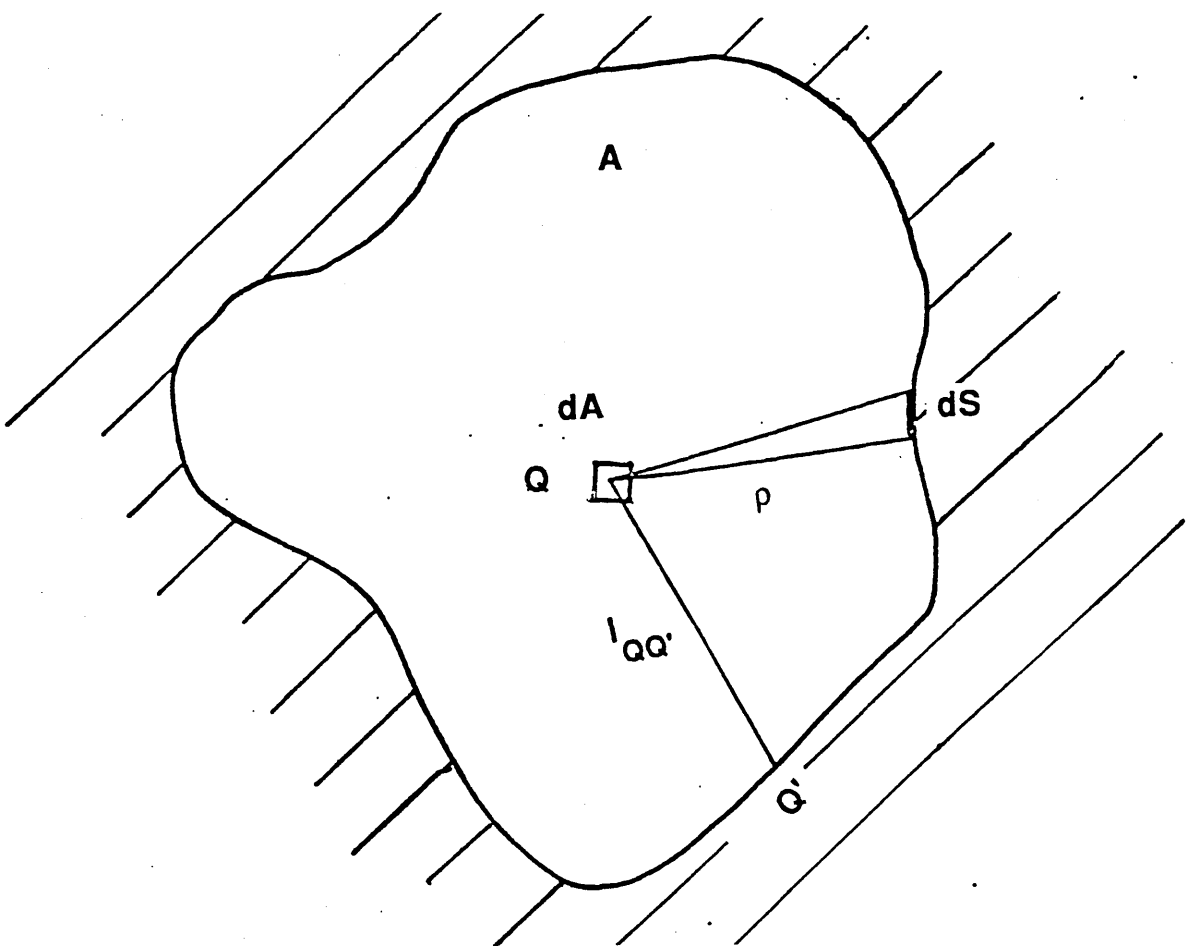

FIG.1.27 An illustration of an irregulate flat crack embedded in an infinite solid subject to an arbitrary normal stress field

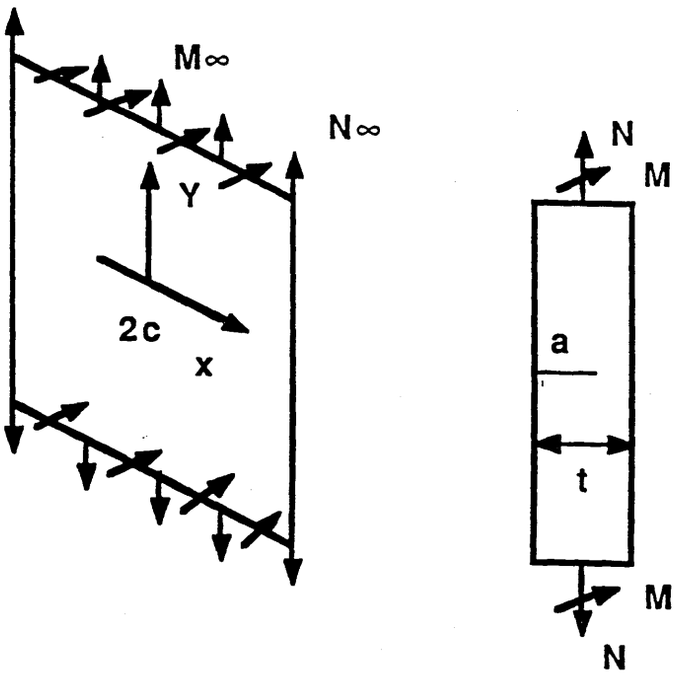

FIG.1.28 An Illustration of line spring concept after Rice and Levy(43)

CHAPTER 2. Non-Linear Fracture Mechanics

Section 2.1 Introduction

If the specimen is large in comparison with the plastic zone size r_y, the effect of the plastic zone on the stress field near the crack tip can be neglected and the material can be regarded as being largely elastic. In this situation, linear elastic fracture mechanics (LEFM) can be used, and the critical stress intensity K_c or the critical elastic energy release rate G_c can be used as parameters which control structural integrity. However when the plastic zone size r_y is comparable with the specimen's dimensions, the LEFM approach is no longer valid, and elastic-plastic fracture mechanics or fully plastic fracture mechanics is required.

Crack extension in elastic-plastic fracture mechanics is currently analysed using either the J integral or the crack opening displacement (COD) approaches. To illustrate these methods it is appropriate to consider the problem of a reactor vessel containing a flaw, which has been discussed by Delorenzi (53) and Wilbening, Delorenzi and Barishpolsky (54).

The calculation was firstly implemented in a 2-Dimensional geometry under plane strain conditions, as illustrated in Fig.2.1, and subsequently as a three dimensional elastic analysis, which is illustrated in Fig.2.2. However, when attempts were made to examine the crack growth or stability of such flawed structures using 2D elastic-plastic analysis or 3D elastic analysis, there were important shortcomings with both types of approximation. The equivalent 2D representations for such flaws ignore the significant stress and strain redistribution which can occur near the ends of the crack. The 3D elastic analysis is able to account for these effects, but is limited to small scale yielding. As both pressure vessel and offshore steels exhibit a significant amount of ductility in the operating

temperature range then the use of linear elastic fracture mechanics can lead to erroneous failure predictions. Later a 3-D elastic-plastic analysis was carried out, and a comparison was made between 2-D elastic-plastic analysis, 3-D elastic analysis and 3-D elastic-plastic analysis.

Fig.2.3 shows the variation of the energy release rate with pressure for the four belt line flaws using a 2D elastic-plastic analysis, 3D elastic analysis and 3D elastic-plastic analysis. From this figure, some useful results can be obtained. At low pressures the result for the 3D elastic analysis and 3D elastic-plastic analysis are necessarily identical, but there is already a significant difference between the 2D result and the 3D results. As the pressure increases, the 2D analysis gives a much more conservative result than the nonlinear 3D analysis. In contrast 3D elastic analysis gives a non-conservative prediction for the energy release rate at the higher pressure.

These analyses above clearly demonstrate the need for performing full 3D elastic-plastic analyses. In practice elastic-plastic or fully plastic behaviour of material may be modelled by an equivalent non-linear elastic material (55,56) as discussed in the following sections.

SECTION 2.2 J-INTEGRAL

The J-integral concept based on the energy balance approach for a non-linear elastic material was introduced by Rice (57), and first discussed in the context of LEFM The energy balance:

$$U=U_0+U_a+U_\gamma-U_F \qquad \text{Eqn.(2-1)}$$

is valid for both linear and non-linear elastic conditions (4). Crack

extension is energetically favorable when

$$d(U_F-U_a)/da \geq dU_\gamma/da \qquad \text{Eqn.(2-2)}$$

In LEFM, J and G are equivalent and given by

$$J=G=d(U_F-Ua)/da \qquad \text{Eqn.(2-3)}$$

Non-linear elastic behaviour can be used to represent plastic behavior of a material provided that no unloading occurs. At the crack tip however a small amount of unloading occurs with crack growth, so J is mainly used to predict the onset of crack extension.

As well as having an energetic definition, J can also be derived as a path independent integral around the crack tip. (57)

$$J=\int_I wdy - T\partial v/\partial x ds \qquad \text{Eqn.(2-4)}$$

where T is the loading vector, v is a displacement vector, w is the strain energy density and I is a closed contour around the crack tip. J can be shown to be path independent using Green's theorem, so that it can be evaluated on any contour, even those remote from the crack tip. In this case, the contour may only involve loads and elastic displacements, and, the effect of the plastic zone can be ignored. Thus an elastic-plastic energy release rate can be obtained from an elastic calculation along a contour for which loads and elastic displacements are known.

During contained plastic flow, the global load deflection curve remains almost linear beyond the initiation of plasticity. Fig.2.4 illustrates

schematically a typical load-displacement curve of a notched plate where initial yielding starts at the point "A", but the load-displacement relationship remains nearly linear well beyond the initial yield load, only eventually becoming nonlinear due to net section yielding. The observation of a near constant stiffness beyond the initiation of plasticity suggests that the equivalence of J and G may be extended beyond the elastic limit load as long as the global stiffness remains largely unchanged. Hence for elastic-plastic loading when the plastic zone is contained, a general relationship for computing J under containing yielding is (58)

$$J_{contained}=(P/P_e)^2 K_e^2/E' \qquad \text{Eqn.(2-5)}$$

Where P_e is some elastic load, P is the actual applied load and K_e is the stress intensity at an elastic reference load P_e.

With continued yielding, the J-integral formula for contained plasticity becomes less appropriate. For such non-linear loading regimes, a general formula for estimating the J-integral can be derived in terms of overall load displacement quantities.

The J-integral can be interpreted as the potential energy difference between two identically loaded specimens having incrementally different crack sizes, that is (59)

$$J= -\frac{1}{B}\frac{\partial U_p}{\partial a} \qquad \text{Eqn.(2-6)}$$

Here U_p is the potential energy, a is the crack length, B is the specimen thickness.

Graphically, the potential energy difference dU_p for two specimens, with

crack lengths a and a+da, is the area between the load versus load-point displacement curves illustrated in Fig. 2.5. This area equals BJda. If f_1 and f_2 designate the load-displacement curves for specimens with crack lengths a and a+da respectively, then the energy difference equals

$$dU_p=U_{p2}-U_{p1}=\int(f_2-f_1)dv \qquad \text{Eqn.(2-7)}$$

Where v denotes the load point displacement of the cracked configuration, substituting this into equation 2-6, gives

$$J=\frac{1}{Bda}\int(f_2-f_1)dv \qquad \text{Eqn.(2-8)}$$

During elastic loading the force-displacement relations are linear

$$f_1=c_1 v \qquad \text{Eqn.(2-9)}$$

and

$$f_2=c_2 v \qquad \text{Eqn.(2-10)}$$

Where c_1 and c_2 are constants. As an approximation (58), the load-displacement curves f_1 and f_2 could be assumed to remain proportional beyond the elastic load of P_1 and P_2. From this hypothesis it follows then that the J-integral is equal to

$$J=\frac{(1-C)}{Bda}\int f_1 dv \qquad \text{Eqn.(2-11)}$$

Where $C=f_2/f_1=c_2/c_1$ is constant. Replacing $(P_1-dP_1)/P_1$ by C, gives

$$J=\frac{1}{Bp_1}\frac{dp_1}{da}\int f_1 dv \qquad \text{Eqn.(2-12)}$$

Finally the expression for J becomes

$$J=\frac{1}{Bp}\frac{dp}{da}\int f\, dv \qquad \text{Eqn.(2-13)}$$

where $P=K(a)v$. If f_2/f_1 is assumed to be constant, the final equation for the J-integral in eqn.(2-13) is relatively simple to evaluate, since all the terms except the integral $\int fdv$ can be determined from purely linear elastic solutions. In addition since stresses are not required for the computation of J, only a relatively coarse mesh is needed in the finite element analysis and this provides a good approximation for intermediate elastic-plastic loading ranges.

SECTION 2.3. The HRR Field

The engineering approach to elastic-plastic fracture analysis assumes the concept of one parameter, characterisation of crack tip deformation. The characterisation of near tip stress and strain fields in a non-linear material by the J-integral is analogous to the use of the stress intensity factor K as the characterising parameter in linear elastic fracture mechanics.

$$\sigma_{ij}=K/\sqrt{(2\pi r)}s_{ij}(\theta) \qquad \text{Eqn.(2-14)}$$

$$\varepsilon_{ij}=K/\sqrt{(2\pi r)}e_{ij}(\theta) \qquad \text{Eqn.(2-15)}$$

In a power law hardening material the plastic tensile strain ε maybe simply related to the tensile stress σ through a uniaxial relationship

$$\varepsilon=\alpha(\sigma/\sigma_y)^{n-1}\sigma/E \qquad \text{Eqn.(2-16)}$$

where E is the Young's modulus, α is a material constant, n is the strain hardening parameter.

This expression can be generalised to multiaxial stress states according to the J_2 deformation theory of plasticity giving

$$\varepsilon_{ij}=3/2.\alpha.(\sigma_e/\sigma_y)^{n-1}.S_{ij}/E \qquad \text{Eqn.(2-17)}$$

where S_{ij} is the stress deviator and σ_e is the effective stress given by

$$\sigma_e{}^2=3/2S_{ij}.S_{ij} \qquad \text{Eqn.(2-18)}$$

Using this power-law description, Hutchinson (60) and Rice and Rosengren (61) showed that, for stationary cracks, the asymptotic stress and strain field in the vicinity of the crack small-scale yielding may be represented by

$$\sigma_{ij}=\sigma_y[EJ/\sigma_y{}^2I_nr]^{(1/n+1)}s_{ij}(\theta,n) \qquad \text{Eqn.(2-19)}$$

$$\varepsilon_{ij}=\varepsilon_y[EJ/\sigma_y{}^2I_nr]^{(n/n+1)}e_{ij}(\theta,n) \qquad \text{Eqn.(2-20)}$$

where J is Rice's J-integral, E is the elastic modulus, and θ and r are cylindrical co-ordinates centred at the crack tip. s_{ij}, e_{ij} are known

dimensionless functions of the circumferential position θ and the hardening exponent n. I_n is a tabulated function of n, given by Hutchinson (60) and Shih(62), and ε_y, σ_y, n are the yield strain, yield stress and strain hardening exponent, respectively as given in Eqn(2-16)

The J-integral thus measures the amplitude of the stress and strain singularity which is often referred to as the "HRR singularity". In elastic conditions this reduces correctly to LEFM.

SECTION 2.4, The COD Approach

As an alternative to the J integral, the crack opening displacement is also widely used to characterise the stress and strain field ahead of crack tips. The COD approach was first introduced by Wells(63). The principle of the method is that plastic deformation at the crack tip causes the crack tip to open and blunt. The crack tip opening displacement COD at the start of crack extension is therefore assumed to have a characteristic critical value for a particular material. Later a theoretical basis for the COD approach was developed by Bilby, Cottrell and Swinden (64), and extended by Burdekin and Stone (65) , who used the Dugdale strip yield model (66) to give an analytic expression for COD,

$$\delta=\text{COD} = 8\sigma_y a \ln\sec(\pi\sigma/2\sigma_y)/\pi E \qquad \text{Eqn.(2-21)}$$

Under LEFM conditions there is a direct relationship between δ and K_I. Irwin's analysis gives the relation (6).

$$\delta = 4 K_I^2/\pi E\sigma_y. \qquad \text{Eqn.(2-22)}$$

While according to Dugdale's analysis (66) the relation is given by

$$\delta = K_I^2/E\sigma_y. \qquad \text{Eqn.(2-23)}$$

These relations show that in the elastic regime the COD approach is compatible with the K dominated LEFM , but the COD approach is not limited to LEFM. Unfortunately, equation (2-21) is formally valid only for an infinite plate (6) in plane stress conditions and the corresponding expressions for many geometries have not been rigorously derived. In order to analyse real structures, a COD design curve has been developed by Burdekin and Stone (65). This curve was proposed to allow critical COD values to provide measures of the maximum permissible strain in the vicinity of cracks. If a general relationship can be established between COD and local strain, then COD tests on laboratory specimens enable an assessment of the maximum permissible value of the local strain for a crack of certain size in an actual structure.

To obtain a general parameter, the initial step was to derive the COD curve from the expression for COD in an infinite centre cracked plate,where $\sigma/\sigma_y<<1$,

$$\delta= K_I^2/E\sigma_y=\pi\sigma^2a/E\sigma_y \qquad \text{Eqn.(2-24)}$$

The second step is to introduce a dimensionless COD defined as,

$$\text{Ø}= \delta.E/2\pi\sigma_y a = \delta/2\pi\varepsilon_y a. \qquad \text{Eqn.(2-25)}$$

The third step requires the determination of the strain over a certain distance in a cracked plate. Finally, the dimensionless COD, Ø is plotted as a function of the relative strain $\varepsilon_L/\varepsilon_y$ for several a/L values (Fig.2.6) where a and L are illustrated in Fig.2.7. Here L is the distance of a point above or

below the crack. Thus, Fig.2.6 provides a design curve for each a/L value. However, in fact, Fig.2.8 shows that there is a significant discrepancy between theory and experiment when $\varepsilon_L/\varepsilon_y$ exceeds 0.5 (6), Later empirical equations were used to describe the relation between Ø and $\varepsilon_L/\varepsilon_y$ for the whole strain range

$$Ø=(\varepsilon_L/\varepsilon_y)^2 \qquad \text{Eqn.(2-26)}$$

for $\varepsilon_L/\varepsilon_y<0.5$,

$$Ø=\varepsilon_L/\varepsilon_y - 0.25 \qquad \text{Eqn.(2-27)}$$

for $\varepsilon_L/\varepsilon_y>0.5$.

As well as numerical methods to relate COD to the applied loading, experimental methods are required to obtain the critical COD. In experimental tests due to the difficulty of measuring the crack tip opening displacement directly, measurements are normally made at the open end of the notch using a double cantilever clip gauge. There are several methods for relating this to the crack tip value of COD. The first method is to measure the crack profile experimentally to obtain a general relationship between Vg, the clip gauge displacement, and the critical COD value (67,68). Another possible method is to determine the relationship between clip gauge displacement, and the near tip COD by using computer methods of stress analysis. Finite element methods appear to offer the most promise in this respect (69)

SECTION 2.5.The Relationship between the COD and J-Integral

The crack tip opening displacement and J -integral are both used to characterise the crack tip stress and strain field and must thus in general be related.

By exploiting the small-scale yielding relationship $J=K^2/E'$, a relationship between J and δ_t was derived by Rice(59)

$$J=\int_0^{\delta_t}\sigma(\delta)d\delta \qquad \text{Eqn.(2-28)}$$

where δ_t is crack tip opening displacement

For perfectly plastic materials, $\sigma(\delta)=m\sigma_y$ and the value of the integral became

$$J=m\sigma_y.\delta_t \qquad \text{Eqn.(2-29)}$$

where m lies in the range 1-2 for both small and large scale yielding. The concepts of J and δ may thus be considered as equivalent methods of characterising the severity of the near tip stress and strain fields.

In elastic-plastic conditions, the relationship between J and δ can also be derived from the Hutchinson-Rice-Rosengren (HRR) singularity. Using Eqn.2-19 and Eqn.2-20. Thus the displacements along the crack edge ($\theta=+/-\pi$) were given by Shih (70)

$$v_y=\delta/2=\alpha\sigma_y/E(EJ/\alpha\sigma_y{}^2I_n)^{(n/n+1)}r^{(1/n+1)}u_y(n) \qquad \text{Eqn.(2-30)}$$

$$v_x=\alpha\sigma_y/E(EJ/\alpha\sigma_y{}^2I_n)^{(n/n+1)}r^{(1/n+1)}u_x(n) \qquad \text{Eqn.(2-31)}$$

where v_x and v_y are the displacements in the x and y direction respectively, and $\delta=2v_y$, and $u_x(n)$ and $u_y(n)$ are dimensionless functions of the hardening exponent n. An operational definition of the crack tip opening displacement δ_t has been given by Rice and Tracey (71) as the opening distance between the intercept of two 45^0-lines, drawn back from the tip with the deformed profile. At the intercept, Fig.2.9 gives:

$$r-v_x=\delta/2 \qquad \text{Eqn.(2-32)}$$

By satisfying Eqn.2-30, 2-31 and 2-32, one obtains:

$$\delta_t=d_n J/\sigma_y \qquad \text{Eqn.(2-33)}$$

where

$$d_n=(\alpha\sigma_y/E)^{1/n}.(u_x(n)+u_y(n))^{1/n}.2u_y(n)/I_n \qquad \text{Eqn.(2-34)}$$

As d_n is mildly dependent on n and σ_y/E under large scale yielding, attempts to relate J and δ_t by a single constant, which is independent of n and σ_y/E, are inadequate. Values of d_n have been derived by a number of investigators and are summarised by Sailor (72) and Shih (70). Generally they fall between the range of values shown in Fig2.10 and Fig2.11 as discussed by Robinson (73).

SECTION 2.6. The Validity of the Elastic-Plastic Fracture Mechanics Approach

McMeeking (74), McMeeking and Parks (75), and Shih and German (76) have

studied the conditions under which J characterises crack tip deformation by considering different geometries with different fully plastic flow fields. Unlike the linear elastic case, they found that the size limitations, for J dominance depend on the specimen type and loading conditions. This can be explained by considering the fully plastic slip line field solution following McClintock(77). For example, a single edge bar subjected to bending, and a centre crack bar subjected to tension and a double edge bar subjected to tension, have fully plastic slip line fields that are radically different, as is illustrated in Fig.2.12.

The size of the J dominated region, R has been discussed by Hutchinson (56) and Shih (76), who found that the geometry dependence was particularly strong for low-hardening materials (high n), and a minimum necessary condition for J-dominance is that the size of the region dominated by the HRR field should be at least of the the order of δ_t to encompass the region in which finite geometry changes to crack blunting are significant. In general,

$$R>3\delta_t \qquad \text{Eqn.(2-35)}$$

The second condition for J dominance is that R should be greater than the size of the fracture process zone. This aspect has been studied by Hutchinson (55,56). Although precise estimates of R are difficult to make, Hutchinson (55,56) has suggested that in small scale yielding

$$R=(1/5 \text{ to } 1/4)r_y \qquad \text{Eqn.(2-36)}$$

where r_y is the radius of the plastic zone, which following Hutchinson (56) and Shih(76) is given by:

$$r_y=\frac{1}{\beta\pi}\frac{n-1}{n+1}\left(\frac{K_I}{\sigma_y}\right)^2$$ Eqn.(2-37)

Here plane stress conditions are defined by ß=2, while for plane strain ß=6. By comparing the full stress and strain distribution for a series of crack configurations with the HRR singularity at the same level of J, Shih and German (76) found that the size of the region (R) dominated by the HRR singularity was much larger in bend specimens than in tension . This can be explained by referring to Fig.2.12 which shows the difference in the slip line fields for bending and for tension. For the bend configuration (and the compact tension specimen) numerical studies (55,56) suggest the R value is some fraction of the uncracked ligament b,

$$R=0.07b$$ Eqn.(2-38)

So, for bend configurations the condition for J-dominance under fully plastic conditions can be obtained by combining (Eqn.2-35) and (Eqn.2-38), and assuming d_n in Eqn 2-33 is 0.6, one obtains

$$b>25J/\sigma_y$$ Eqn.(2-39)

Similarly, for center cracked tensile configurations and assuming (62)

$$R=0.01b$$ Eqn.(2-40)

then,the condition for J-dominance is

$b>200J/\sigma_y$ Eqn.(2-41)

For cracked geometries subject to combined bending and tension, a situation which often occurs in real structures, the size requirement depends on the ratio of the bending moment to the tensile force times the length of the ligament of the specimen as discussed by Shih (78) .

SECTION 2.7. Methods for Obtaining J and COD

Several methods of determining J have been proposed, including calibration techniques (79), virtual crack extension (26) and the line spring method (45,47,80). These methods are now briefly reviewed as a precursor to their application to offshore structures.

2.7.1 J Calibration Methods

J calibration methods can be used without extensive computation, as they use a data base of two dimensional standard geometries.

On the basis of power law deformation theory plasticity, a complete J analysis has been produced for several geometries using the Ramberg-Osgood power hardening relation :

$\varepsilon/\varepsilon_y = \sigma/\sigma_y + \alpha(\sigma/\sigma_y)^n$ Eqn.(2-42)

The J value under elastic-plastic conditions can be estimated by combining linear elastic and fully plastic terms (79)

$J=J^e(a_e)+J^p(a,n)$ Eqn.(2-43)

Similarly for the crack opening displacement,

$$\delta=\delta^e(a_e)+\delta^p(a,n) \qquad \text{Eqn.(2-44)}$$

where $J^e(a_e)$ and $\delta^e(a_e)$ are the elastic contributions based on an adjusted crack length a_e which is Irwin's effective crack length modified to account for strain hardening. Here a_e is given by Kumar and Shih(81)

$$a_e=a+\phi r_y \qquad \text{Eqn.(2-45)}$$

where

$$\phi=1/[1+(P/P_0)^2] \qquad \text{Eqn.(2-46)}$$

where P_0 is the limit or reference load per unit thickness based on the stress σ_y defined by

$$P_0=fb\sigma_y \qquad \text{Eqn.(2-47)}$$

where f is the constraint factor which may depend on the ratio of relevant structure dimensions and b is the length of the uncracked ligament. $J^p(a,n)$, $\delta^p(a,n)$ are the plastic contributions based on the material hardening exponent n, given by Goldman and Hutchinson as (82)

$$J^p=\alpha\sigma_y\varepsilon_y a[P/P_0]^{n+1} f^{p'}(a/t,n) \qquad \text{Eqn.(2-48)}$$

$$\delta^p=\alpha\varepsilon_y a[P/P_0]^{n}\delta^{p'}(a/t,n) \qquad \text{Eqn.(2-49)}$$

The dimensionless quantities $f^{p'}$ and $\delta^{p'}$ are functions only of a/t and n

and are independent of the applied load.

As an illustration, the relevant parameters for some standard geometries are now given

2.7.1.1 Compact Tension Specimen

(i) Fully Plastic Solutions

The fully plastic solution for a compact tension specimen, given by Kumar and Shih (81) is expressed in Eqn (2-48 and 2-49). Here P is the applied load per unit thickness, a is the crack length, t is the specimen width and b=t-a is the uncracked ligament. The reference load P_0 is given by

$$P_0=1.455\eta b\sigma_y \qquad \text{Eqn.(2-50)}$$

for plane strain and by

$$P_0=1.071\eta b\sigma_y \qquad \text{Eqn.(2-51)}$$

for plane stress, where, η is defined as

$$\eta=[(2a/b)^2+2(2a/b)+2]^{1/2}-[2a/b+1] \qquad \text{Eqn.(2-52)}$$

(ii) Elastic Estimation Formulae

By using standard texts (11), the elastic solutions can be given in the form

$$J=f_1 P^2/E' \qquad \text{Eqn.(2-53)}$$

$$\delta = f_2 P/E' \qquad \text{Eqn.(2-54)}$$

The functions f_1 and f_2 are given by Tada, Paris and Irwin (11)

(iii) Elastic-Plastic Estimation Formulae

Estimation formulas for the entire range of elastic-plastic deformation can now be written as

$$J = f_1(a_e)P^2/E' + \alpha\sigma_y\varepsilon_y c h_1(a/t,n)(P/P_0)^{n+1} \qquad \text{Eqn.(2-55)}$$

$$\delta = f_2(a_e)P/E' + \alpha\varepsilon_y c h_2(a/t,n)(P/P_0)^{n} \qquad \text{Eqn.(2-56)}$$

Similarly, the elastic-plastic estimation formulas for a centre-cracked plate in tension can be given in the same form as in eqn(2-55 and 2-56): where

$$f_1 = \pi a F_1^{\,2}/4t^2 \qquad \text{Eqn.(2-57)}$$

$$f_2 = 2aF_2/t \qquad \text{Eqn.(2-58)}$$

Here, F_1 and F_2 are given by Kumar et al. (79). The corresponding expressions for a single edge cracked plate in-uniform tension are now given as

$$f_1 = \pi a F_1^{\,2}/t^2 \qquad \text{Eqn.(2-59)}$$

$$f_2 = 4aF_2/t \qquad \text{Eqn.(2-60)}$$

For other geometries, detailed results have been given by EPRI (79).

2.7.2 Virtual Crack Extension

Recalling eqn.1-46, the potential energy of a finite element model can be given by

$$U_p=\Sigma\int(wdv_i-T(x)^T[u]=\Sigma W_i(x,u)-T(x)^T[u] \qquad \text{Eqn.(2-61)}$$

where $\forall_i$ is the volume of the ith element of the mesh, w is the stress energy density, T is the vector of nodal force and x and u are the vectors of nodal point coordinates and displacements, and W_i is the integral of strain energy over the ith element. Now consider a small virtual crack increment Δa of all nodes on and within the interior contour 1 shown in Fig.1.22. Therefore, the nodes on element boundaries connecting the contour 1 and 2 are advanced by a small amount.

Following Parks(27) the change of the potential energy is

$$\delta U_p=\Sigma[\partial W_i/\partial u-T^T]\,\delta u+\Sigma[(\partial W_i/\partial x)^T-u^T(\partial T/\partial x)]\,\delta x \qquad \text{Eqn.(2-62)}$$

If δu is assumed to be very small and the nodal force is due to forces applied outside the crack tip element and the equation reduces to

$$\delta U_p=\Sigma(\partial W_i/\partial x)^T\,\delta x \qquad \text{Eqn.(2-63)}$$

For a planar configuration under deformation theory plasticity the decrease in potential energy with respect to the crack length equals the path independent integral J (59)

$$J\delta a=-\delta U_p=-\Sigma(\partial W_i/\partial x)^T\,\delta x \qquad \text{Eqn.(2-64)}$$

According to Parks (27) W_i has the form

$$W_i=0.5[u]^T k_i[u] \qquad \text{Eqn.(2-65)}$$

and

$$(\partial W_i/\partial x)^T \delta x = 0.5[u]^T \delta k_i[u] \qquad \text{Eqn.(2-66)}$$

where δk_i is the stiffness different for element i. From Eqn.(2-66) it is clear that the method is close to the virtual crack extension method used in LEFM, discussed in the context of Chapter 1.

2.7.3. Elastic-Plastic Line Spring Finite Element for Surface Cracked Problems

For real structures, 3D elastic-plastic solutions using virtual crack extension can be used to obtain accurate results. However, the computer memory and CPU time required inhibit its use for the analysis of a wide range of cracked structures. Elastic line spring analysis gives an accuracy within a few percent of that obtained from detailed 3D numerical models of the same simple configuration (47). The basic features of an elastic-plastic line spring model have been used to model part through surface cracks in plates and shells by Parks(45), Parks and White (47) and Ezzat and Erdogan (83). Parks (45) noted that the transition from linear elastic to fully plastic conditions in an simple spring model can be smoothed by use of a plastically adjusted "effective" crack depth a_{eff}. In order to obtain an estimate of the J-integral in an edge-cracked specimen, J can be taken as the sum of an elastic and a plastic parts: $J=J^{(e)}+J^{(p)}$. The elastic component

$J^{(e)}$ is related to current load Q_i and crack length through the stress intensity factor K_I which the loads would produce according to an elastic analysis

$$J^{(e)}=K_I^2(1-\upsilon^2)/E \qquad \text{Eqn.(2-67)}$$

where

$$K_I = Q_i f_i(a,t) \qquad \text{Eqn.(2-68)}$$

and the stress intensity factor calibrations f_i for tension (i=1) or bending (i=2) are obtained, from standard handbooks (11).

The plastic contribution $J^{(p)}$ can be expressed in terms of the plastic crack tip opening displacement $\delta^{(p)}$:

$$J^{(p)}=m\sigma_y\delta_t^{(p)} \qquad \text{Eqn.(2-69)}$$

where the scalar m is expected to depend on the overall deformation pattern in the plastic regime (84) as discussed in detail by Rice (84) The plastic crack tip opening $\delta_t^{(p)}$ can also be related to the macroscopic displacement increments $\dot{\theta}^{(p)}$ and $\dot{\delta}^{(p)}$

$$\dot{\delta}_t^{(p)}=\dot{\delta}^{(p)}+(t/2-a)\dot{\theta}^{(p)} \qquad \text{Eqn.(2-70)}$$

where $\dot{\delta}_t^{(p)}$,$\dot{\delta}^{(p)}$and $\dot{\theta}^{(p)}$ are shown in Fig.2.13. In this figure, $\dot{\delta}^{(p)}$ and $\dot{\theta}^{(p)}$ can be regarded as the rate of the displacement and rotation of the line spring respectively. From this equation, $\delta_t^{(p)}$ can be obtained by integrating through the applied load increments.

Parks and co-workers(85) have examined the accuracy of non-linear line springs by comparing them with detailed continuum solutions for a pressure vessel containing a circumferental external crack of constant depth subject to combination of remote tension and internal pressure. They found the agreement was within 10% for the total range of loads up to 150% of the plastic collapse load for axial loading, while comparison for multi-axial loading was less accurate.

2.7.4 J-Integral for Deeply Cracked Specimens Subjected to Bending

If A is the area under the load-displacement record of a cracked specimen, J can be determined by comparing specimens with incrementally different crack length a and a+δa.

$$J=\frac{1}{B}\text{Lim}_{\delta\to 0}\frac{\delta A}{\delta a} \qquad \text{Eqn.(2-73)}$$

where $\delta A=A_a-A_{a+\delta a}$, If δa is very small then

$$BJ\delta a=\delta A \qquad \text{Eqn.(2-74)}$$

It is always possible to obtain J from specimens with incrementally different crack lengths, but this is very inconvenient both experimentally and computationally. However for deep crack specimens subject to bending, Rice (86) has proposed a method using only one specimen

Fig.2.14 shows the side view of a specimen which has a sufficiently deep crack that deformation only occurs in the ligament. If the reduction factor is (1-m) as defined using the notation of Fig 2.14(a) and (b) then,

$$\delta b = mb \qquad \text{Eqn.(2-75)}$$

and,

$$\delta a = \delta b \qquad \text{Eqn.(2-76)}$$

also,

$$\delta P = mP \qquad \text{Eqn.(2-77)}$$

so,

$$A_a = \int_0^P P_a \, d\Delta a$$

$$A_b = \int_0^P P_b \, d\Delta b \qquad \text{Eqn.(2-78)}$$

Since the ligament is reduced by a factor of (1-m). The load would be decreased as a factor 1-m as well, then

$$P_b = P_a - mP_a = (1-m)P_a \qquad \text{Eqn.(2-79)}$$

and

$$\Delta b = (1-m)\Delta a \qquad \text{Eqn.(2-80)}$$

As a result,

$$A_b=\int_0^P (1-m)^2 P_a d\Delta a=(1-m)^2 A_a \qquad \text{Eqn.(2-81)}$$

In this case,

$$BJ\delta a=A_a-A_b=m(2-m)A_a \qquad \text{Eqn.(2-82)}$$

Replacing δa with mb and proceeding to the limit , one obtains

$$J=2A_a/Bb \qquad \text{Eqn.(2-83)}$$

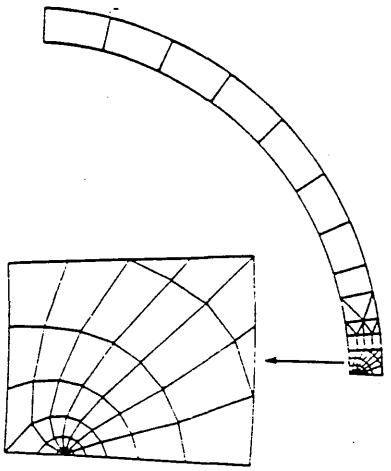

FIG.2.1 A 2-D finite element model of 90 degree sector after Delorenzi (53)

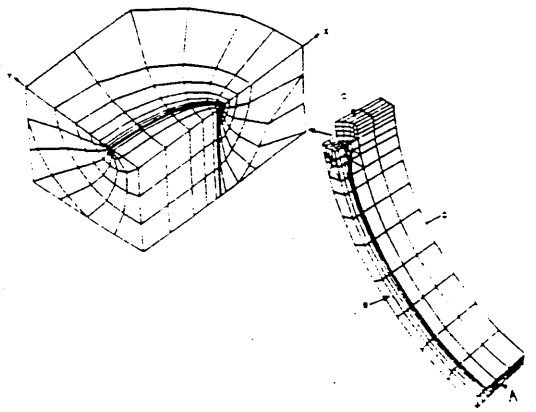

Fig.2.2 A 3-D finite element model of belt-line flaw after Delorenzi (53)

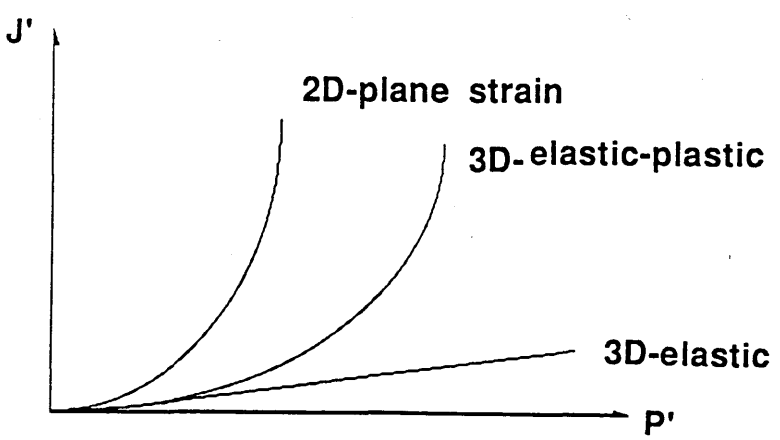

FIG.2.3 The variation of the energy release rate with Pressure

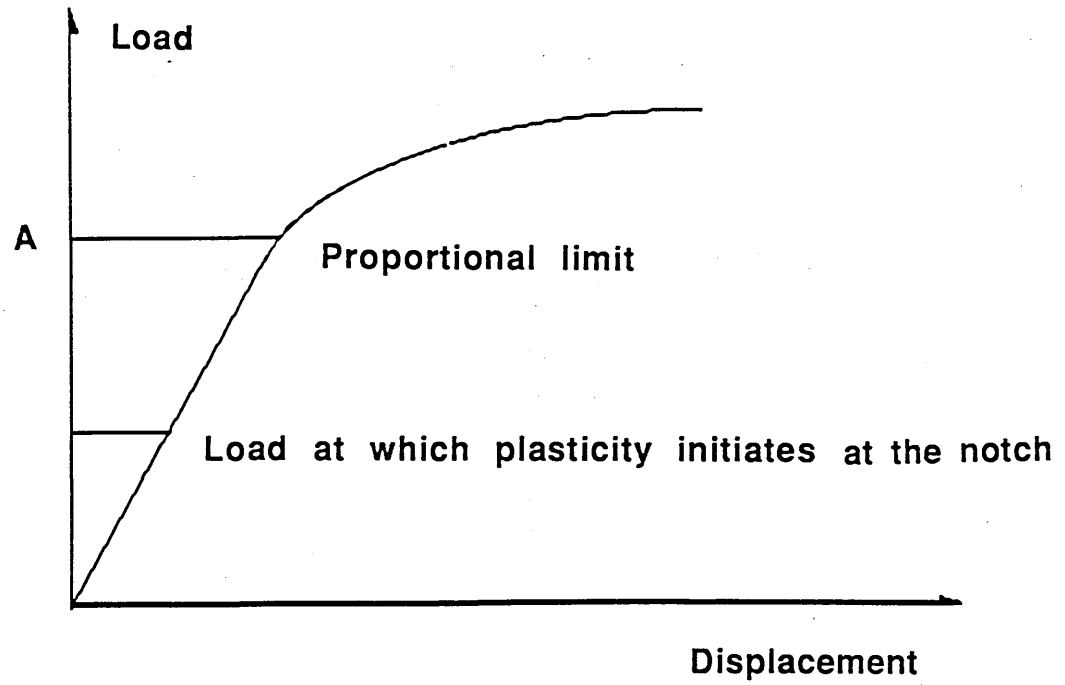

FIG.2.4 A schematic illustration of typical load-displacement curve of a notched plate

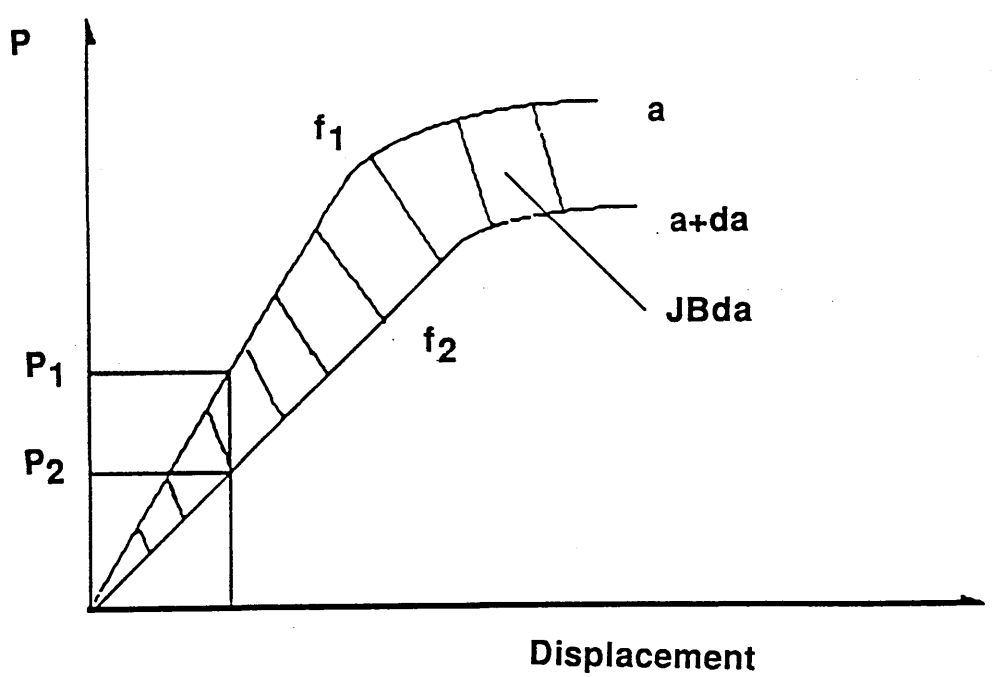

FIG.2.5 The potential energy for two specimen with crack length a and a+da

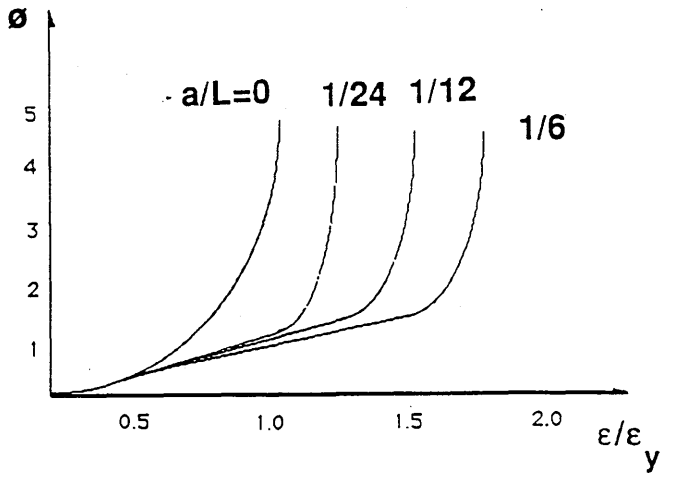

FIG.2.6 The relative strain $\varepsilon_L/\varepsilon_y$ versus a/L

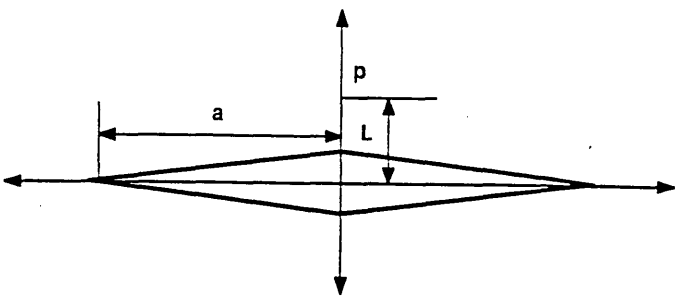

Points p distance L above and below the centre of a crack of length 2a

FIG.2.7 An Illustration of a and L

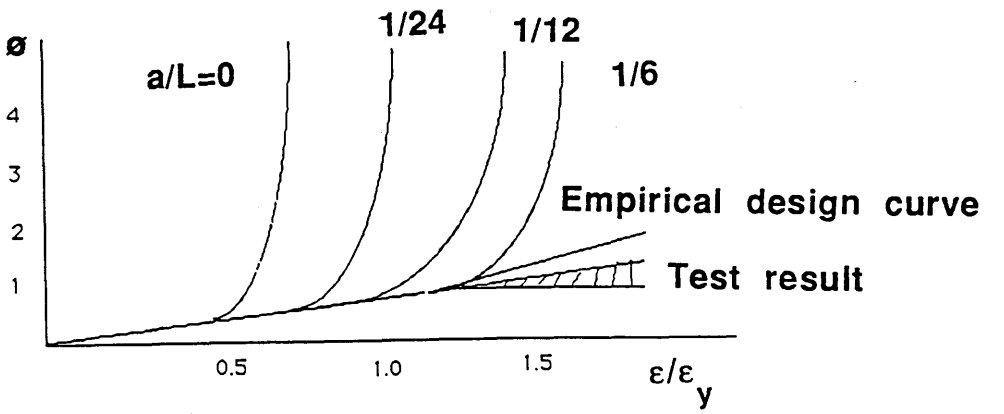

FIG.2.8 The non-dimensional crack open displacement versus relative strain $\varepsilon_L/\varepsilon_y$

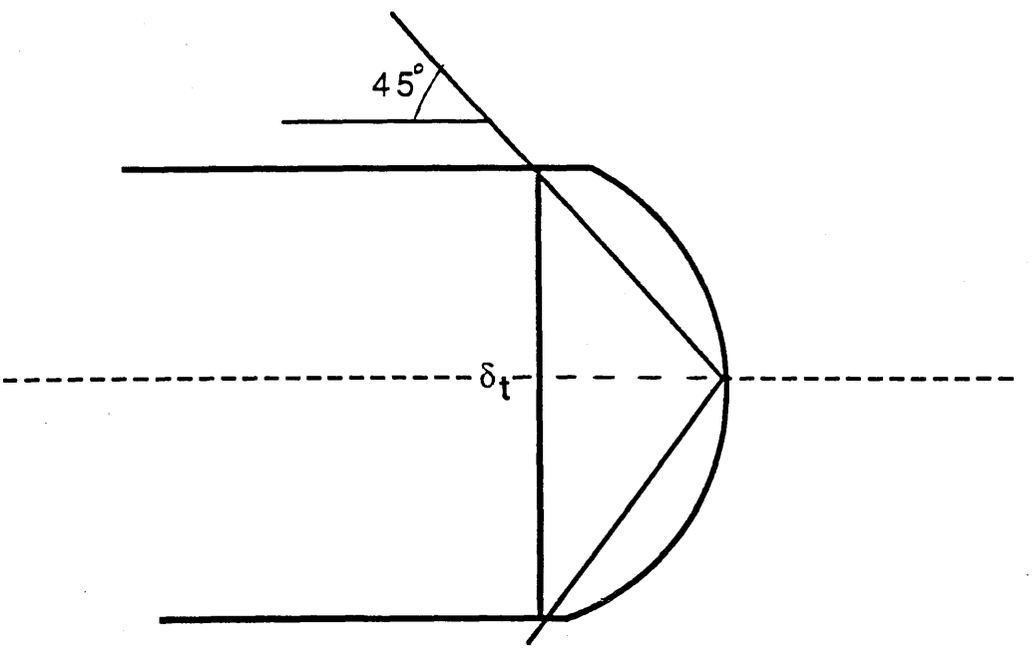

FIG.2.9 The definition of crack tip opening displacement after Rice and Tracey(71)

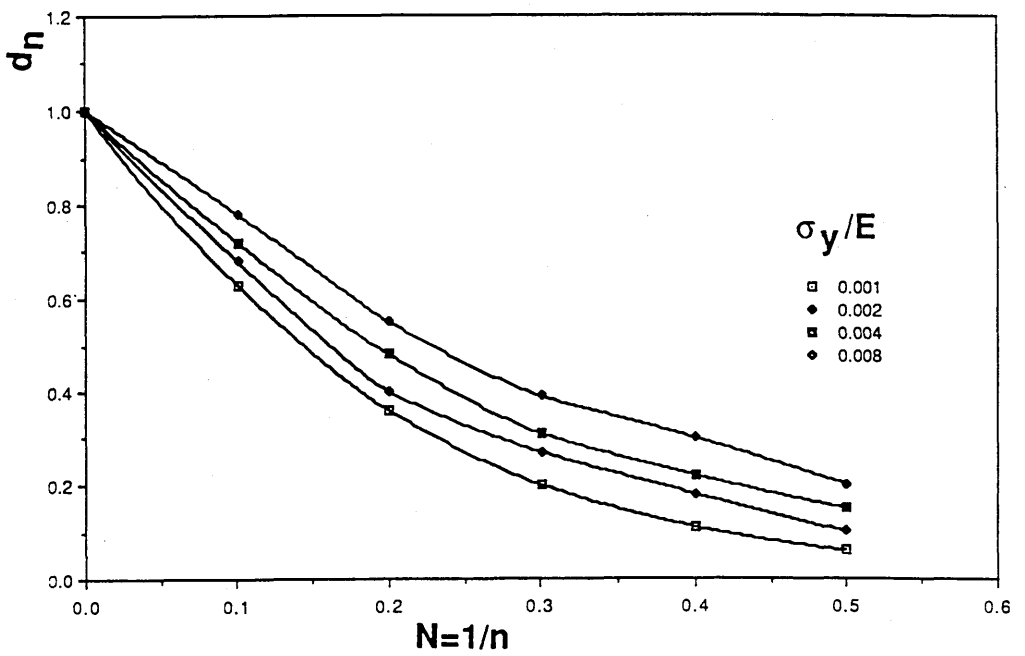

FIG.2.10 The non-dimensional function d_n against n and σ_y/E after Sailor (72)

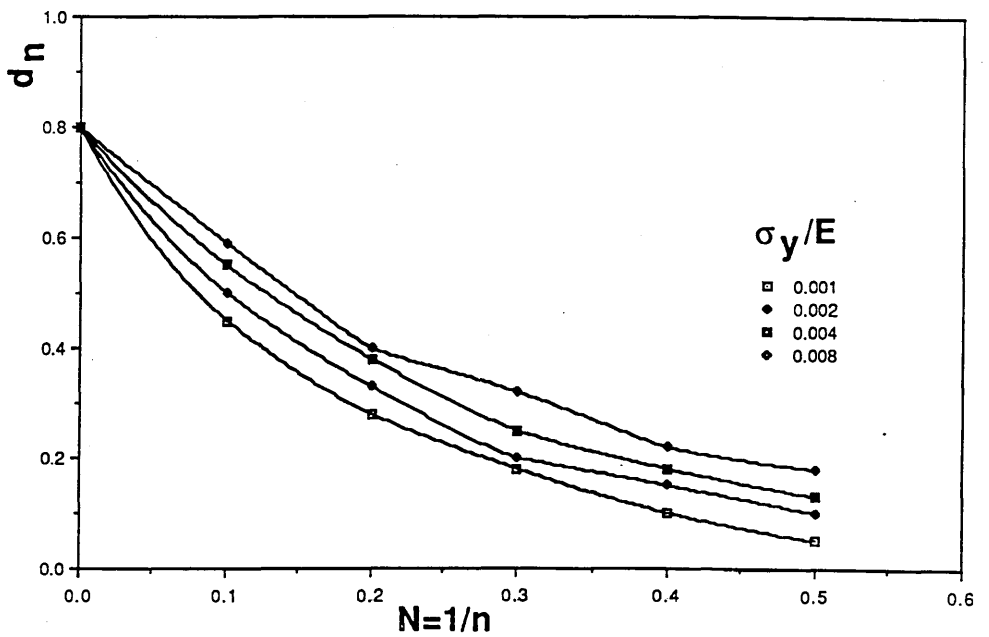

FIG.2.11 The non-dimensional function d_n against n and σ_y/E after Shih(70)

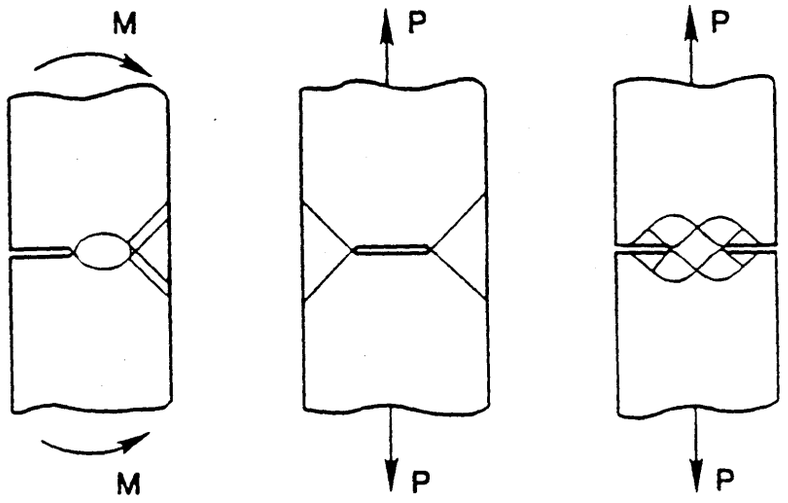

FIG.2.12 The perfectly plastic slip-line fields for cracked bend bar, center cracked panel,and a double edge notched specimen

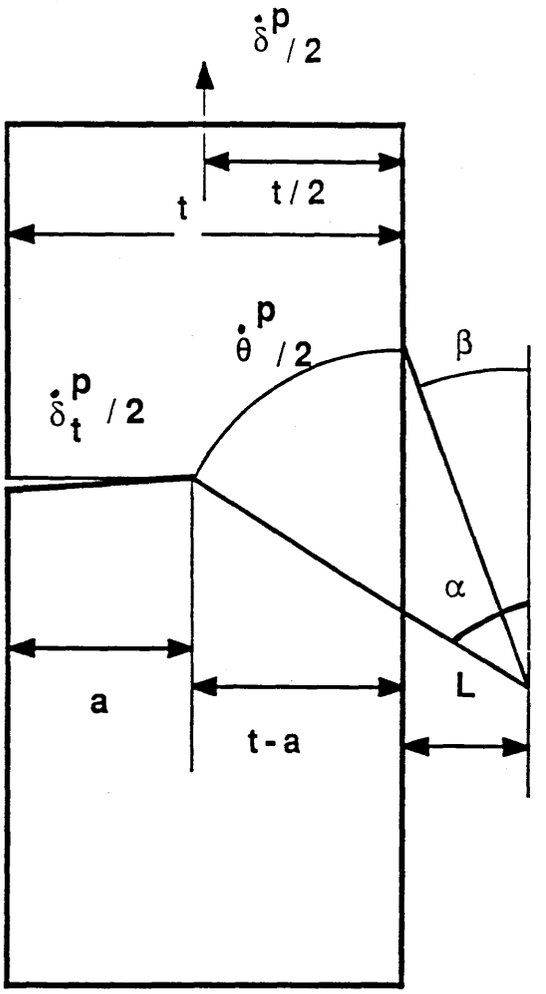

$$\dot{\delta}_t^p = \dot{\delta}^p + (t/2-a)\,\dot{\theta}^p$$

FIG.2.13 The kinematics of crack tip opening in terms of generalised load point displacements

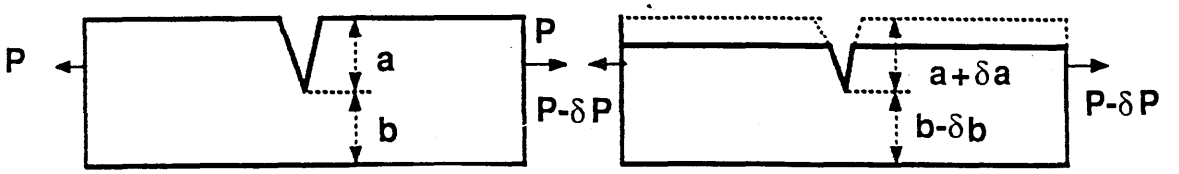

FIG.2.14 The side view of a deeply cracked specimen

CHAPTER 3. Stress Intensity Factors of Semi-Elliptical Cracks in a Tubular Welded Joint Using Line-Springs and 3D Finite Elements

SECTION 3.1. Introduction

The life of offshore structures is largely determined by fatigue, induced by the action of the marine environment which produces semi-elliptical surface cracks in the sites of stress concentration at tubular welded joints. Much work has already been devoted to determining the stress concentration factors for a wide range of joint, and the results are widely available in the form of parametric equations such as those given by Kuang (3) or Wordworth and Smedley (2).

Although the design of joints against fatigue is usually based on an S-N approach in conjunction with the relevant stress concentration factors; routine inspection frequently reveals the presence of cracks which compromise the integrity of the structure and which demand a fracture mechanics approach. For a rigorous fracture mechanics fatigue analysis, it is necessary to understand the three dimensional stress intensity factor distribution near the tubular intersection. The stress intensity factors of cracks in such joints have been inferred from large scale experiments as typified by the work of Dover et.al (20) and Noordhoek et al. (52) in which the fatigue crack growth rate has been correlated with the growth rate determined from standard fracture mechanics specimens whose stress intensity factors are already known. Such laboratory experiments elucidate the features of the problem, but are generally expensive, and are inconvenient for analysing the very wide range of cracks shapes found in the joints of real structures under the complex loading conditions which apply offshore. It is therefore necessary to be able to analyse the integrity

of joints containing cracks by computational methods, such as weight functions, (36,37,38,40), or finite element methods.

Although there are many methods of determining the stress intensity factors of semi-elliptical cracks, the line spring method of Rice and Levy (43) has been widely applied to tubes and flat plates (45) because of its computational efficiency. In this method the crack is represented by a series of generalised line springs which act across a discontinuity in a thin shell as illustrated in Fig.1.28, and a detailed description of this method has given in Chapter 1. This basic method for mode 1 loading, devised by Rice and Levy (43), has been further generalised in the same spirit by Parks (45) and Desvaux (48) to incorporate both mode 2 and mode 3 loadings and is implemented in the finite element code ABAQUS (87) .

Huang and Hancock (51) have applied this technique to semi-elliptical cracks formed near the stress concentration associated with a tubular welded joints, although it was not possible to verify their accuracy by reference to full three dimensional solutions. In the present work, this problem has been addressed for a series of cracks which are normal to the chord wall and a tubular welded T joint containing a series of semi-elliptical cracks of increasing depth located near the chord-brace intersection, has been analysed using shell elements with the cracks modelled by the line spring concept of Rice and Levy (43). The same problem has also been analysed modelled by a finite element method involving 20 noded bricks allowing the stress intensity factors to be determined by virtual crack extension.

SECTION 3.2. Numerical Methods and Finite Element Models

3.2.1. Mesh Generation of the Brick Element Model

The problems of modelling a complex three-dimensional flaw geometry with an appropriate finite element mesh are significant. At an early stage, much effort was put into generating the finite element mesh using a commercial code known as FEMGEN (88). However as the cracks were not planar and the crack surfaces were curved, it was very difficult to control the shape of the elements near to the crack tips. Later this problem was alleviated by using a commercial code SESAM (89) which can be used to introduce semi-elliptical cracks into warped surfaces.

This package was specifically written for the stress analysis of offshore tubular joints. The program consists of three parts: a mesh generator called PRETUBE(90), a finite element solution program and a post-processing program. PRETUBE (90) can automatically generate the mesh for a surface semi-elliptical crack at the toe of the weld connecting the tubular members. This is achieved by specifying the dimension of the brace, chord and the coordinates of the end of the crack tip along the crack surface length. The surface crack is implanted normal to the shell surface. The overall geometry of the tubular welded joint is shown in Fig.3.1. In this Figure, the chord and brace have been largely modelled with eight noded doubly curved shell elements, while the critical region of the chord-brace intersection was initially modelled using twenty-noded isoparametic brick elements which allow a quadratic displacement function. Compatibility between the bricks and shells was maintained using transition elements which had 18, 12 and 15 nodes as shown schematically in Fig.3.2. In the ABAQUS (version 4.5.8) finite element code there are no explicit 18, 12 or 15 noded brick elements in the library but these can be produced by degenerating twenty noded bricks with the use of coincident nodes, which

were attached to corresponding nodes in the shell elements with appropriate constraints. For example the transition element illustrated in Figure 3.3a) is made from the twenty noded brick shown in Fig 3.3b) by constraining nodes 5,13 and 6 at the site of node 13; node 8, 15 and 7 at the site of node 15, and node 16 and 14 at the midpoint between them. In addition to the 15 noded bricks it was also necessary to use one twelve noded and one eighteen noded brick. The geometry of these bricks is illustrated in Fig.3.3c,d). Figure 3.3e) shows the way in which the chord-brace intersection, modelled with brick elements, was blended into the tubular joints, modelled with shell elements, by the use of transition elements. In addition, a super-element technique was used, this provides a additional saving as the substructure which is near the crack front is used more than once for different crack depth geometries.

As the SESAM (90) package does not explicitly optimise the problem, that is. it can not explicitly renumber the elements, as a result the allocated workspace and the maximum degrees of freedom wavefront of finite element mesh are initially very large. This leads to an increase in the CPU time and may even result in a failure to run the problem. Later meshes generated by PRETUBE (90) were optimized for ABAQUS (87) which uses a frontal solution technique by renumbering the elements following the procedure given by Sloan and Randolph (91), for finite element codes which use a frontal solving technique requiring renumbering of the elements. For the T-joint, this program has decreased the allocated workspace to about one third of the original requirements. Consequently, the CPU time was decreased to three quarters of the original time, and makes the nonlinear analysis of T-joint practical. In order to identify the element numbers in the brace and the chord after the elements were renumbered, a package called FEMVIEW (92) was used to convert ABAQUS (87) input data into a

visual form.

3.2.2 Mesh Generation of the Shell Element Model

The same joint was also completely modelled using eight noded doubly curved shell elements. In this case the cracks were represented by the line spring concept of Rice and Levy (43) as implemented in ABAQUS (87).

Mesh generation was accomplished using FEMGEN (88) for the shell element model. To provide a satisfactory model for this analysis, the smallest elements were concentrated in the regions of the intersection between brace and chord, since the highest stress gradients occur in the immediate vicinity of this region. Near the ends of the chord and the brace where the stresses were more uniformly distributed the elements may be considerably larger.

3.2.3 Loading Conditions and Numerical Methods

The models were subject to a uniform axial force on the brace, while the ends of the chord were built in. The symmetry of the configuration allows the structure to be represented by one symmetric quarter as shown in Fig.3.4. In addition, one of the models was subjected to an out of plane bending moment on the brace, requiring the model to be represented by half of the whole geometry as shown in Fig.3.5 .

The number and type of elements in each model as well as the number of degrees of freedom of the system is given in Table (3.1). Typically for the axial loading case, the models which used three dimensional bricks involved approximately 12000 degrees of freedom and were thus much larger than the shell models which only involved 4000 degrees of freedom. Both types

of problem were analysed on a Cyber 205 computer. The formulations using brick elements required about 320 seconds,cpu time, compared to 56 seconds for the shell analyses using line springs. For out of plane bending, the number of degrees of freedom and the CPU time were almost twice as the axial loading case.

Cracks initiate at the site of maximum stress concentration which under axial loading occurs at the toe of the weld at the saddle point as shown schematically in Fig 3.6. Under out of plane bending, the cracks were located at the same position as the axial loading case. The cracks were situated on the chord side of the chord-brace intersection and three crack geometries have been analysed. These consist of three semi-elliptical cracks with a maximum depth to thickness ratio a/T of 0.2, 0.6 and 0.9, and a constant surface length 2c/T=4, for the axial loading case and a/T=0.6 for the out of plane bending case. Here T is the thickness of the chord.

In the line spring analyses the mesh consisted only of shell elements and the crack was located at a position representative of the weld toe at the chord-brace intersection. This was chosen to be one brace wall thickness from the center line intersection. Three line-spring elements, were used to model this crack. Calculations by Huang(93), and Huang and Hancock (51) on cracked two dimensional joints under plane strain conditions have shown this to give good agreement between calculations using plane strain continuum elements and a shell analysis with a line spring of the crack. In the present work several mesh variations were tried near the crack, and although similar results were always obtained at the deepest point, the presence of tied nodes significantly changed the results near the ends of the crack. A mesh which avoided tied nodes near the line springs was thus always preferred.

In the formulation using brick elements the three-dimensional elements were arranged as a focused mesh with three rings of elements concentric

with the crack tip as shown in Fig 3.7. Each ring had six elements. The inner ring of elements consisted of bricks with collapsed sides producing independent coincident nodes at the crack tip and with the radial the mid-side nodes located at the quarter point positions: a procedure which allows the elements to adopt the correct form of displacement function for the elastic singularity as discussed by Barsoum (94) and Henshell and Shaw (95). The stress intensity factors were determined by evaluating the J integral around three crack tip contours using the virtual crack extension method of Parks (22) as implemented in ABAQUS. Although J was largely path independent, the values obtained entirely from the second contour using the outer corner nodes of the second ring of elements were preferred. Experience has this contour shown to produce the most reliable data, for reasons that are generally considered to be more fortuitous than fundamental.

The crack front was represented by four elements sets with boundaries orthogonal to the crack front, thus providing nine sites at which J could be determined. Due to the curvature of the crack front, the elements at the intersection with the chord surface were somewhat distorted as shown in Fig 3.8.

J is of course directly equivalent to the strain release rate G under linear elastic fracture mechanics conditions which can be written in terms of the stress intensity factors for the mixed mode loading

$$J = G = (1-\upsilon^2)K_I^2/E + (1-\upsilon^2)K_{II}^2/E + (1+\upsilon)K_{III}^2/E \qquad \text{Eqn.(3-1)}$$

The contribution of each of the modes was resolved by examining the displacements of the quarter point nodes at corresponding sites on the

upper and lower crack faces using a method described by Shih et al (96), and Tracey (97) for two dimensional problems and for three dimensions by Ingraffea and Manu (98).

The combined displacements are given by :

$$u=(1+\upsilon)/4E\sqrt{(2r/\pi)}\{K_I[(5-8\upsilon)Cos(0.5\theta)-Cos(1.5\theta)]+K_{II}[(9-8\upsilon)Sin(0.5\theta)+Sin(1.5\theta)]\}+0(r)$$

$$v=(1+\upsilon)/4E\sqrt{(2r/\pi)}\{K_I[(7-8\upsilon)Sin(0.5\theta)-Sin(1.5\theta)]-K_{II}[(3-8\upsilon)Cos(0.5\theta)+Cos(1.5\theta)]\}+0(r)$$

$$w=2(1-\upsilon^2)E\sqrt{(2r/\pi)}K_{III} \qquad \text{Eqn.(3-2)}$$

Substituting $\theta=+/-\pi$ to obtain the displacement difference across the crack flanks, gives a simpler result

$$\Delta u=2(1-\upsilon^2)\ /E\sqrt{(2r)}K_{II}$$

$$\Delta v=2(1-\upsilon^2)\ /E\sqrt{(2r)}K_I$$

$$\Delta w=2(1-\upsilon^2)E\sqrt{(2r/\pi)}K_{III} \qquad \text{Eqn.(3-3)}$$

The displacement difference parallel to the crack plane, Δu, is proportional to K_{II} while the displacement difference normal to the crack plane, Δv, is proportional to K_I. From equation (3-3) the K_I and K_{II} components can thus be separated. This method has been used at the deepest point of the crack where symmetry conditions demand that K_{III} is zero. In order to assess the accuracy of this approach for separating stress intensity factors, a bar with a slant crack inclined at 22.5 degrees to the normal direction with an (a/T) ratio 0.5 was examined under tension and bending. Good agreement was obtained with the data given by Wilson (99) as shown in Table 3.2, the discrepancy being less than 1% for both tension and

bending. For the line spring calculations the mixed modes are resolved from the appropriate displacements from the generalised line spring models developed by Desvaux (48) and Parks(45) and implemented in ABAQUS.

SECTION 3.3. Results

A comparison of the line spring and three dimensional element calculations is shown in Figures 3.9, 3.10 and 3.11 for the axial loading case and Fig.5.12 for the out of plane bending case. The results are presented in a non-dimensional form in which J is normalised with respect to the nominal applied stress in brace σ_n and the maximum crack depth a. The crack front position is defined by the distance x from the plane of symmetry normalized by the chord thickness T. The deepest point of the crack is thus located at the origin. In addition, the non-dimensional J values at the deepest point of the crack under axial loading are plotted against a/T in Fig.3.13 for both the line-spring and three dimensional calculations.

SECTION 3.4. Discussion

The stress concentration factors for tubular joints can be regarded as arising from two components. Firstly the overall geometry of the tubular joint and its loading produce membrane forces and bending moments in the tubes. If the tubes are regarded for the purpose of analysis as being thin walled, the stress distribution through the wall thickness is linear and appropriately analysed by shell analyses with the results being widely used as parametric equations of the 'hot spot' stress (2,3). However the details of the weld geometry produce a local stress concentration in which can not be modelled by shell analysis, but requires the use of three dimensional

elements. This local stress concentration however only affects the stress near the surface of the tubes where the stresses deviate from thin shell theory as shown schematically in Fig.3.14 which is taken from the work of Chu (100) reported by Burdekin (101) in which the local stress concentration affects about twenty per cent of the plate thickness. Similarly, calculations by Maddox (102) and Huang and Hancock (51) indicated that the stress intensity factor of crack is unaffected by the weld geometry at depths greater than 20%.

In the present work semi-elliptical cracks have been centred at the site of maximum stress concentration in a tubular welded joint under axial loading and out of plane bending. The cracks were normal to the chord wall, and were modelled by line springs and also by three dimensional element formulations. For the deepest crack a/T=0.9, the stress intensity factor for the line spring analysis and the three dimensional analyses agreed to within 3.5 percent at the deepest point and show good agreement throughout the crack front. The largest discrepancy occurred at the mid-side nodes of the three dimensional elements at the free surface. For all three crack profiles this contour exhibited an anomolously low value. Inspection of the focused mesh around the crack front, shown in Figure 3.8 indicated that this occurred in a single brick element which is required to represent a highly curved section of crack front. It seems likely then that the line spring analysis is to be preferred at this point, even though the physical basis of the line spring model is less secure near the ends of the cracks.

The intermediate depth crack, again shows similar features. The discrepancy in the stress intensity factors between the line spring analysis and the solution using three dimensional brick elements is 2.5 percent at the deepest point, for the axial loading case and 8% for out of plane bending, while the agreement throughout the length is excellent. The agreement between the 3 dimensional and line spring solutions for

intermediate and deep cracks essentially indicates that any local stress concentration due to the weld profile, which is not modelled in the line spring shell analysis has no effect. In contrast the shallow crack analysis shows a significant discrepancy between the line spring and the 3D element calculations. This is most likely to come from the different stress concentration produced by shell and 3D analyses for the uncracked geometries. The stress concentration factor from the 3D element analysis is significantly higher than produced by shell analysis, as the former incorporates the local geometrical stress concentration arising from the weld geometry. The brick element analysis is likely then to give higher stress intensity factors for short cracks located in the locally enhanced stress field. For the present T-joint under axial loading, the stress concentration factor was 11.9 obtained from 3D brick analysis (103) as opposed to 9.6 for the shell analysis. Interestingly, however, the experimental data of Dover et al (20) gave a value which was within 13% for the effective stress intensity factor for the deepest point of the crack in somewhat better agreement with the line spring calculations. The three dimensional element solutions is 25% higher than the experimental result, but for shallow cracks, it is important to realise that the exact location of the crack and the exact weld profile are important since the stress intensity factor distribution depends on the detail of the local stresses near the weld toe.

In the present work, to extend the validity of line spring method to shallow cracks, a correction factor f_L accounted for the effect of the weld geometry has been introduced. This was obtained by considering some two dimensional butt joints made with flat plates. The ratio of the crack depth to the thickness was varied from 0.05 to 0.2. In this simple system, the stress intensity factors have been determined by two different methods

(virtual crack extension method with continuum elements and line springs). Here, as an example, it is only necessary to consider one simple T butt joint which was idealised as shown In Fig.3.15. In the first case shown Fig.3.15a) the joint was represented by 30 elastic 8 noded shell elements which do not allow the details of the weld geometry to be modelled. The crack was represented by an elastic line spring located at a position representative of the weld toe which was taken to be one plate thickness from the center line of the vertical plate. When using a continuum approach the joint was represented by approximately 130 elastic 8 noded plane strain isoparametric elements. In contrast to shell analysis these elements allow the details of the local weld geometry to be modelled specifically, and seven idealised weld profiles have been considered. The first case models a smoothly radiused weld profile, the next five cases involve straight weld profiles with weld angles at 15 degree increments between 15^0 and 75^0. Finally the weld profile was removed completely. The meshes corresponding to these models are shown in Fig.3.15b) . In each case the crack tip was modelled by a focused mesh with the mid-side nodes located at the quarter point positions. Three different loading cases were considered. Firstly, a uniformly distributed force was applied at the end of the vertical plate while the two ends of the horizontal plate were built in. Secondly, a pure moment was applied at the two ends of the horizontal plate and the end of the vertical plate was free. Finally a uniformly distributed force was applied at the ends of the horizontal plate while the end of the vertical plate was allowed to remain free. The correction factor f_L can be regarded as the ratio of the stress intensity factor obtained using continuum element to that using line springs and shell elements. When the crack depth is zero, f_L is the ratio of stress concentrations as given in Fig.3.16. These figures clearly demonstrate how the correction factor f_L varies with weld

angle and crack depth. In the region a/t=0.05-0.2, f_L increases with the weld angle and decreases with the crack depth, being mainly dependent on weld profile, and slightly dependent on loading type. Application of the correction factor to 3 dimensional T-joint, makes the line spring solution and experimental data agree within 4% difference, as opposed to 17% before correction for a weld angle of 75^0 and a non-dimensional crack depth of a/T=0.2.

The engineering approach requires the use of some simple structural parameters to represent the stress intensity factors solutions. In order to apply the current results to a similar welded tubular joint in linear elastic conditions J has been scaled with respect to applied load according to:

$$J=f(a/T)P^2/TE' \qquad \text{Eqn.(3-4)}$$

Here f(a/T) is a function of a/T only. A comparison of f(a/T) for the linesprings and 3 dimensional brick element models is given in Fig.3.17. In this way the data can be expressed by the empirical formula:

$$f(a/T)=1.49\times10^{-3}+1.29\times10^{-3}(a/T)-4.3\times10^{-3}(a/T)^2+1.52\times10^{-3}(a/T)^3$$

(C/T=2) Eqn.(3-5)

Although there is limited data for this expression it is now introduced as elastic-plastic analyses used later requires an interpolation function between elastic solutions with different crack depths.

The contributions of mode 1 and mode 2 at the deepest point of the crack are given in Table (3.3) and Figure 3.18, while Figure 3.18 shows the ratio of (K_I/K_{II}) for the line spring and 3 dimensional element calculations. The increasing K_{II} component for deep cracks implies that fatigue cracks are not likely to adopt a path normal to the chord wall but develop along a curved path. This evidence also indicated by experimental data given by

Noordhock et al. (52). However, the present calculations only apply to the situation in which the crack is normal to the chord wall. The problem of determining crack paths and stress intensity factors for a curved semi-elliptical crack in tubular T joint using numerical method is to be discussed in Chapter 6. Nevertheless, as a necessary preliminary to understanding the behaviour of semi-elliptical crack in 3D structures, the problem of some through curved cracks and slant cracks in some simple two dimensional geometries will be discussed in Chapters 4 and 5.

SECTION 3.5 , Conclusions

Line spring calculations of the stress intensity factor of semi-elliptical cracks in a tubular joint gave closely similar results to full three dimensional solutions for (a/T)=0.9 and 0.6, while agreeing with experimental values at (a/T) =0.2. For shallower cracks the line spring and shell analysis is unlikely to give an adequate account of the effect of a crack in a local stress concentration, and requires the application of correction factor to take into account the stress concentration due to the weld profile.

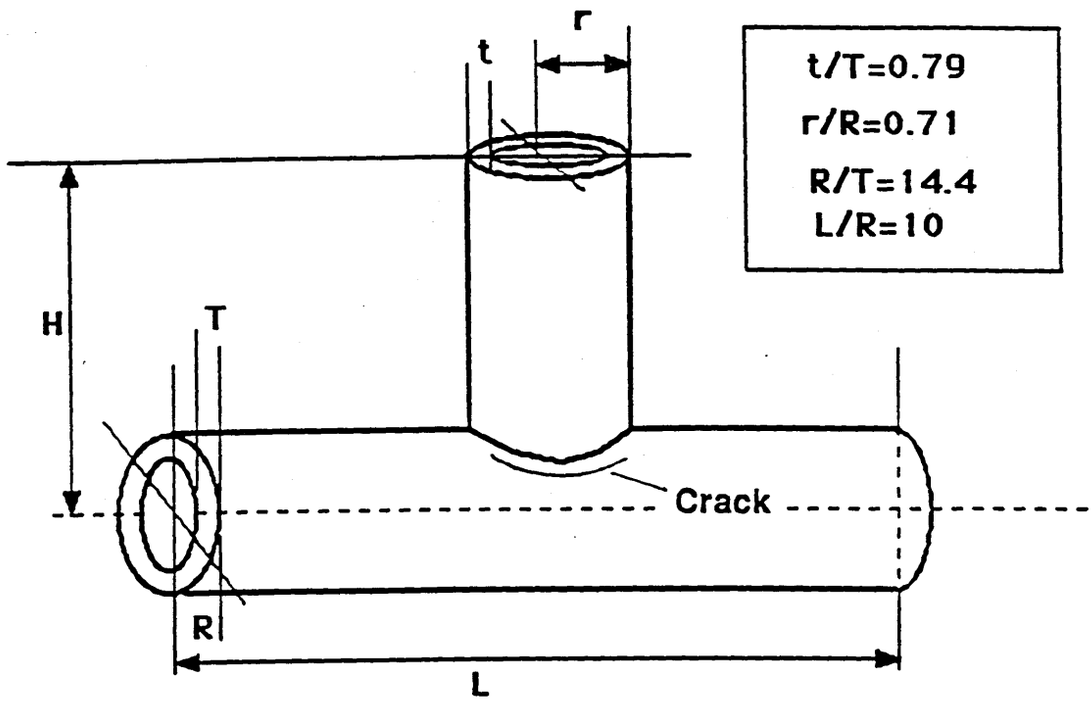

FIG.3.1 The geometry of the tubular welded T joint.

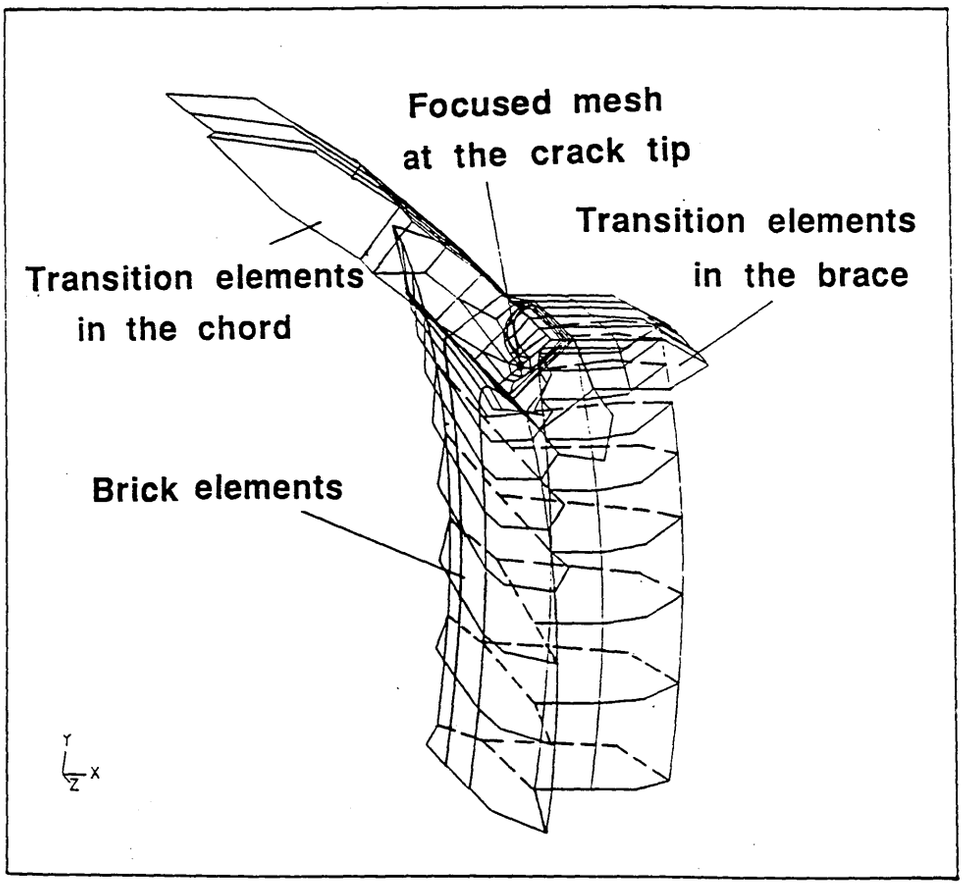

FIG.3.2 A schematic Illustration the connection of bricks, shells and transition elements

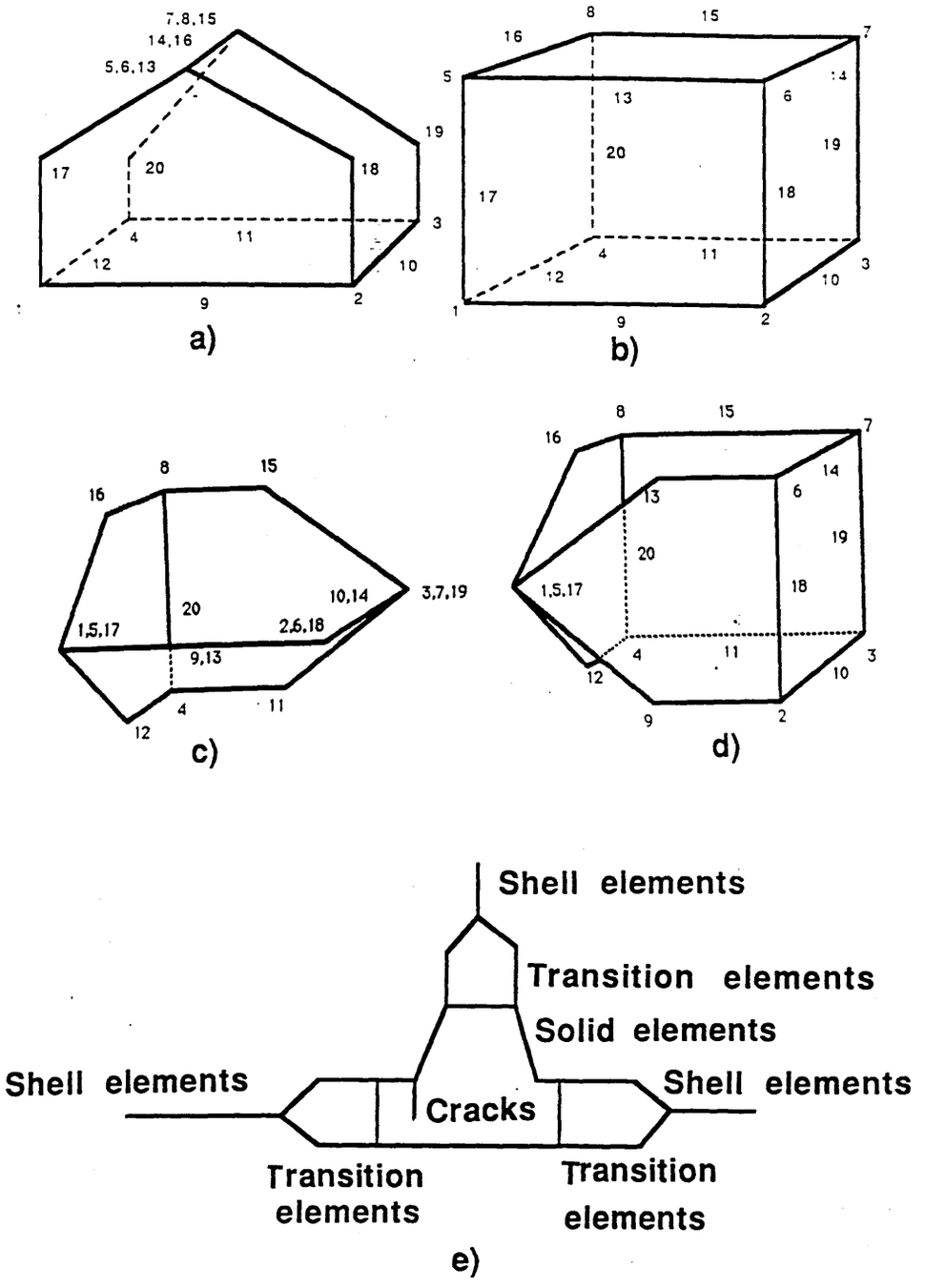

FIG.3.3 a) A fifteen noded transition element made by degenerating a twenty noded brick element.

b) A twenty noded brick element.

c) A twelve noded transition element made by degenerating a twenty noded brick element

d) An eighteen noded transition element made by degenerating a twenty noded brick element

e) A schematic cross section through the weld, illustrating the brick elements,the transition elements, the shell elements and the crack

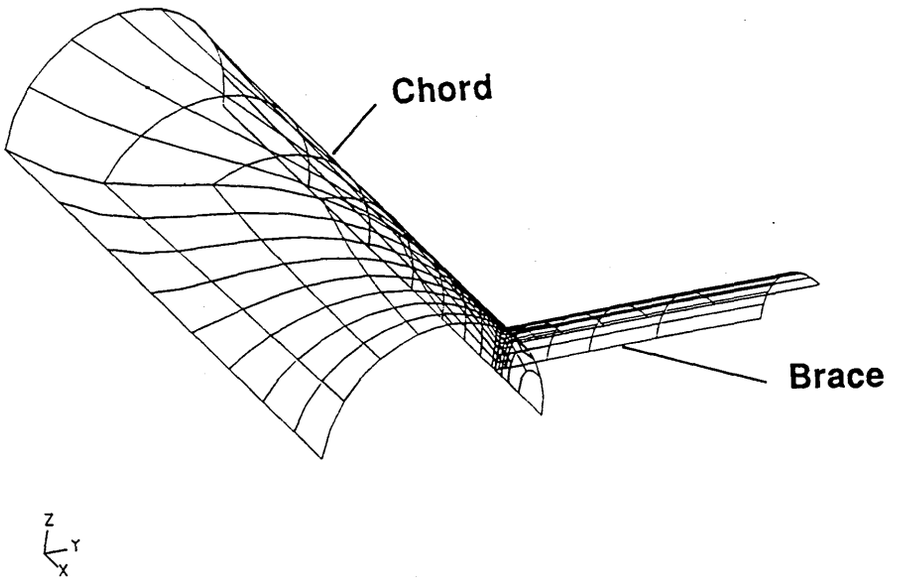

a)

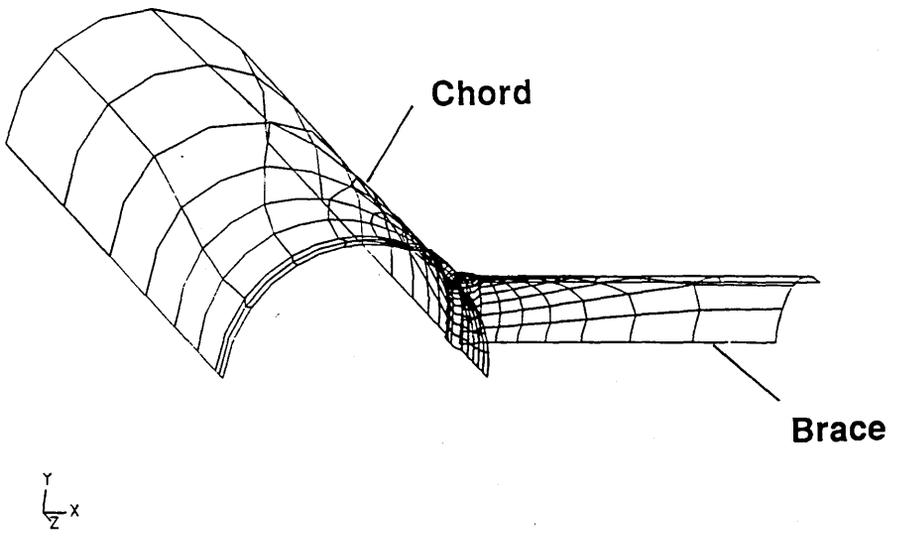

b)

FIG.3.4 a) A finite element mesh using shell elements and line springs for axial loading case
b) A finite element mesh using shell and brick elements for axial loading case.

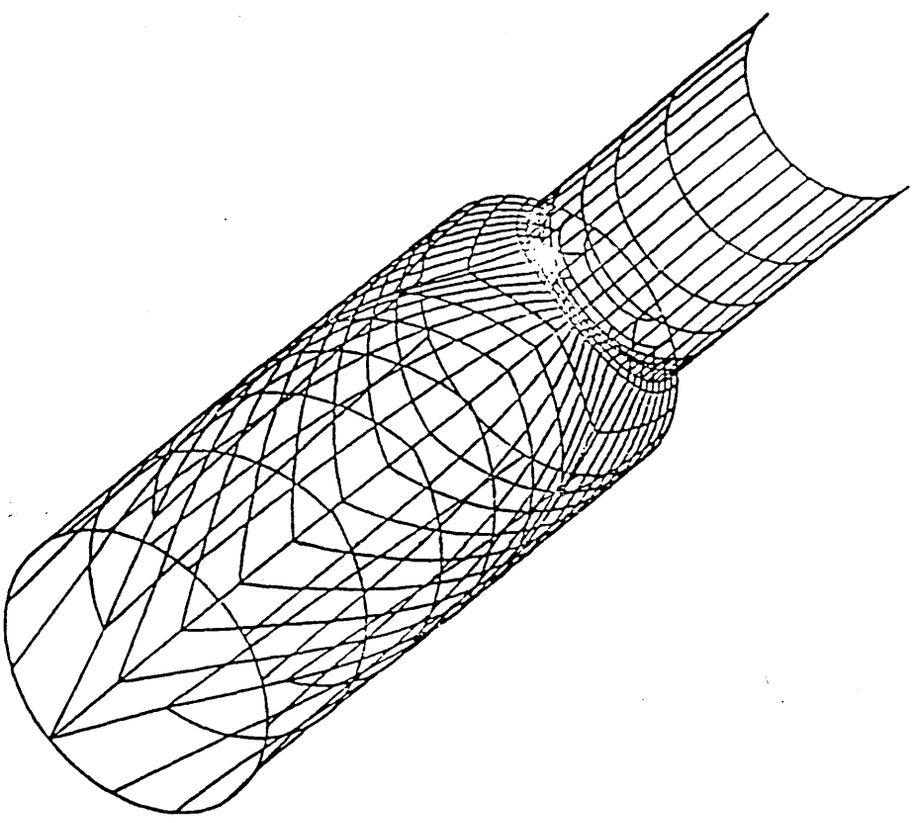

FIG.3.5 A finite element mesh using shell for the out-plane bending case

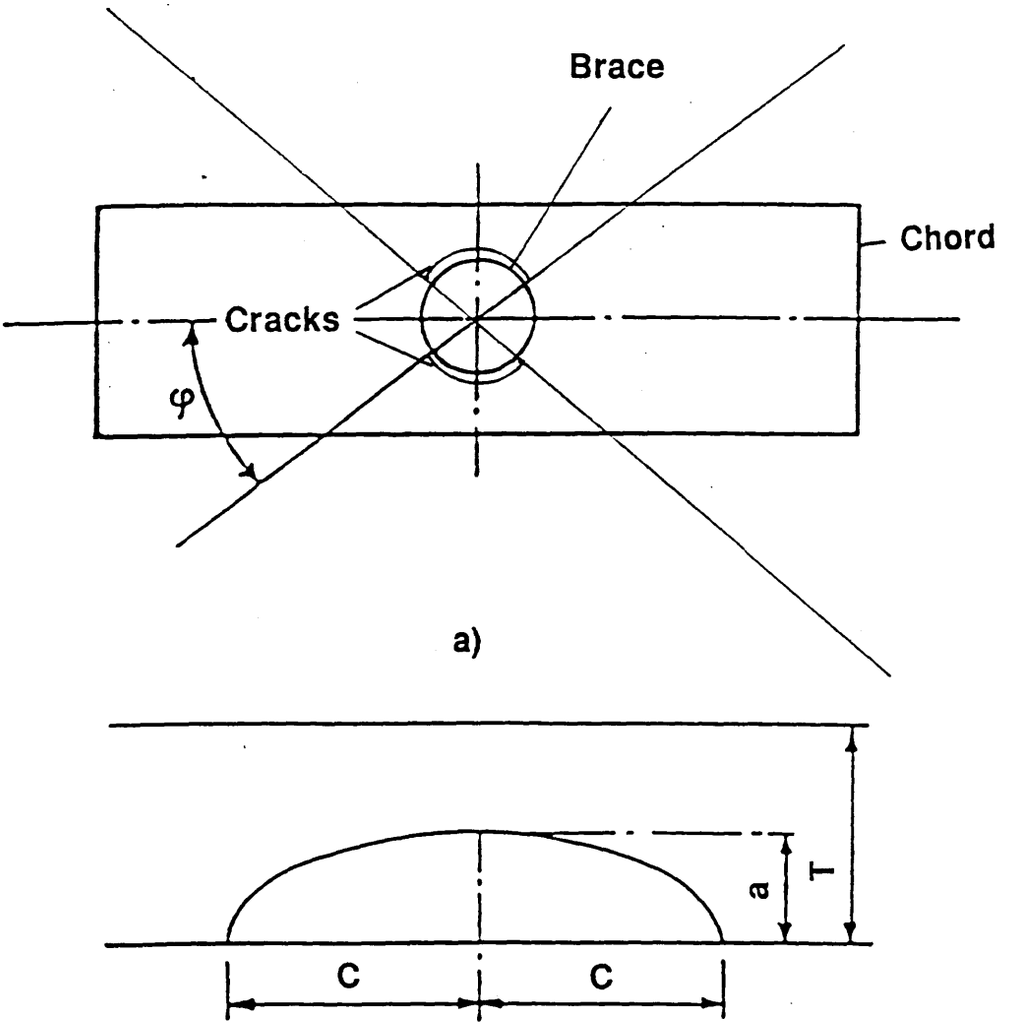

FIG.3.6 a) The location of the semi-elliptical cracks.
b) The crack geometry.

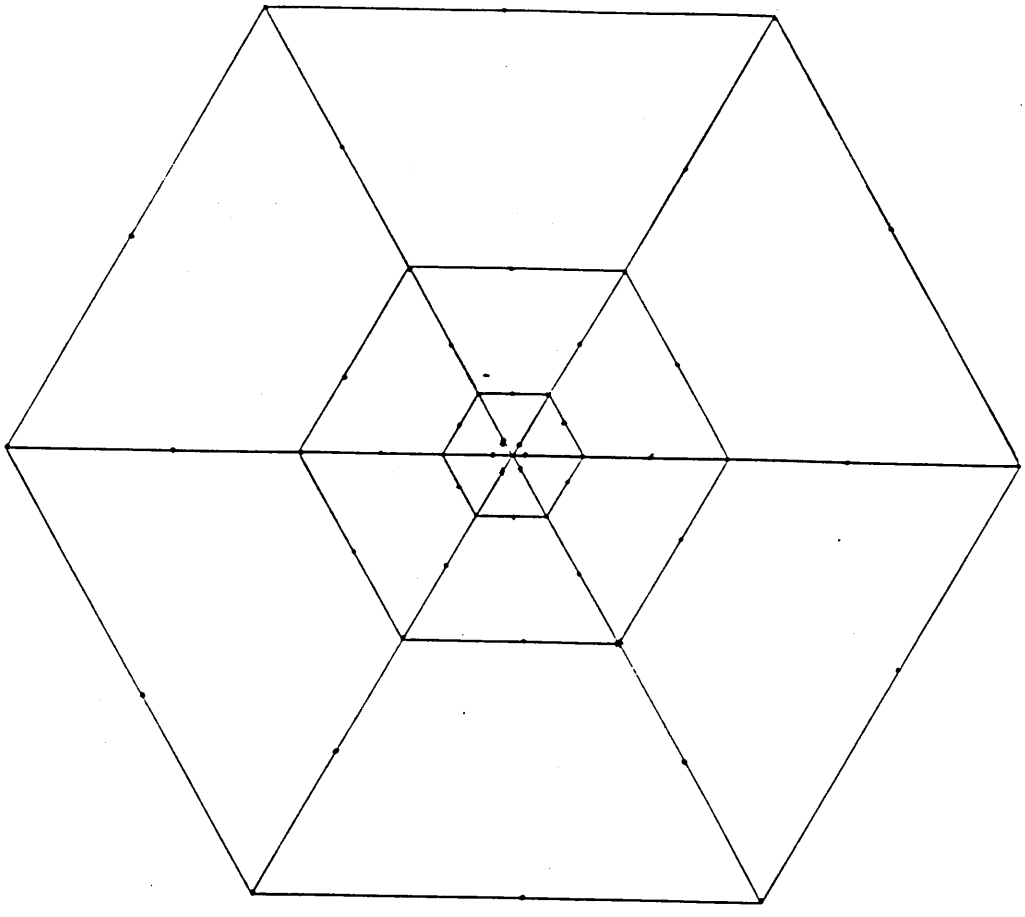

FIG.3.7 A focused mesh of brick elements

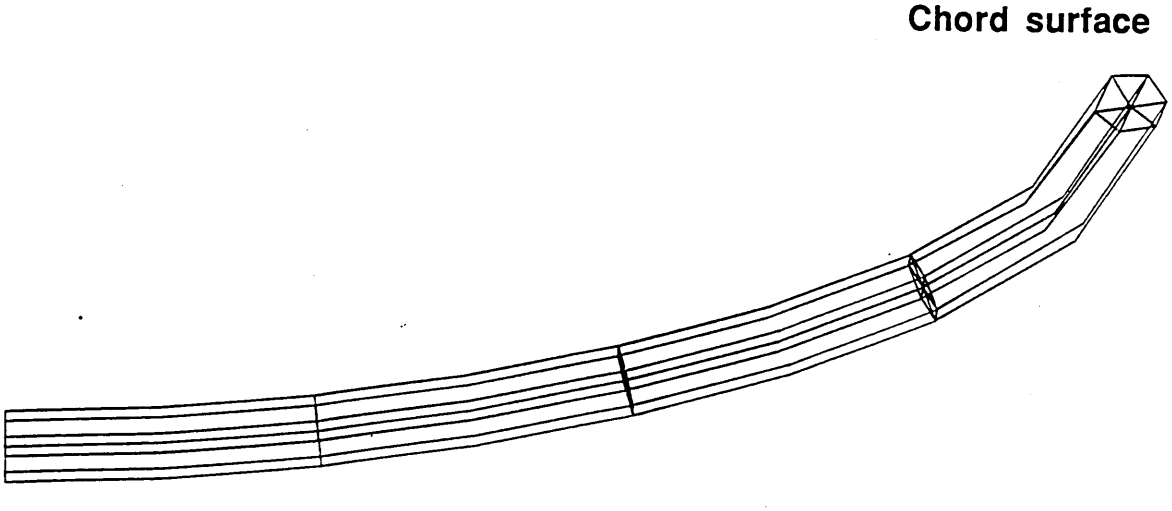

FIG.3.8 The brick elements along the crack front.

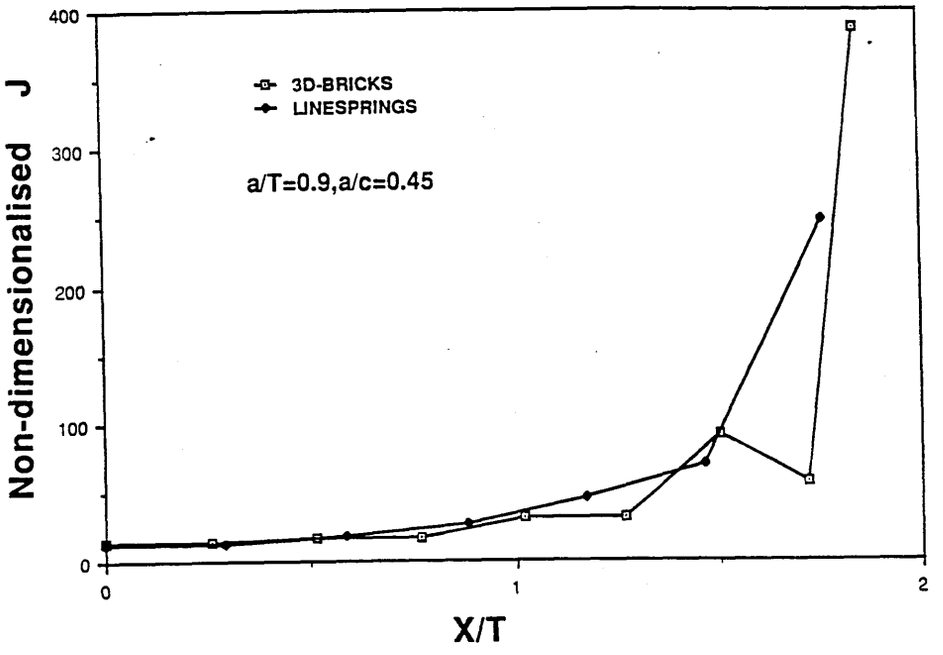

FIG.3.9 A comparison of the non-dimensionalised $J=EJ/\sigma_n^2(1-\upsilon^2)a$ around the crack front from the line-spring and brick element calculations under axial loading. The crack geometry is defined by a/T=0.9,a/c=0.45

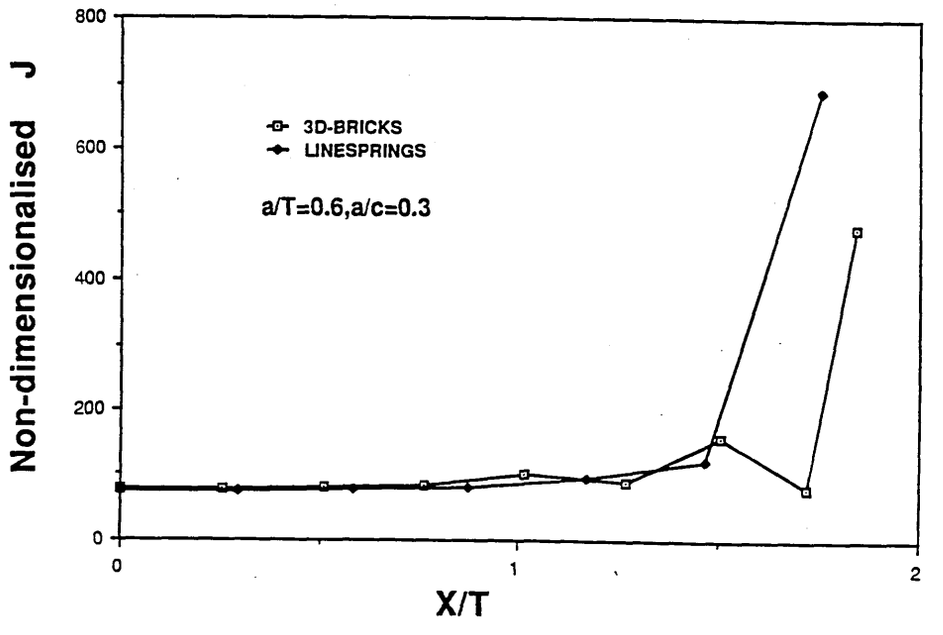

FIG.3.10 A comparison of the non-dimensionalised $J=EJ/\sigma_n^2(1-\upsilon^2)a$ around the crack front from the line-spring and brick element calculations under axial loading, The crack geometry is defined by a/T=0.6,a/c=0.3

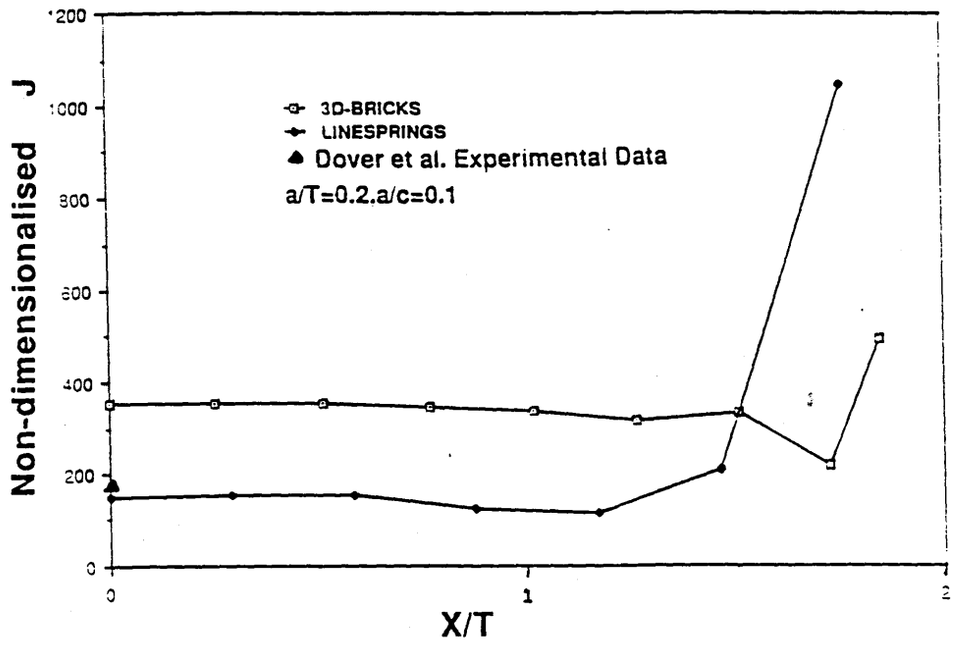

FIG.3.11 A comparison of the non-dimensionalised $J=EJ/\sigma_n^2(1-\upsilon^2)a$ around the crack front from the line-spring and brick element calculations under axial loading. The crack geometry is defined by a/T=0.2,a/c=0.1

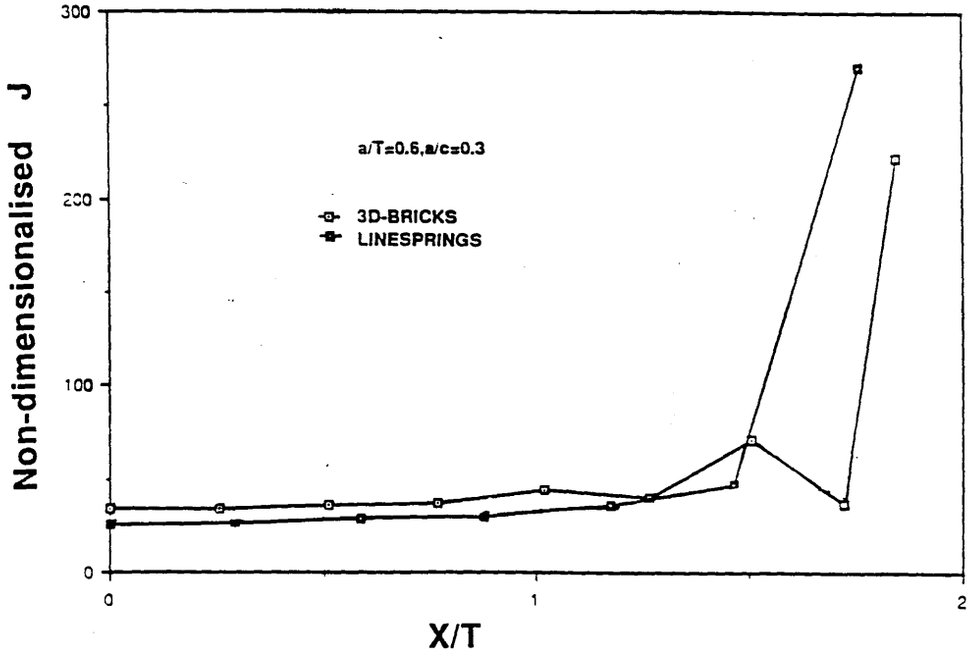

FIG.3.12 A comparison of the non-dimensionalised $J=EJ/\sigma_n^2(1-\upsilon^2)a$ around the crack front from the line-spring and brick element calculations under outplane bending. The crack geometry is defined by a/T=0.6,a/c=0.3

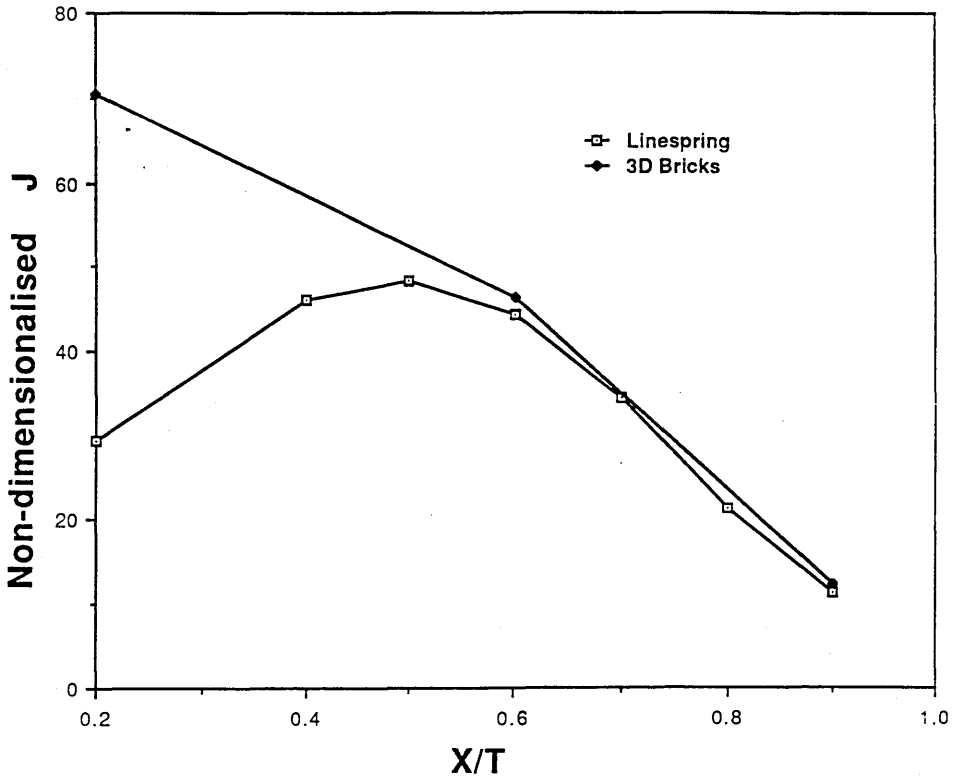

FIG.3.13 A comparison of the non-dimensionalised $J=EJ/\sigma^2(1-\upsilon^2)T$ at the deepest point from the line-spring and brick element calculations under axial loading

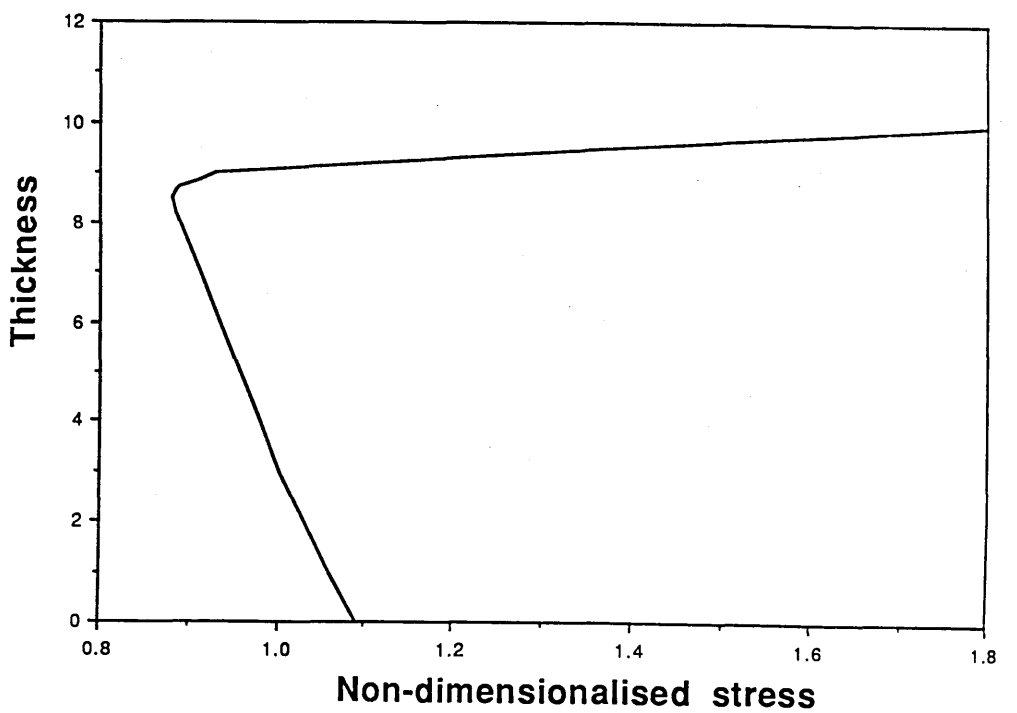

FIG.3.14 Stress Distribution through the wall following Chu (100) and Burdekin (101)

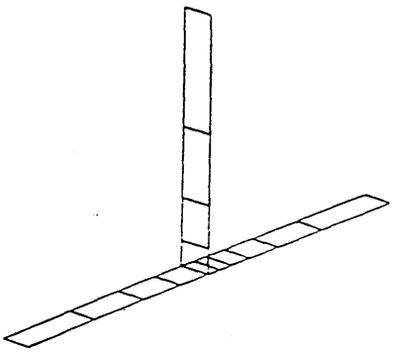

a)

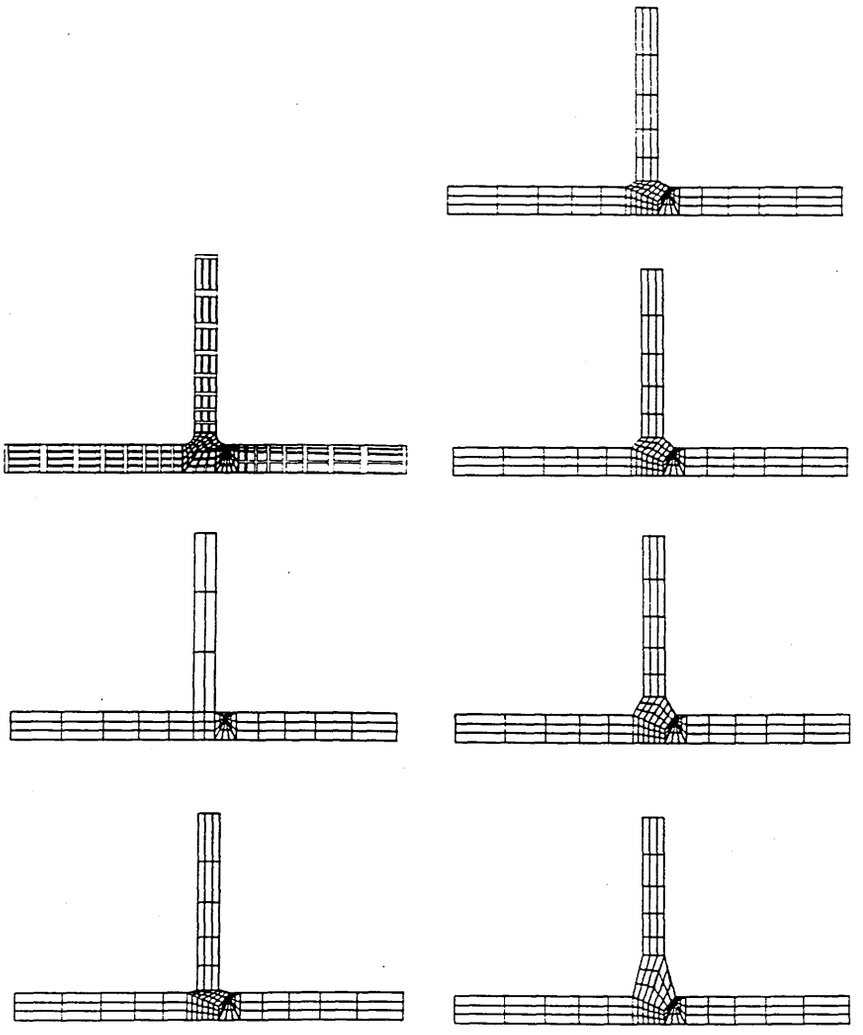

b)

FIG.3.15 Simple T butt joint modelled by shell elements and continuum elements

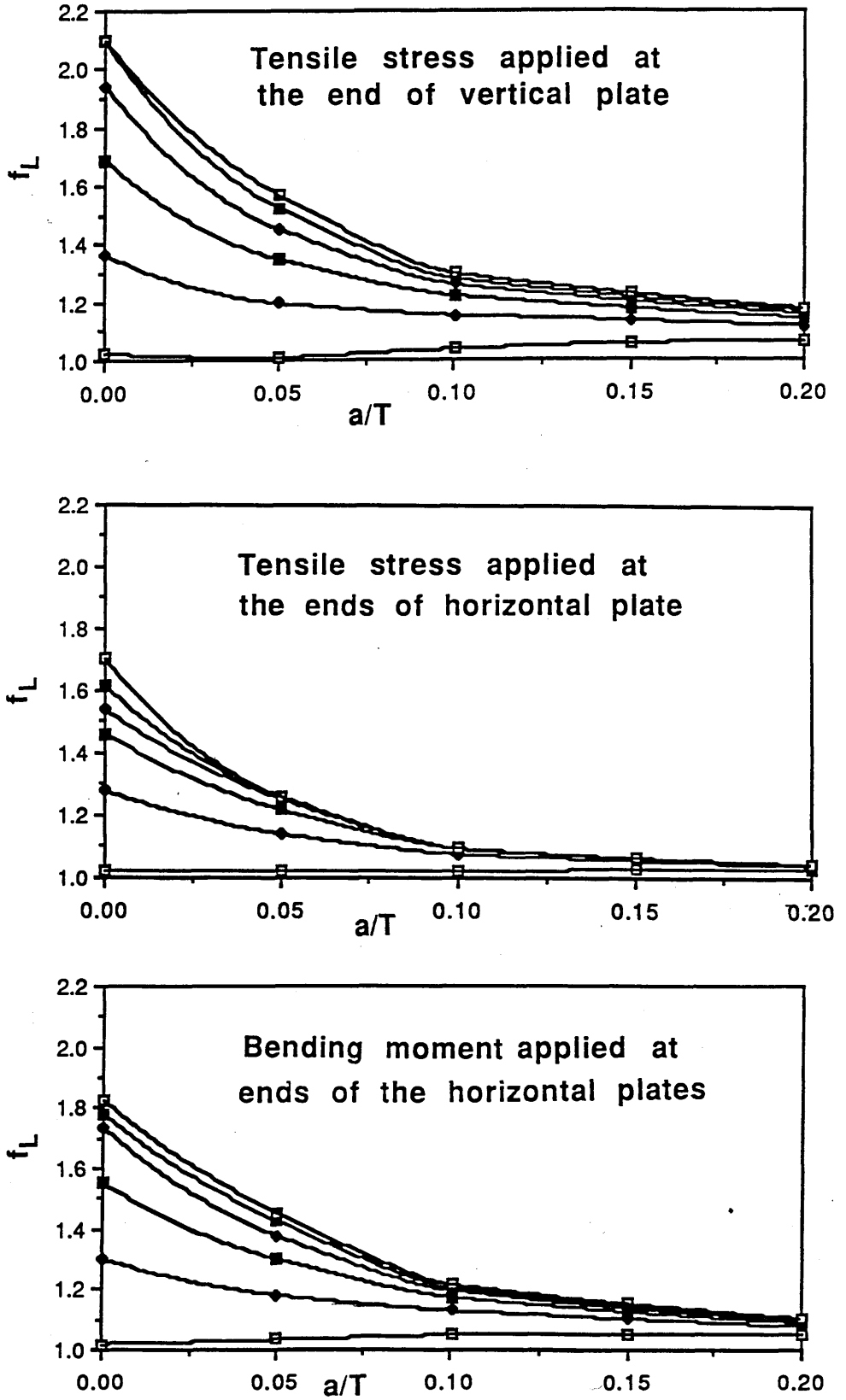

FIG.3.16 Non-dimensional function f_L as a function of a / T

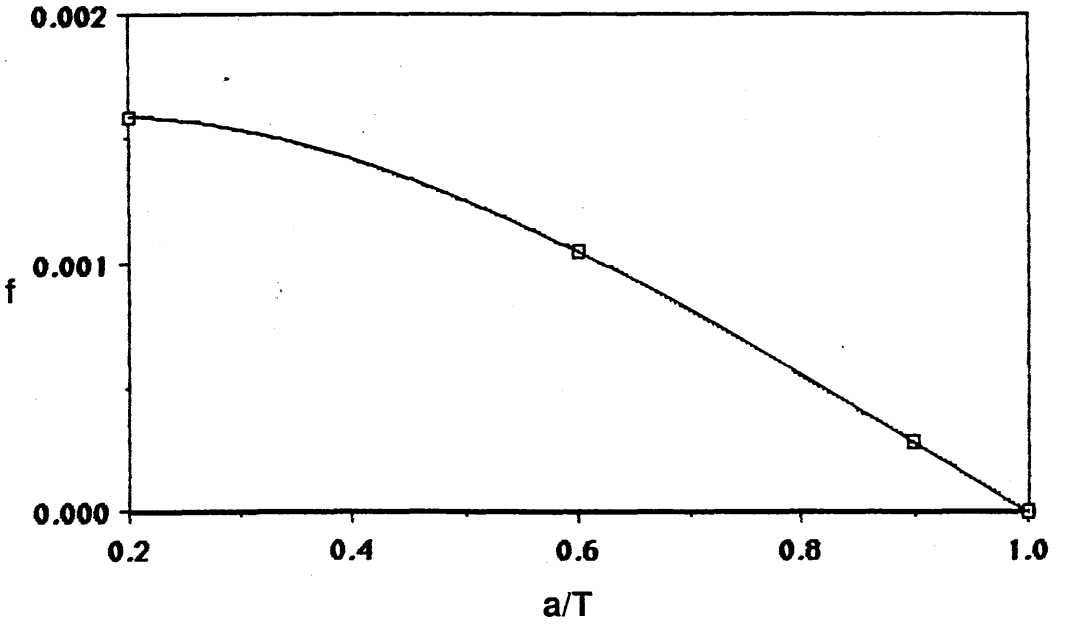

FIG.3.17 Non-dimensionalised $f(a/T)=TJE'/P^2$ at the deepest point as a function of a/T

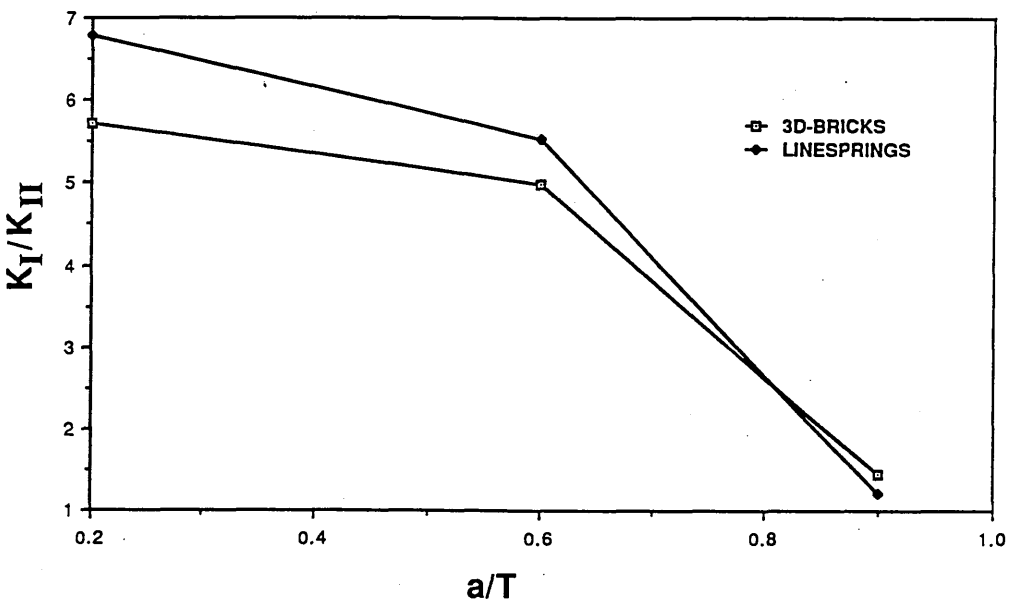

FIG.3.18 A comparison of K_I/K_{II} for line-spring and 3D Element calculations.

THREE DIMENSIONAL SOLUTIONS				
a/T	c/T	NO.OF SHELL ELEMENTS	NO. OF BRICKS	DEGREES OF FREEDOM
0.2	2	215	160	12012
0.6	2	215	160	12012
0.9	2	248	160	12012
SHELL SOLUTIONS				
a/T	c/T	NO. OF SHELL ELEMENTS	NO. OF LINE SPRING ELEMENTS	DEGREES OF FREEDOM
0.2 0.6 0.9	2	210	3	4170

Table 3.1 **The number and type of element as well as the number of degrees of freedom of the system for both shell model and 3D brick model**

	Non-dimensional K_I		Non-dimensional K_{II}	
	Bending	Tension	Bending	Tension
STANDARD DATA GIVEN BY WILSON	2.25	4.02	0.40	0.87
Finite element Results	2.27	4.02	0.41	0.87

Table 3.2 A comparison of the non-dimensionalised $K_I=K_I/\sigma\sqrt{\pi a}$ and $K_{II}=K_{II}/\sigma\sqrt{\pi a}$ from current finite element calculations and the data given by Wilson (99)

	3 DIMENSIONAL FINITE ELEMENT		LINE SPRING	
a/T	Non dimensional K_I	Non dimensional K_{II}	Non dimensional K_I	Non dimensional K_{II}
0.9	3.04	2.10	2.71	2.23
0.6	8.62	1.73	8.42	1.52
0.2	18.50	3.23	11.96	1.76

Table 3.3 **A comparison of the non-dimensionalised $K_I=K_I/\sigma\sqrt{a}$ and $K_{II}=K_{II}/\sigma\sqrt{a}$ at the deepest point of the semi-elliptical crack from the line-spring and brick element calculations under axial loading**

CHAPTER 4. Determination of the Crack Extension Direction for Some Two Dimensional Cracked Geometries

SECTION 4.1.Introduction

The use of fracture mechanics in offshore structures depends on measurements of the crack length and orientation. In this context it is necessary to realise that measurement by A.C potential drop techniques only gives the curved length of the crack flanks, while magnetic particle inspection only gives the surface length. If the joint looses structural stiffness when it penetrates the chord wall, as shown both by the calculations of Huang and Hancock (51) and by the experiments of Dover et al. (20), this will occur at a total crack length greater than the chord thickness, if the crack path is curved. Similarly, fatigue predictions of the life of the joint might typically involve integrating the fatigue crack growth rate from an initial depth to chord penetration, and the assumption that the crack path is normal to the wall may introduce significant errors.

As far as the direction of propagation is concerned, it is now commonly accepted that under mixed mode loading, defects and cracks in structural members seldom grow in a self similar manner but rather tend to turn and curve depending on the combined effect of geometry and loading. In 1968, Sih et al. (104) applied the maximum stress theory of fracture to the determination of the crack path. They assumed that the crack would extend along a path normal to the direction of the greatest tensile stress, or equivalently in direction in which the shear stress was zero. However it is not very convenient to determine the crack path directly using the maximum tensile stress theory, and as an alternative it is frequently postulated that cracks develop in such a way as to maximise the mode 1 stress intensity component(105). Alternatively, it has been suggested that the path

maximises the strain energy release rate (23, 105).

In linear elastic fracture mechanics, the strain energy release rate G is related to the stress intensity factors by the relationship

$$G=K_I^2(1-\upsilon^2)/E + K_{II}^2(1-\upsilon^2)/E+ K_{III}^2(1+\upsilon)/E \qquad \text{Eqn.(4-1)}$$

The direction of crack growth which maximises strain energy release rate for each direction of infinitesimal crack extension, can be addressed using a modification of the virtual crack extension method (22). In addition, solutions for a small angled kink at the tip of a straight crack derived by Bilby et al. (105), Hussain et al (106) Masihiro et al (107), and Kagayama et al.(108) are useful in giving insight into the crack growth direction. Of these equations, Masihiro et al.'s equation was derived using the maximum tensile stress theory by considering a crack extending in a non-coplanar fashion along a plane inclined to the original crack plane. Calculations and experiments have been performed on simple two dimensional geometries as a precursor to predictions on three dimensional tubular joints.

SECTION 4.2. The Experimental Procedures

The object of the experimental programme was to measure the crack path under controlled mixed mode loadings produced in simple geometries in order to verify the numerical techniques which could be later used on tubular welded joints. To achieve this, two different geometries were used; rectangular bars specimens made of polymethyl methacrylate sheet (hence forth perspex) and steel, and T butt joints made of perspex. The steel specimens were tested under three point bending under both monotonic loading and fatigue loading, while the perspex specimens were tested only

under monotonic loading.

4.2.1 Off-axis Three Point Bending

4.2.1.1 Perspex Specimens

Asymmetric three point bend tests were performed on edge cracked bars of length 11T, and width 2T, where T was the thickness of the plate. This was chosen to be 25.4mm (1 inch). The distance between the two outer loading points was 8T. Specimens were machined from perspex and tested under three point bending using an Instron testing machine under cross head control. To produce a mixed mode loading, the crack was not located at the centre of the specimen, but at a distance x=2T away from the central loading point. The crack was thus subject to mixed mode loading consisting of mode I and mode II combination, as a shear stress occurs in the crack plane as shown in Fig.4.1. The same technique has been used in steel specimens by Hua et al.(109).

The specimens contained a straight saw cut notch with non-dimensionalised crack depths a/T between 0.14 and 0.85, as illustrated in Fig.4.1. As perspex is a very brittle material, unstable crack growth occurred at the load maximum. For the purpose of the test, attention was focused on the crack path as a function of the ratio of crack depth to the specimen thickness (a/T).

In addition to this test, two specimens with pre-existing cracks with a/T=0.14 and a/T=0.5 were tested when the initial crack was located at a distance x=3T from the central loading point. The ratio of shear force to bending moment at the crack plane is equal to 1/(L/2-x), where x and L are given in Fig.4.1. As x increases, the ratio of the shear force to the bending moment increases. This is illustrated in Fig.4.2 which shows the ratio of the bending moment to the shear force times the fixed distance L as a

function of the distance (x/L) between the central load point and the site of the crack.

The crack paths were documented by measuring the angle between the tangent to the crack path and the normal to the plate length. Photographs of broken asymmetric 3 point bend specimen are shown in Fig.4.3 for x=2T. The angles at which the crack started to grow are plotted against a/T in Fig.4.4. Similar photographs for x=3T are given in Fig.4.5, and the angles at which the crack started to grow were 19^0 for a/T=0.14 and 32^0 for a/T=0.5.

4.2.1.2 Steel Specimens.

Two rectangular specimens made of a carbon manganese steel described as 50D under B.S.4360 were used to study the crack path in fatigue. The overall dimensions of the specimens were the same as those of the perspex specimens. The first specimen (Code A) was initially tested under constant amplitude fatigue loading to introduce a fatigue crack from a V notch under mode I conditions by using symmetric three point bending at cyclic applied loads of 25+10 KN and a frequency of 5 HZ. As soon as the crack had grown to a depth of 10mm, the specimen was moved to locate the crack a distance 2T away from the central loading point and the test was continued. The applied load was 30±20 KN, which was small enough to maintain the specimen under plane strain conditions with respect to the plastic zone.

The second fatigue specimen (Code B) was initially tested under symmetric three point bending, until a/T=0.5, using an applied load of 20±15KN. The specimen was then moved to locate the crack a distance 2T from the central loading point, and the test was continued at an applied load of 22±21KN.

In the fatigue tests, the crack depth was monitored using a D.C. potential

drop technique using current of 67amps applied through leads at the specimen ends. Probes were located on each side of the crack to measure the potential drop across the crack, and the results were recorded on a data logger.

The first steel specimen is shown in Fig.4.6 after fracture. The angle of crack growth has been plotted as a function of the ratio of crack depth to the thickness of the specimen, in Fig.4.7. A photograph of the second specimen after fracture is shown in Fig.4.8 and the relationship between the angle of the crack growth and the normalised depth a/T is given in Fig.4.9.

4.2.2 T-Butt Joint Specimens

To extend the experimental programme to geometries more representative of welded joints , two T-butt joints made of perspex shown in Fig.4.10 were used. Cracks were simulated by saw cut notches at a position representative of the weld toe. The ratio of the initial notch crack depth to the thickness was 0.2. The horizontal ends of the first specimen were built in, while a tensile force was applied to the end of the vertical plate as illustrated in Fig.4.10 a) For the second specimen, the upper surfaces of the two ends of the horizontal plate were fixed in the vertical direction but rotation and horizontal displacements were allowed, while a tensile force was applied to the end of the vertical plate as illustrated in Fig.4.10 b). The crack path was obtained by measuring angle between the tangent to the crack path and the direction of the horizontal plate thickness. Photographs showing these specimens after fracture are given in Fig.4.11 and Fig.4.12 and the angle of the crack growth has been plotted as a function of a/T in Fig.4.13 .

SECTION 4.3, Numerical Methods

4.3.1 Crack Path using the Maximum g Theory

The purpose of the present calculations was to determine the crack growth direction in mixed mode loading using finite element analyses. The analyses were implemented with a finite element code ABAQUS (87) using the virtual crack extension method of Parks (21). If g is interpreted as the energy release rate corresponding to virtual crack extension at some crack angle, the direction of crack growth is that at which the maximum crack driving force occurs. The small letter g is now used to denote the strain energy release rate for crack extension at some arbitrary angle, while the capital letter G is preferred for the classical concept of strain energy release rate when coplanar crack propagation occurs.

When g was calculated by virtual crack extension, the direction cosines of the normal to the plane of the crack were defined in the input file by the direction cosines of the normal to the assumed crack extension direction. Parks (110) has commented that two conditions must be met for this process to be valid. Firstly the crack tip elements must be small and secondly they must be symmetric about the crack plane.

4.3.2,Numerical Results for Off-Axis Three Point Bending

Finite element models with the same dimensions as the experimental specimens were modelled with 8 noded isoparametric plane strain elements provided by the finite element code ABAQUS (87). The meshes generated using a commercial mesh generator called FEMGEN (88). are shown in Fig.4.14. In these models, the crack tip was modelled as a focused mesh in which the mid-side nodes were located at the quarter point positions: a

procedure which allows the elements to adopt the correct form of displacement function for the elastic singularity, as discussed by Barsoum (94) and Henshell and Shaw (95). Typically, each model involved approximately 550 nodes and 160 elements, thus giving a system with 1200 degrees of freedom. For each model, a series of crack extension directions was input by giving the normal to the direction of crack extension as 5,8,10,15,30,45,60,75, 80 and 90 degrees to the main crack (off-axis crack extension). All the problems were analysed on a Vax11/750, on which each model required about 30 mins Cpu time. The off-axis strain energy release rate g is plotted as a function of crack growth angle as shown in Fig.4.15 for X=2T and in Fig.4.16 for X=3T. For each crack depth, g was obtained as a function of the crack extension direction. The angle corresponding to the maximum g values was plotted as a piece-wise linear function of a/T in Fig.4.17 for x=2T. When the applied loading point was located a distance 3T away from the crack., the angle was 19^0 when a/T=0.14 and 30^0 when a/T=0.5.

The off-axis virtual crack extension method has the disadvantage of requiring a large amount of CPU time as it is necessary to recalculate g for each input angle, although to avoid re-reading bulk data, such as, elements, nodes,element sets and node sets, several steps were processed in one ABAQUS main program. Subsequently a more elegant method which required only one finite element calculation for a normal crack in conjunction with the kinked crack solutions introduced by Bilby et al.(105), Hussain et al. (106), Masahiro et al.(107) and Kagayama et al.(108) was devised.

4.3.3 The Crack Path using Maximum k_I Theory

4.3.3.1 Theory

The relations between the stress intensity factor for a kinked crack

denoted k shown in Fig.4.18 and the stress intensity factor, (K), for the main crack have been established by using equations given by Bilby(105), Hussain(106), Masahiro et.al(107) and Kagayame et al.(108). The corresponding strain energy release rate for the kinked tip is denoted by the small letter g and can be calculated by combining k_I and k_{II} using equation 4-1.

All the equations can be written in the form:

$$k_I = c_{11}(\alpha)K_I + c_{12}(\alpha)\, K_{II}$$
$$k_{II} = c_{21}(\alpha)\, K_I + c_{22}(\alpha)K_{II} \qquad \text{Eqn.(4-2)}$$

where Hussain (106) gives

$$c_{11}=\left(\frac{\pi-\alpha}{\pi+\alpha}\right)^{\alpha/2\pi}\frac{4\cos\alpha}{3+\cos^2\alpha}$$

$$c_{12}=\left(\frac{\pi-\alpha}{\pi+\alpha}\right)^{\alpha/2\pi}\frac{6\sin\alpha}{3+\cos^2\alpha}$$

$$c_{21}=\left(\frac{\pi-\alpha}{\pi+\alpha}\right)^{\alpha/2\pi}\frac{-2\sin\alpha}{3+\cos^2\alpha}$$

$$c_{22}=\left(\frac{\pi-\alpha}{\pi+\alpha}\right)^{\alpha/2\pi}\frac{4\cos\alpha}{3+\cos^2\alpha} \qquad \text{Eqn.(4-3)}$$

while Masahiro (107) gives

$$c_{11}=0.5\cos(\alpha/2)\ (1+\cos(\alpha))$$
$$c_{12}=-1.5\cos(\alpha/2)\sin(\alpha)$$
$$c_{21}=0.5\cos(\alpha/2)\ \sin(\alpha)$$
$$c_{22}=0.5\cos(\alpha/2)(3\cos(\alpha)-1) \qquad \text{Eqn.(4-4)}$$

and Kagayama (108) gives

$$c_{11}=0.5\cos(\alpha/2)(1+\cos(\alpha/2))(1+0.051\zeta^4)$$
$$c_{12}=-1.5\cos(\alpha/2)\sin(\alpha)(1+0.06\zeta^2+0.064\zeta^4)$$
$$c_{21}=0.5\cos(\alpha/2)(3\cos(\alpha)-1)+0.242\zeta^2-0.085\zeta^4$$
$$c_{22}=0.5\cos(\alpha/2)\sin(\alpha))(1-0.048\zeta^2+0.033\zeta^4) \qquad \text{Eqn.(4-5)}$$

where $\zeta=\alpha/90$

Finally, the values of c_{ij} given by Bilby are shown in Table 4.1.

In order to compare these results, it is convenient to plot c_{ij} as shown in Fig 4.19 a) and b). It is clear from this figure and Eqn.4-2 that the results of these equations are broadly similar although different in detail.

To obtain the maximum mode 1 stress intensity factor k_I for the kinked crack, three steps were involved:

Firstly, the strain energy release rate for the main crack was calculated by the use of the virtual crack extension method. Secondly, the mode 1 and mode 2 stress intensity factors were separated by examining the displacements of the quarter point nodes at corresponding sites on the upper and lower crack faces using Eqn(3-3). Finally, the values of k_I for the kinked crack corresponding to every angle were obtained using Eqn4.3, 4.4 or 4.5 to determine the maximum k_I.

4.3.3.2 Three Point Bending

Using the G value for the normal crack and following the steps mentioned above, the k_I component as a function of crack growth angle was obtained and is plotted in Fig.4.20 for x=2T. The crack extension direction which maximised k_I was obtained using Hussain's Equation (4-5), for which the angle is simply equal to $\tan^{-1}(2K_{II}/K_I)$. The predicted crack path has been expressed a graph showing the crack growth angle as a function of a/T in Fig.4.21. Fig.4.22 illustrates the k_I component as a function of the crack growth angle for a/T=0.14 and 0.5 for x=3T. For a/T=0.14, the angle between the tangent to the crack path and the normal of the plate length which maximised k_I was 19^0, while for a/T=0.5, the corresponding angle was 30^0

4.3.3.3. Numerical Results for the T-butt Joint Specimens

Finite element meshes of the T plate joint were generated using FEMGEN (75) . Meshes with crack depths a/T between 0.2 and 0.95 are shown in Fig.4.23. Typically, each model comprised 685 nodes and 195 elements, giving systems with 1370 degrees of freedom, which were examined under two different boundary conditions. In the first, the two ends of the horizontal plate were built in, in the second, the nodes at the upper surfaces of the two ends of the horizontal plate were fixed in a vertical direction but allowed to rotate. Both were analysed using the finite element code (ABAQUS) mounted on a Vax11/750 which needed approximately 20 mins cpu time for each model.

For each crack depth, the k_I component non-dimensionalised with respect to the remote stress applied at the end of the vertical plate and crack depth (a) was determined as a function of the crack growth angle . These results

have been plotted in Fig.4.24 when the two ends of the horizontal plate were built in, and in Fig.4.25 for the case in which the two ends of the horizontal plate were allowed to rotate. The crack growth path also has been displayed by plotting the ratio of crack depth to the thickness against the angle in Figs.4.26 and Fig.4.27.

SECTION 4.4. Discussion

The angles which maximise k_I and g using off-axis virtual extension method are not very different. For the off axis three point bending problems, the difference between these two approaches is typically 2^0. Both sets of numerical results have been plotted, and compared with the experimental data in Fig.4.28 and Table4.2. From this data, it is clear that crack growth path using maximum g theory and maximum k_I theories are closely similar, and both agree with the experimental data for the mixed mode loading conditions produced by off-axis three point bend tests.

Comparing the crack extension angles at the same crack depth for x=3T and x=2T, shows that the former is much larger than the latter. For a/T=0.14 the angle is 19^0 compared to 11^0, and for a/T=0.5 the angle is 30^0 as opposed to 17^0. This can be explained as the effect of an increased K_{II} component, resulting from an increase in the ratio of the shear force to the bending moment in the crack plane.

For T-butt joints, the average difference between the finite element calculations and the experimental data was about 3^0. A detailed comparison is given in Fig.4.29 and Fig.4.30.

When the two ends of the horizontal plates were fixed, the crack growth angle increased with the crack depth and there was a marked change in angle at a/T=0.75. The actual crack length was very much greater than the

thickness, indicating that fatigue life predictions obtained by integrating the growth rate from an initial depth through the chord thickness will be erroneous. However, when rotation was allowed, the angle between the direction of crack growth and normal to the length of the horizontal plate was initially 4^0, then decreased with crack depth becoming zero at a/T=0.75. The direction of the path then changed and the angle increased with the crack depth. This behaviour corresponds to a change in the sense of the shear producing K_{II}, from positive to negative. In this case, the actual crack length is not very different from the thickness of the horizontal plate,. which agrees with the experimental data as shown in Fig.4.30

SECTION 4.5.Conclusion

The direction of crack growth under mixed mode loading can be obtained by off-axis virtual crack extension or from solutions for kinked cracks. Both the maximum k_I component and g theories provide good description of the experimental data which can be modelled by finite element calculations in simple two dimensional systems. The experimental verification of numerical methods of predicting crack paths in 2 dimensional structures has given confidence for the prediction of crack path in tubular joints which is pursued in Chapter 6.

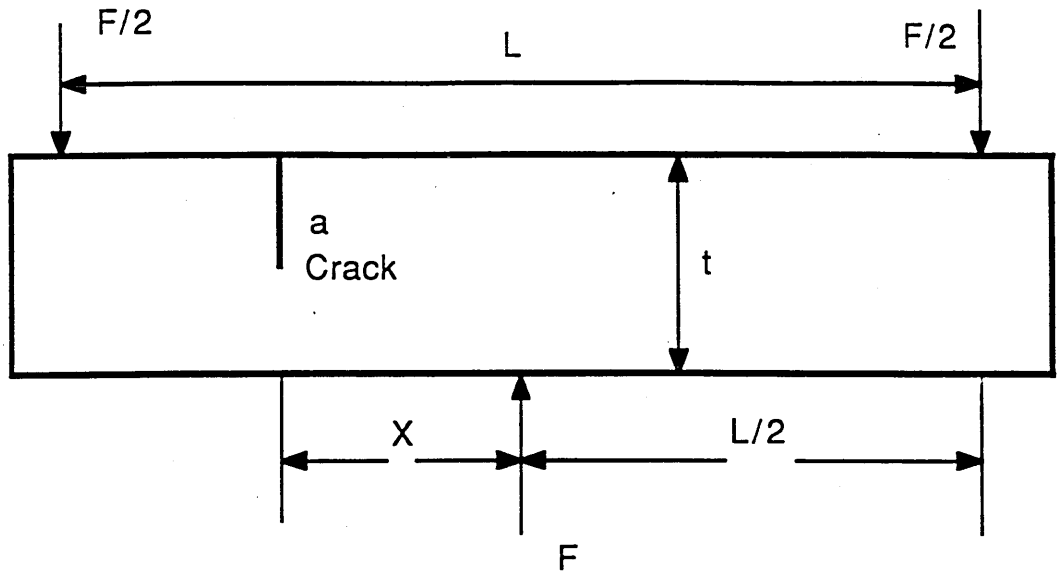

FIG.4.1 A rectangular specimen with an edge crack under three point bending where the crack is located a distance X from the central loading point

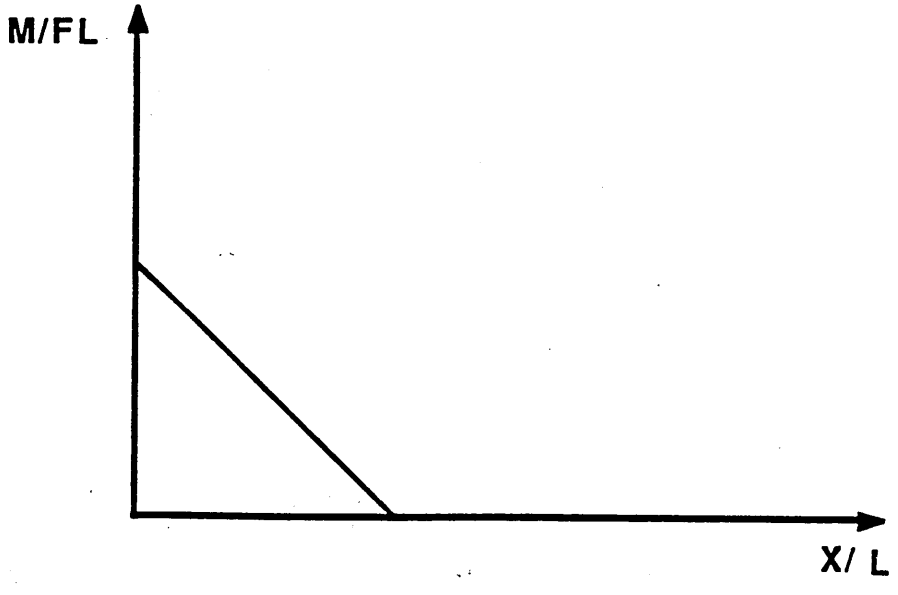

FIG.4.2 The ratio of shear force to the bending moment as a function of X/L

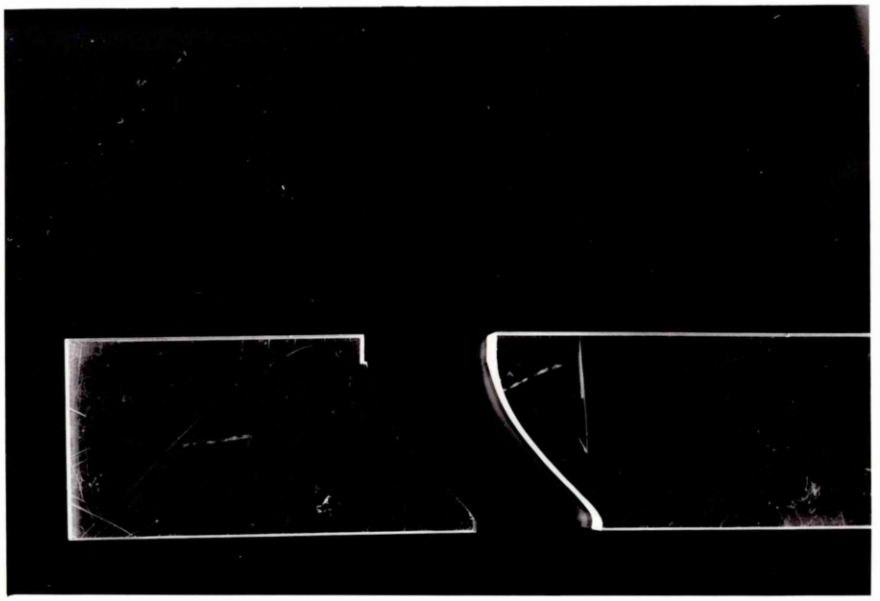

a) a/T=0.14

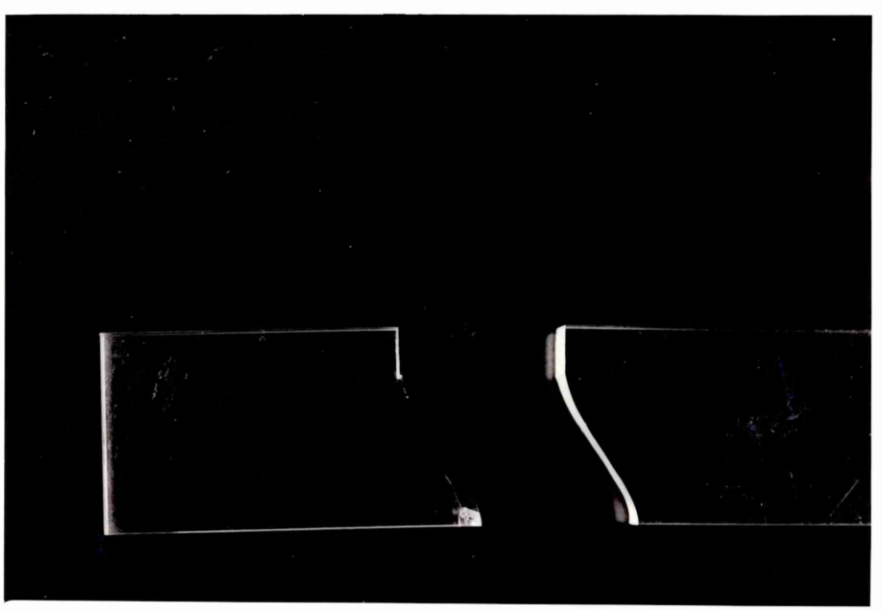

b) a/T=0.25

c) a/T=0.35

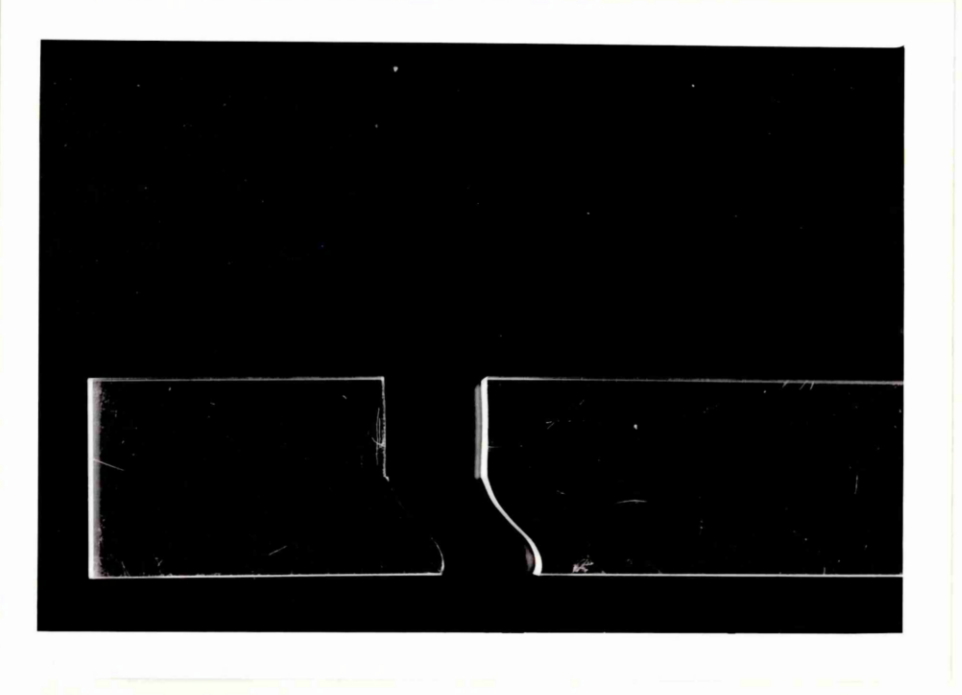

d) a/T=0.5

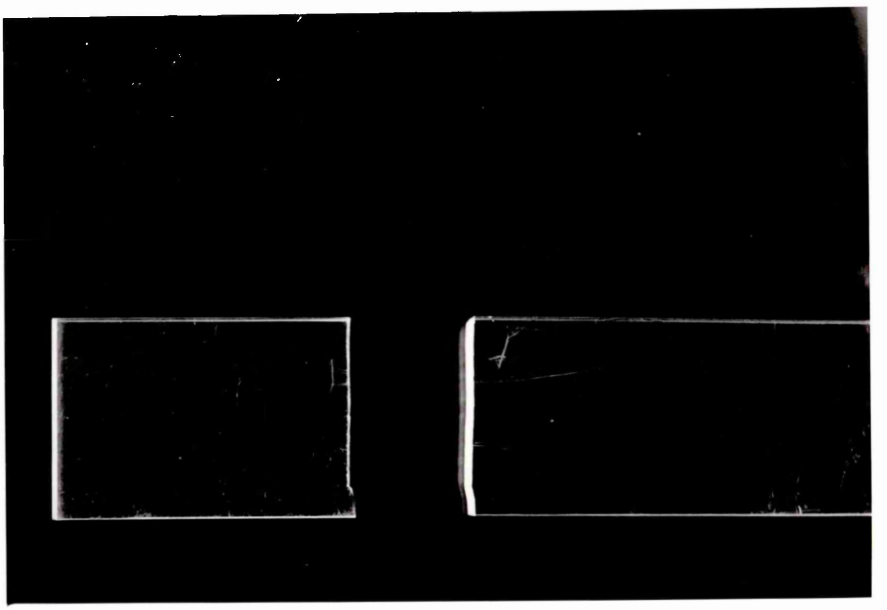

e) a/T=0.85

FIG.4.3 Photographs of broken asymmetric 3 point bend perspex specimens,in which the crack was located at 2T away from the central loading point

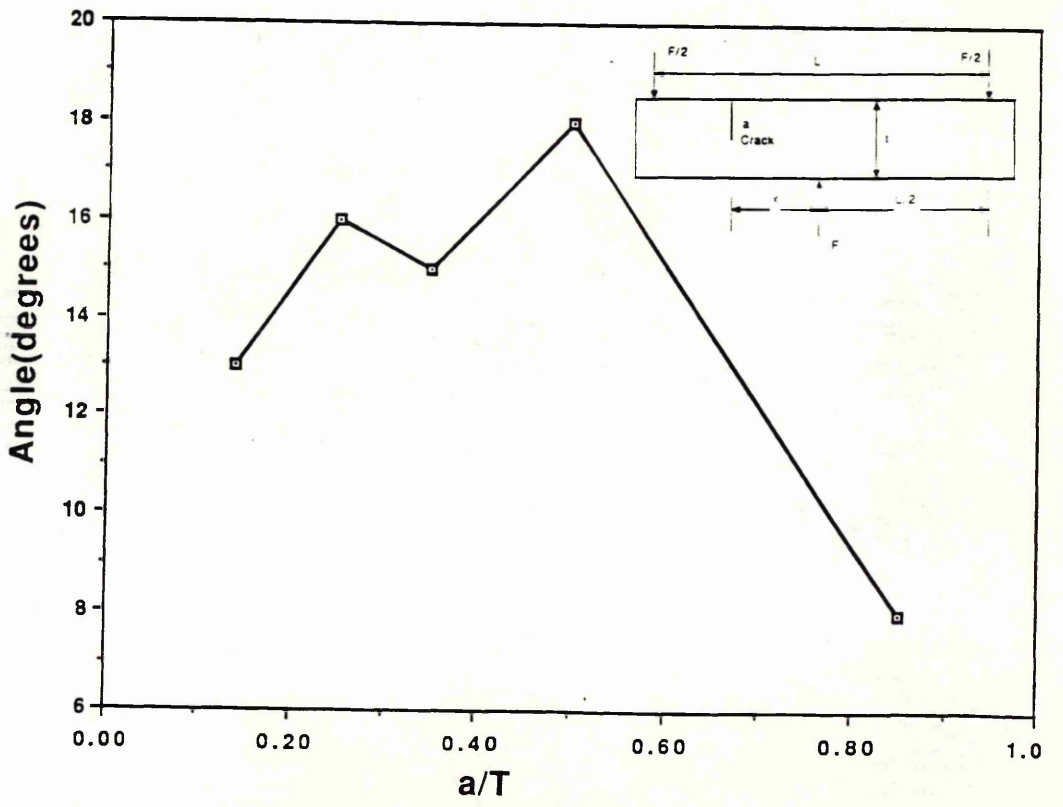

FIG.4.4 The angle at which the crack started to grow as a function of a/T (X=2T)

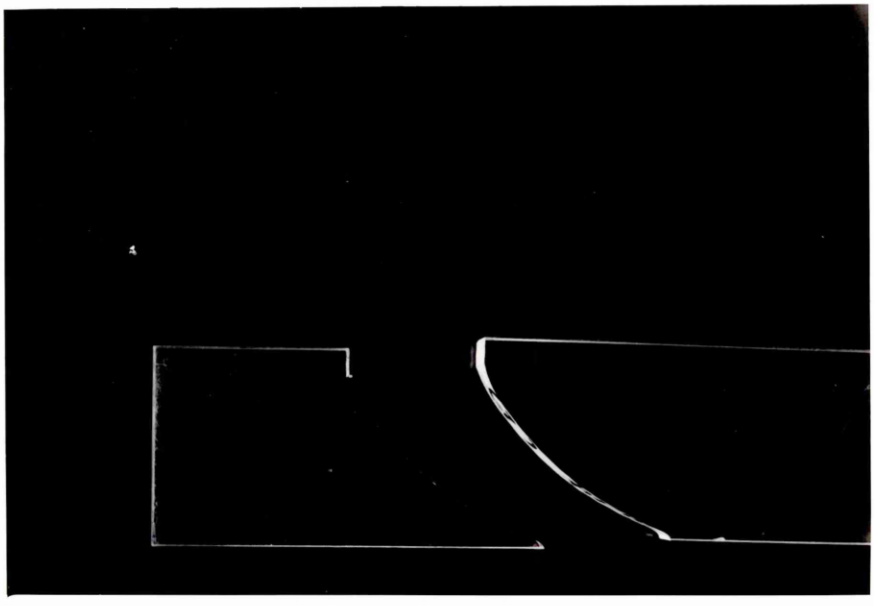

a) a/T=0.14

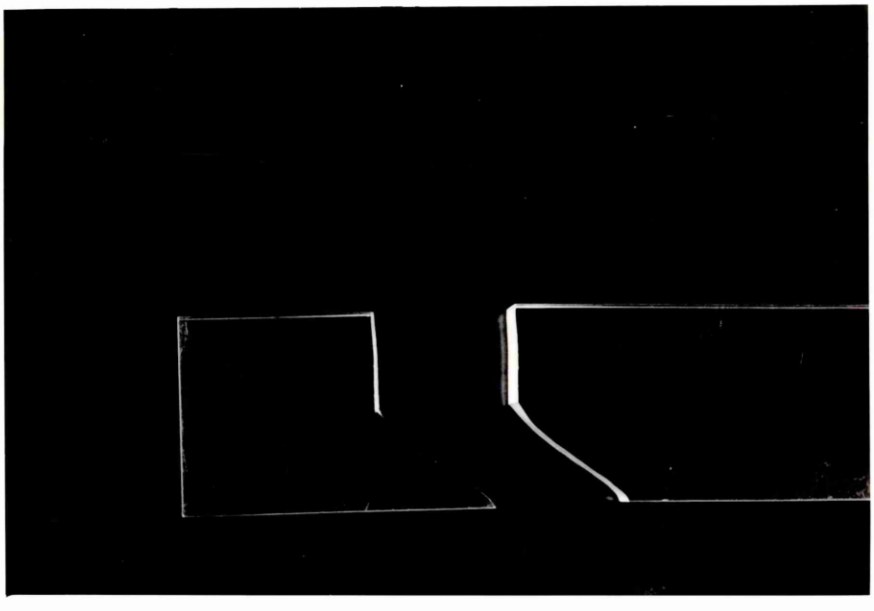

b) a/T=0.5

FIG.4.5 Photographs of broken asymmetric 3 point bend perspex specimens. The crack was located at 3T away from the central loading point

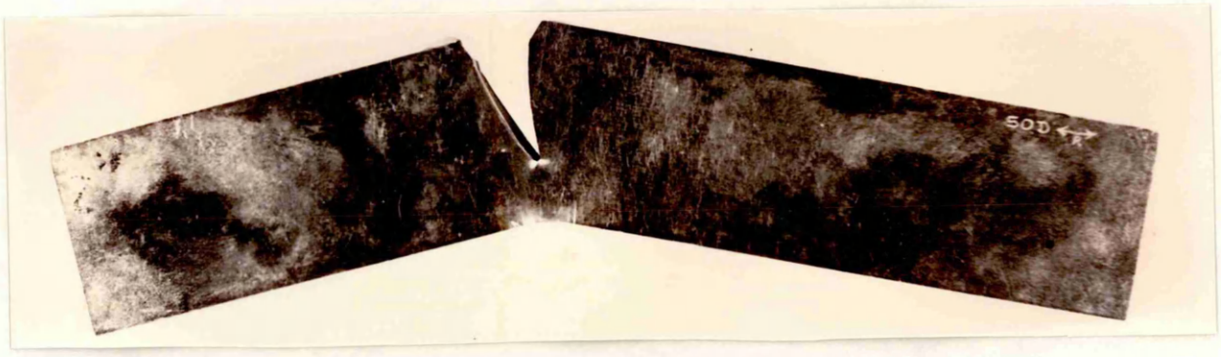

a/T=0.14

FIG.4.6 A photograph of a broken asymmetric 3 point bend steel specimen, (code A) in which the crack was located 2T away from the central loading point

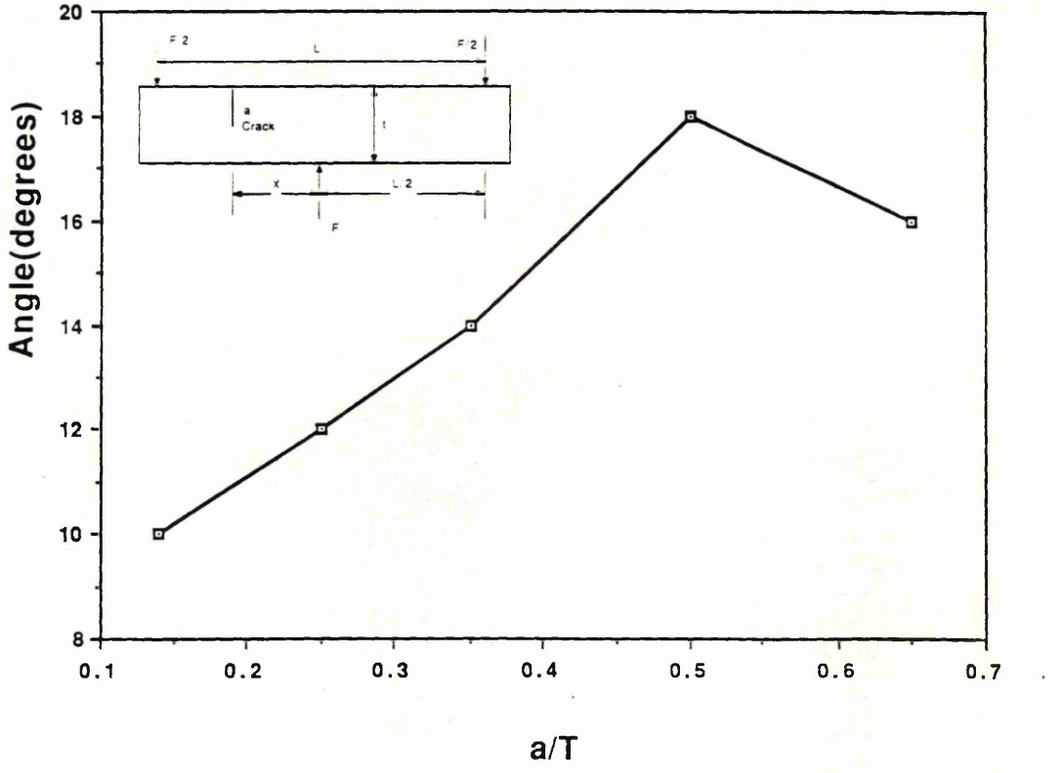

FIG.4.7 The angle of crack growth as function of a/T for the steel specimen (code A)

FIG.4.8 A photograph of a broken asymmetric 3 point bend steel specimen, (code B) in which the crack was located 2T away from the central loading point

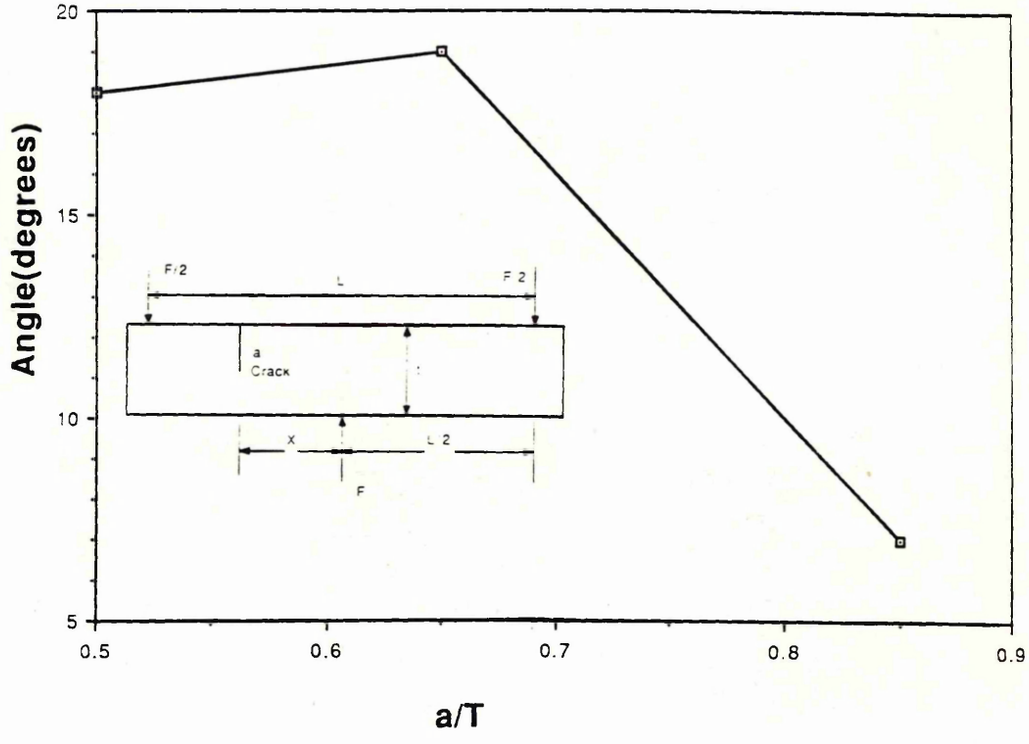

FIG.4.9 The angle of crack growth as function of a/T for the steel specimen (Code B)

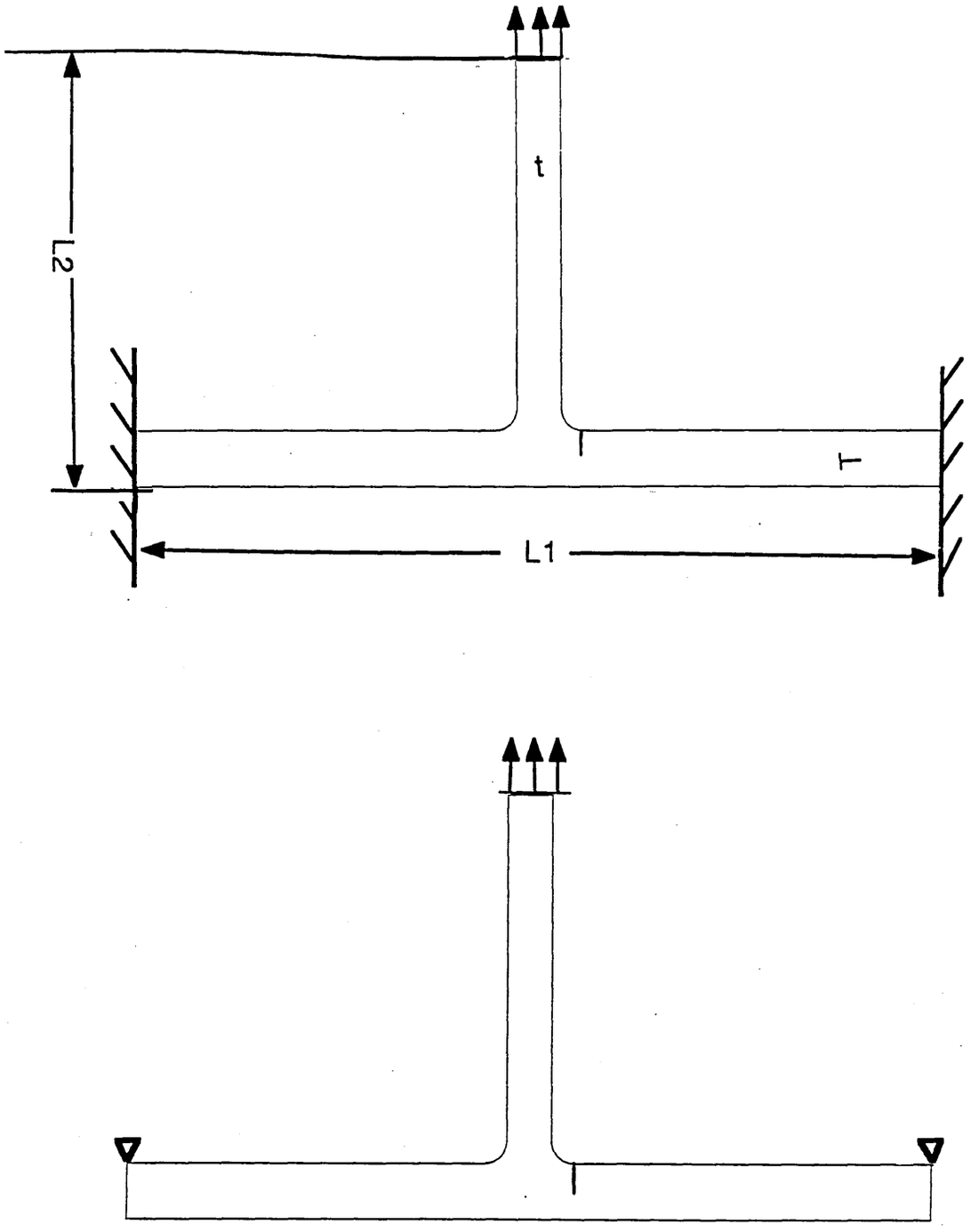

FIG.4.10 Two T plate joints with a through crack in the horizontal plate

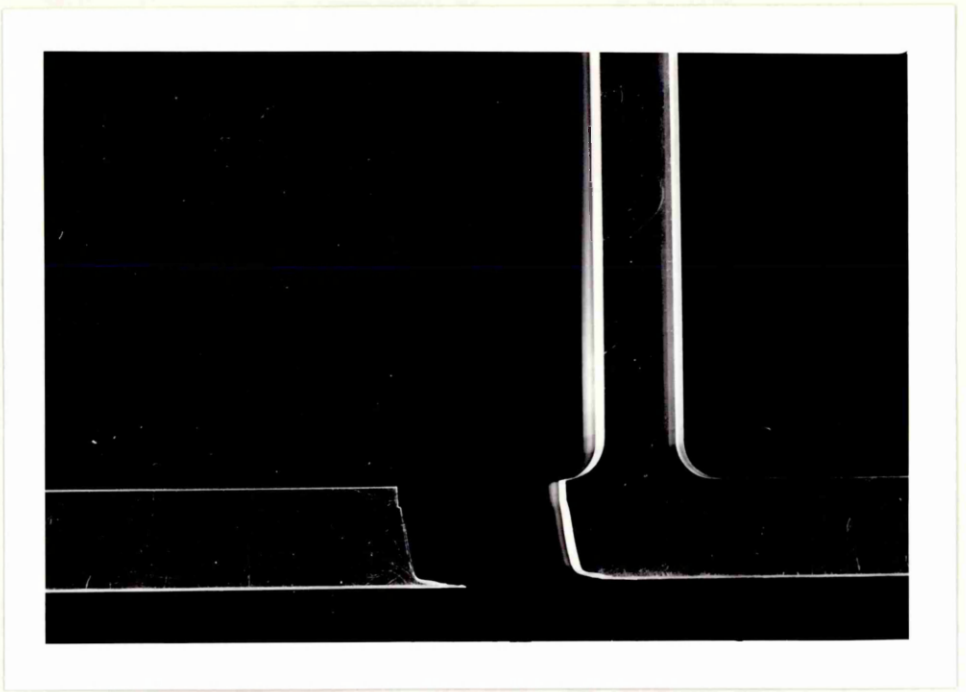

FIG.4.11 Photographs of the first T plate joint after fracture

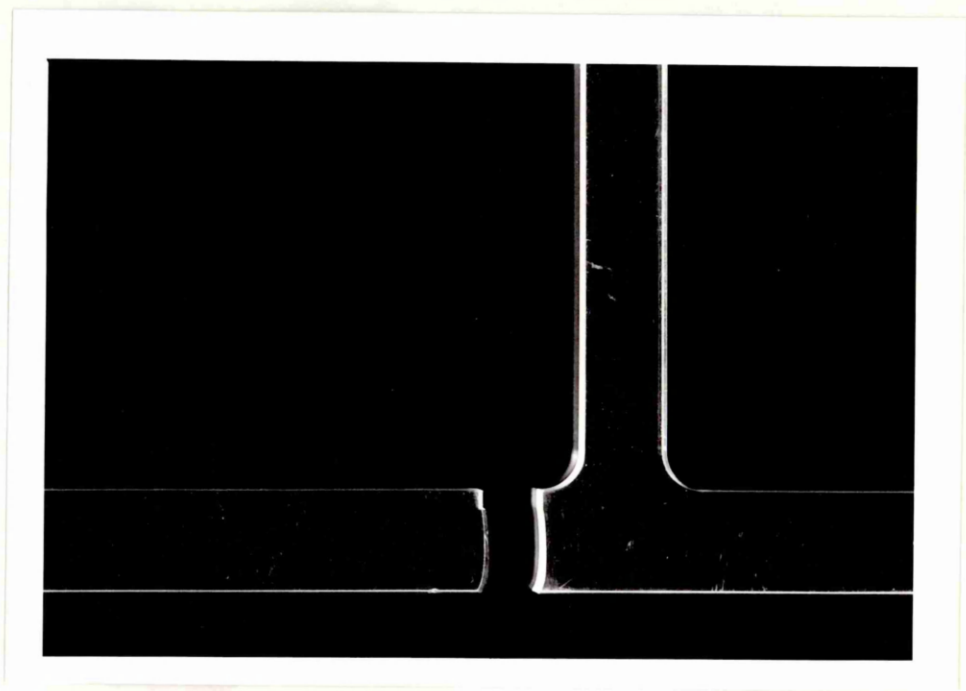

FIG.4.12 Photographs of the second T plate joint after fracture

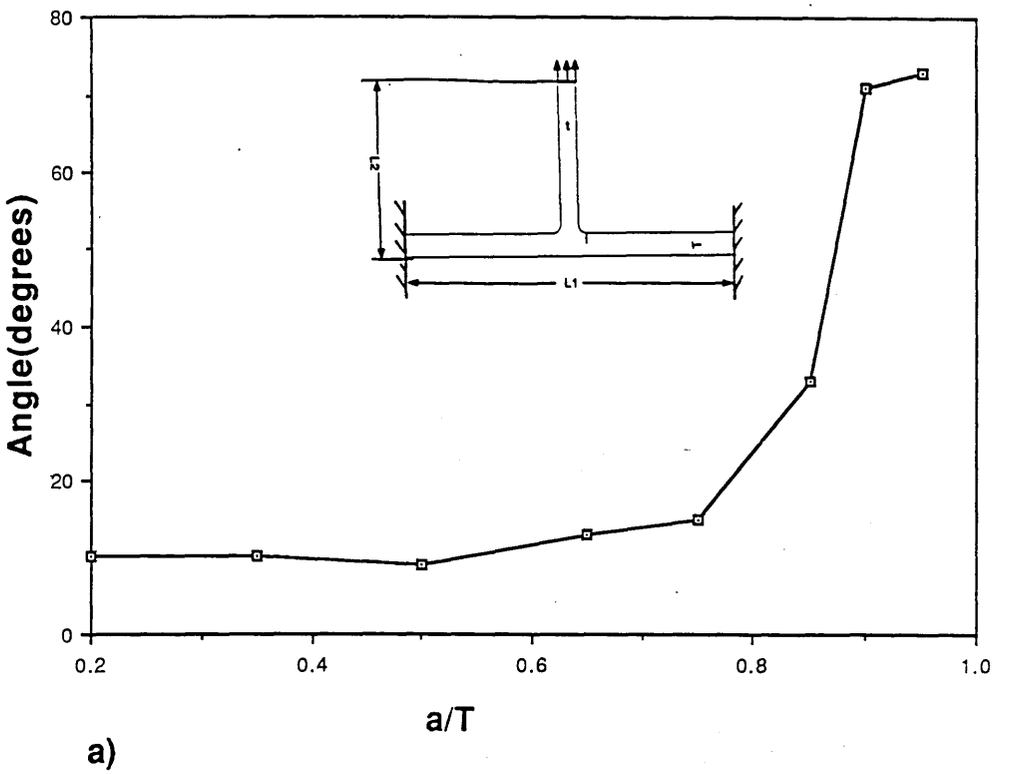

a)

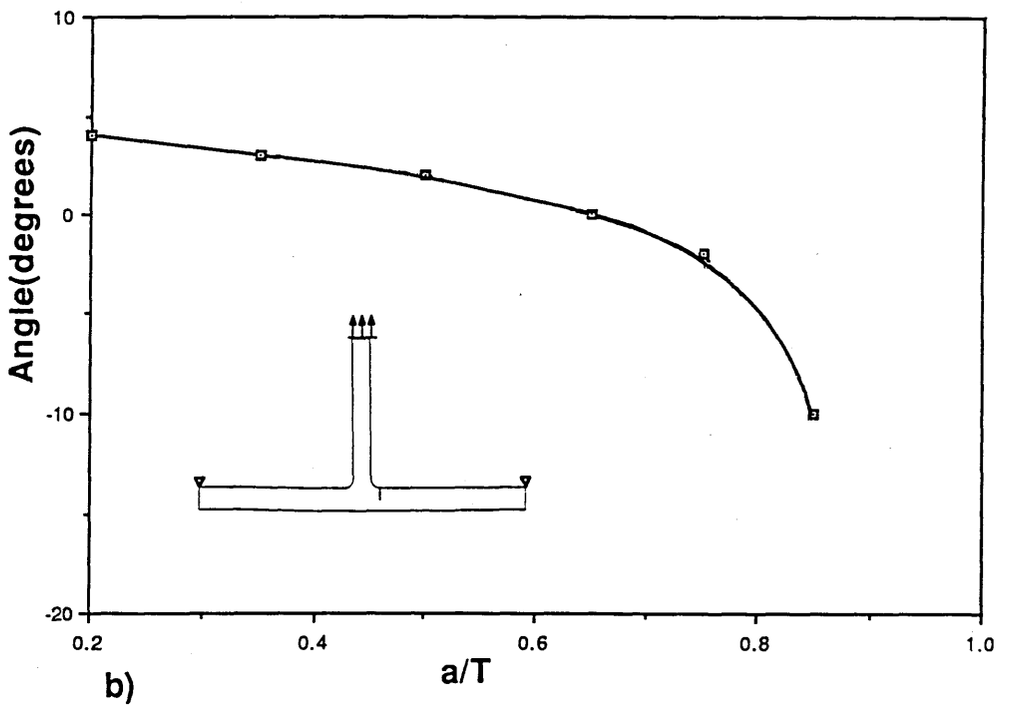

b)

FIG.4.13 The angle of the crack growth as a function of a / T

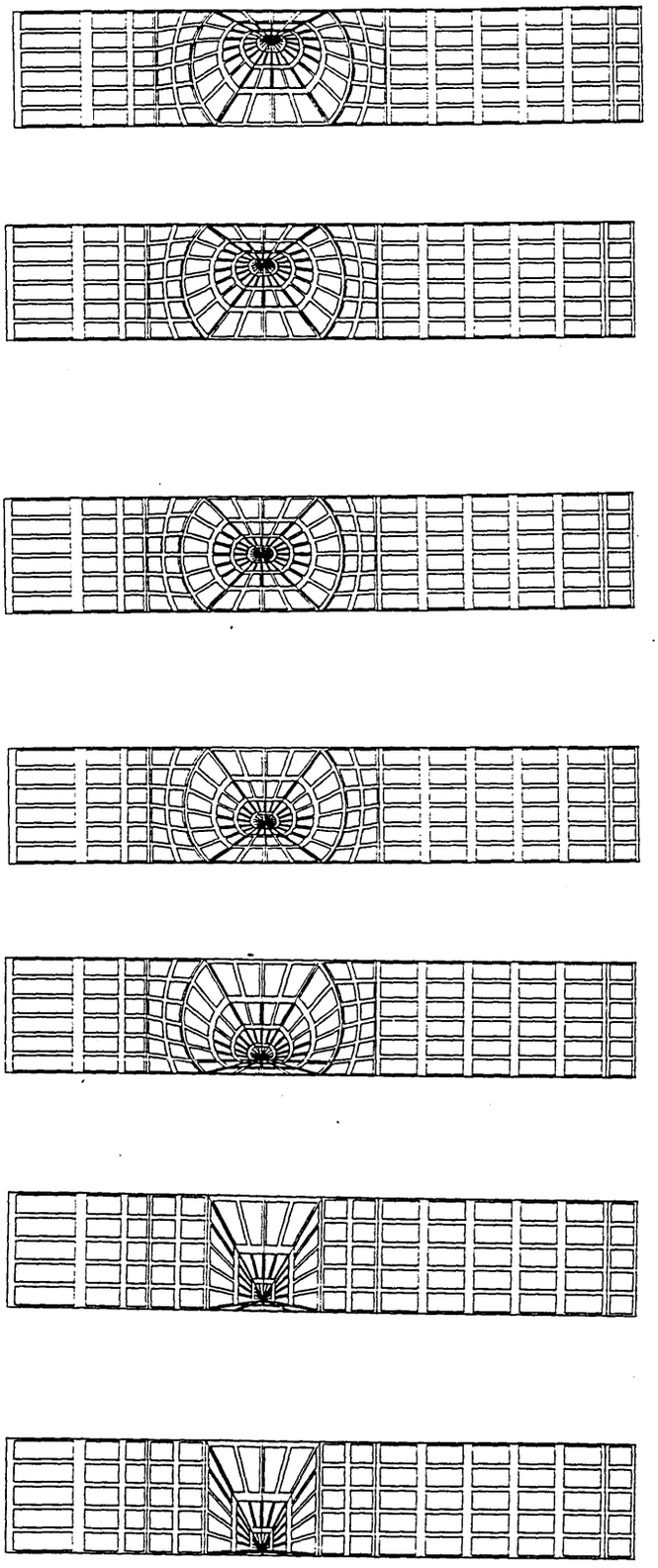

FIG.4.14 Meshes for the asymmetric rectangular specimens

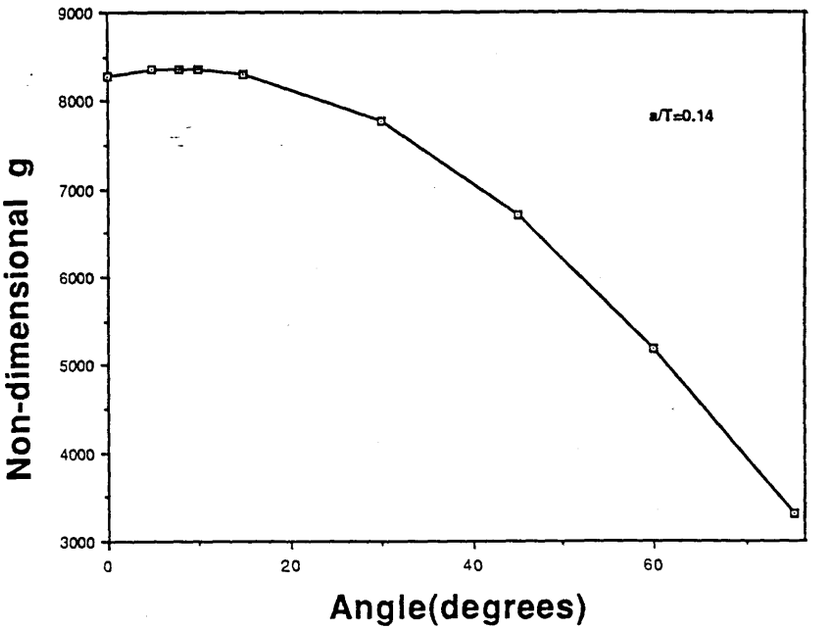
Non-dimensional g
9000
8000
7000
6000
5000
4000
3000
0
20
40
60
Angle(degrees)
a/T=0.14

a)

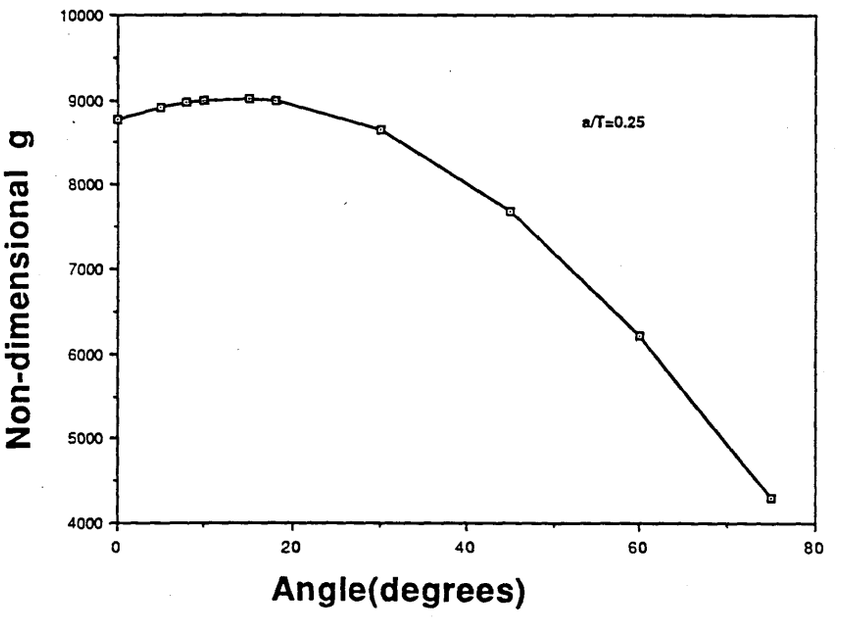
Non-dimensional g
10000
9000
8000
7000
6000
5000
4000
0
20
40
60
80
Angle(degrees)
a/T=0.25

b)

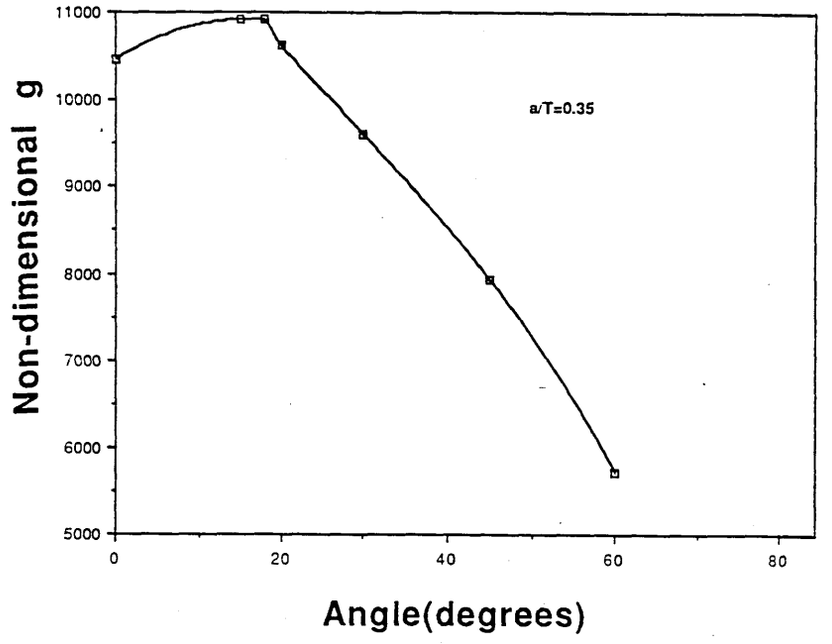
11000
10000
9000
8000
7000
6000
5000
Non-dimensional g
a/T=0.35
0
20
40
60
80
Angle(degrees)

c)

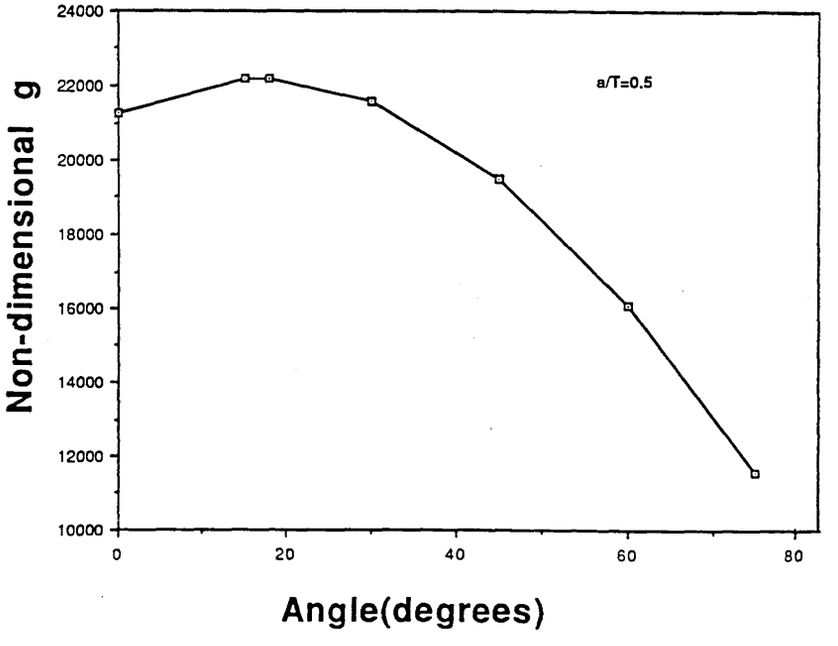
24000
22000
20000
18000
16000
14000
12000
10000
Non-dimensional g
a/T=0.5
0
20
40
60
80
Angle(degrees)

d)

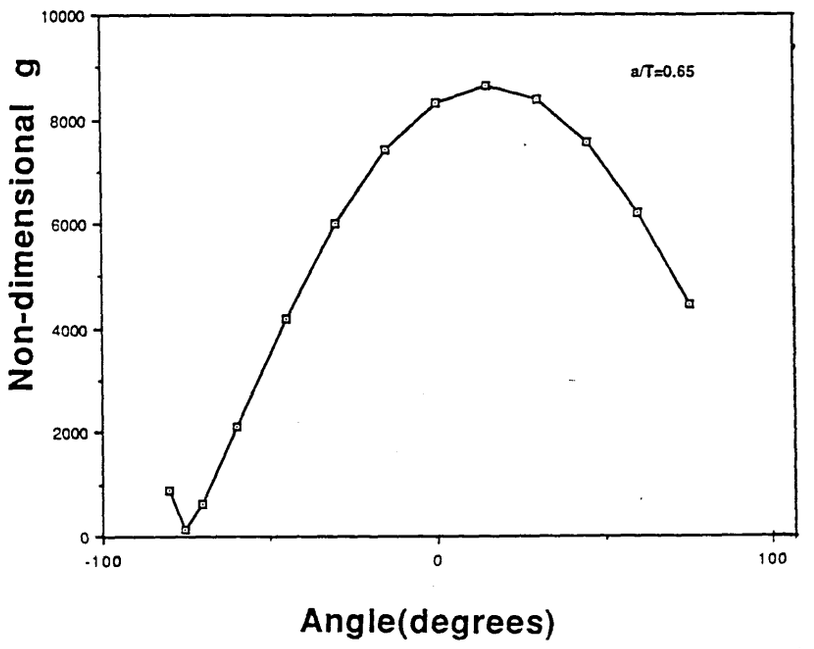
10000
8000
6000
4000
2000
0
-100
0
100
a/T=0.65
Non-dimensional g
Angle(degrees)

e)

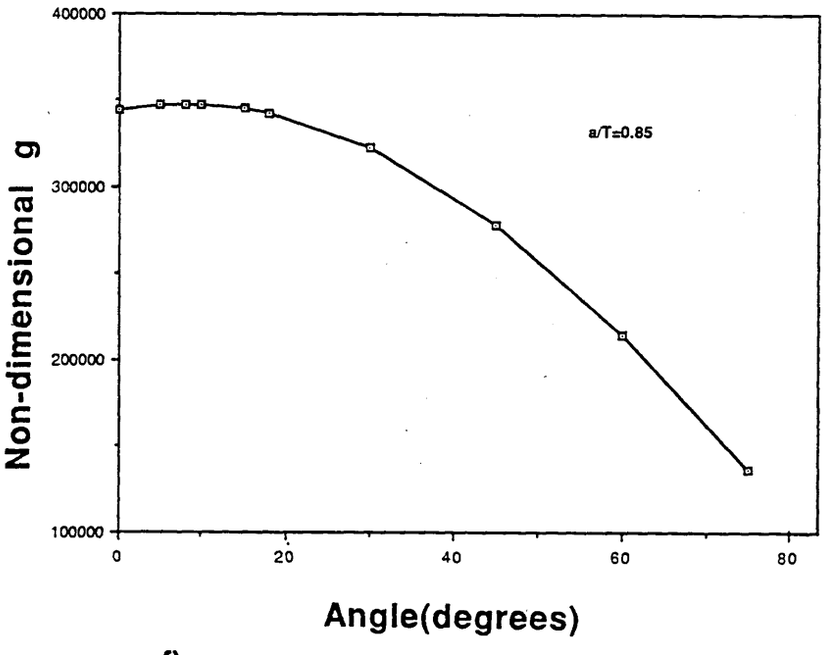
400000
300000
200000
100000
0
20
40
60
80
a/T=0.85
Non-dimensional g
Angle(degrees)

f)

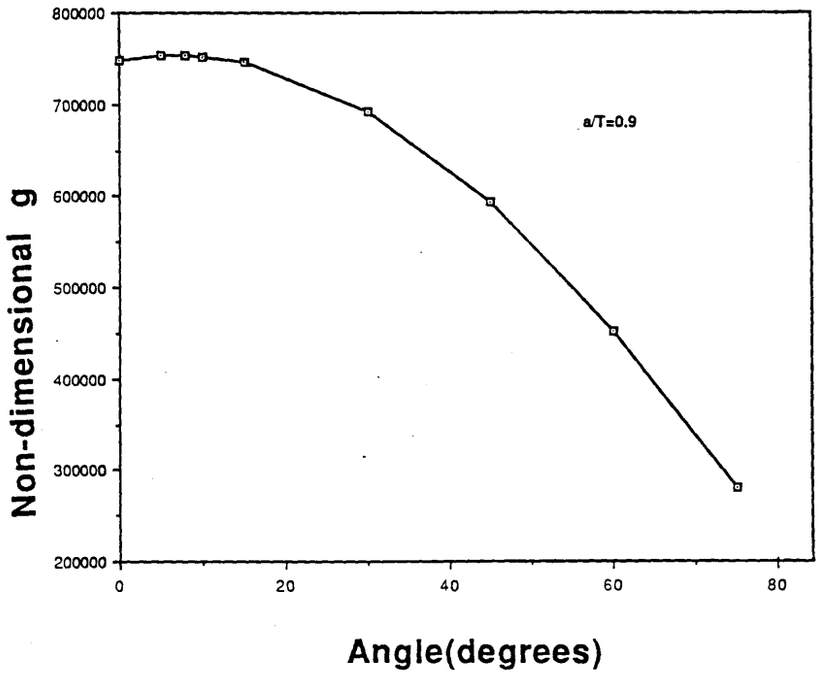

g)

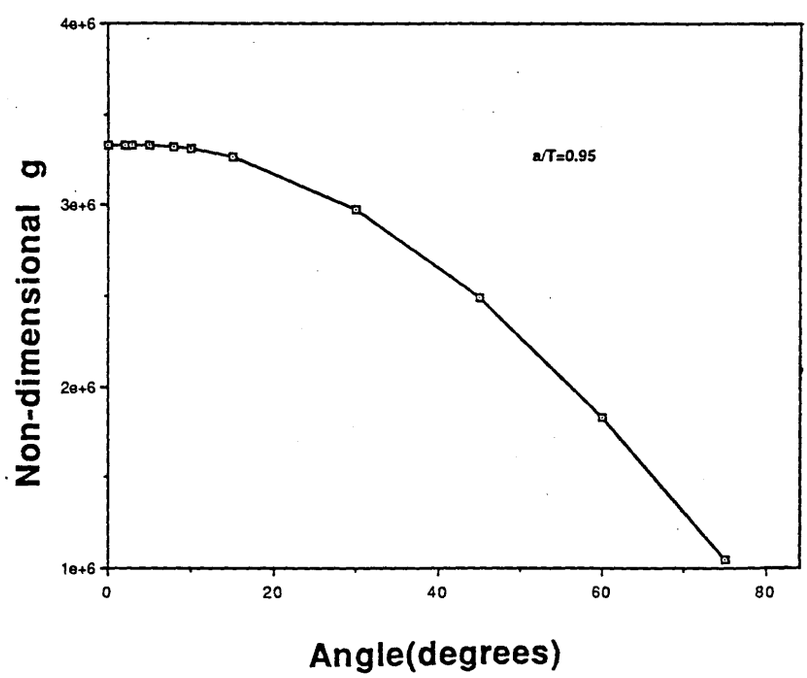

h)

FIG.4.15 The strain energy release rate as a function of crack growth angle for the rectangular specimens (X=2T)

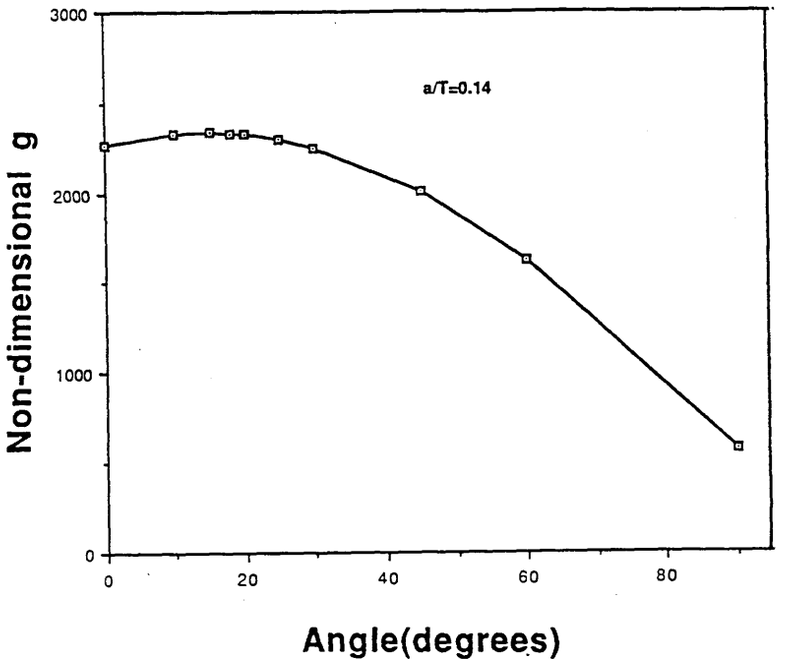

a)

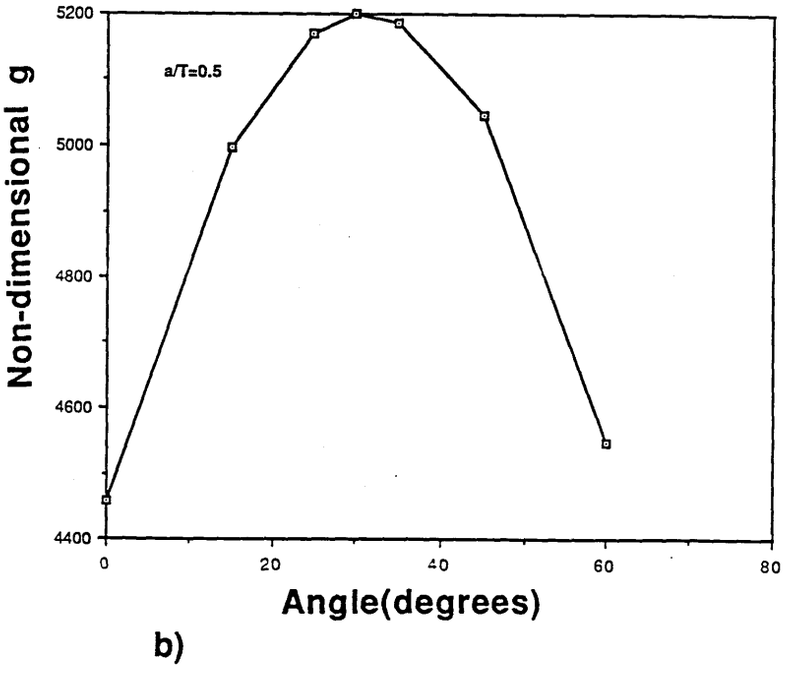

b)

FIG.4.16 The strain energy release rate as a function of crack growth angle for the rectangular specimens (X=3T)

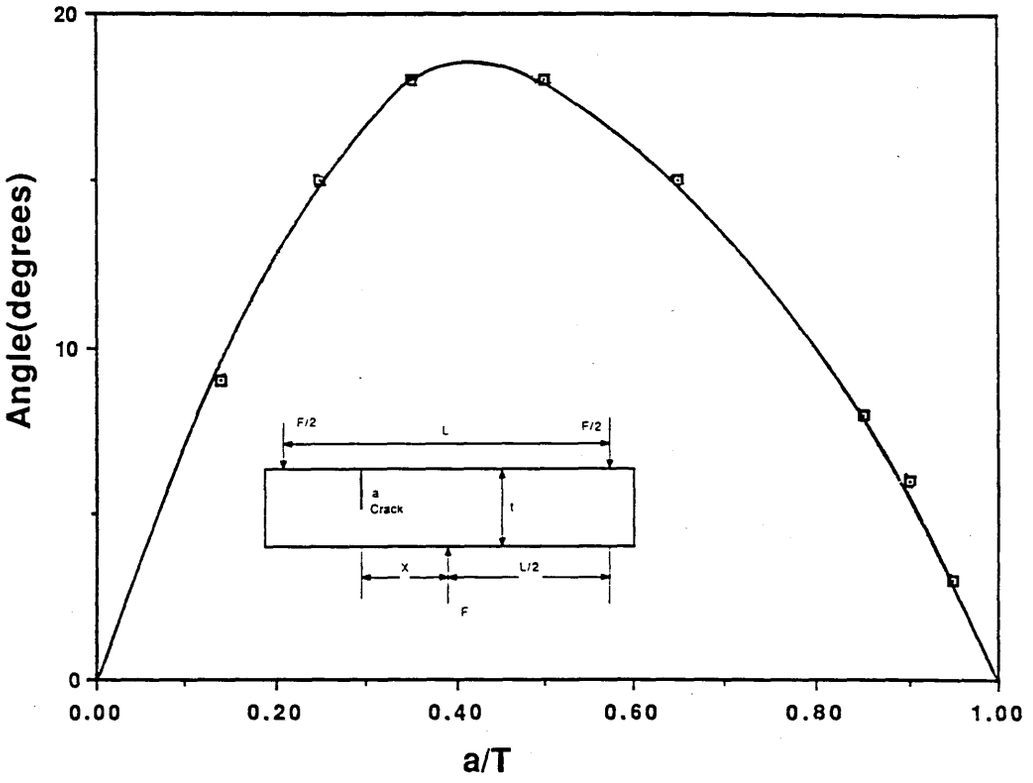

FIG.4.17 The angle indicating the maximum g as a function of a/T (X=2T)

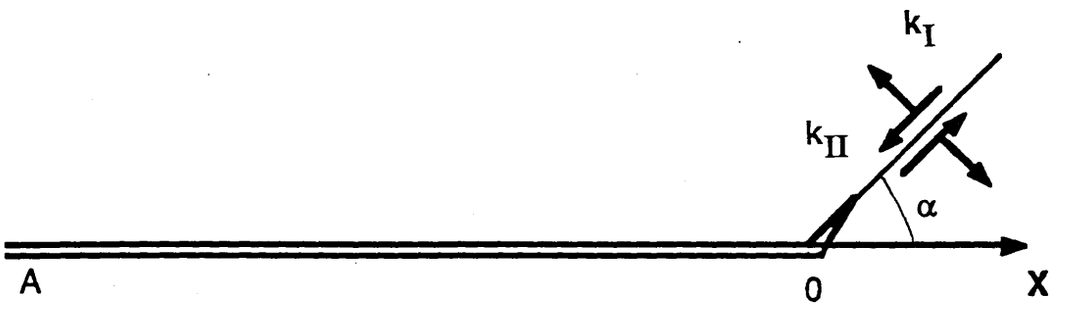

FIG.4.18 A schematic Illustration of a small angled kink crack ahead of the main crack

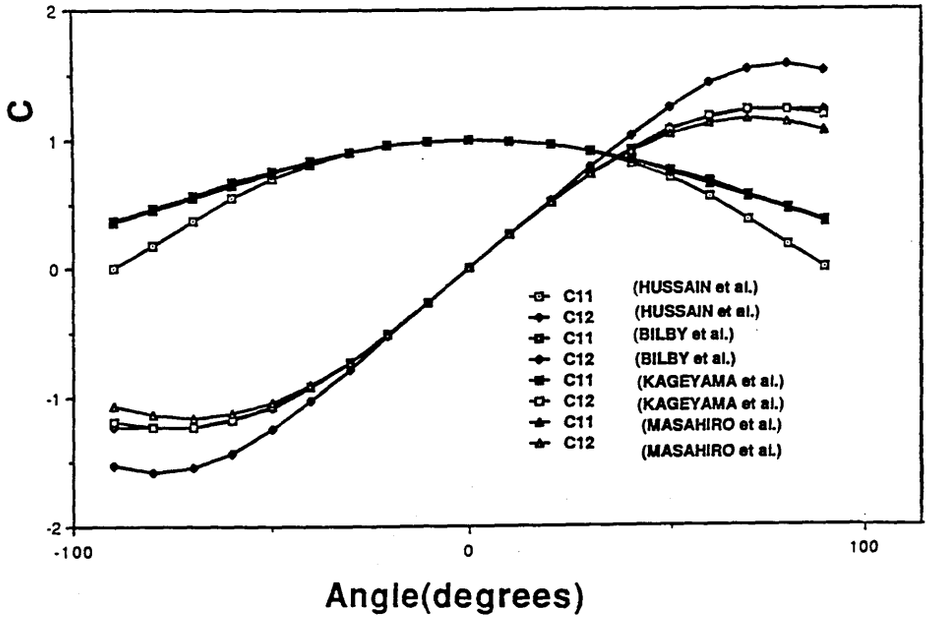

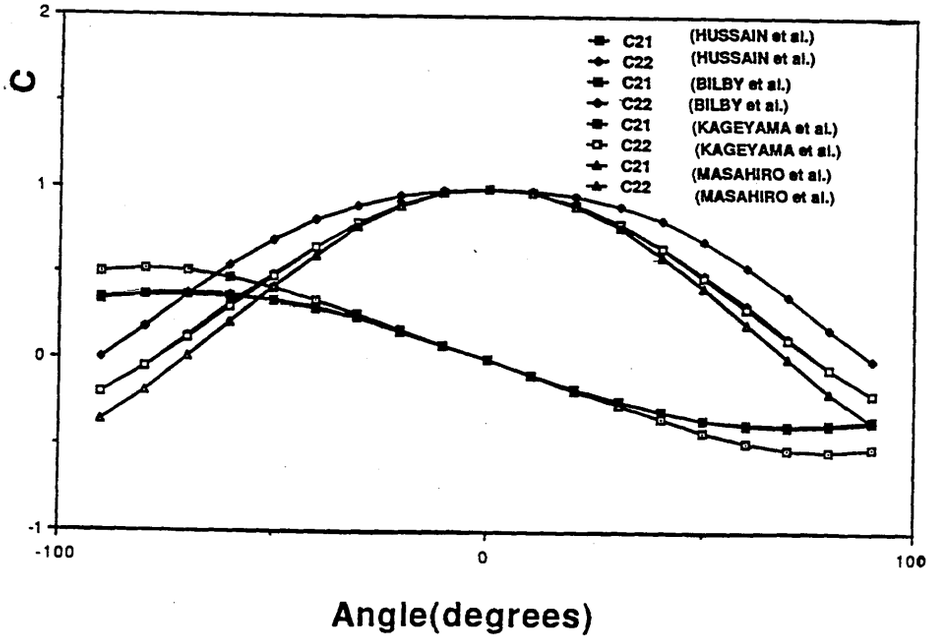

FIG.4.19 C_{ij} as a function of the angle for the kink crack

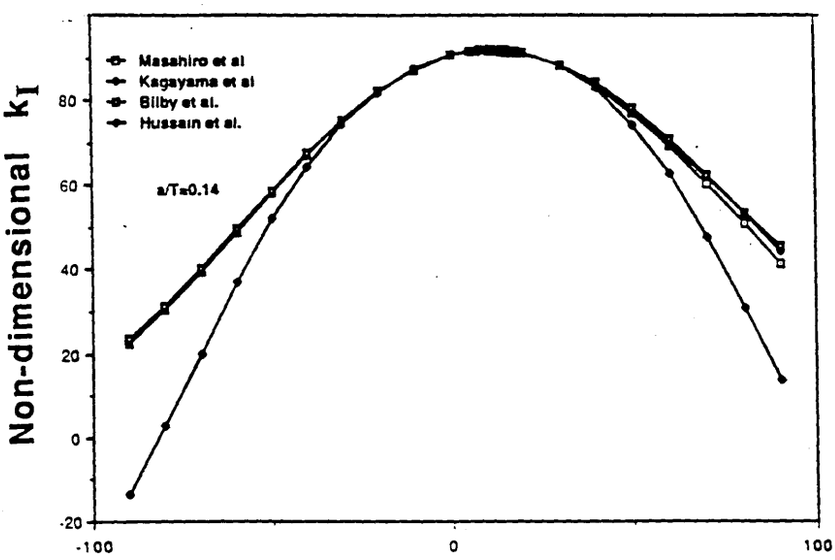
Masahiro et al
Kagayama et al
Bilby et al.
Hussain et al.
a/T=0.14
Non-dimensional k_I
80
60
40
20
0
-20
-100
0
100
Angle(degrees)

a)

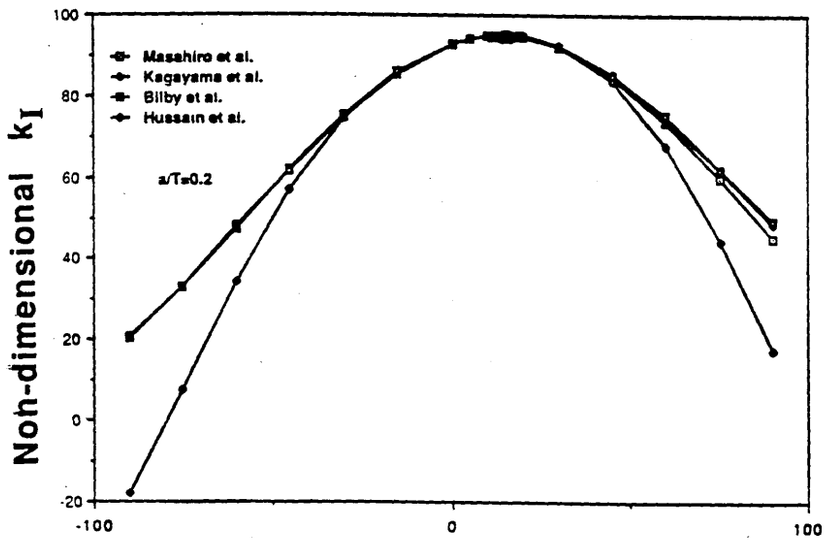
Masahiro et al.
Kagayama et al.
Bilby et al.
Hussain et al.
a/T=0.2
Noh-dimensional k_I
100
80
60
40
20
0
-20
-100
0
100
Angle(degrees)

b)

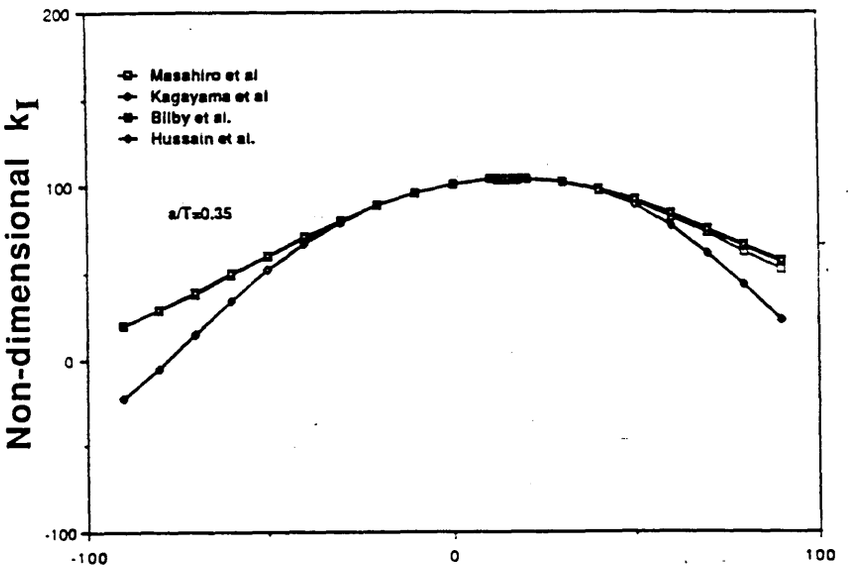
Masahiro et al
Kagayama et al
Bliby et al.
Hussain et al.
a/T=0.35
Non-dimensional k_I
200
100
0
-100
-100
0
100
Angle(degrees)

c)

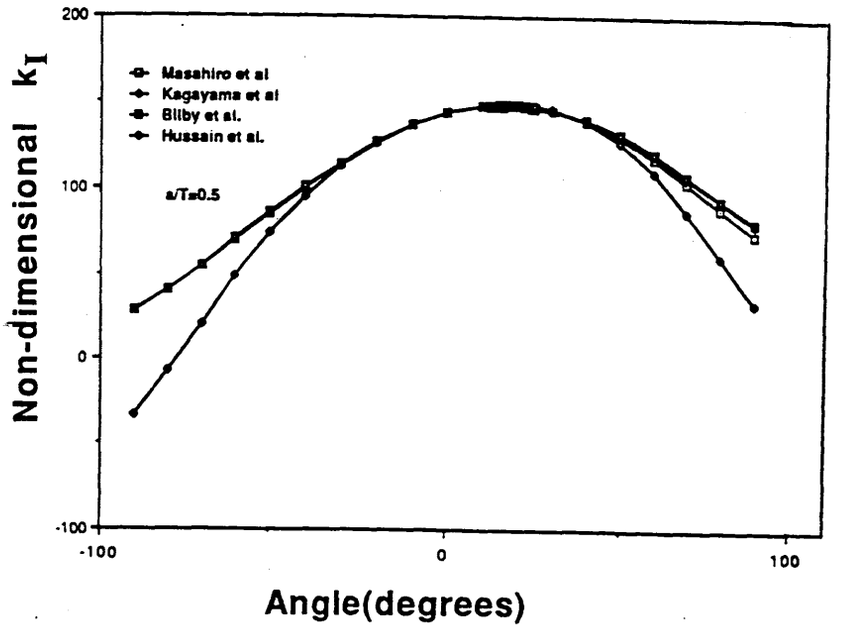
Masahiro et al
Kagayama et al
Bliby et al.
Hussain et al.
a/T=0.5
Non-dimensional k_I
200
100
0
-100
-100
0
100
Angle(degrees)

d)

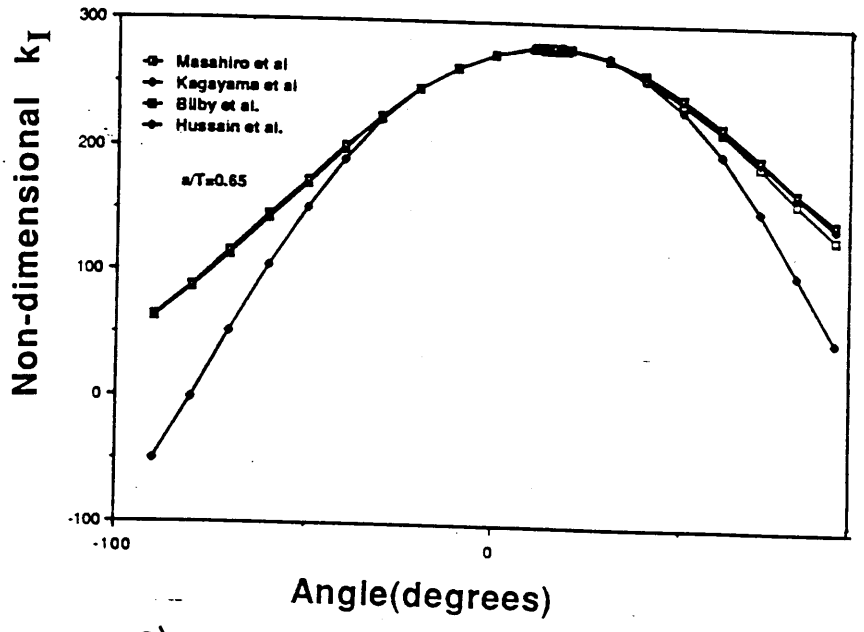
Masahiro et al
Kagayama et al
Bilby et al.
Hussain et al.
a/T=0.65
Non-dimensional k_I
Angle(degrees)
300
200
100
0
-100
-100
0

e)

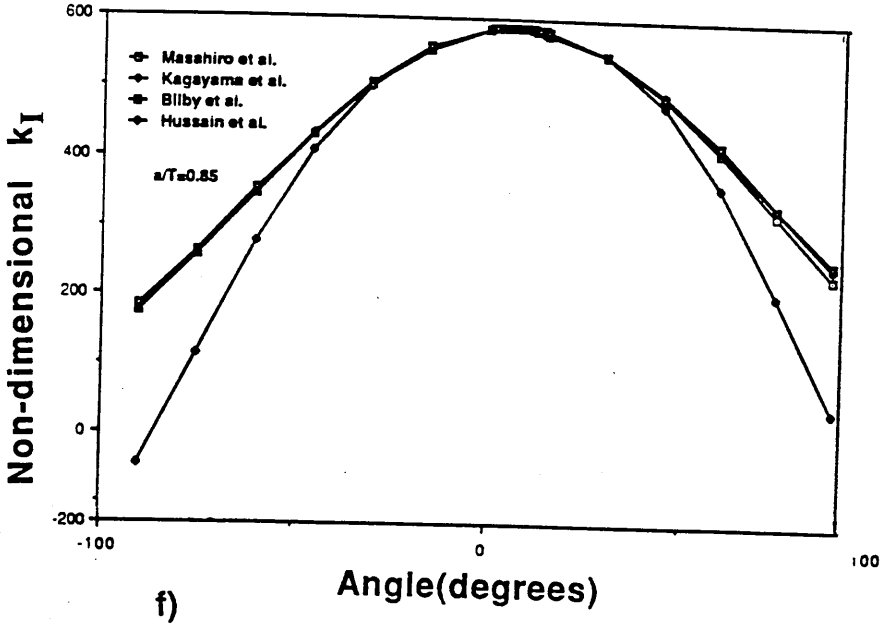
Masahiro et al.
Kagayama et al.
Bilby et al.
Hussain et al.
a/T=0.85
Non-dimensional k_I
Angle(degrees)
600
400
200
0
-200
-100
0
100

f)

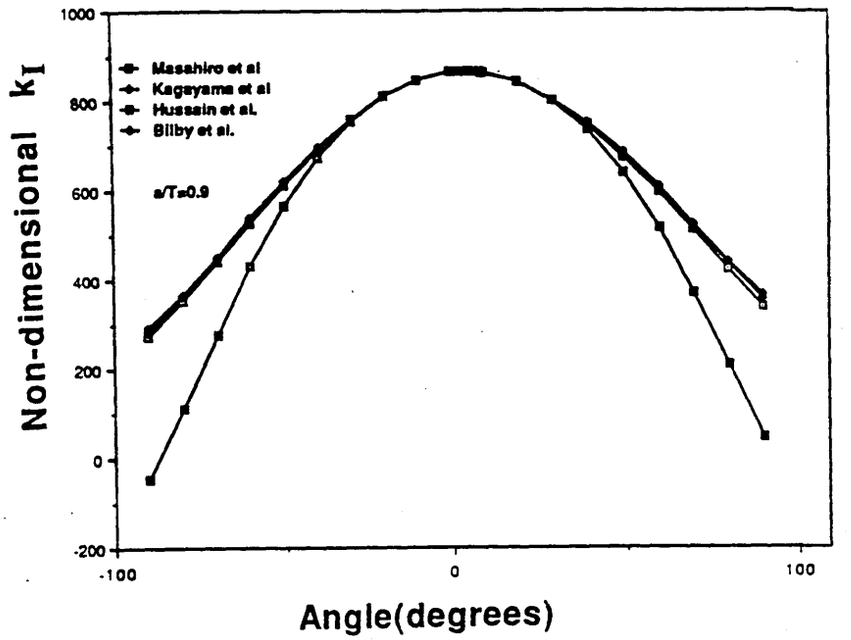

g)

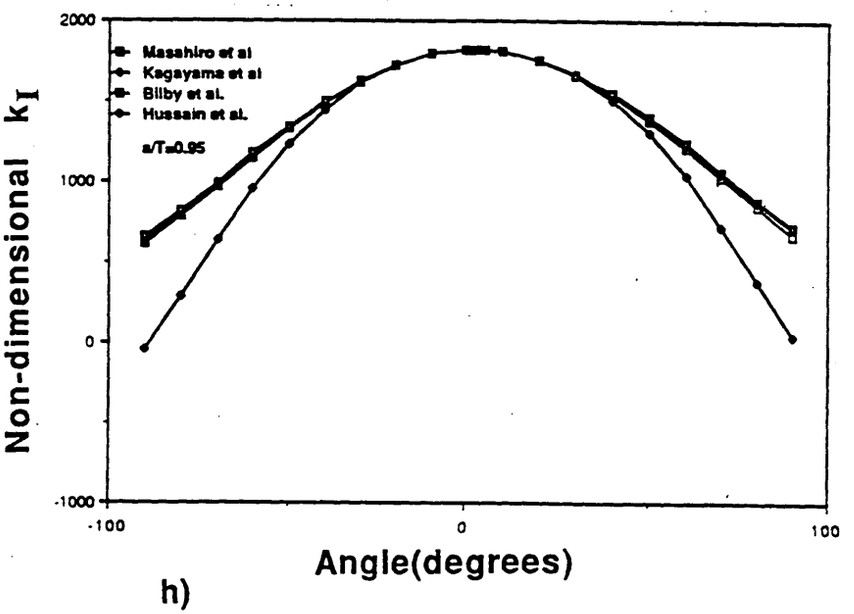

h)

FIG.4.20 Non-dimensionalised $k_I=k_I/\sigma\sqrt{a}$ as a function of crack growth angle for the rectangular specimens (X=2T)

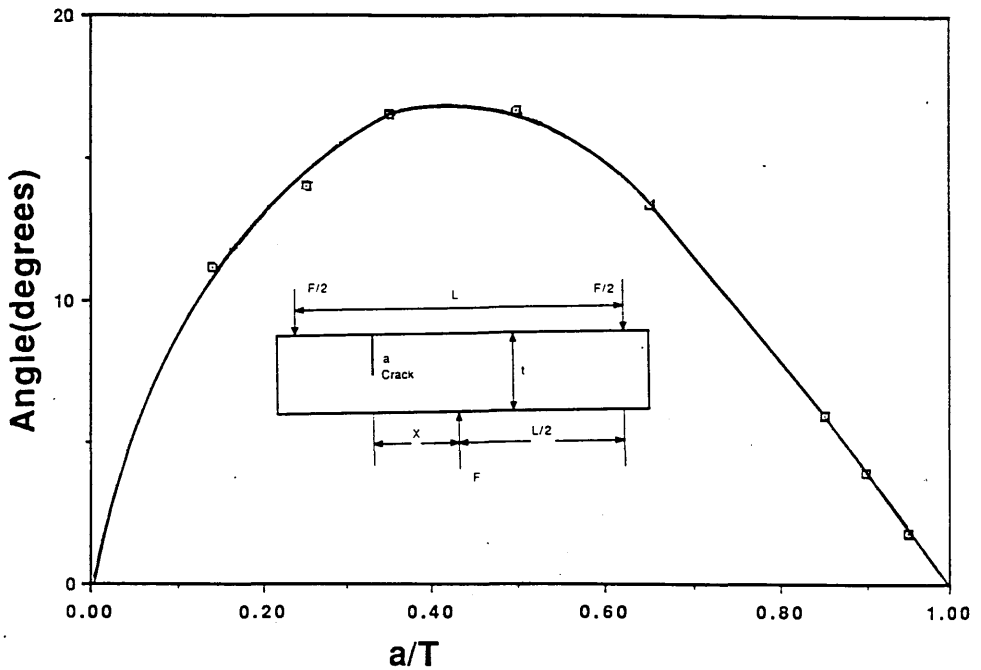

FIG.4.21 The angle of maximum k_I as a function of a/T (X=2T)

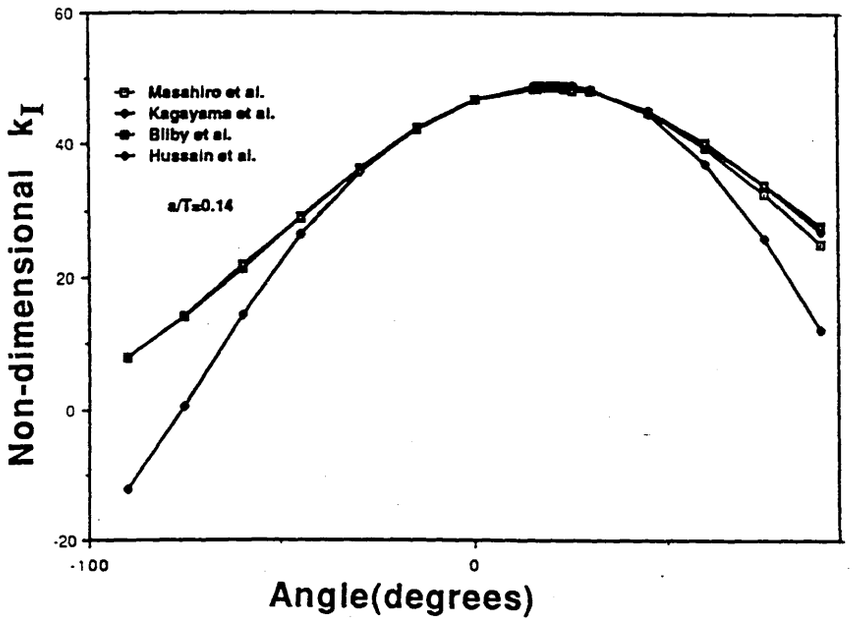

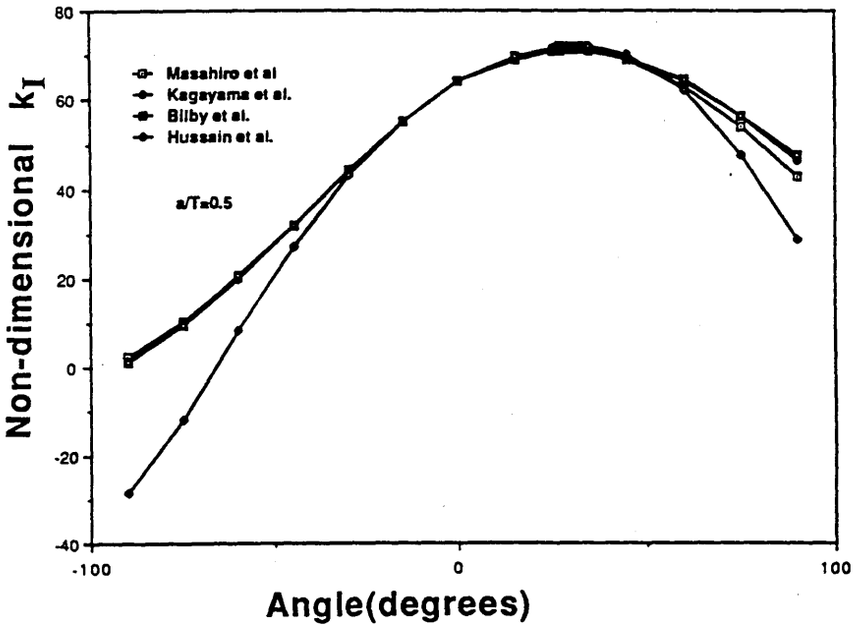

FIG.4.22 Non-dimensionalised $k_I=k_I/\sigma\sqrt{a}$ as a function of crack growth angle for the rectangular specimens (X=3T)

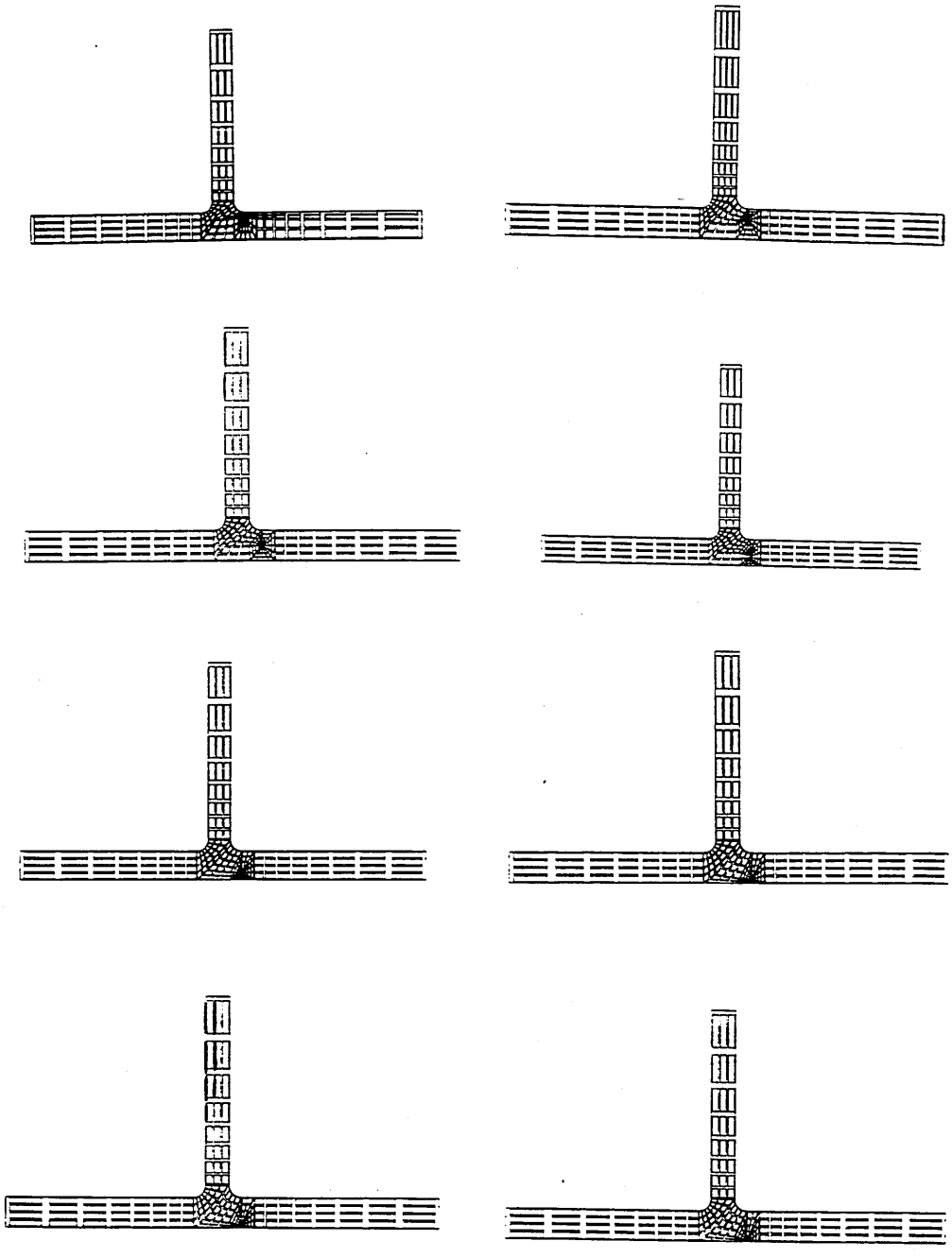

FIG.4.23 Meshes for the T plate joint specimens

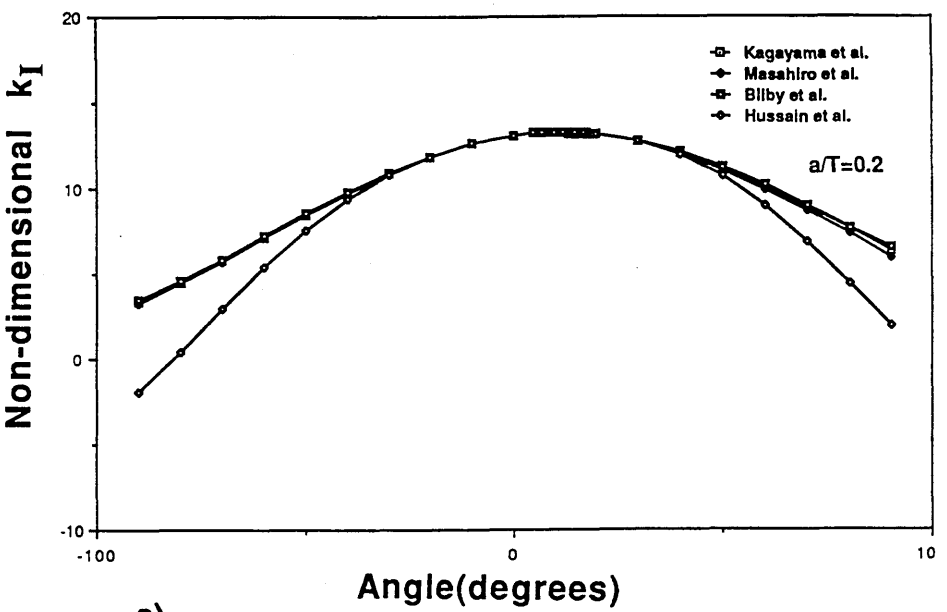
Kagayama et al.
Masahiro et al.
Bilby et al.
Hussain et al.
a/T=0.2
Non-dimensional k_I
Angle(degrees)
20
10
0
-10
-100
0
10

a)

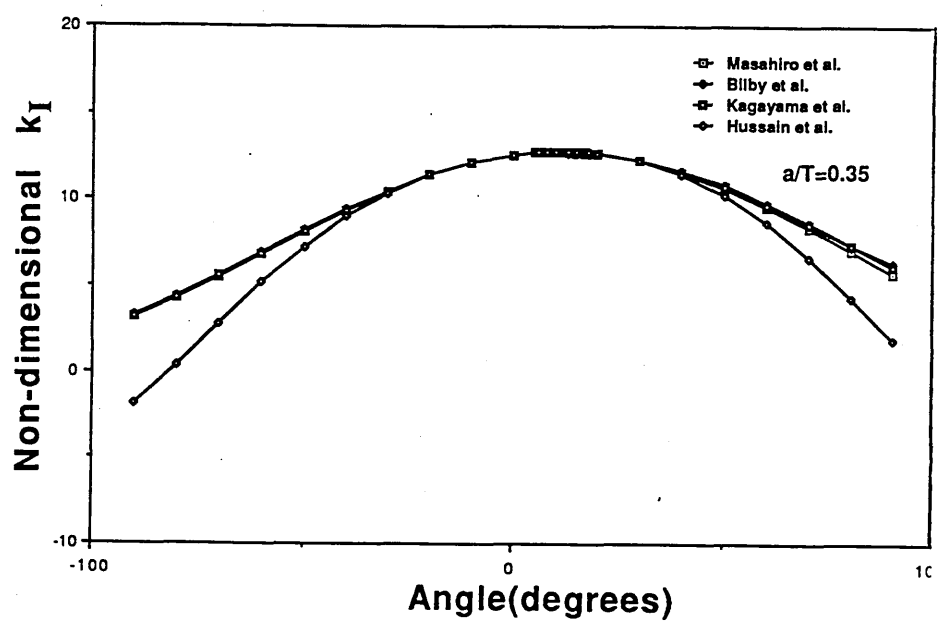
Masahiro et al.
Bilby et al.
Kagayama et al.
Hussain et al.
a/T=0.35
Non-dimensional k_I
Angle(degrees)
20
10
0
-10
-100
0

b)

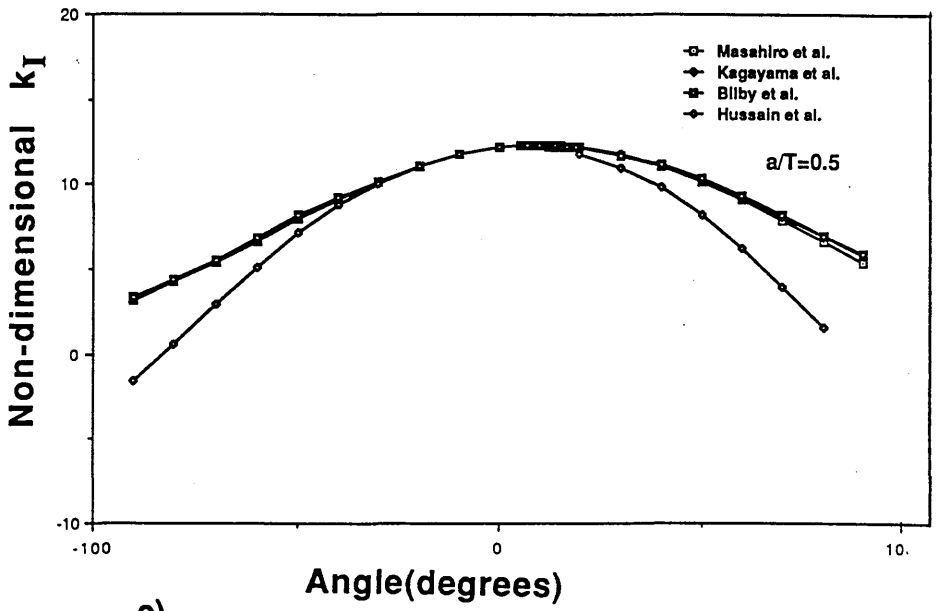
Masahiro et al.
Kagayama et al.
Bliby et al.
Hussain et al.
a/T=0.5
Non-dimensional k_I
Angle(degrees)
20
10
0
-10
-100
0
10

c)

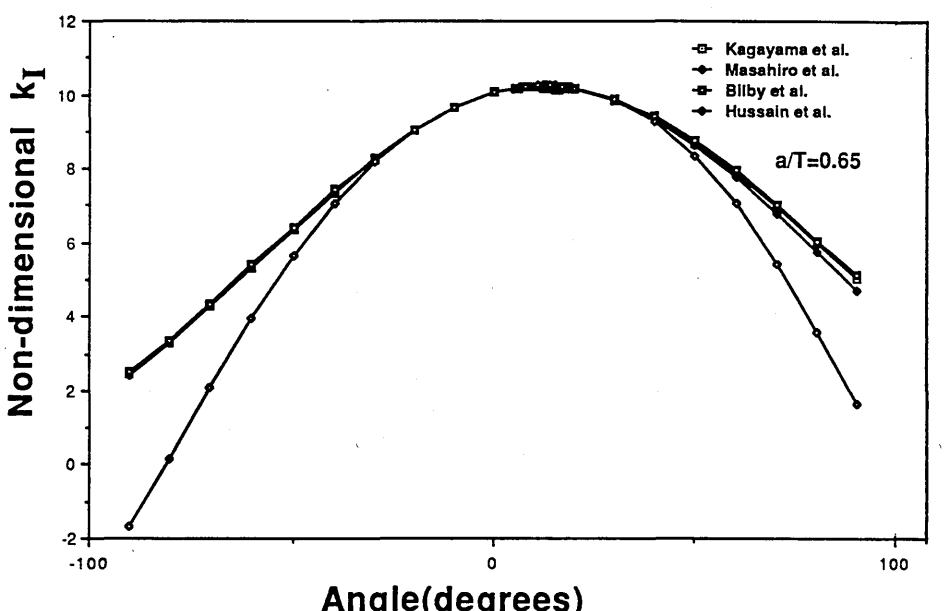
Kagayama et al.
Masahiro et al.
Bliby et al.
Hussain et al.
a/T=0.65
Non-dimensional k_I
Angle(degrees)
12
10
8
6
4
2
0
-2
-100
0
100

d)

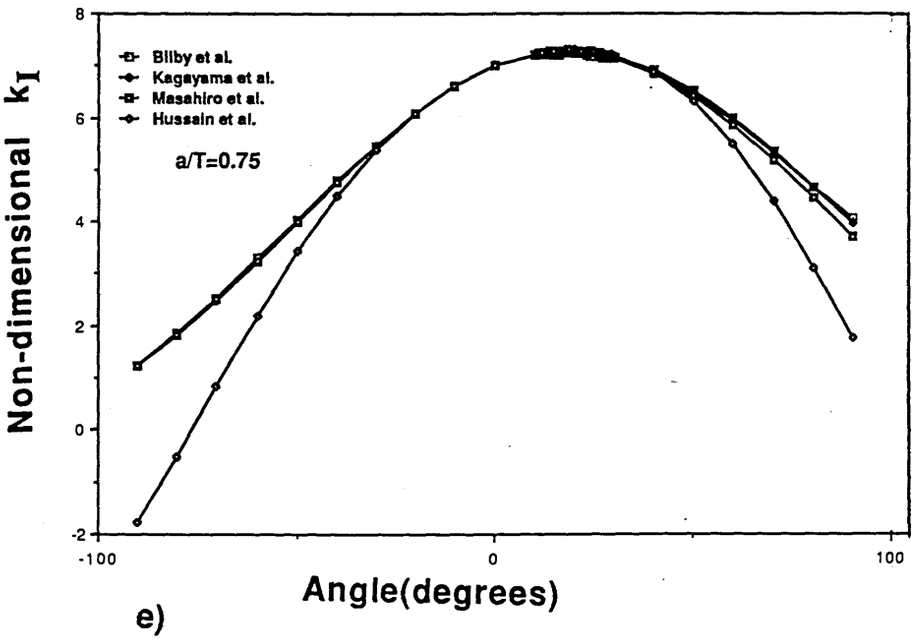
Bilby et al.
Kagayama et al.
Masahiro et al.
Hussain et al.
a/T=0.75
Non-dimensional k_I
Angle(degrees)
8
6
4
2
0
-2
-100
0
100

e)

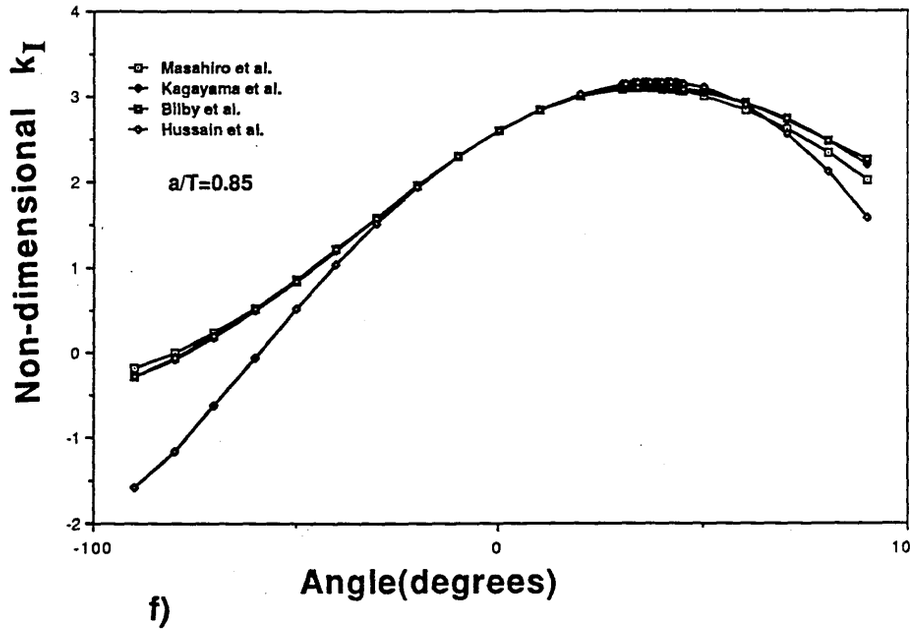
Masahiro et al.
Kagayama et al.
Bilby et al.
Hussain et al.
a/T=0.85
Non-dimensional k_I
Angle(degrees)
4
3
2
1
0
-1
-2
-100
0
10

f)

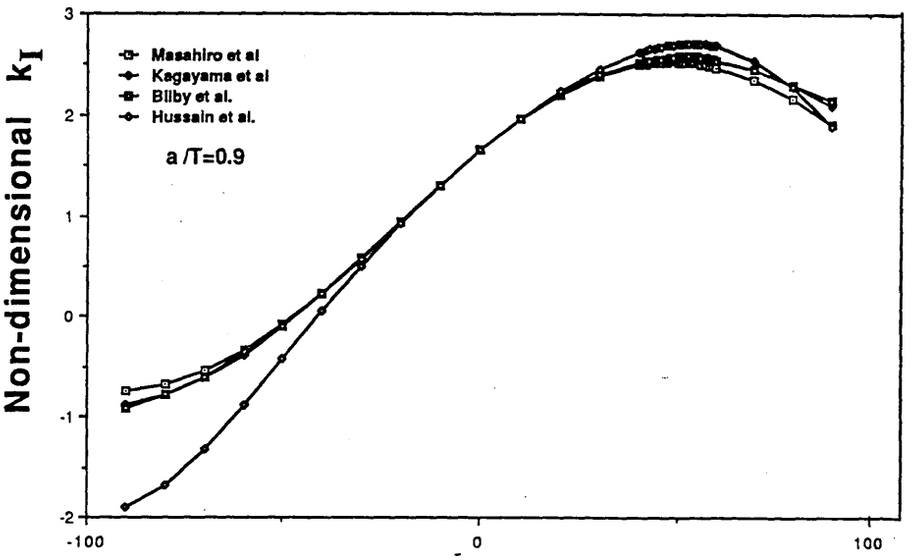

g) Angle(degrees)

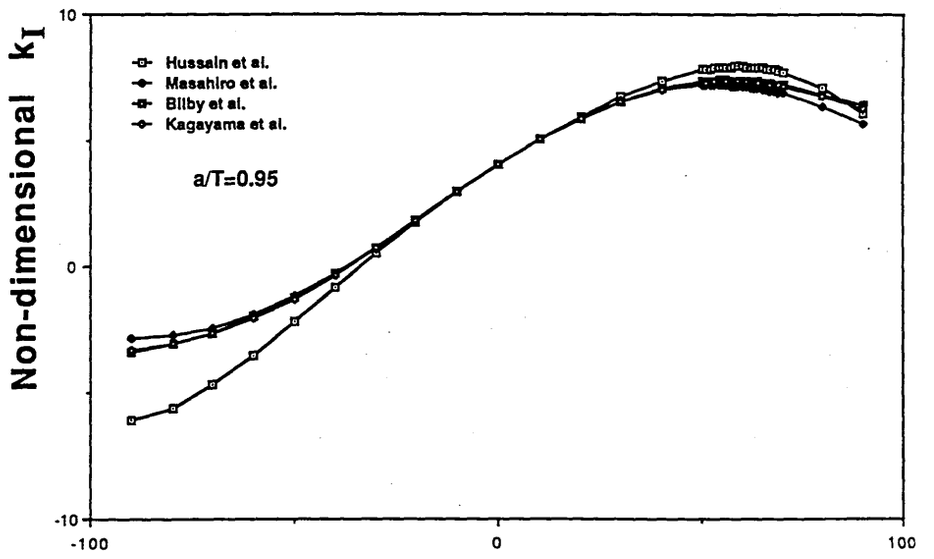

h) Angle(degrees)

FIG.4.24 Non-dimensionalised $k_I=k_I/\sigma\sqrt{a}$ as a function of the crack growth angle for the T plate joint specimens (Two ends are built in).

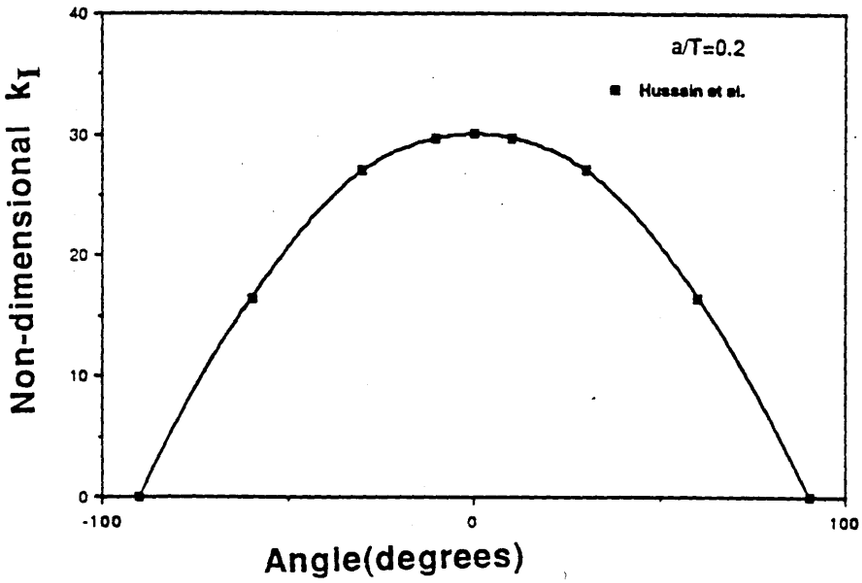
a/T=0.2
Hussain et al.
Non-dimensional k_I
Angle(degrees)
40
30
20
10
0
-100
0
100

a)

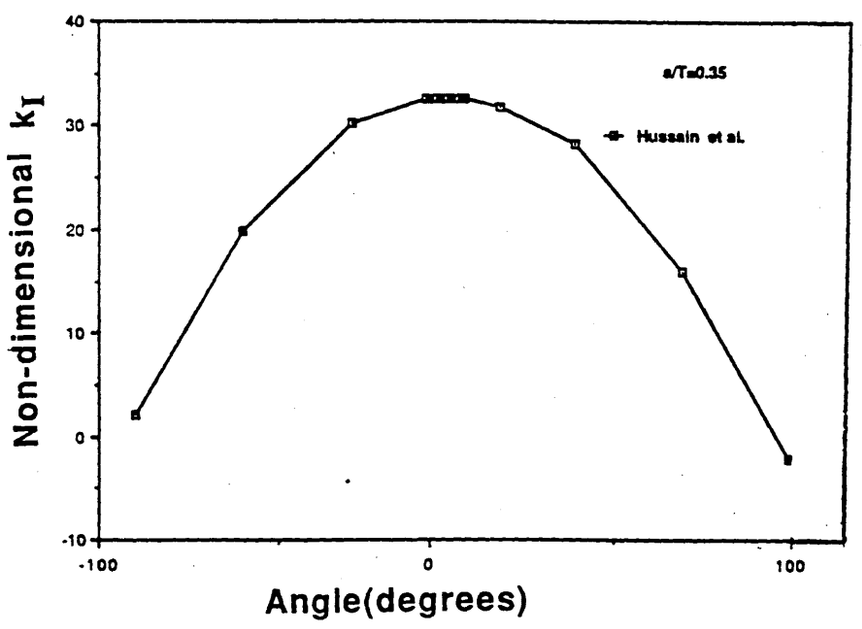
a/T=0.35
Hussain et al.
Non-dimensional k_I
Angle(degrees)
40
30
20
10
0
-10
-100
0
100

b)

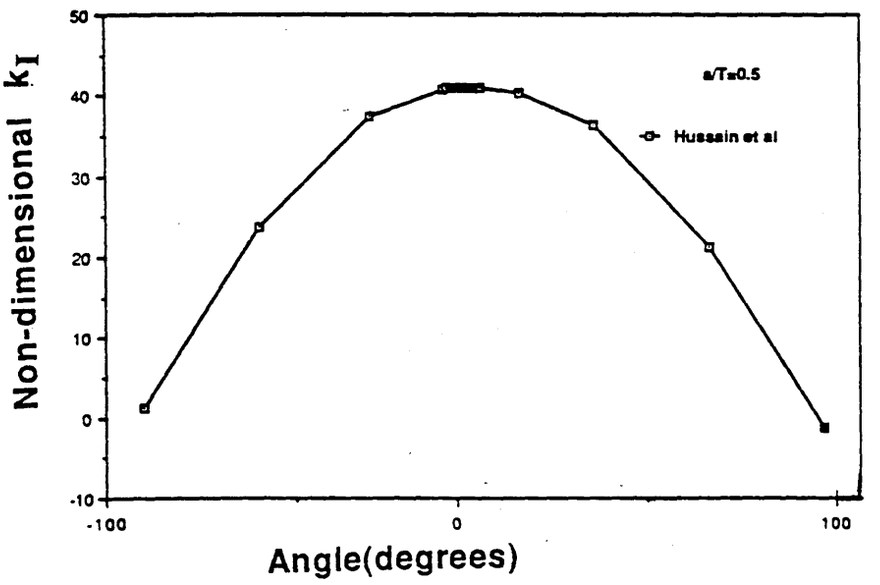
Non-dimensional k_I
50
40
30
20
10
0
-10
-100
0
100
Angle(degrees)
a/T=0.5
Hussain et al

c)

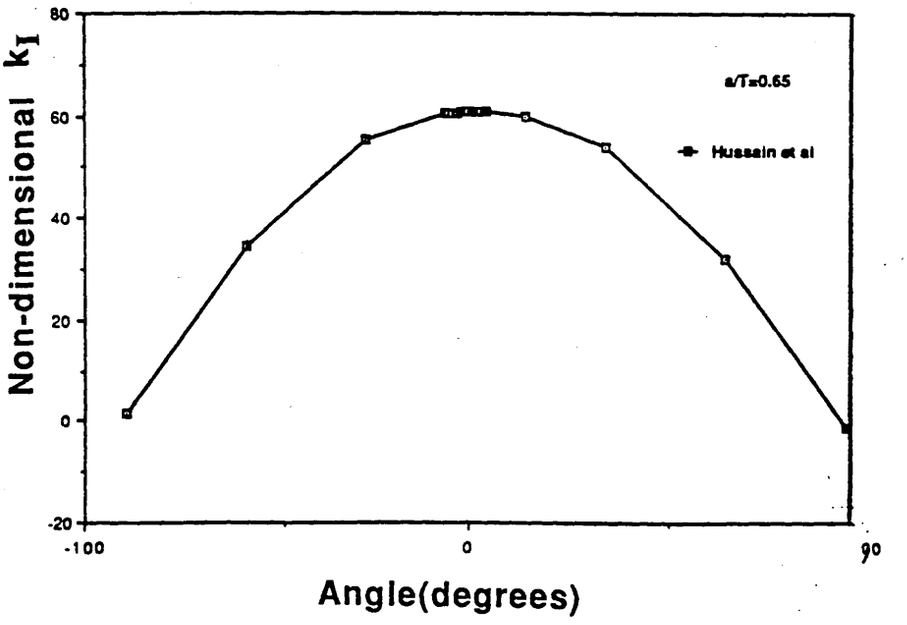
Non-dimensional k_I
80
60
40
20
0
-20
-100
0
90
Angle(degrees)
a/T=0.65
Hussain et al

d)

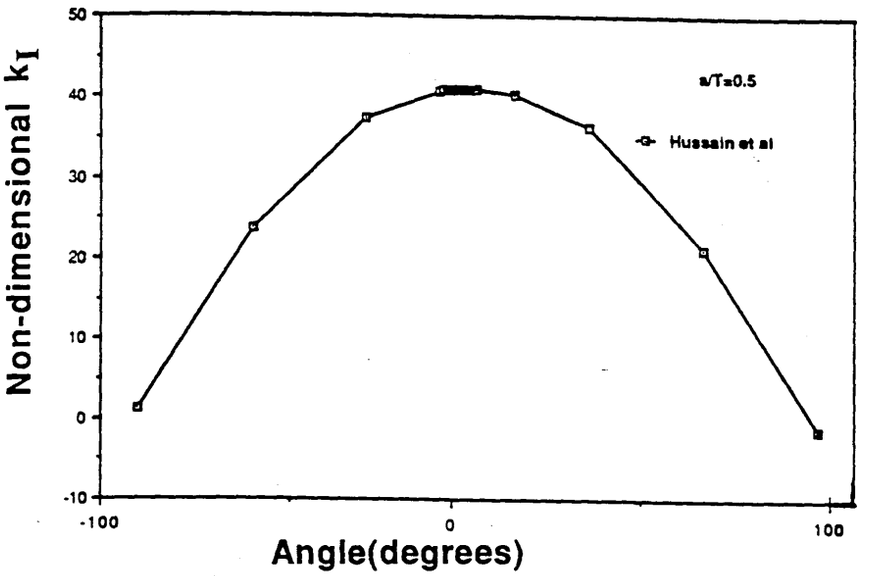
Non-dimensional k_I
50
40
30
20
10
0
-10
-100
0
100
Angle(degrees)
a/T=0.5
Hussain et al

e)

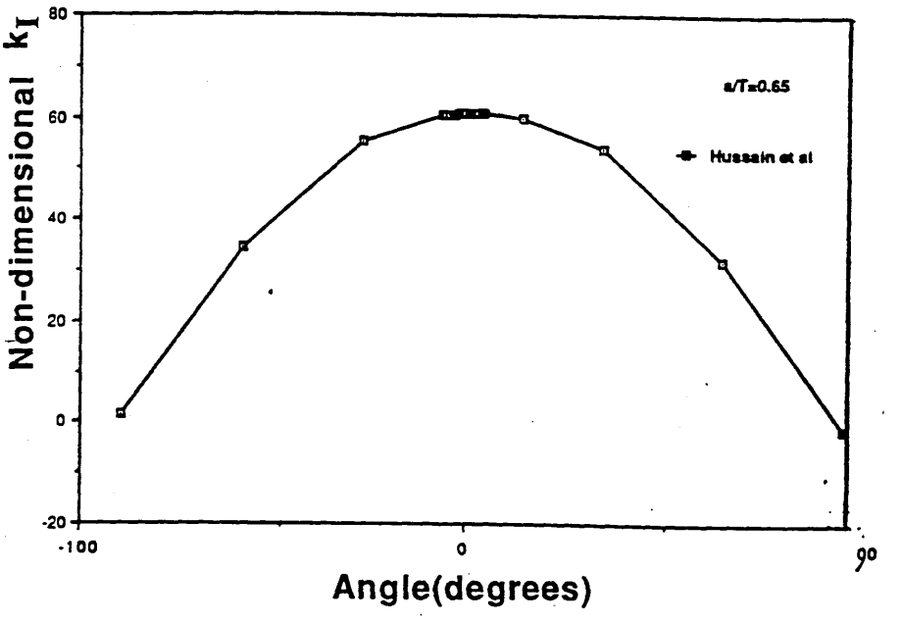
Non-dimensional k_I
80
60
40
20
0
-20
-100
0
90
Angle(degrees)
a/T=0.65
Hussain et al

f)

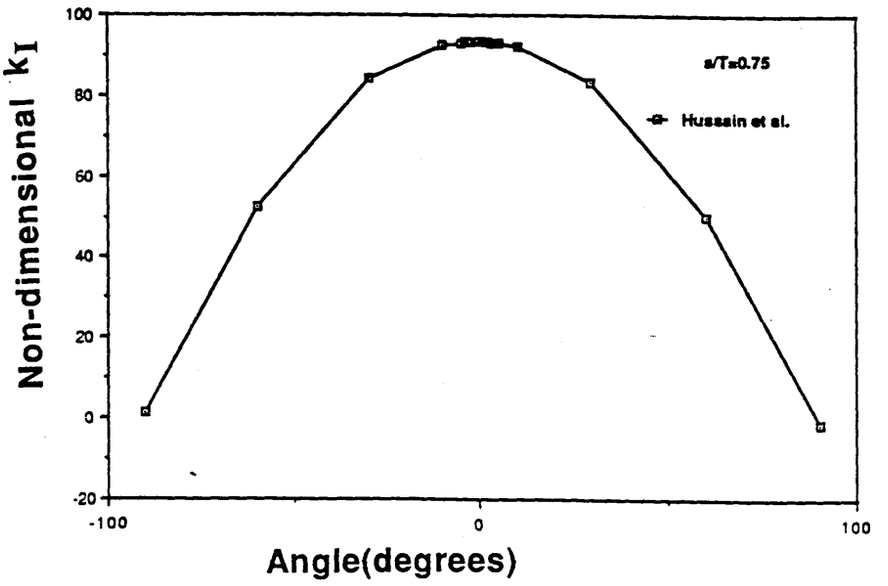

g)

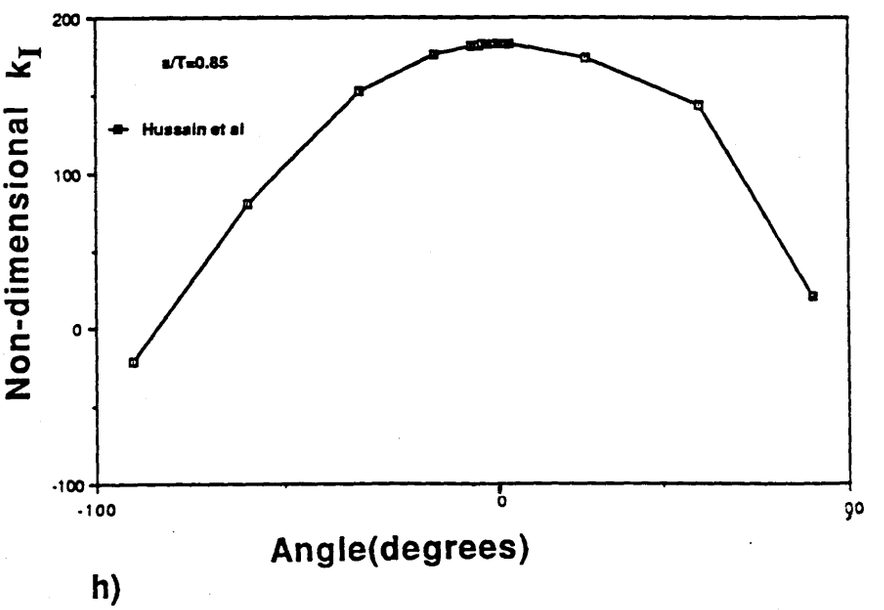

h)

FIG.4.25 Non-dimensionalised $k_I=k_I/\sigma\sqrt{a}$ as a function of crack growth angle for the T plate joint specimens (Rotations are allowed at the two ends)

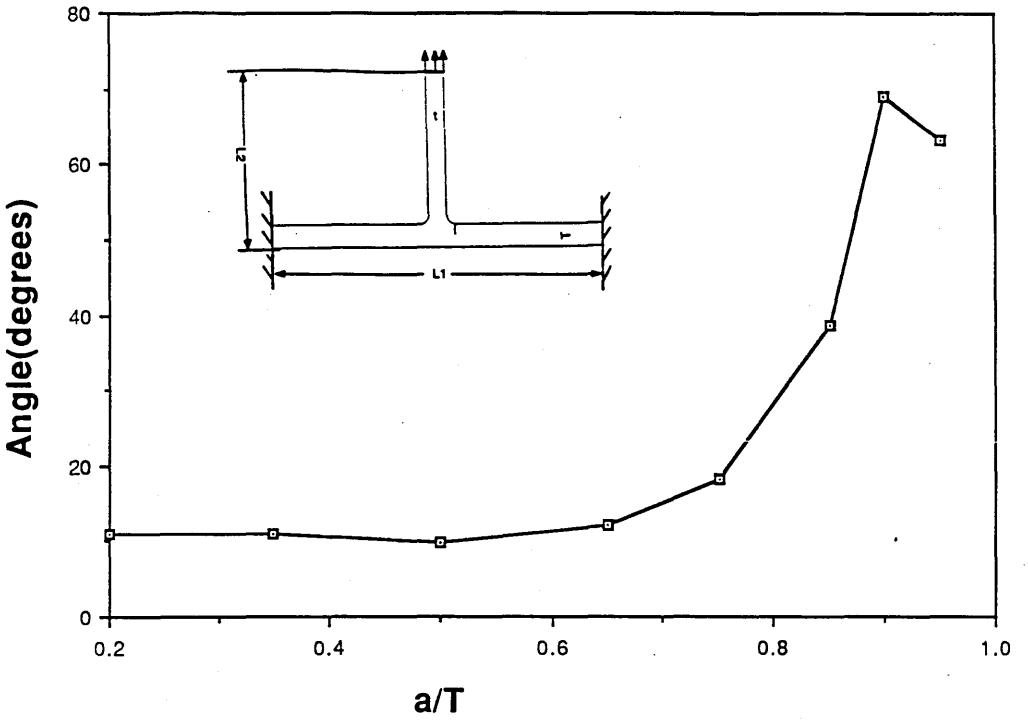

FIG.4.26 The angle of maximum k_I as a function of a/T (Two ends are built in)

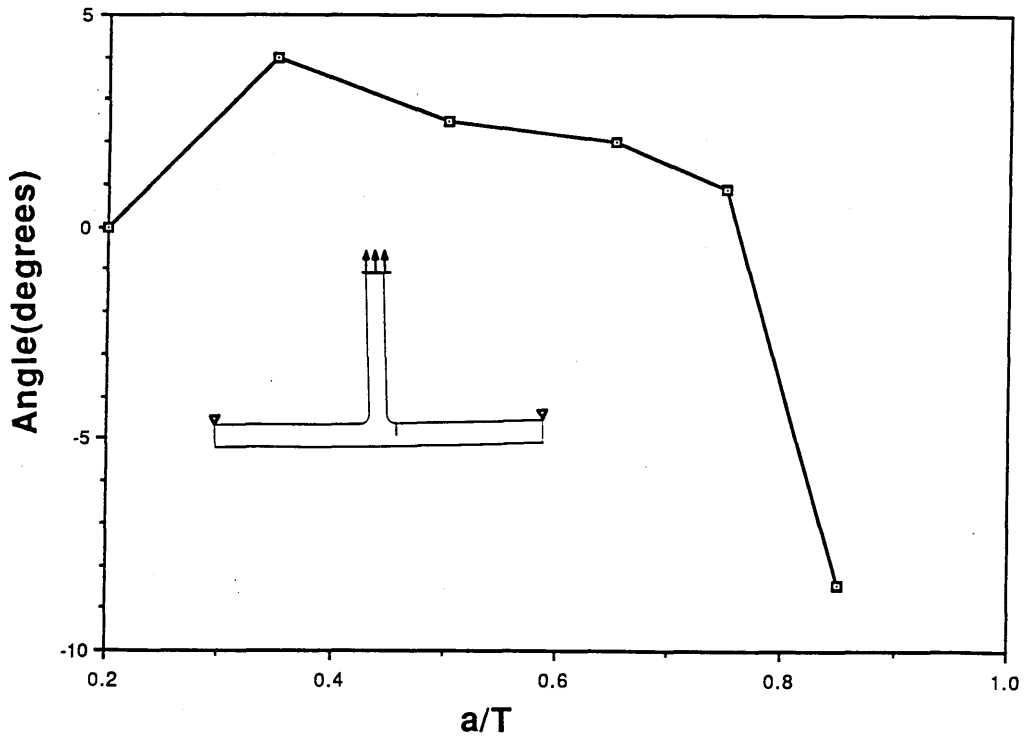

FIG.4.27 The angle of maximum k_I as a function of a/T (Rotations are allowed at the two ends)

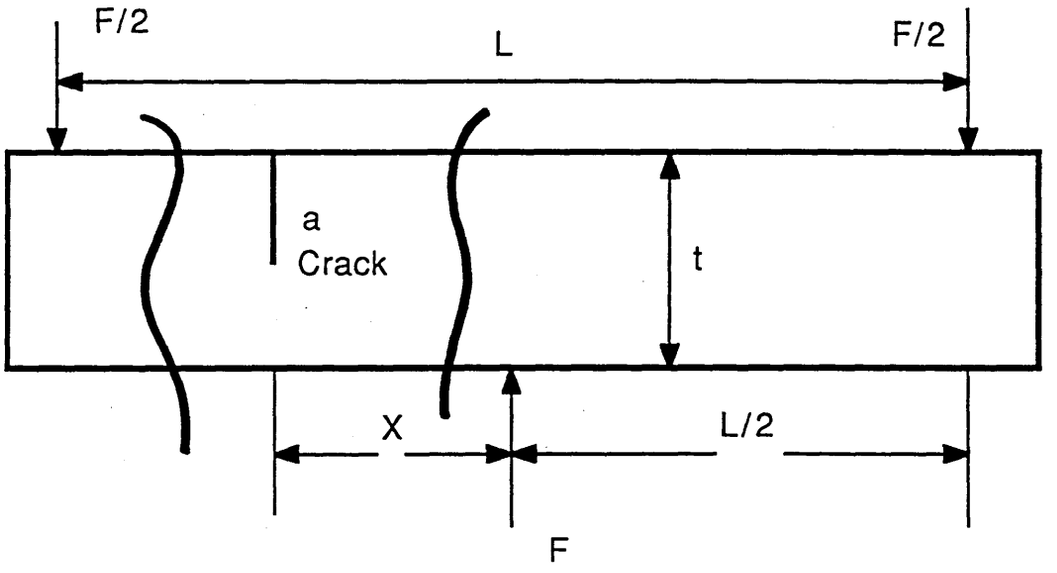

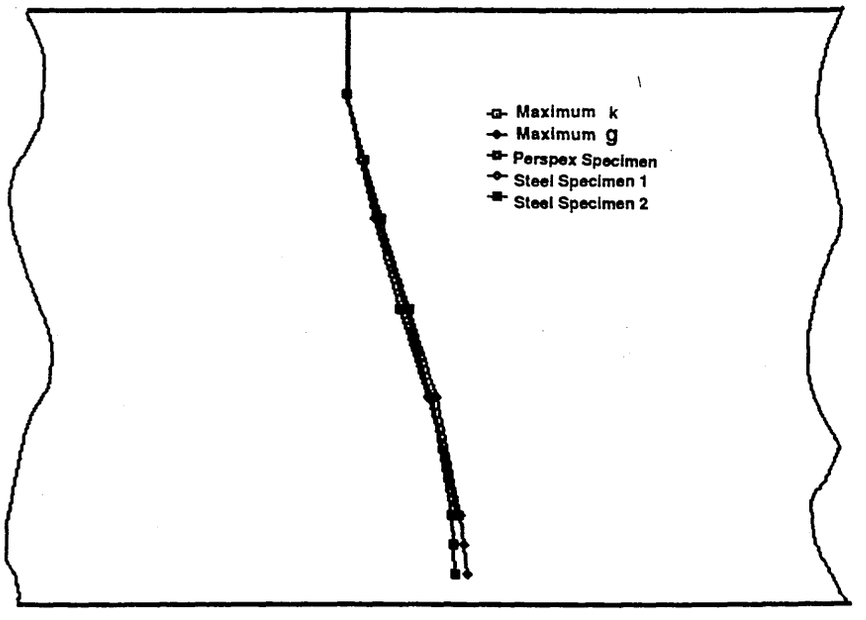

FIG.4.28 A comparison of the crack path predicted using maximum g and maximum k theory with experimental data for the asymmetric specimens (X=2T)

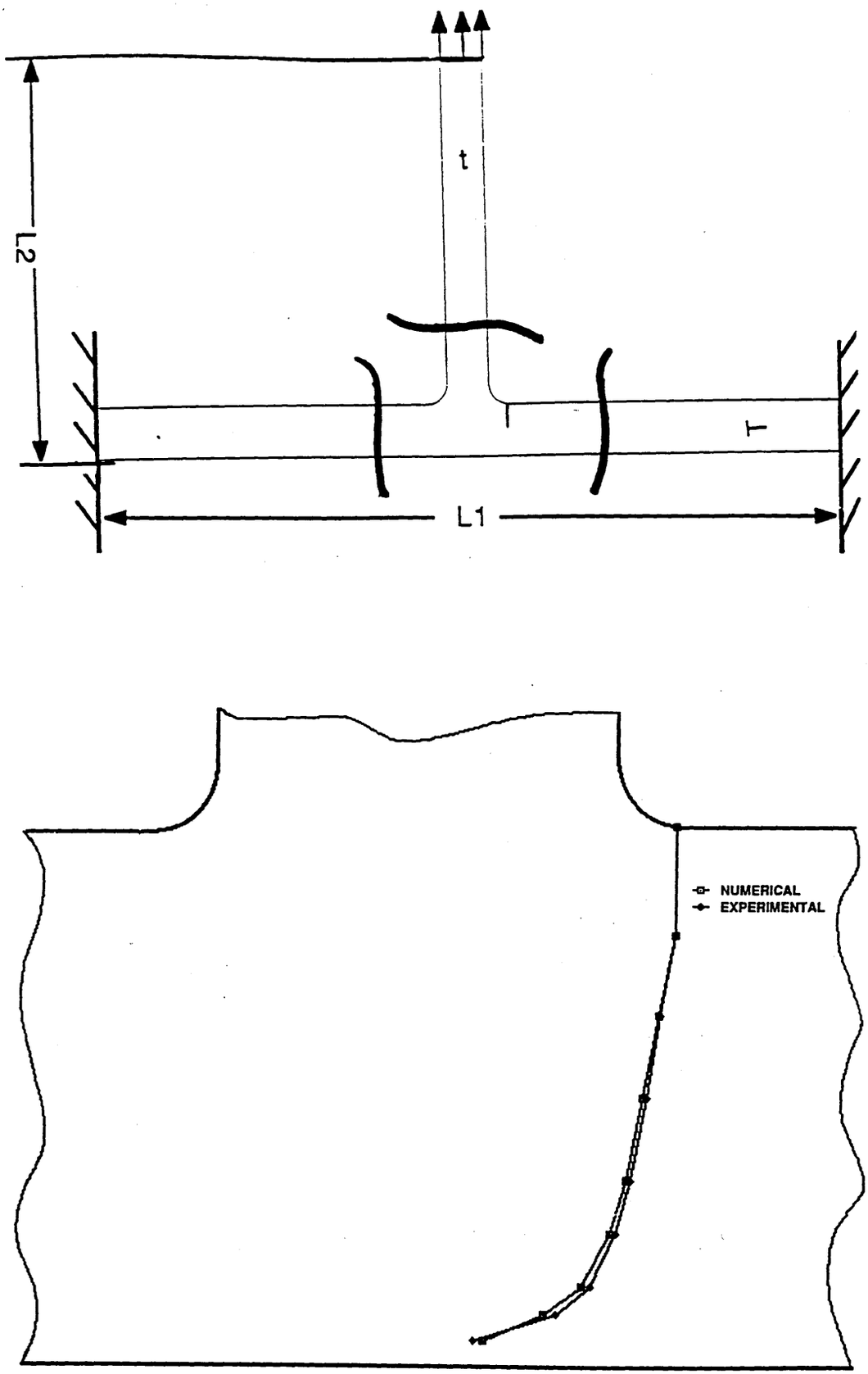

FIG.4.29 A comparison of the crack path predicted using maximum k theory with experimental data for the T plate specimens (Two ends were fixed)

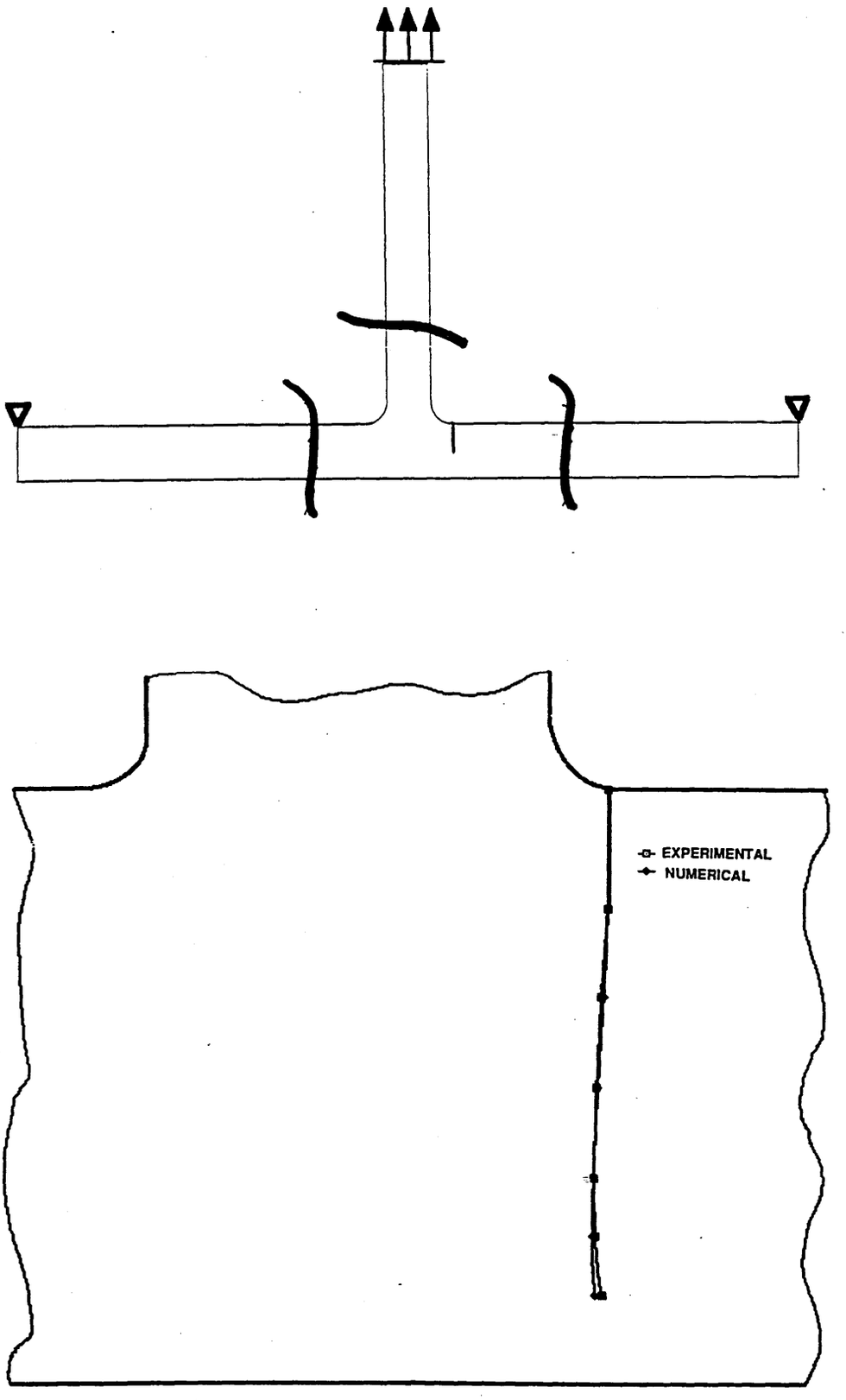

FIG.4.30 A comparison of the crack path predicted using maximum k theory with experimental data for the T plate specimens (Rotations were allowed at the two ends)

ANGLE	C11	C12	C21	C22
90	0.379464	-1.2232	0.35714	-0.20089
-80	0.46652	-1.2276	0.375	-0.04464
-70	0.564732	-1.223214	0.379464	0.13839
-60	0.66444	-1.16	0.366667	0.32222
-50	0.754464	-1.071428	0.34598	0.49107
-40	0.837053	-0.915178	0.294643	0.658482
-30	0.9	-0.73111	0.24222	0.79777
-20	0.955556	-0.50667	0.16667	0.90889
-10	0.98863	-0.25948	0.086493	0.97349
0	1.0	0.0	0.0	1.0
90	0.379464	1.2232	-0.35714	-0.20089
80	0.46652	1.2276	-0.375	-0.04464
70	0.564732	1.223214	-0.379464	0.13839
60	0.66444	1.16	-0.366667	0.32222
50	0.754464	1.071428	-0.34598	0.49107
40	0.837053	0.915178	-0.294643	0.658482
30	0.9	0.73111	-0.24222	0.79777
20	0.955556	0.50667	-0.16667	0.90889
10	0.98863	0.25948	-0.086493	0.97349

Table 4.1 C_{ij} as a function of the angle for the kink crack derived by Bilby et al. (105)

		a/T=0.14	a/T=0.5
Experimental Data Angle(degrees)		19	32
Maximum g Angle(degrees)		18	30
Maximum k_I Angle (degrees)	Masahiro et al.	18	29
	Kageyama et al.	18	30
	Hussain et al.	20	30
	Bilby et al.	20	31

Table 4.2 A comparison of the crack growth angle predicted using maximum g and maximum k_I theory with experimental data for the asymmetric specimens (x=3T)

Chapter 5. Determination of the Stress Intensity Factors of Slant and Curved Cracked Geometries

Section 5.1 Introduction

The complexity of the three dimensional geometry of curved cracks in real structures, such as a tubular welded joints inhibit complete modelling. Therefore, in order to assess the stress intensity factors of inclined or curved cracks, it is proposed to simplify the problem, by establishing relationships between the stress intensity factors of straight normal cracks and slant or curved cracks.

Initially, this problem has been addressed by considering the relationship between the stress intensity factor of normal cracks and straight slant cracks in simple plates. Solutions for slant cracked bars have been given by Wilson (99) and from these the K_I and K_{II} components on the main crack allow the orientation which maximises k_I on an angled kink to be determined. The corresponding k_I values have therefore obtained and been compared with the K_I values for a straight normal crack of the same depth. In addition, in order to test the applicability of these results to welded joints, an idealised two dimensional plane strain T joint which is more representative of welded joints has been considered.

Section 5.2 Numerical Methods

5.2.1 Stress Intensity Factor for Edge Slant Cracked bars

A bar with a single slant edge crack was considered,under tension and bending as shown in Fig.5.1. The orientation of the crack was arbitrarily chosen to be 22.5,45 and 60 degrees to the plate normal, and the ratio of the crack depth to the thickness was varied from 0.3 to 0.9. When $a/T \leq 0.6$,

the stress intensity factors were obtained from the data given by Wilson(99), but for a/T≥0.6, the stress intensity factors were evaluated using finite element methods in conjunction with Eqn.3-3 allowing the K_I and K_{II} components to be separated. The meshes for the slant edge cracked bars are shown in Fig.5.2, for cracks inclined at 22.5, 45 and 60 degrees. Typically, each model involved 95 eight noded isoparametric elements and 350 nodes, producing systems with approximately 660 degrees of freedom. The crack tip was modelled as a focused mesh in which the mid side nodes of the inner ring of elements were located at the quarter point positions.

In order to obtain the maximum k_I for the slant cracks, a small angle kinked crack ahead of the slant crack for this bar was considered, the stress intensity factors for the kink crack (k_I and k_{II}) were then calculated using the equations of Hussain et al. (Eqn. 4-3) which relate the stress intensity factors for a kinked crack to that of the main crack.

5.2.2 Stress Intensity Factor for Edge Cracked bars

Corresponding to the slant cracked bars, bars with normal cracks, which had the same normal depth were studied as shown in Fig.5.3. Again, when a/T≤0.6, the stress intensity factors were obtained from the data given by Wilson (99), but for (a/T) greater than 0.6, the stress intensity factors were determined by finite element calculations, one of the meshes for a normal crack at the edge of the bar is given in Fig.5.4. Typically each model involved 95 elements and 350 nodes, giving a system with 660 degrees of freedom.

5.2.3 Stress Intensity Factors for Central Slant Cracked bars

In addition to the edge cracked bars, a bar with a central slant crack shown in Fig.5.5 was considered. The slant cracks were chosen to be inclined 30,45 and 60 degrees to the normal to the length of the bar. The ratio of the crack depth to the thickness was varied from 0.1 to 0.6 under tension. The stress intensity factors for these geometries were obtained from the data given by Wilson(99) and the maximum k_I obtained using Masahiro's equation(107).

Corresponding to the central slant cracked bars, bars with centre normal cracks, which had the same normal depth were considered, the stress intensity factors were given by Wilson(99).

5.2.4 Stress Intensity Factor for a Curved Crack in a Two Dimensional Joint

The plane strain T-plane joint specimen shown in Fig.5.6 was analysed under a loading system in which a tensile force was applied at the end of the vertical plate while the two ends of the horizontal plate were built in. An initial defect with a depth a/T=0.2 was extended in a piece-wise linear fashion such that the direction of crack extension for each increment of crack growth maximised the off axis strain energy release rate g. The stress intensity factors for the curved cracks were compared with those for a straight crack of an equivalent depth. The meshes for the joints with a straight normal crack and with a curved crack are shown in Fig.5.7. Both have the same normal crack depth. Typically, each model involved 200 elements and 690 nodes giving systems with 1370 degrees of freedom.

SECTION 5.3, Results

The maximum k_I for the slant crack non-dimensionalised with respect to

the applied stress and the normal crack depth a was compared with the non-dimensional maximum k_I for the normal crack. This comparison is made in Fig.5.8 and Fig.5.9 for edge slant cracks under tension and bending, and in Fig.5.10 for the centre slant cracks under tension.

The maximum k_I for the curved crack non-dimensionalised with respect to its applied load and the normal crack depth a, is in compared with the non-dimensional maximum k_I for the normal crack with the same normal crack depth for a T-plate joint in Fig.5.11. In addition, the maximum k_I and K_I for the normal crack are also plotted as a function of a/T in Fig.5.12.

Section 5.4 Discussion

The non-dimensional off-axis maximum stress intensity factors (k_I) for edge cracked bars with slant cracks or normal cracks in tension and bending are very similar. The average difference is within 4%, the worse case gave a discrepancy of 12% at a/T=0.4 in bending, when the crack was inclined at 60 degrees. The results for the central slant crack and the normal crack in tension were also similar. The average difference was within 8%, the largest discrepancy being 14% at a/T=0.4 in tension, when the angle was 60 degrees. This indicates that the off-axis maximum stress intensity factor k_I is largely dependent on the length of the ligament and the loading mode.

For the T plate joint with a curved crack, the average difference between the stress intensity factors of the curved and normal cracks was within 3.5%, while the biggest difference was about 4.5% when a/T=0.65.

When the crack depth was less than 60% of the wall thickness, the strain energy release rate of a normal crack is quite close to the maximum off axis strain energy release rate. This indicates that the strain energy release rate of a normal crack is acceptable in fracture mechanics

calculations. However, when the crack grows deeper, the discrepancy between the maximum strain energy release rate of a straight and curved cracks increases due to the fact that the orientation of the cracks also increases. In this case, significant errors in fatigue and structural integrity calculation will result by assuming that cracks develop normal to the plate surface.

Section 5.5.Conclusion

As slant or curved cracks subject to mixed mode loadings will in reality propagate in the direction which maximise k_I or g, the stress intensity factors controlling fatigue crack growth are closely similar, to those of normal cracks of the same depth given that they both are subject to the same simple loading. The implication is that reasonable estimates of the stress intensity factor of curved cracks can be obtained by considering a straight crack of the same depth. This significantly simplifies the determination of appropriate stress intensity factor for angled cracks in structures such as tubular joints and although care must necessarily be taken of the curved cracks which run into a radically different stress field from that different of the straight crack.

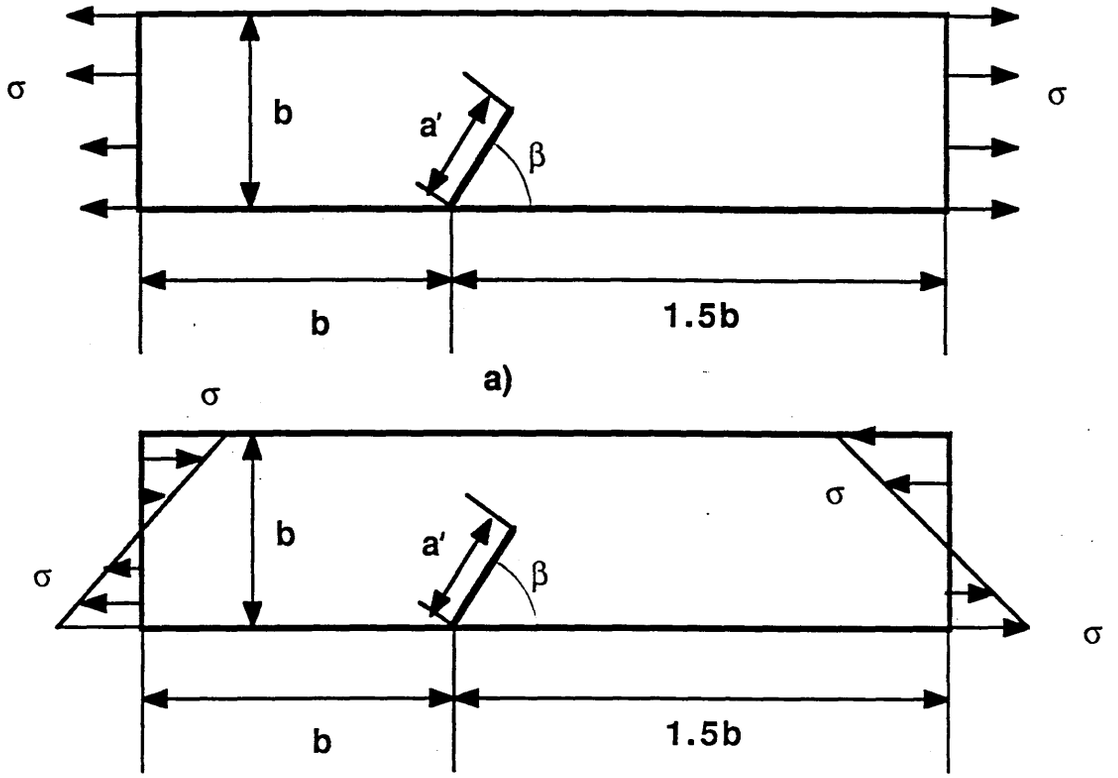

FIG.5.1 A bar with a single slant edge crack under tension and bending

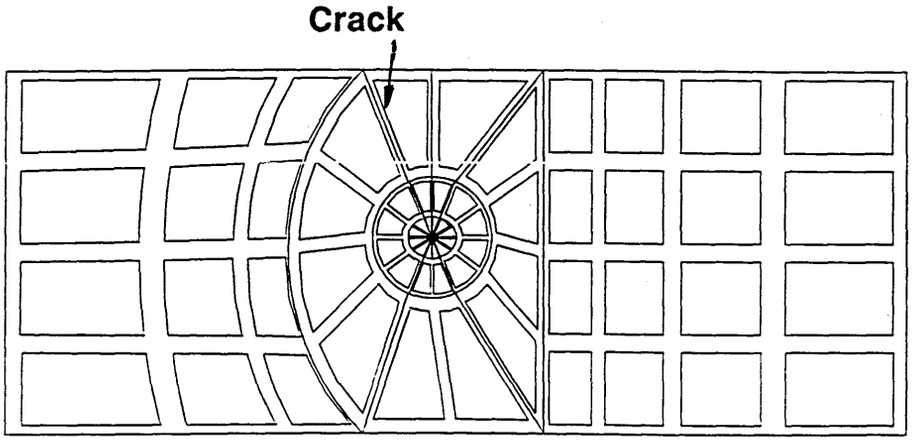

FIG.5.2 A mesh of the slant crack geometries.

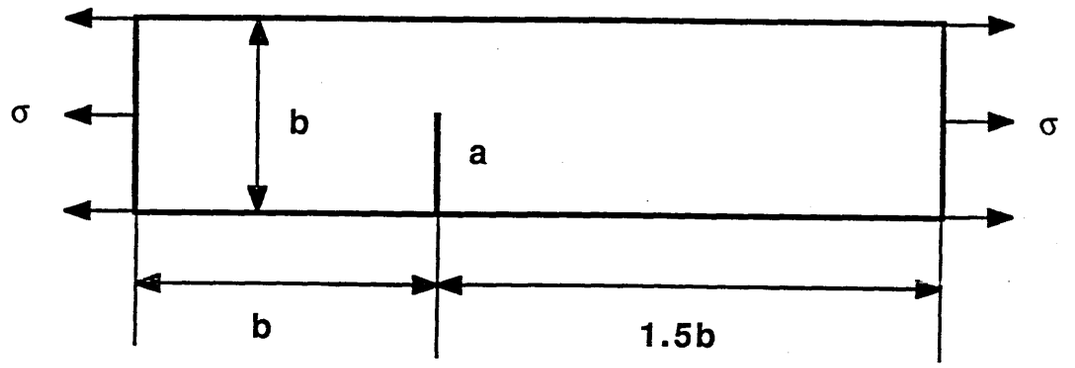

FIG.5.3 A single edge cracked bar

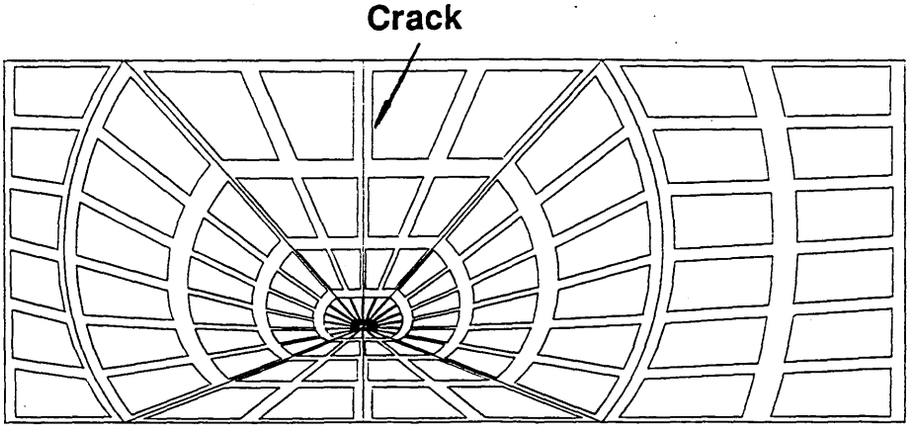

FIG.5.4 A mesh of the single edge cracked bar.

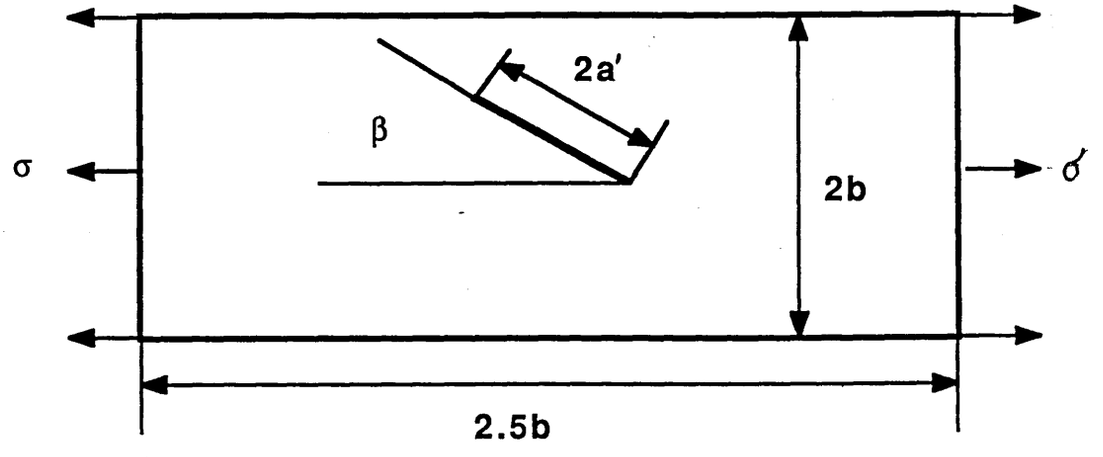

FIG.5.5 A central slant cracked bar

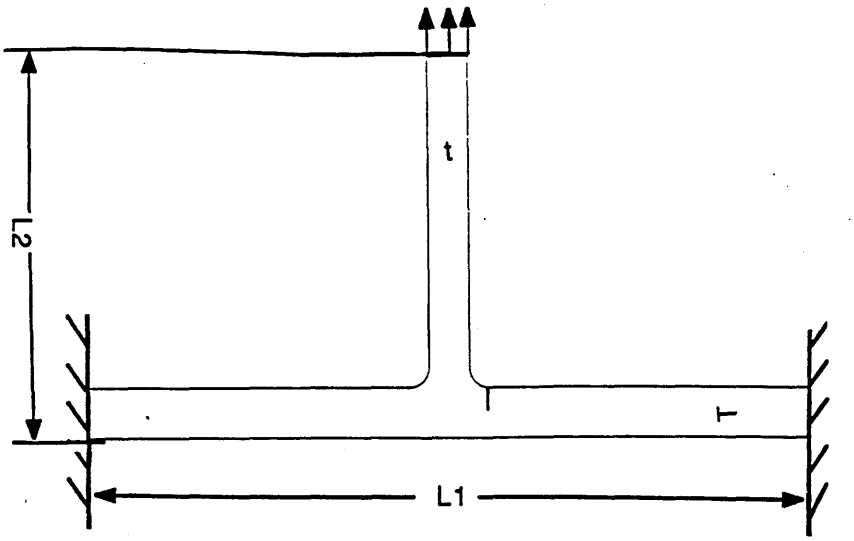

FIG.5.6 A T plate joint geometry

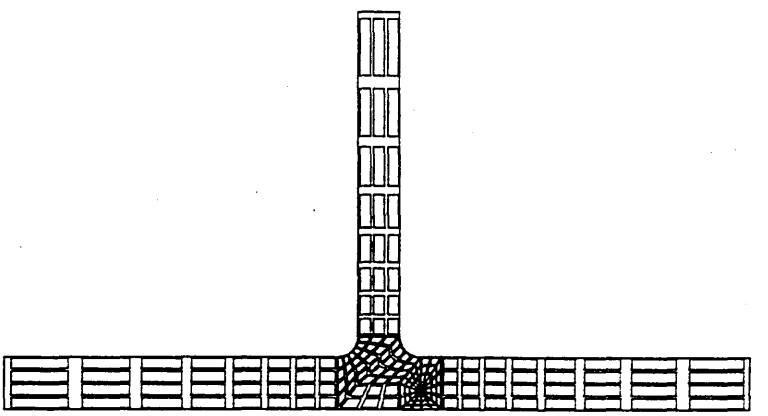

a)

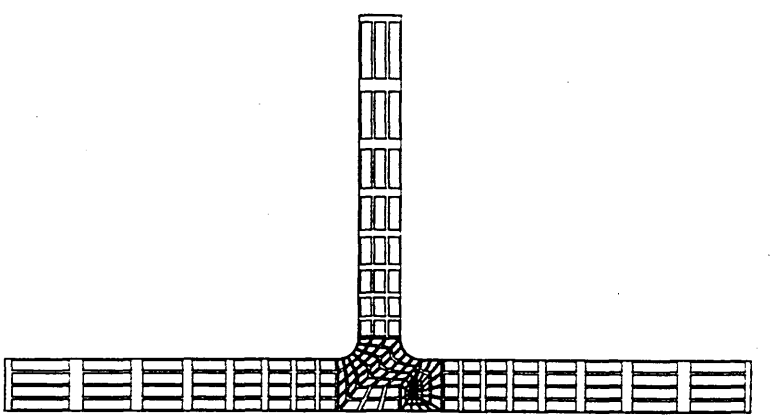

b)

FIG.5.7 a) A mesh of a T plate joint with a straight normal crack

b) A mesh of a T plate joint with a curved crack

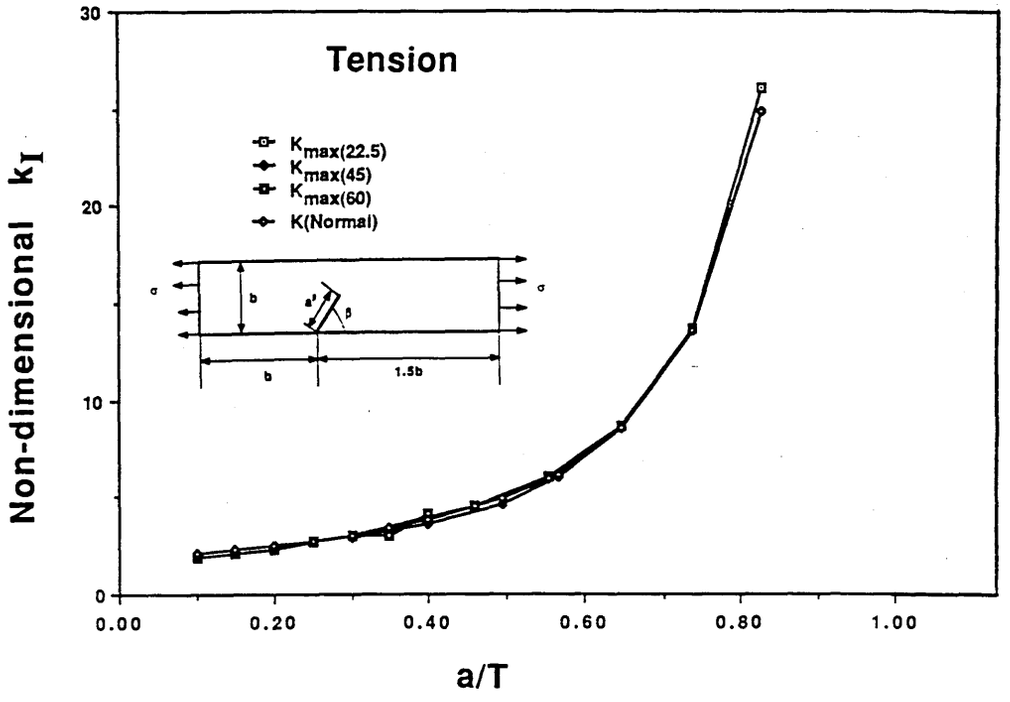

FIG.5.8 A comparison of the non-dimensionalised maximum $k_I=k_I/\sigma\sqrt{a}$ for a single edge slant cracked bar and a single edge normal cracked bar under tension

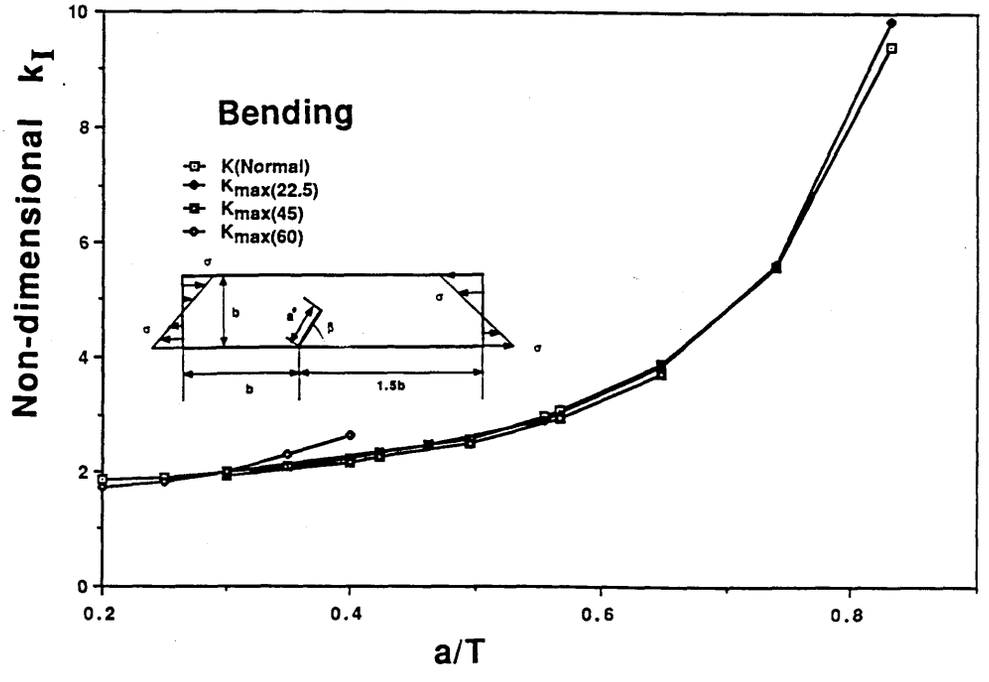

FIG.5.9 A comparison of the non-dimensionalised maximum k_I ($k_I/\sigma\sqrt{a}$) for a single edge slant cracked bar and a single edge normal crack bar cracked bar under bending

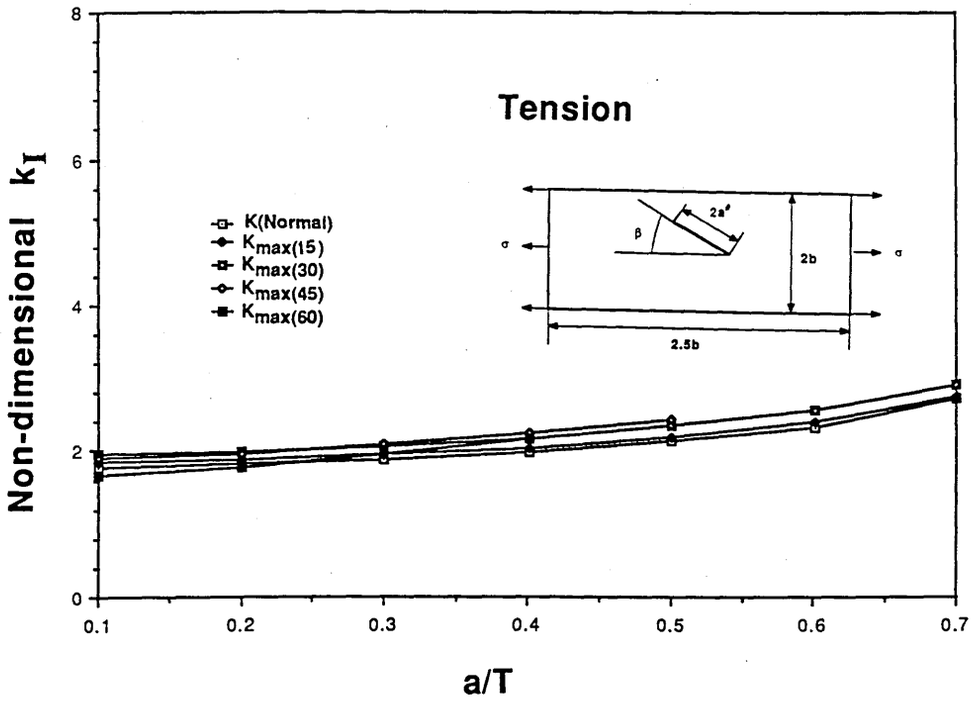

FIG.5.10 A comparison of the non-dimensionalised maximum k_I ($k_I/\sigma\sqrt{a}$) between a central slant cracked bar and a central normal cracked bar under tension

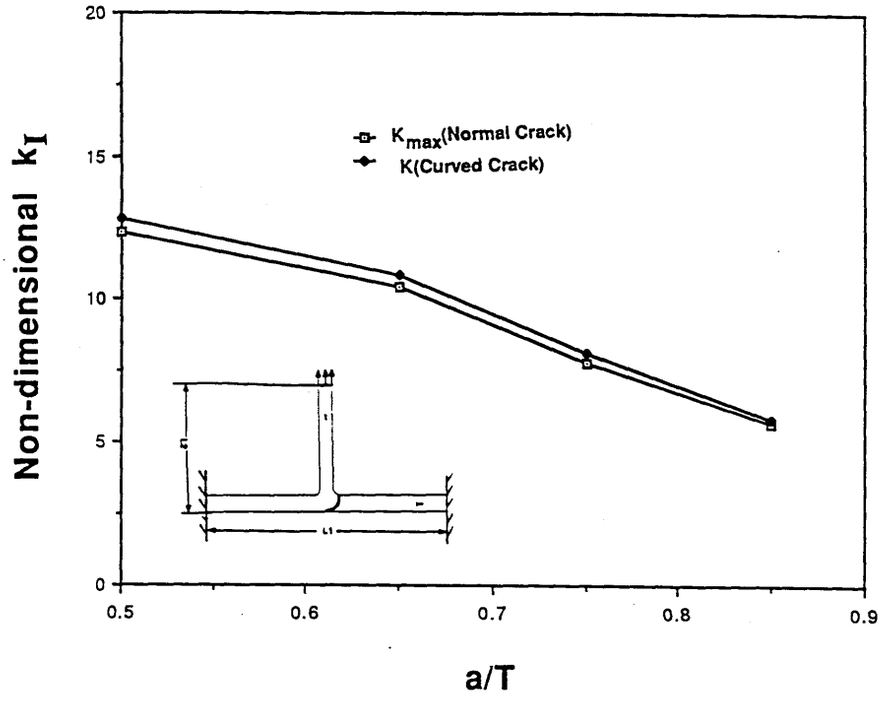

FIG.5.11 A comparison of the non-dimensionalised maximum k_I ($k_I/\sigma\sqrt{a}$) between T-plate joint with a normal crack and a T-plate joint with a curved crack

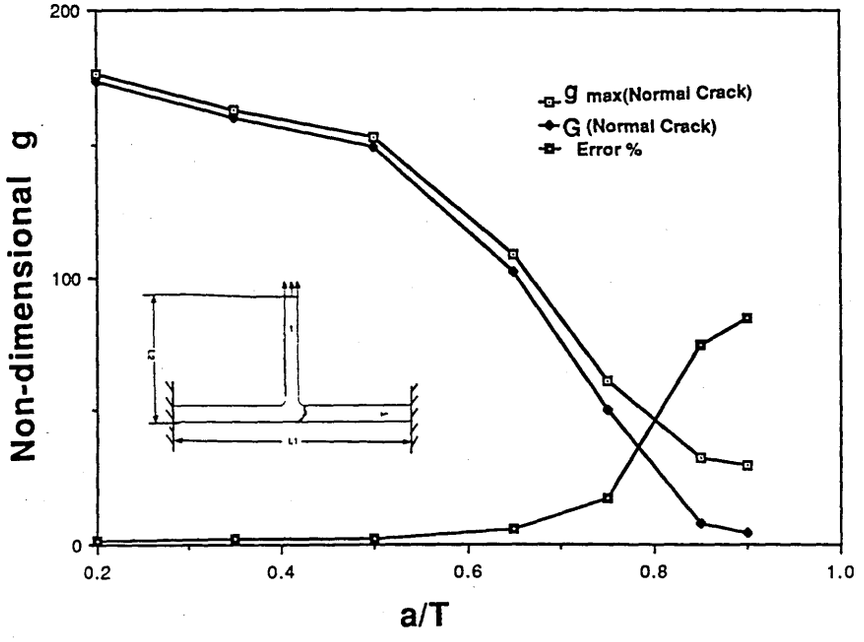

FIG.5.12 Non-dimensionalised Maximum g, $Eg/\sigma^2(1-\upsilon^2)a$ for a kinked crack and non-dimensionalised G, $EG/\sigma^2(1-\upsilon^2)a$ for the normal main crack in a T plate joint as a function of a/T

Chapter 6 Determination of the Crack Path and the Stress Intensity Factors in a Tubular T Joint

Section 6.1 Introduction

The stress intensity factors of semi-elliptical cracks which are normal to the chord wall in a tubular welded joint have been determined by both virtual crack extension with three dimensional elements and line springs. The accuracy and simplicity of the line spring method has enhanced the ability to analyse complex offshore structures using fracture mechanics. However, there is an important shortcoming of current numerical methods in that it is often only practical in a complicated structure such as a tubular joint to model a crack normal to the wall. For tubular joints under axial loading, however, there is experimental evidence (52) to indicate that cracks grow along a curved path under the chord-brace intersection. Similarly, the numerical results shown in (Fig.3.18) indicate that the ratio of K_{II}/K_I increases with the crack depth. This also implies that the crack will grow along a curved path under the chord-brace intersection and the actual crack length will be greater than the thickness of the chord wall at penetration. Therefore, the determination of the crack path in tubular joints and the corresponding stress intensity factors is a significant problem, which is the subject of this Chapter.

In Chapters 4 and 5, the direction of a growing fatigue crack and the stress intensity factors of curved and slant cracks in some simple two dimensional geometries under both bending and tensile stress field were studied. It was found (105) that the cracks developed in such a way as to maximise the mode 1 component, k_I. Alternatively, it has been suggested (23,105) that the path maximises the strain energy release rate g, although in practice these criteria are not significantly different. In addition, the

stress intensity factor of a curved crack can be obtained by referring to the maximum stress intensity factor of a normal crack. The successful prediction of the crack path and the determination of the stress intensity factor for a curved crack for two dimensional geometries has encouraged the author to apply both maximum k_I and maximum g theories to determine the crack path of semi-elliptical cracks in a tubular welded joint and assess the stress intensity factors of semi-elliptical cracks in a real structures. This is undertaken by comparing the finite element results with experimental data(20,52)

Section 6.2 The Crack Path of Semi-Elliptical Cracks in a Tubular Weld Joint

The ratio of K_{II}/K_I determined from both line-spring and three dimensional brick calculations changes rapidly with crack depth. For shallow cracks the loading is predominantly mode 1. The mode 2 component, however, increases markedly with crack depth until at a/T=0.9, K_I and K_{II} have a similar magnitudes implying that there is a strong tendency for the crack to deviate from the plane as the crack grows deeper. To address this problem an off-axis virtual crack method has been used to estimated the crack-path using the g maximum criterion. This was achieved by modifying the direction cosine of the normal to the assumed crack extension direction in ABAQUS input data. For both three dimensional and line spring models the direction of crack extension was also inferred from calculations of the stress intensity factors of an angled kink at the crack tip, enabling the direction of crack extension to be inferred from the maximum k_I theory.

The local mode 1 and mode 2 stress intensity factors denoted k_I and k_{II} can be expressed in terms of the mode 1 and mode 2 components, denoted K_I

and K_{II} on the main crack following the work of Bilby (105), Hussain et al (106), Masahiro et al (107) and Kagayama et al.(108). The stress intensity factor at the deepest point of the crack has been calculated on the basis that the crack extends at some arbitrary angle ø to the main crack. By comparing k_I for a range of angles for each crack depth, the maximum k_I and the corresponding crack growing direction were obtained.

Section 6.3 Results of the Crack Path Calculation

The crack paths were obtained by calculating the angle between the tangent to crack path and the normal to the chord wall. For the three dimensional brick elements model,the non-dimensional k_I with respect to the applied stress and the normal crack depth as a function of the angle is given in Fig.6.1, 6.2 and 6.3 for a/T=0.2,0.6 and 0.9. For the shell model the results are given in Fig. 6.4, 6.5 and 6.6. In a similar way the non-dimensionalised g using off-axis virtual crack methods as well as those derived from Eqn.4-1 are plotted against the crack extension angle in Figures 6.7,6.8 and 6.9 for the 3D brick model. All the analyses show broad agreement while differing in detail. The angle of the kink which maximises k_I is close to 18 degrees for a/T=0.2, 20 degrees for a/T=0.6 and approximately 55 degrees for a/T=0.9. The local strain energy release rate g can also be obtained by the virtual crack extension method of Parks (22). In the present case the crack path which maximises k_I and the path which maximises g are closely similar, and are plotted as piece wise linear segments in Fig6.10 and compared with that observed experimentally by Noorkhord (52) indicating excellent agreement between numerical results and the experimental data.

Section 6.4 The Stress Intensity Factor of the Semi-Elliptical Crack

It has been shown that the non-dimensional stress intensity factors of curved cracks and the non-dimensional maximum stress intensity factor for a normal crack are very similar if they have the same normal crack depth in simple two dimensional geometries under both tension and bending. Confidence has thus been obtained to apply this method to the full three dimensional problems. The K_I and K_{II} values for the normal crack in tubular T joints which subject to axial loading were extracted from Huang and Hancock(51) in which the cracks shapes satisfied Dover et al 's experimental data (20) that is.

$$a/c=0.167(a/T)+0.05 \qquad (a/T)\geq 0.2 \qquad \text{Eqn.(6-1)}$$

Using Hussain's equation for the kinked crack (106), the crack extension direction was obtained assuming that the crack growth direction maximises the stress intensity factor k_I at the deepest point of the crack. On this basis, the crack growth path and k_{Imax} value for the deepest point were calculated in a piece linear manner. A comparison has been made between the maximum k_I obtained from line spring methods in conjunction with kinked crack solutions and the effective K derived from Dover et al's experimental data (20) in Fig.6.11 for a T-joint under axial loading. The data is non-dimensionalised with respect to the chord wall thickness and the nominal stress at the end of the brace. From this figure, it is clear that the agreement between k_{Imax} and K for the experimental data is much better than that between the K which equals to $\sqrt{E'G}$ for the crack normal to the chord wall and K for the experimental data when the crack grows deeper.

For the current 3 dimensional solid brick model which has a fixed crack length C/T=2, the maximum off-axis k_I was obtained using kinked crack solutions. This value was compared with the effective stress intensity factors at the deepest point of a normal crack. Both sets of data are non-dimensionalised with respect to the applied stress and crack depth a, in Fig.6.12. This figure demonstrates that when the crack depth is less than 60% of the wall thickness, the non-dimensional effective stress intensity K_{eff} for the main crack is close to the maximum non-dimensional maximum stress intensity factor k_I. However, when the crack grows deeper, the discrepancy between the maximum stress intensity factor and the stress intensity factor for the main crack becomes larger. In this case, the latter can no longer be substituted for the former as a parameter to characterise the crack tip stress and strain field. This is consistent with the behaviour of the two dimensional T plate joint shown in Fig.5.12.

Section 6.5 Conclusion

The direction of crack extension on the basis of k_I and g maximum theories has been shown to be similar in this configuration and both theories agree with experimental observation that under axial loading the cracks curve under the chord-brace intersection. The stress intensity factors for such cracks in tubular joints can be obtained from calculations using straight cracks normal to the chord wall, and of an equivalent depth.

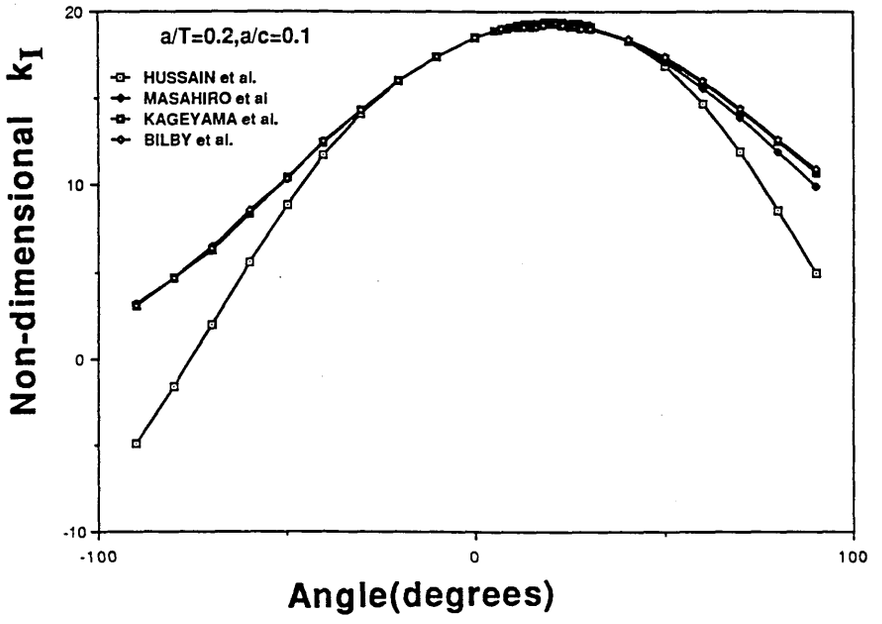

FIG.6.1 The non-dimensionalised maximum k_I ($k_I/\sigma\sqrt{a}$) for the 3 dimensional brick model as a function of the angle, a/T=0.2, a/c=0.1

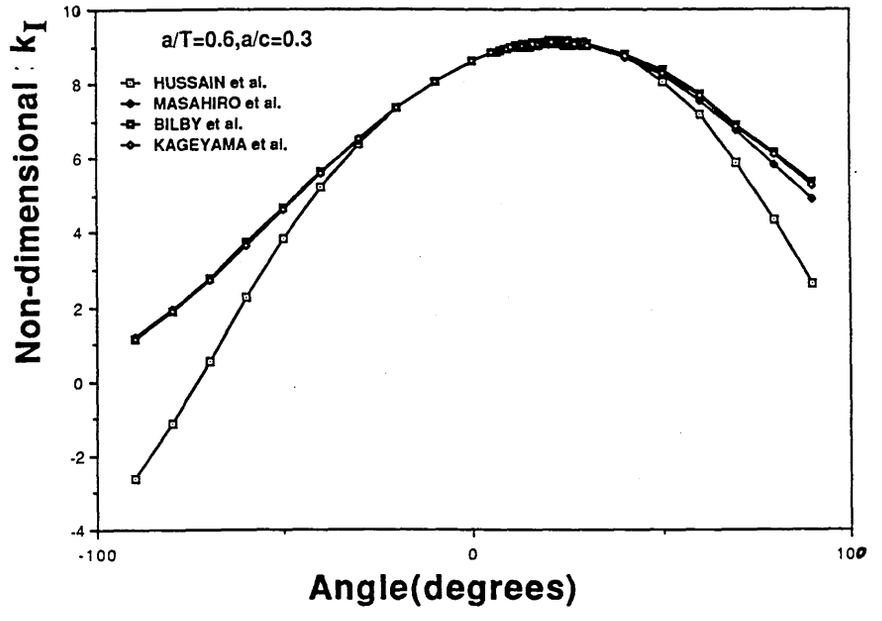

FIG.6.2 The non-dimensionalised maximum k_I ($k_I/\sigma\sqrt{a}$) for the 3 dimensional brick model as a function of the angle, a/T=0.6, a/c=0.3

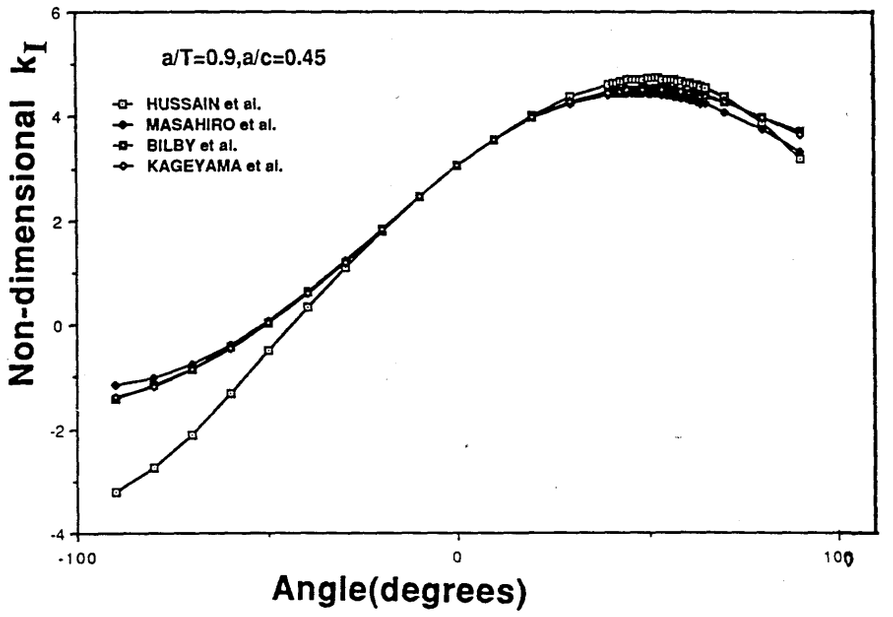

FIG.6.3 The non-dimensionalised maximum k_I ($k_I/\sigma\sqrt{a}$) for the 3 dimensional brick model as a function of the angle,a/T=0.9, a/c=0.45

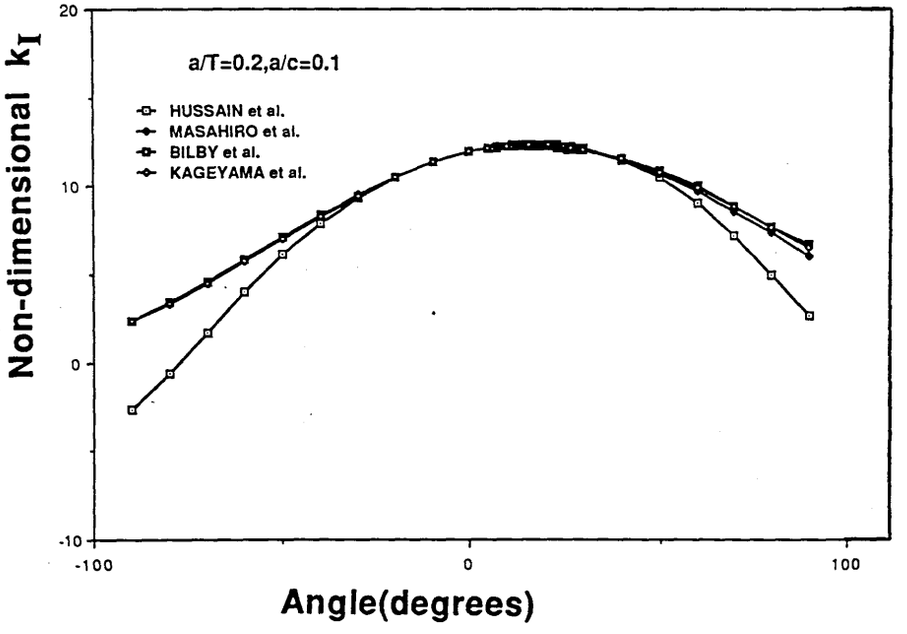

FIG.6.4 The non-dimensionalised maximum k_I ($k_I/\sigma\sqrt{a}$) for the shell model as a function of the angle, a/T=0.2, a/c=0.1

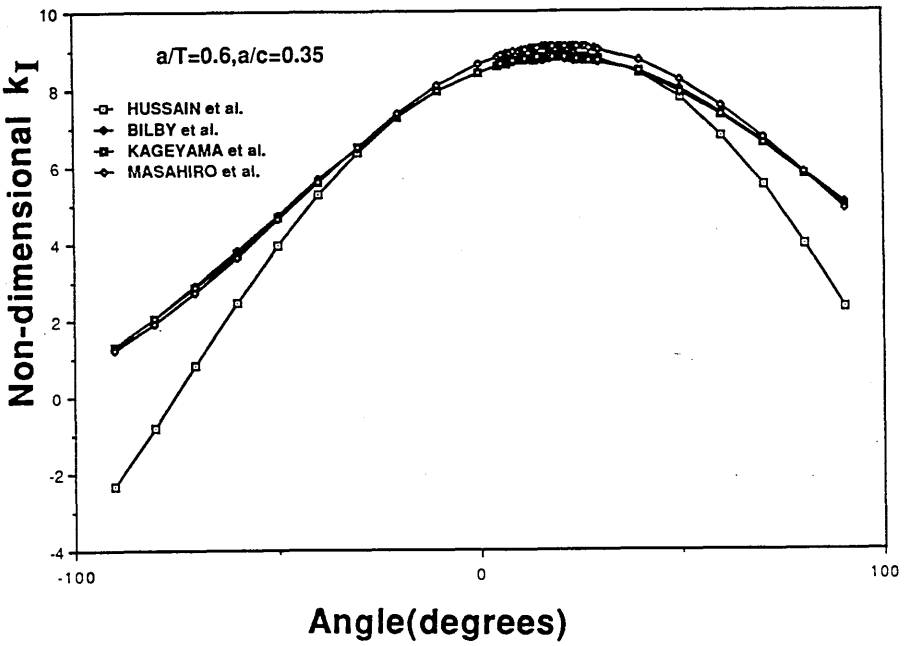

FIG.6.5 The non-dimensionalised maximum k_I ($k_I/\sigma\sqrt{a}$) for the shell model as a function of the angle, a/T=0.6, a/c=0.3

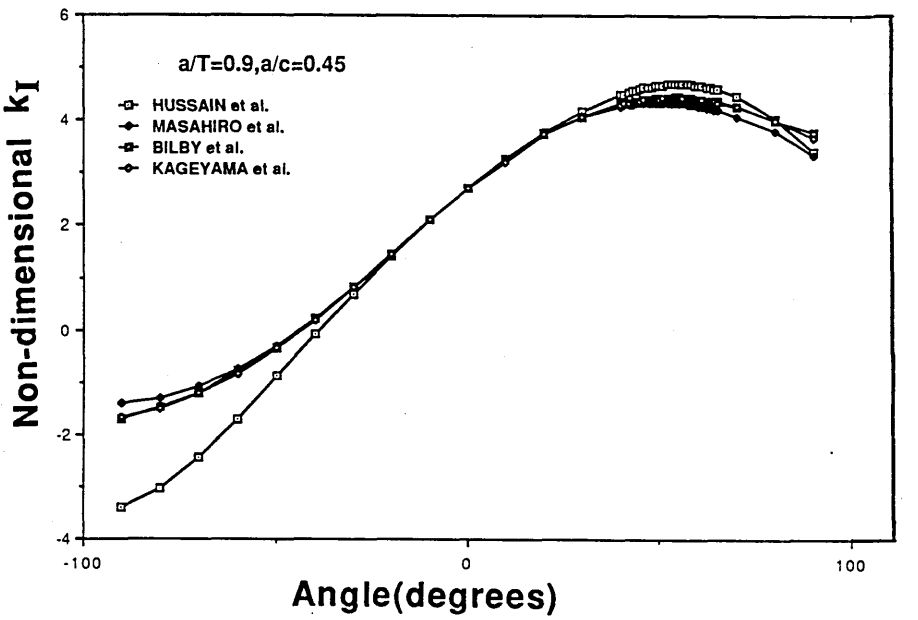

FIG.6.6 The non-dimensionalised maximum k_I ($k_I/\sigma\sqrt{a}$) for the shell model as a function of the angle, a/T=0.9, a/c=0.45

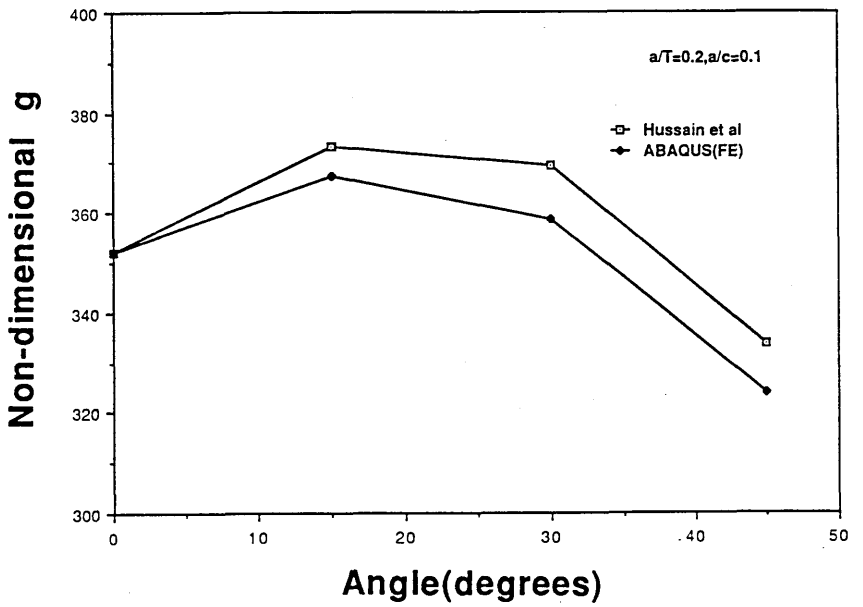

FIG.6.7 The non-dimensionalised g ($E'g/\sigma^2 a$)for the 3 dimensional bricks model as a function of the angle, a/T=0.2, a/c=0.1

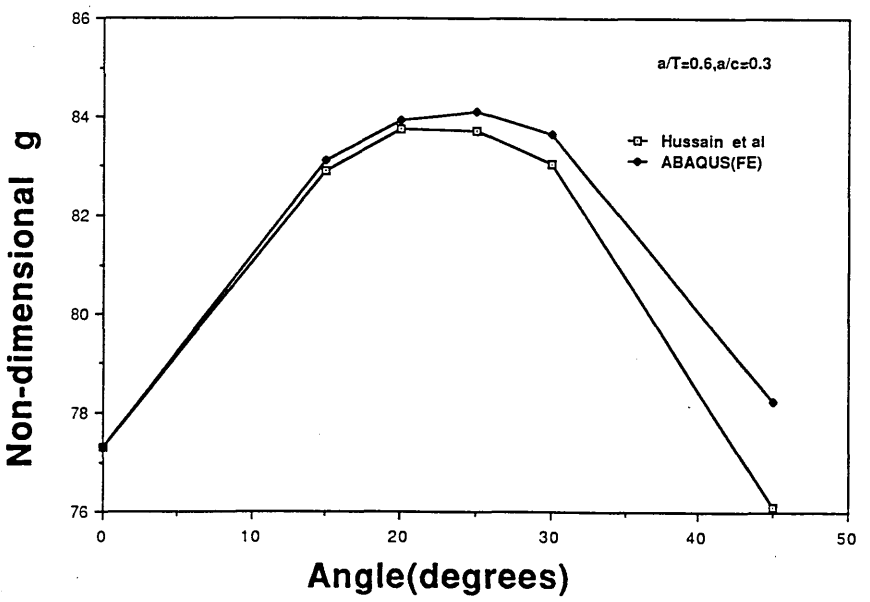

FIG.6.8 The non-dimensionalised g ($E'g/\sigma^2 a$) for the 3 dimensional bricks model as a function of the angle,a/T=0.6, a/c=0.3

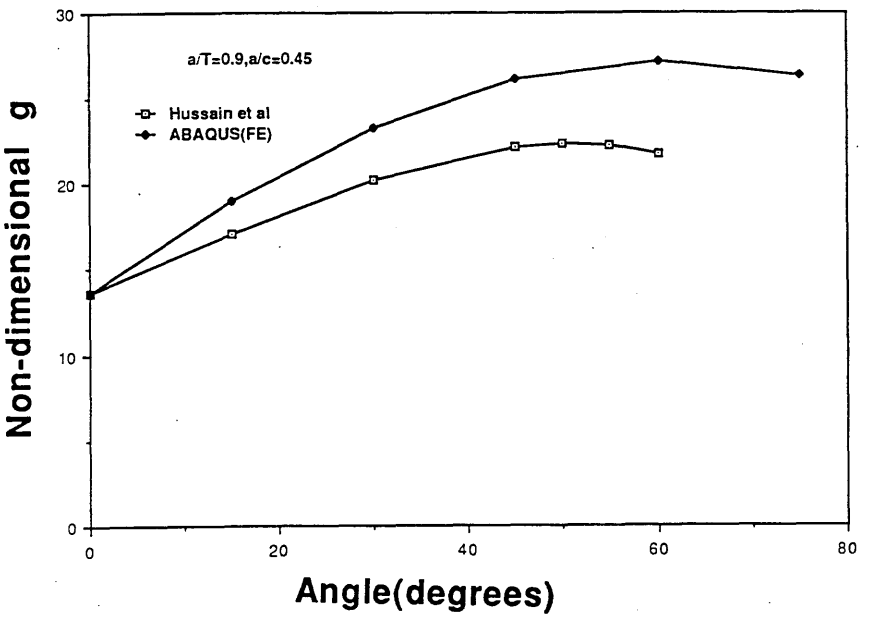

FIG.6.9 The non-dimensionalised g ($E'g/\sigma^2 a$) for the 3 dimensional bricks model as a function of the angle, a/T=0.9, a/c=0.45

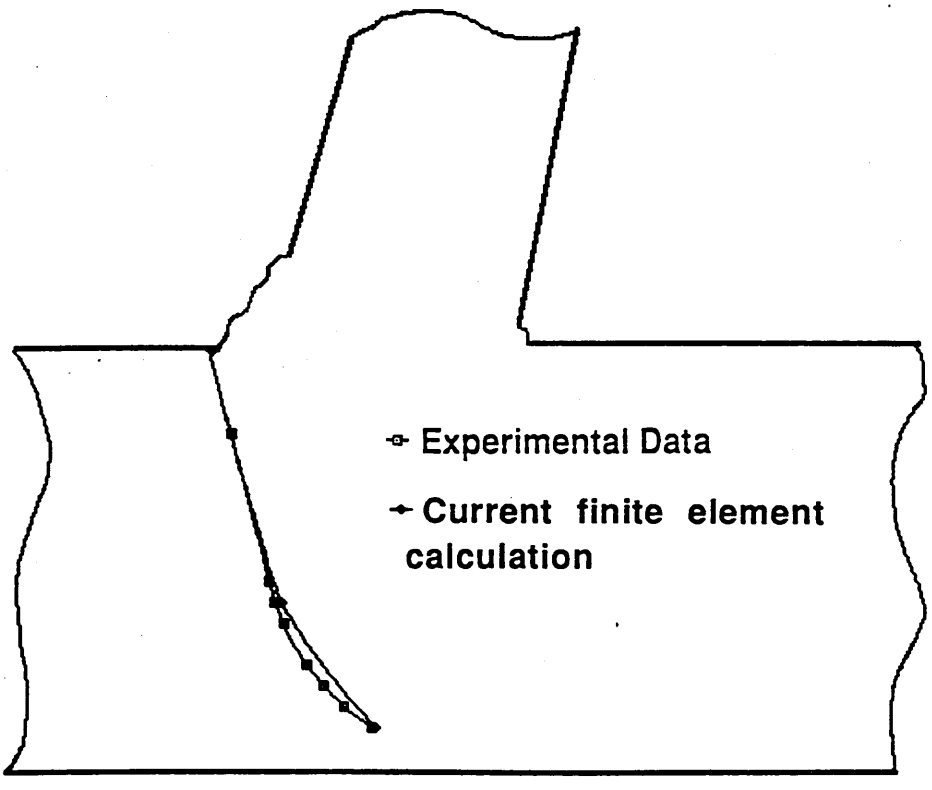

FIG.6.10 The predicted crack path and the experimental observation (52)

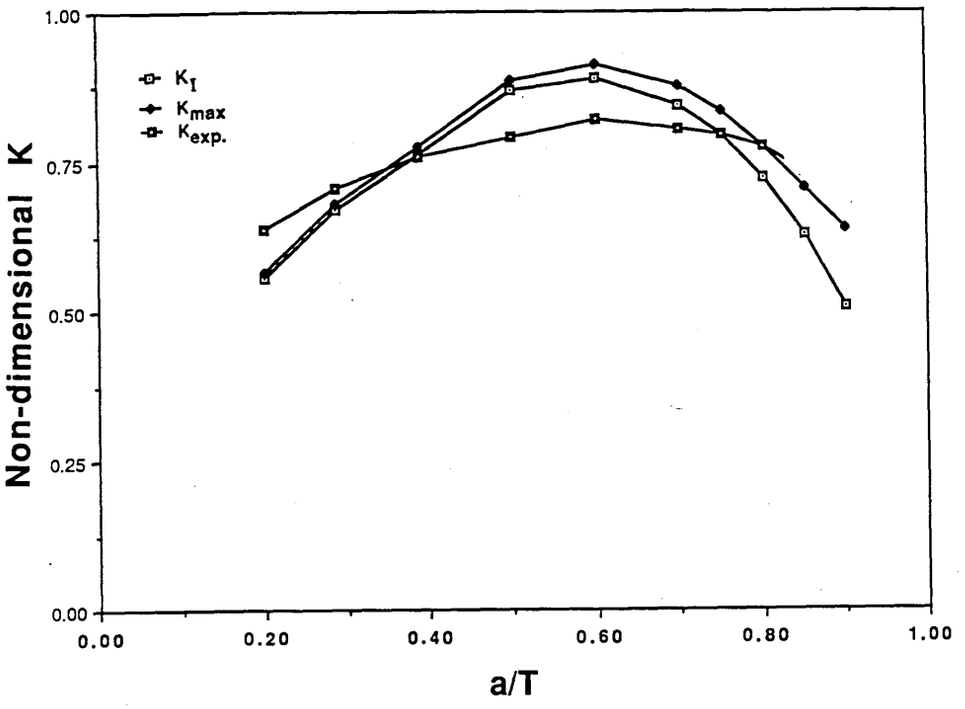

FIG.6.11 A comparison between the non-dimensionalised maximum k_I ($k/\sigma_h\sqrt{T}$) obtained numerically and the experimental data K_{exp} ($K_{exp}/\sigma_h\sqrt{T}$) for axial loading

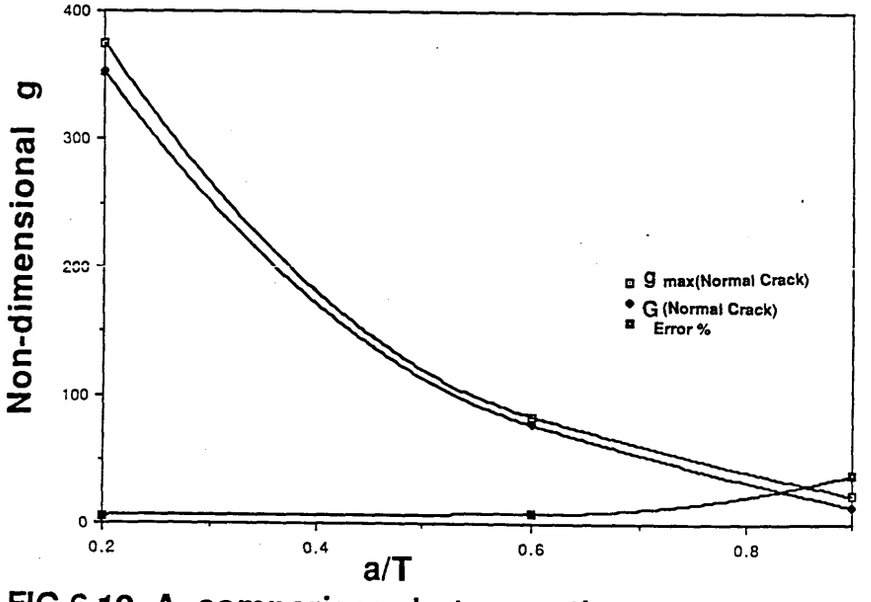

FIG.6.12 A comparison between the non-dimensionalised Maximum g, $Eg/\sigma^2(1-\upsilon^2)a$ and non-dimensionalised G, $EG/\sigma^2(1-\upsilon^2)a$ for the normal main crack

CHAPTER 7. Elastic-Plastic Stress Analysis of Semi-Elliptical Cracks in a Tubular Welded T Joint

SECTION 7.1. Introduction

In the previous Chapters the effect of semi-elliptical cracks on the structural integrity of a tubular welded joint has been considered by evaluating stress intensity factors using a finite element method which used three dimensional brick elements and a method involving elastic line springs. Although the development of cracks by fatigue can be largely understood by reference to linear elastic fracture mechanics, it is also necessary to determine the conditions under which cracks propagate under the overloads which arise in storm conditions. In order to ensure structural integrity under these conditions it is necessary to understand the elastic-plastic behaviour of tubular welded joints containing semi-elliptical defects. In this Chapter, attention is largely focussed on elastic-plastic behaviour using a finite element formulation involving twenty noded hybrid brick elements and one utilising non-linear line springs.

For simple geometries, both elastic and fully plastic solutions for the J-integral, crack opening displacement and load point displacements are readily available in data bases(11,12,79). The method for calculating J under elastic-plastic conditions is based on interpolation between yielding and elastic conditions, so that J can be written as sum of a linear elastic and a fully plastic contributions.

However such solutions are only available for simple geometries which can not be easily re-interpreted for tubular welded joints. As a result, it is necessary to determine fully plastic solutions for a broad range of configurations for which elastic solutions are already available. For the fully plastic solution, the J-integral can be expressed in the form of Eqn.

2-48 provided the loading is monotonically increasing and the crack is stationary. In this equation, f'P(a/T,n) is a function which depends only on the crack depth (a/T) and strain hardening rate (n). In general the function must be computed numerically, however, once obtained, it can be catalogued and used for similar joints, and this is the object of the present work.

Due to the fact that three dimensional finite element applications require large computer storage and running times, only a small number of fully three-dimensional elastic-plastic analyses have been performed, especially for complex geometries such as tubular joints. For the same reason the number of rings of element sets concentric with the crack tip was necessarily limited. To assess the accuracy of such solutions, preliminary bench-marking calculations were undertaken using the plane strain edge cracked bar shown in Fig.7.1 with the same crack tip element configuration and material response as the tubular welded T joint.

SECTION 7.2. The Finite Element Procedure for the Preliminary 2D Model

The finite element analyses were based on small strain flow plasticity theory and employed the Prandtl-Reuss flow rule (J_2 flow theory). If the tensile stress and strain relation behaviour is modelled by the Ramberg-Osgood relationship given in Eqn.2-42, the appropriate incremental form of J_2 flow theory is

$$d\varepsilon_{ij}/\varepsilon_y=(1+\upsilon)d\sigma_{ij}/\sigma_y-\upsilon d\sigma_{kk}/\sigma_y\delta_{ij}+3/2\ n\alpha(\sigma_e/\sigma_y)^{n-2}\sigma_{ij}/\sigma_y\ d\sigma_e/\sigma_y \qquad \text{Eqn.(7-1)}$$

Here δ_{ij} is the Kronecker delta and σ_{kk} is the trace of the stress tensor. In

the computations, Poisson's ratio was set at 0.3, and the ratio of the yield stress σ_y to the elastic modulus E was 0.001, and α was set at 3/7. Solutions were obtained numerically by employing incompressible eight noded isoparametric plane strain hybrid elements with 3 by 3 Gauss points. The J-integral was determined by the virtual crack extension method of Parks (27) as implemented in ABAQUS. The paths for J evaluation were defined along element boundaries, and only three paths enclosing the crack tip were defined. The reported value of J is that given by the second contour since experience has shown this to give high accuracy in both elastic and elastic-plastic calculations. Two finite element models were used. The first model, shown in Fig.7.2, was loaded by uniform tensile force imposed on the ends of the specimen. The second model shown in Fig.7.3 was subjected to three point bending. The ratio of the crack depth to the thickness was 0.5 for both models. Each model involved 120 elements and 430 nodes, giving a system with 1200 degrees of freedom. Both problems were analysed on a Vax11/750 with a strongly hardening material (n=3) modelled by the Ramberg-Osgood relationship. Between 20 and 50 load increments were taken to reached the limit load state, requiring approximately 15 hours cpu time.

The results are compared with formulae proposed by Kumar and co-workers (79) for tension and bending. The results agree to within 0.3% for the elastic problem, while at an applied load equal to twice the non-hardening limit load, P_0, the results agree to within 4.5% for tension. Details of the comparison are illustrated in Fig7.4 for axial loading and Fig.7.5 for three point bending, and these figures indicate the accuracy that may be expected in 3D calculations on tubular joints.

Since it has been shown acceptable results can be obtained in two dimensional problems with a relatively few elements around the crack tip,

confidence has been obtained for attempting a three dimensional problem with a similar crack tip configuration.

SECTION 7.3.The Material Model and Finite Element Procedure For the Tubular Joint

In this analysis the same material response was chosen as is documented in section 2. The material hardening parameters were chosen arbitrarily and do not necessarily represent the behaviour of a particular material. The hardening parameters which determine the character of the nonlinear portion of the curve, were however chosen to represent a high strain hardening rate n=3 and a low strain hardening rate n=13.

The crack location and shapes considered in this study were identical to the tubular welded T joint discussed in the elastic analysis of Chapter 3.

The joint was subject to uniform tension with a uniformly distributed force applied at the end of the brace, while the ends of the chord were fixed. The symmetry of this geometry allowed the problem to be reduced to one quarter. The finite element mesh used for the numerical analysis is shown in Fig.3.4. For the non-linear analyses, hybrid solid brick elements were used to model the joint, as this avoids the problem of mesh locking associated with incompressible deformation (111).

The parameters which control the processing of non-linear problems, including the load increment size, and the convergence tolerance, need to be considered very carefully. As many problems involve a history dependent response, the solution is obtained as a series of increments which the solutions are changed iteratively to satisfy the equilibrium and compatibility within each increment. The load increment is related to a time increment, in which time is interpreted by an algorithm, as the arc length along the equilibrium solution path in the load-displacement. The

time period and time increment values on the data cards serve to indicate the initial load increment as a fraction of the total magnitudes supplied on the loading cards. Minimum and maximum time increments may therefore be used. The time increment size must be kept small (in the sense that rotation and strain increments must be small) to ensure correct modelling of history dependent effects, but most commonly the choice of increment size is a matter of computational efficiency. If the increments are too large, additional iterations will be required. Newton's method has a finite radius of convergence, which means that too large an increment can prevent any solution from being obtained because the initial state is too far away from the equilibrium state that is being sought. Thus there is an algorithmic restriction on the increment size.

For most cases the automatic incrementation scheme in the program was preferred, because it selected increment sizes based on the rate of convergence observed in the iteration process at each increment and the cycle parameter of the step card. If after four iterations, the solution had not converged, the program checked the convergence rate and estimated whether or not convergence could be obtained within the maximum number of iteration allowed. If convergence was likely, iteration continued, if not, the increment size was reduced by a factor of four. If this result was smaller than the minimum specified, the run was terminated. If convergence was achieved in less than one half of the cycle parameter value in two consecutive increments, the increment size was increased by a factor of 1.5. Therefore, when the job was submitted, the maximum CPU time, time increment size and the specified cycle parameter must be chosen carefully. If too few load increments are used, the solution may converge to an incorrect result. In the extreme case of only one load increment, the computation will resemble a deformation theory as opposed

to the incremental theory.

When the applied load is increased during an elastic-plastic analysis, the extent of plastic deformation increases rapidly as plastic collapse of the structure is approached. In the numerical solutions, convergence becomes more difficult to achieve; requiring more iterations and CPU time. In the present work the tolerance was chosen to be less than 10% of the nodal loads acting on the brace.

For incremental theory the path independence of the J integral is lost, as J is not exactly equal to the true potential energy release rate. However in practice it is found that J remains sensibly constant over a range of contours, and as long as the discrepancies are within the engineering tolerance, it has a role to play in design analysis. For elastic-plastic problems, the strain energy is defined as the actual elastic strain energy plus the plastic dissipation, so that the equivalent hypo-elastic material is considered.

Section 7.4. Results for the Three Dimensional Brick Element Model

This problems were run on a Cyber 205 computer in the University of Manchester Region Computer Centre (U.M.R.C.C.). Formulations using brick elements required about 2000 seconds for a step of 3 increments when P was less than $0.2P_0$. The limit load, P_0, was simply defined as the yield stress times the cross section area of the brace. Full plasticity of the uncracked ligament was typically achieved in 50 increments each of which used about 4 iterations using Newton's method to obtain equilibrium with a Jacobian formed from the elastic-plastic tangent stiffness and requiring a total cpu time of the order of 40,000 seconds.

Under elastic-plastic conditions attention was focused on the deepest point of the crack where the development of J with applied load is given in Fig.7.6. This figure also gives a comparison between the elastic material, the strongly strain hardening material (n=3) and the lightly strain hardening material (n=13) for a/T=0.9. Fig.7.7 gives the corresponding results for a/T=0.6 and Fig.7.8 for a/T=0.2. The J values are presented in a non-dimensional form in which J is non-dimensionalised with respect to the yield stress σ_y and the maximum crack depth a. The relations between force and the load point displacement are shown in Fig.7.9 for the elastic material, the strongly strain hardening material (n=3) and lightly strain hardening material (n=13) for a/T=0.9. The corresponding results for a/T=0.6 are given in Fig.7.10 and Fig.7.11 for a/T=0.2.

Section 7.5. Nonlinear Line-Spring Calculations

7.5.1 Finite Element Model

In addition to the brick element model, a shell element model in which the crack was represented by non-linear line springs was also analysed. The same model was initially used to calculate the stress intensity factors along the crack front for a semi-elliptical cracks under linear-elastic conditions. Reasonable agreement was obtained with brick element models. Detailed comparisons have been given in Chapter 3 and (112). In the present work, attention was focussed on determining J values at the deepest point of the semi-elliptical cracks using a non-linear line spring approach.

The theory for combining the elastic stiffness with the description of a non-hardening yield surface to obtain the elastic-plastic modulus implemented in ABAQUS has been given by Parks and co-workers (85). The elastic local tangent compliance was obtained by referring to a single plane strain edge crack bar. The effect of local plasticity was accounted for by

using Irwin's correction (9), while the plastic tangent compliance was obtained by considering the numerical solution obtained by Shih and Hutchinson (114) for a plane strain half space containing a semi-infinite crack. Consequently, when the springs were distributed across a through crack in a structure, the resulting equations could be solved for the kinematic fields $\delta(X)$ and $\theta(X)$ in the spring elements. These lead to the determination of the generalised forces N(x), M(x) along the cut, allowing the line spring provide a estimate of the stress intensity as well as the local value of J.

In the present work, non-linear line springs have been applied to represent a semi-elliptical crack in a tubular joint. Due to symmetry, one quarter of the body needed to be modelled as shown in Fig.3.4. A total of 210 eight noded doubled curved shell element were used, thus giving the system 4000 degrees of freedom. Due to the non-linear behaviour of the material of the shell, the number of integration points used to calculate stresses in the shell section was increased to five, which is adequate for routine non-linear applications.

The T-joint was subjected to a uniformly distributed force at the end of the brace, while the ends of the chord were fixed. Three different crack depths were considered: a/T=0.2, 0.6 and 0.9 while the crack length was fixed. Three six noded line spring elements were used to model the surface crack. In carrying out these computations, the parameters in the Ramberg-Osgood relation were assigned the same values as for the brick element model, and the equilibrium tolerance value was set again to be less than 10% of the applied nodal forces on the brace.

7.5.2 Results

The problems were implemented using the finite element code, ABAQUS (4.7) mounted on a Vax11/750 computer. Typical solution times for each iteration were of the order of 30 mins. When the behaviour was largely elastic, convergence solution was obtained in one global iteration. When the material was largely plastic, 3-4 global iterations per increment were needed. The total solution time for a problem to achieve full plasticity was approximately 60 hrs.

It should be noted that the J value given by the non-linear line springs only takes account of the mode I response and is the sum of K_I^2/E and J_I^p, in order to compare with J value obtained using virtual crack extension method, the elastic mode II components $J_{II}^{el}=K_{II}^2/E$ were added to the result: the J_{III} components being zero at the deepest point of the crack. The results were plotted as a function of the applied load normalized with respect to the limit load P_0 defined, in Fig.7.12, Fig.7.13 and Fig.7.14 for a/T=0.2,a/T=0.6 and a/T=0.9 with n=3 and Fig.7.15, and Fig.7.16 for a/T=0.6 and a/T=0.9 for n=13. In addition , the relationship between applied force and the load point displacement obtained using both line spring method and virtual crack extension are given in Fig.7.17, Fig.7.18 and Fig.7.19 for a/T=0.2, a/T=0.6 and a/T=0.9 with n=3 while the corresponding data for a/T=0.6 and a/T=0.9 with n=13 are given in Fig.7.20 and Fig.7.21.

Section 7.6 Discussion

When the applied load is less than 20% of the plastic collapse load P_0, the J value for the 3-D elastic predictions is identical to the elastic-plastic analyses as plastic flow of the material around the crack front is so small

that an elastic analysis is adequate. As the applied load increases, the 3-D elastic prediction deviates from the elastic-plastic prediction and becomes non-conservative. Moreover it was found that the J value for elastic-plastic analysis for the lightly hardening material was higher than that for elastic-plastic analysis of a strongly strain hardening material at the same load. It is also clear that the force is no longer proportional to the displacement and becomes increasingly non-linear when the applied force is greater than $0.2P_0$, due to large plastic deformation in the ligament. It is also clear that plots of J versus applied load become nearly vertical for the low-hardening material in full plasticity , so that a small change in applied load manifests itself as a large change in J .

Under axial loading, an uncracked tubular joint under axial loading has been studied by Rhee(115,116) who found the ratio of the bending stress to the tension stress was about 3. For the cracked geometries, the ratio of M/Fb on the ligament as a function of crack length (a/T) is easily determined using line spring method and is given in Fig.7.22. The values of M/Fb varied between 0.5 and 9, and the cracked ligament is predominantly subject to bending. Under these conditions the criterion for J dominance is that the ligament must be greater than $20\sim50J/\sigma_y$ (76) for deep cracks.

Under elastic-plastic conditions, with a constant applied load, the applied tearing modulus $(dJ/da)E/\sigma_y^2$ is also negative implying that an increasing load history is required to maintain elastic-plastic growth at the deepest point, for cracks of depth greater than (a/T=0.6). As the crack develops in the through thickness direction the loads to produce a given remote displacement are similar for both a/T=0.6 and a/T=0.9 under elastic-plastic conditions. This parallels the elastic observation (51) that the stiffness of the joint is maintained until the crack penetrates the chord wall. Constant remote loading and displacement conditions thus produce similar results, and the applied tearing modulus will be negative for both cases favouring

stable crack growth in the through thickness direction.

The key to the engineering approach for the tubular joint is to tabulate the fully plastic solutions. Following to Goldman and Hutchinson(82). J can be considered as the sum of a plastic contribution J^p, and an elastic contribution $J^{el}(a_e)$, calculated with an effective crack length a_e.

$$J^p=J-J^{el}(a_e) \qquad \text{Eqn.(7-2)}$$

The solution for $J^{el}(a)$ is available for a/T=0.2, 0.6 and 0.9 (n=1,3 and 13), the remaining problem is to obtain $J^{el}(a_e)$. K is given by $\sqrt{EJ^{el}/(1-\upsilon^2)}$, and the effective crack length is defined as

$$a_e=a+\phi(n-1)/6\pi(n+1)(K/\sigma_0)^2 \qquad \text{Eqn.(7-3)}$$

where $\phi=1/1+(P/P_0)^2$

If $J^{el}(a_e)$ is defined to have the form $f(a_e/T)P^2/TE'$, then $f(a_e/T)$ is given in Fig.3.17.

Combining Equations (7.2 and 7.3), $f^{p'}(a/T,n)$ defined in Eqn.(2-48) can be obtained as illustrated in Table7.1

The agreement between the line spring and continuum solutions is good. For the deepest crack geometry, the difference between J for the line spring solution and 3D brick element solution is less than 12% up to the load at which J dominance is lost, that is $C\sigma_y/J=50$ for n=3 and within 7% for n=13. Furthermore the agreement between load point displacements for the two cases is also acceptable. Typically, the difference is 5% for n=3 and 3% for n=13.

For the intermediate crack geometry a/T=0.6 and a/c=0.3, the difference

between J obtained from the line spring and 3D solutions is within 18% for n=3 and 12% for n=13, again the load point displacement between 3D calculation and line spring solution agree to within 10% for n=3 and 6% for n=13. The agreement between line spring method and the solution using 3D brick elements indicates the line spring gives reasonably accurate estimates of J and load the point displacement for deep cracks.

The discrepancy between the brick element and line spring solutions may arise from three sources. Firstly, the shell model can not cope with a local stress concentration which arise over distance less than the shell thickness. Secondly, the non-linear response only incorporates the mode I response, and for deep cracks the mode I and mode II component have a similar magnitudes. The third reason is that the plastic compliance formulation of the line spring adopts the deep crack solution instead of using the full plastic solution for the single edge notched bars of a finite width and this can cause problems for short cracks. Detailed comparison by Nakamura et al. (113) found that the accuracy of the solution increased with increased a/T and with increased strain hardening exponent n in accord with the recent results..

Section 7.6 Conclusion

Line spring calculations give reasonable accurate estimates of J and other fracture parameters for deep cracks and low hardening rate. The virtue of the line spring method comes from its simplicity as well as the saving in computing time which are typically 7-10 times less than the corresponding 3D brick element solution which can only be run with a very limited number of elements.

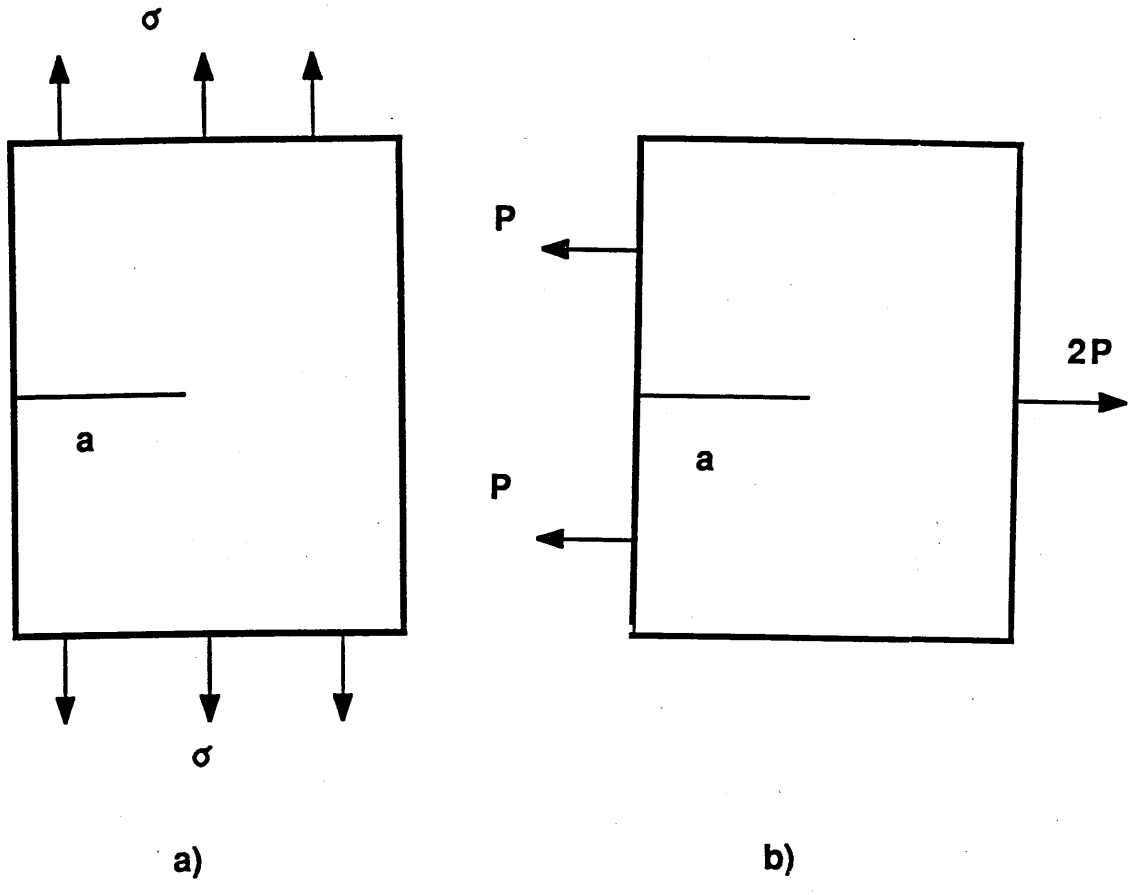

FIG.7.1 The geometry of a edge cracked bar

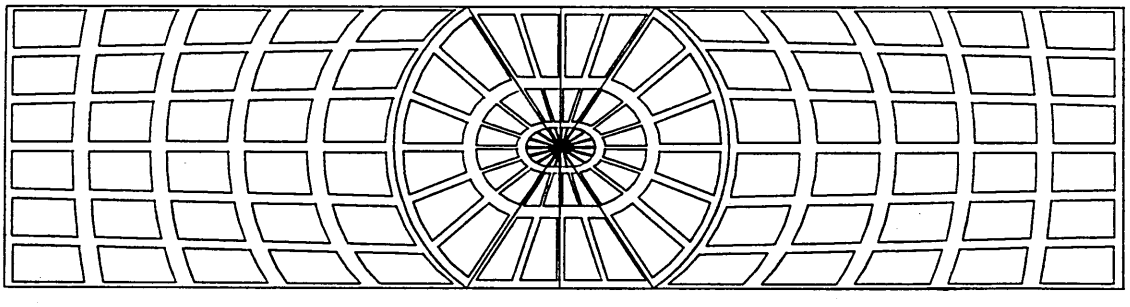

FIG.7.2 The mesh of a single edge cracked bar loaded by force

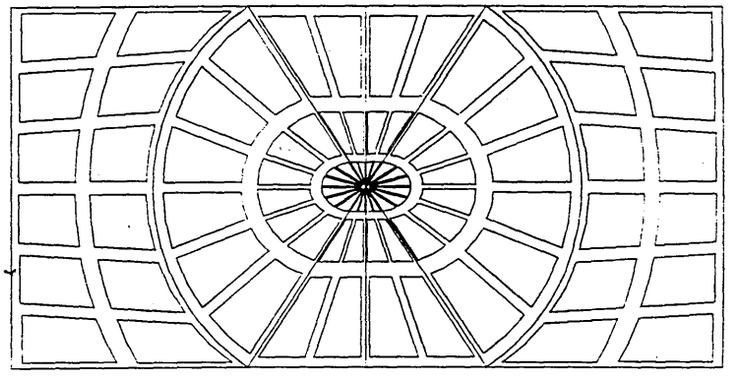

FIG.7.3 The mesh of a single edge cracked bar under three point bending

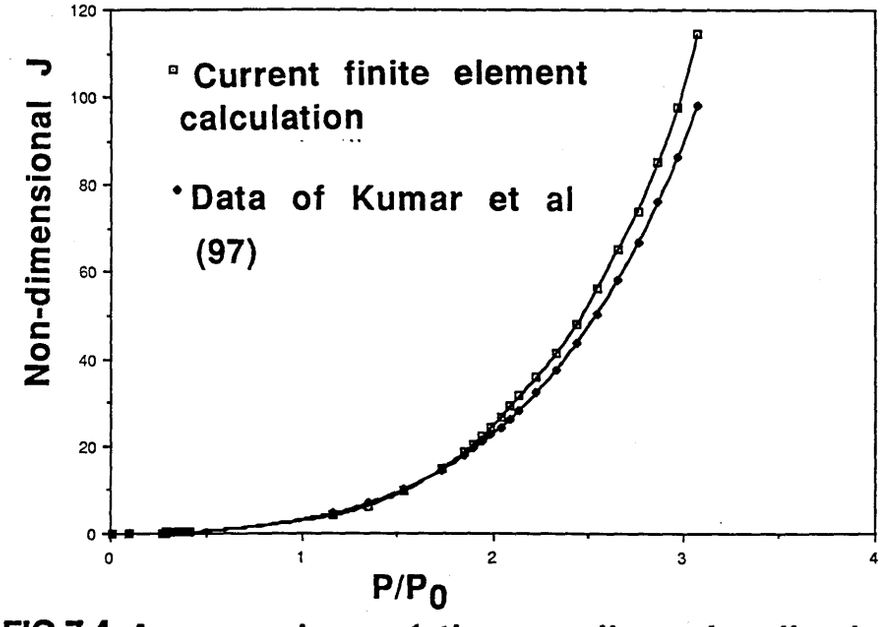

FIG.7.4 A comparison of the non-dimensionalised $J=E'J/\sigma^2 a$ for the present finite element calculation and the data of Kumar et al. (79) for a bar under axial loading

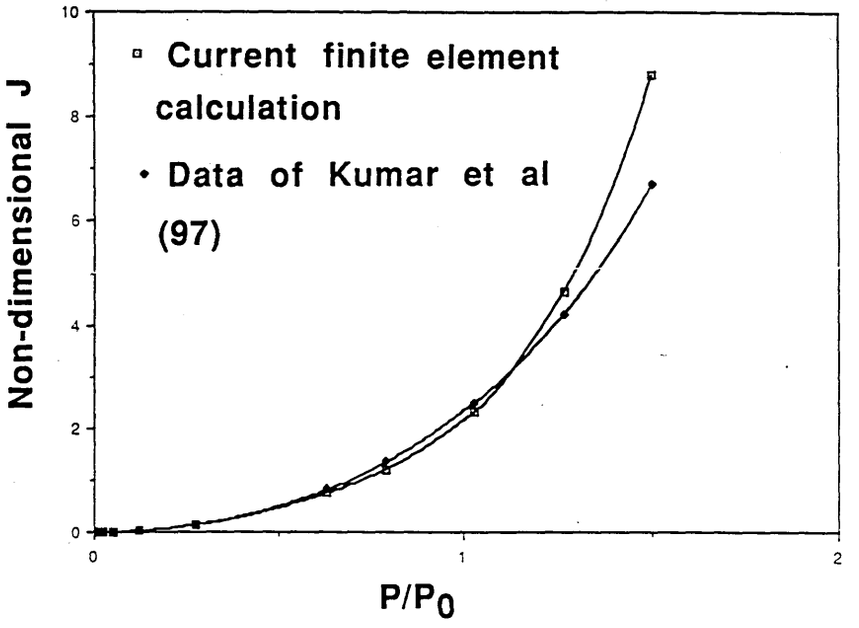

FIG.7.5 A comparison of the non-dimensionalised $J=E'J/\sigma^2 a$ for the present finite element calculation and the data of Kumar et al. (79) for a bar under three point bending

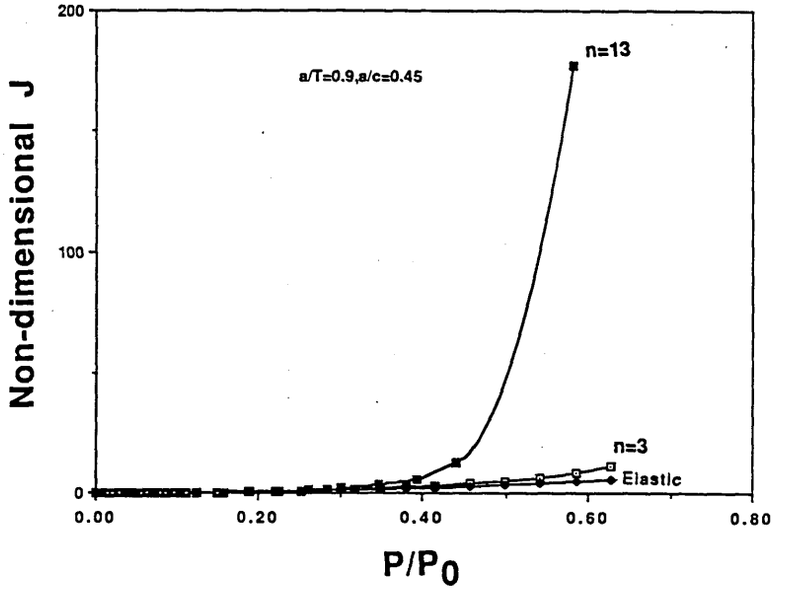

FIG.7.6 A comparison of the non-dimensionalised $J=E'J/\sigma_y^2 a$ at the deepest point of a semi-elliptical crack in a tubular T-joint under axial loading for the elastic material,the strain hardening material and the light strain hardening material when a/T=0.9,a/c=0.45

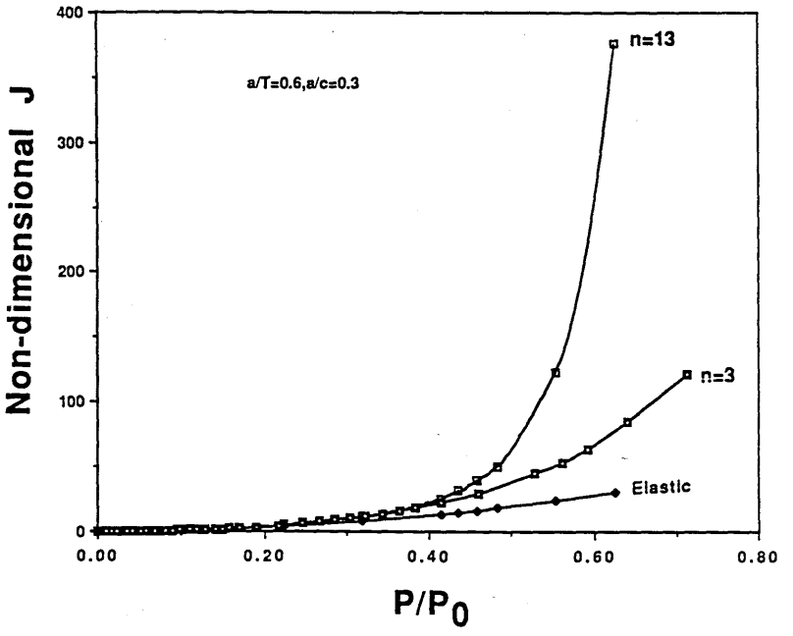

FIG.7.7 A comparison of the non-dimensionalised $J=E'J/\sigma_y{}^2a$ at the deepest point of a semi-elliptical crack in a tubular T-joint under axial loading for the elastic material,the strain hardening material and the light strain hardening material when a/T=0.6, a/c=0.3

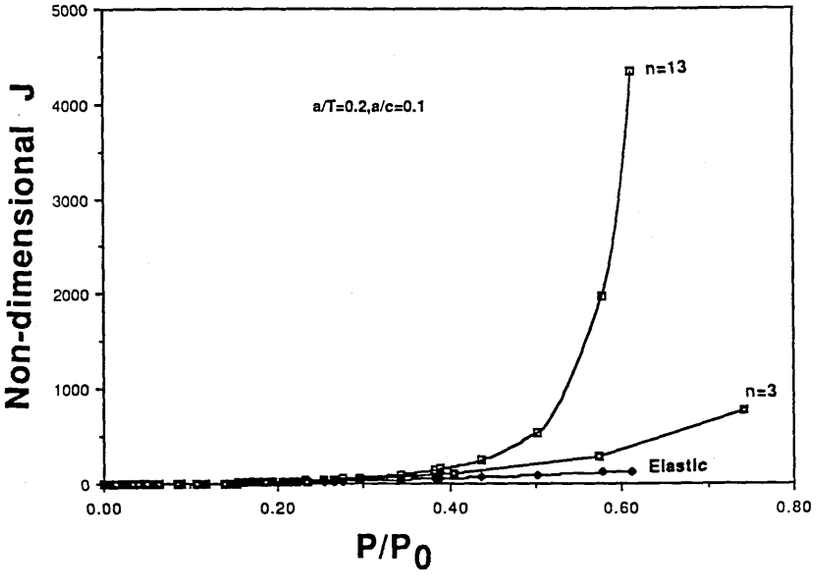

FIG.7.8 A comparison of the non-dimensionalised $J=E'J/\sigma_y{}^2a$ at the deepest point of a semi-elliptical crack in a tubular T-joint under axial loading for the elastic material,the strain hardening material and the light strain hardening material when a/T=0.2,a/c=0.1

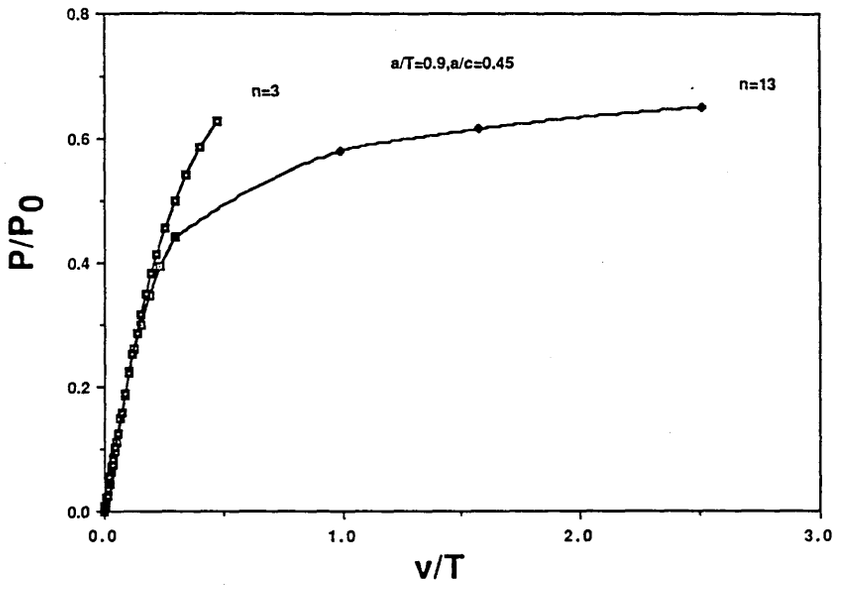

FIG.7.9 The relationship between the non-dimensionalised applied force $P/\sigma_y A$, and the non-dimensionalise load point displacement v/T, where A is the section area of the brace and T is the thickness of the chord when n=3 and n=13 for a/T=0.9 a/c=0.45

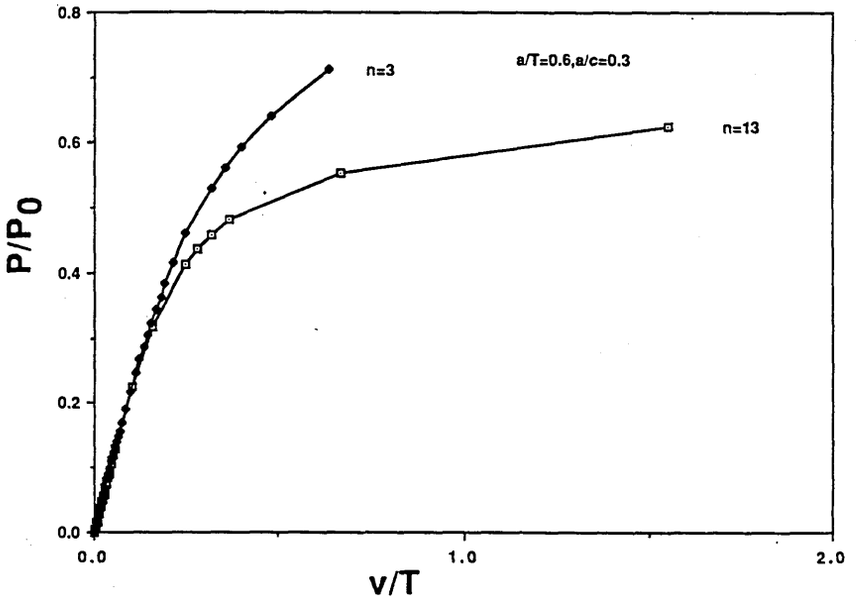

FIG.7.10 The relationship between the non-dimensionalised applied force $P/\sigma_y A$, and the non-dimensionalised load point displacement v/T, where A is the section area of the brace and T is the thickness of the chord when n=3 and n=13 for a/T=0.6 a/c=0.3

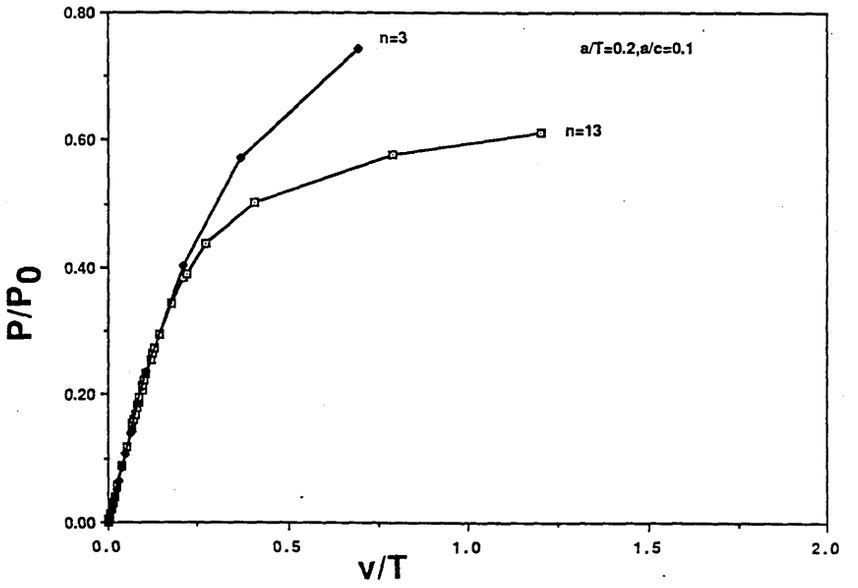

FIG.7.11 The relationship between the non-dimensionalised applied force $P/\sigma_y A$, and the non-dimensionalised load point displacement v/T, where A is the section area of the brace and T is the thickness of the chord when n=3 and n=13 for a/T=0.2 a/c=0.1

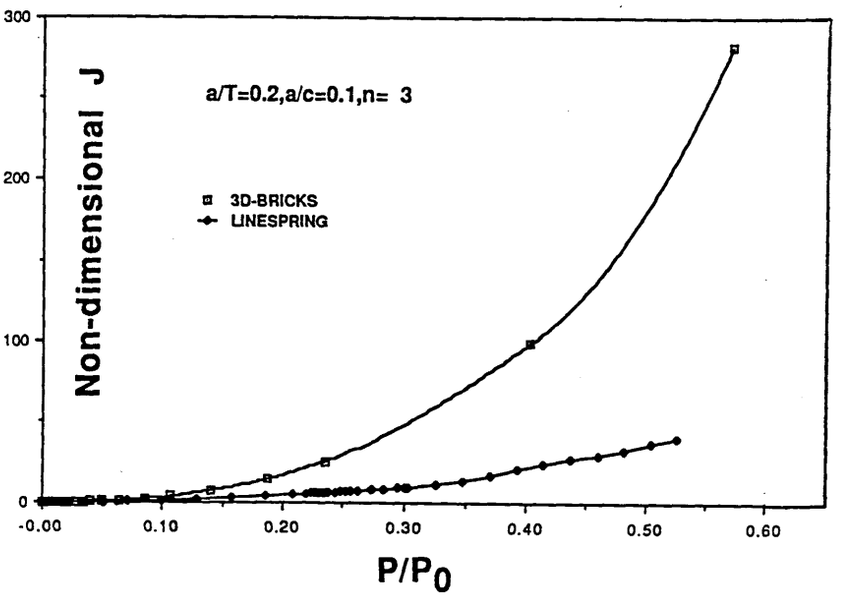

FIG.7.12 A comparison of the non-dimensionalised $J=E'J/\sigma_y{}^2a$ at the deepest point obtained both from line spring solution and three dimensional brick element for a/T=0.2,a/c=0.1,n=3

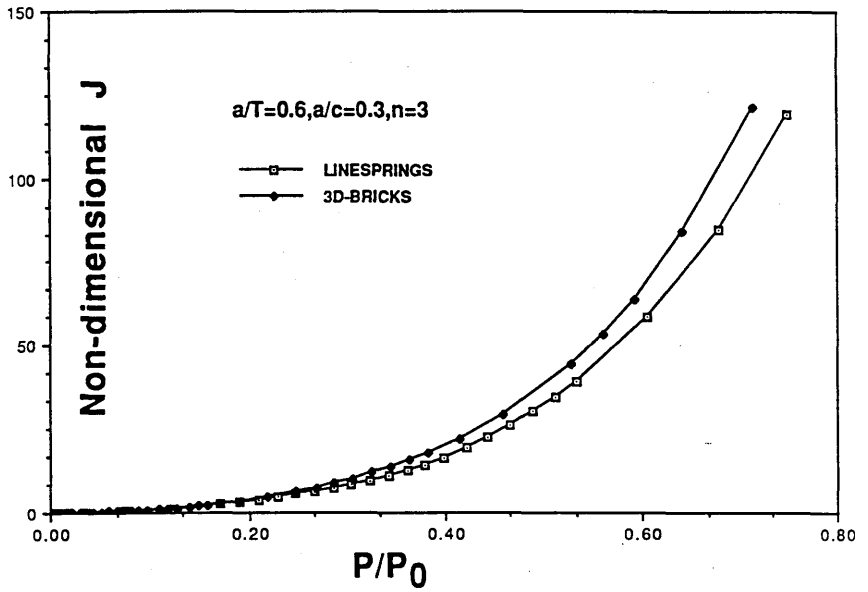

FIG.7.13 A comparison of the non-dimensionalised $J=E'J/\sigma_y{}^2a$ at the deepest point obtained both from line spring solution and three dimensional brick element for a/T=0.6,a/c=0.3,n=3

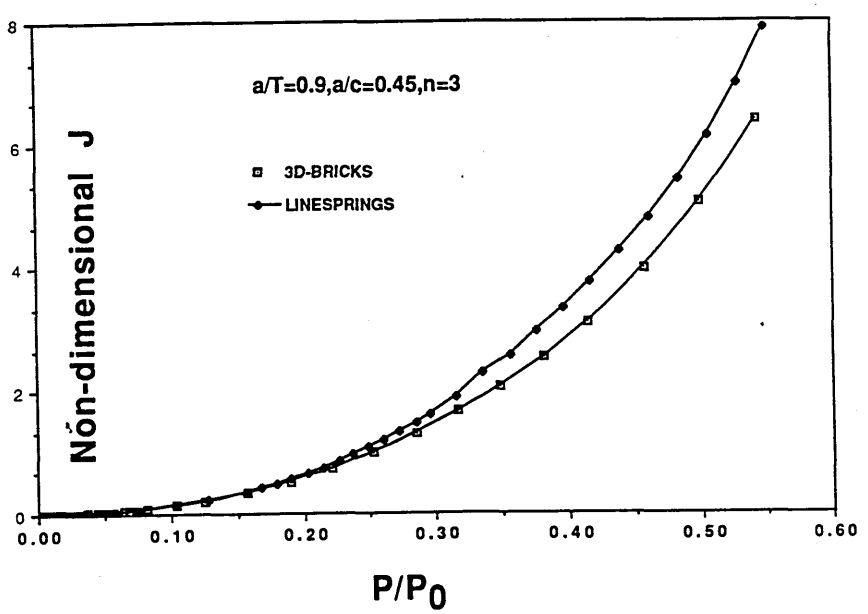

FIG.7.14 A comparison of the non-dimensionalised $J=E'J/\sigma_y{}^2a$ at the deepest point obtained both from line spring solution and three dimensional brick element for a/T=0.9,a/c=0.45,n=3

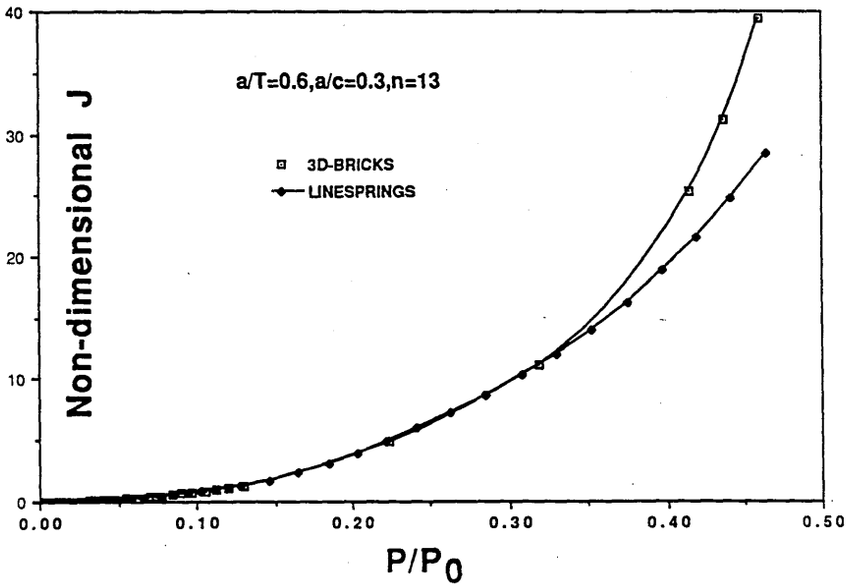

FIG.7.15 A comparison of the non-dimensionalised $J=E'J/\sigma_y{}^2a$ at the deepest point obtained both from line spring solution and three dimensional brick element for a/T=0.6,a/c=0.3, n=13

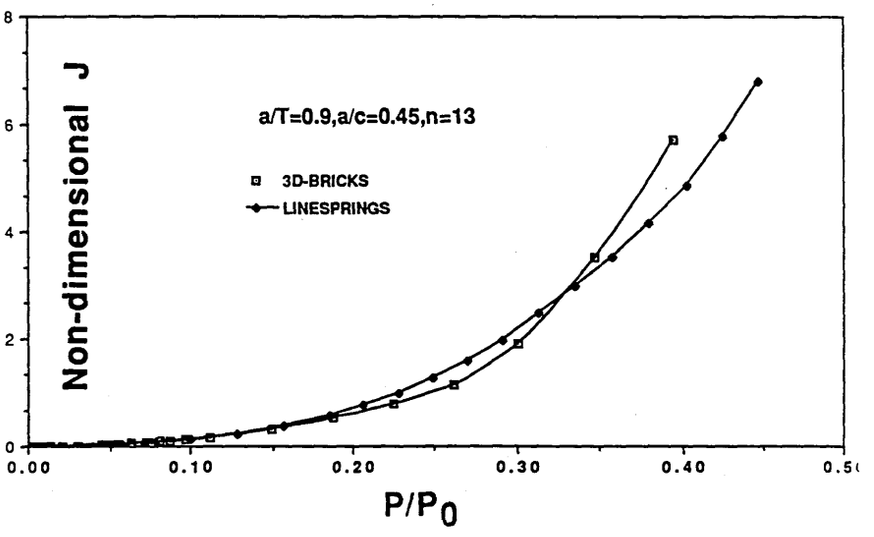

FIG.7.16 A comparison of the non-dimensionalised $J=E'J/\sigma_y{}^2a$ at the deepest point obtained both from line spring solution and three dimensional brick element for a/T=0.9,a/c=0.45,n=13

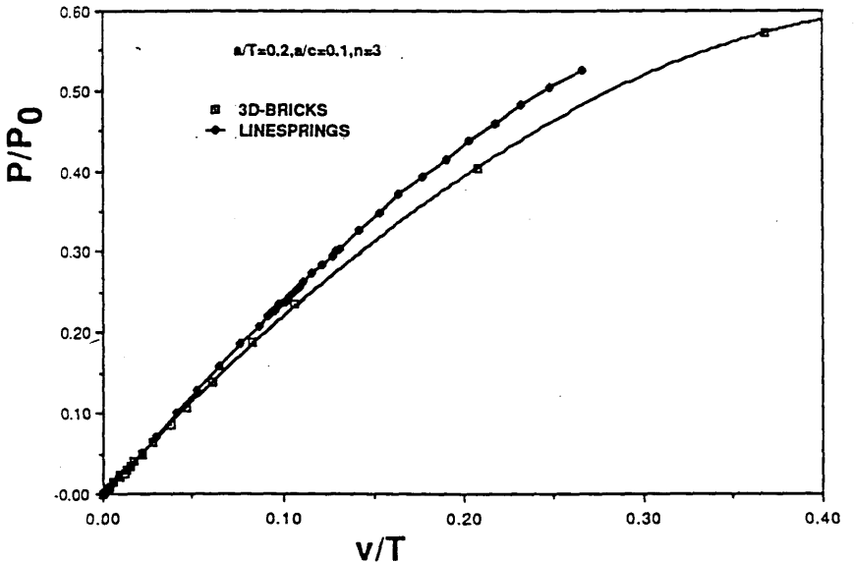

FIG.7.17 A comparison of the non-dimensionalised load point displacement v/T obtained both from shell analysis and three dimensional brick element for a/T=0.2,a/c=0.1,n=3

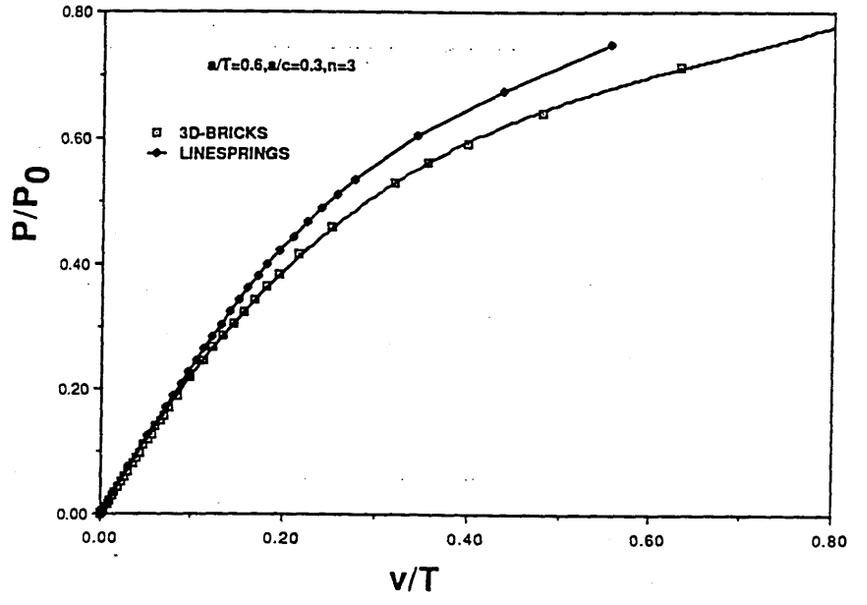

FIG.7.18 A comparison of the non-dimensionalised load point displacement v/T obtained both from shell analysis and three dimensional brick element for a/T=0.6,a/c=0.3,n=3

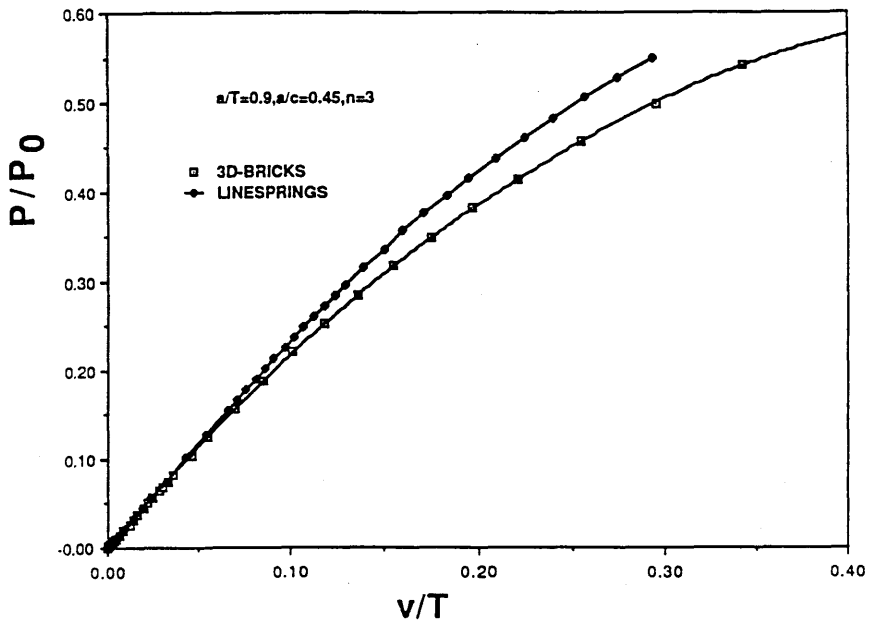

FIG.7.19 A comparison of the non-dimensionalised load point displacement v/T obtained both from shell analysis and three dimensional brick element for a/T=0.9,a/c=0.45,n=3

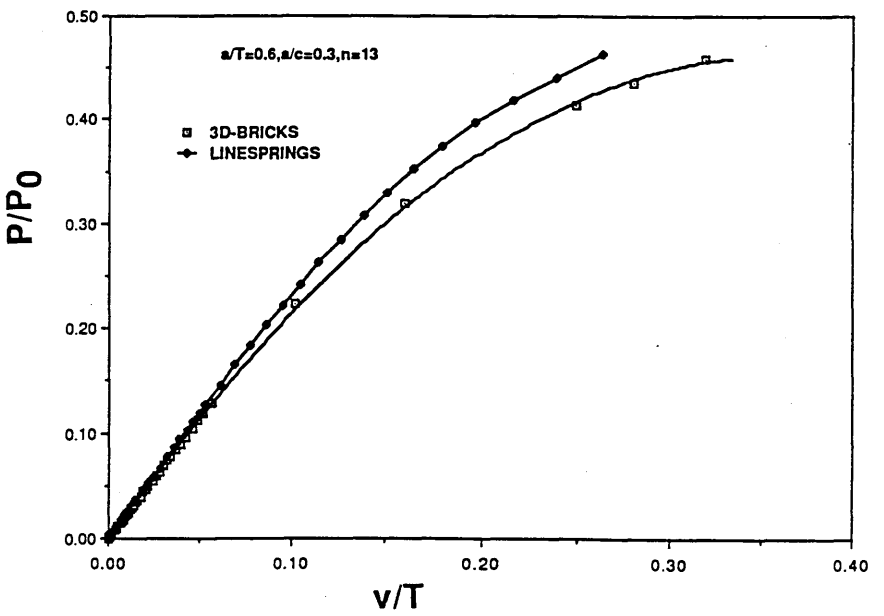

FIG.7.20 A comparison of the non-dimensionalised load point displacement v/T obtained both from shell analysis and three dimensional brick element for a/T=0.6,a/c=0.3,n=13

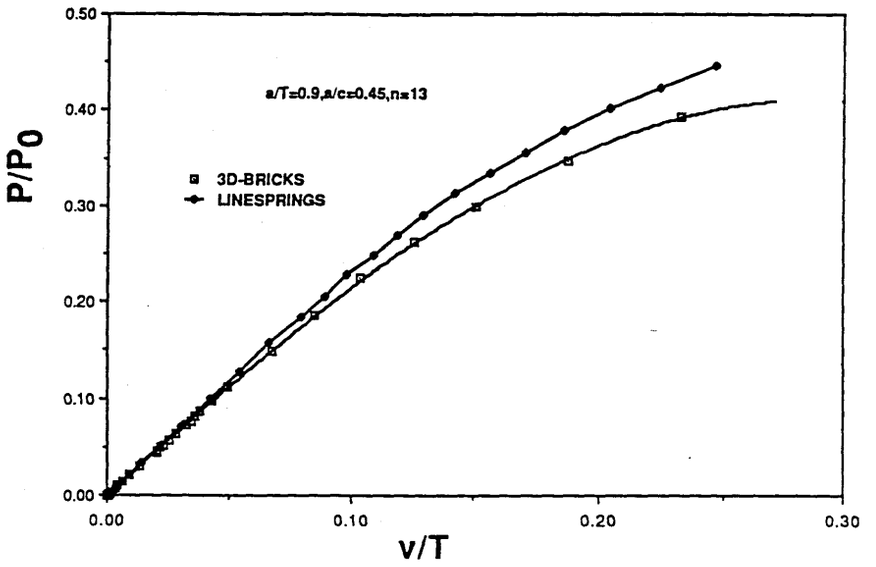

FIG.7.21 A comparison of the non-dimensionalised load point displacement v/T obtained both from shell analysis and three dimensional brick element for a/T=0.9,a/c=0.45,n=13

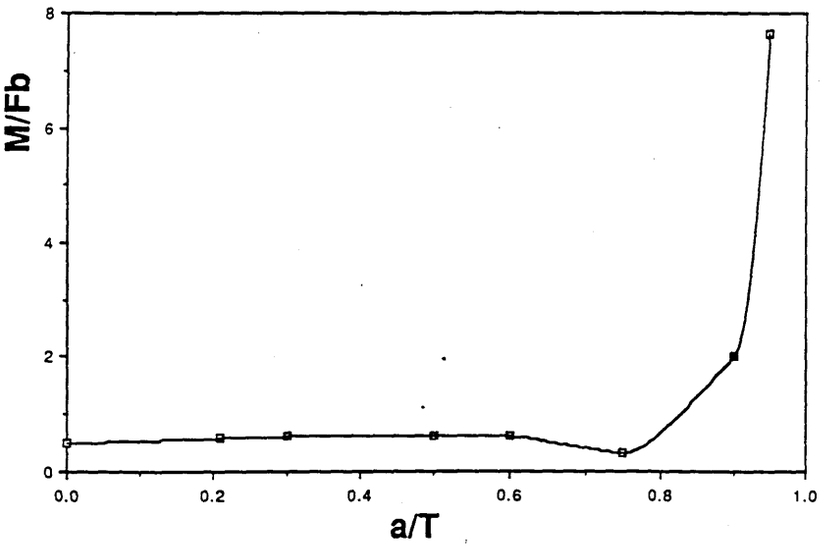

FIG.7.22 The ratio of bending moment to force times the ligament length as a function of a/T

	a/T=0.2	a/T=0.6	a/T=0.9
n=1	320	70.3	12.4
n=3	4522	1080	138
n=13	11.7 E6	3.8E6	8.86E5

Table 7.1 A dimensionless quantity $f^{p'}=J^{p}/\alpha\sigma_y\varepsilon_y a(P/P0)^{n+1}$ as a function of a/T and n

Chapter 8 Singular Behaviour in Mixed-Mode Plane Strain Crack Problems

Section 8.1 Introduction

Asymptotic solutions to plane strain crack problems in which the stress distribution is either symmetric (Mode I) or anti-symmetric (Mode II) with respect to the crack plane have been presented by Hutchinson (60) and Rice and Rosengen (61). The near tip field is dominated by an HRR singularity field characterised by the path independent line integral given by Rice (57), if minimum size requirements as discussed by Shih et al.(76) are met.

For mixed-mode elastic problems which combine mode I and mode II, the singularity can be expressed as a linear combination of mode I and mode II singularities following Westergaard (8). Thus the asymptotic elastic mixed mode solution is of the form

$$\sigma_r=\frac{K_I}{\sqrt{2\pi r}}\left(\frac{5}{4}\cos(\theta/2)-\frac{1}{4}\cos(1.5\theta)\right)+\frac{K_{II}}{\sqrt{2\pi r}}\left(-\frac{5}{4}\sin(\theta/2)+\frac{3}{4}\sin(1.5\theta)\right)$$

Eqn.(8-1)

$$\sigma_\theta=\frac{K_I}{\sqrt{2\pi r}}\left(\frac{3}{4}\cos(\theta/2)+\frac{1}{4}\cos(1.5\theta)\right)+\frac{K_{II}}{\sqrt{2\pi r}}\left(-\frac{3}{4}\sin(\theta/2)-\frac{3}{4}\sin(\theta/2)\right)$$

Eqn.(8-2)

$$\tau_{r\theta}=\frac{K_I}{\sqrt{2\pi r}}\left(\frac{1}{4}\sin(\theta/2)+\frac{1}{4}\sin(1.5\theta)\right)+\frac{K_I}{\sqrt{2\pi r}}\left(\frac{1}{4}\cos(\theta/2)+\frac{3}{4}\cos(1.5\theta)\right)$$

Eqn.(8-3)

where r and θ are the polar coordinates of a point ahead of the crack tip. However, it is convenient to use other parameters, (k_{Imax}), and the angle between the original crack plane and the direction in which k_I is maximum to characterise the stress field ahead of the crack tip. The relation between the off axis maximum stress intensity factor and the maximum strain energy release rate is given by

$$k_{Imax}=\sqrt{E'g_{max}} \qquad \text{Eqn.(8-4)}$$

Suppose that a straight crack, denoted A0 in Fig.8.1, subject to a combined mode I and II (denoted K_I and K_{II}), extends in a non-planar fashion along a plane inclined to the original crack plane by an arbitrary angle, θ. If k_I and k_{II} are the stress intensity factors at the tip 0 of the straight crack defined in the manner as shown in Fig.8.1, using the formulation given by Masahiro et al. (107), which is equivalent to the maximum tensile stress theory, one has

$$k_I=0.5\text{Cos}(\theta/2)[K_I(1+\text{Cos}\theta)-3K_{II}\text{Sin}\theta]$$

$$k_{II}=0.5\text{Cos}(\theta/2)[K_I\text{Sin}\theta+K_{II}(3\text{Cos}\theta-1)] \qquad \text{Eqn.(8-5)}$$

If the angle between the original crack plane and the crack growth direction at which k_I is maximum and k_{II} is zero, is denoted α, one obtains from eqn(8-5);

$$k_{Imax}=0.5\text{Cos}\alpha[K_I(1+\text{Cos}\alpha)-3K_{II}\text{Sin}\alpha]$$

$$0=0.5\text{Cos}\alpha/2[K_I\text{Sin}\alpha+K_{II}(3\text{Cos}\alpha-1)] \qquad \text{Eqn.(8-6)}$$

using k_{Imax} and α to represent K_I and K_{II}, one has

$$K_I = \frac{-(1-3\cos\alpha)2\sin(\alpha/2)}{(1+\cos\alpha)\sin\alpha} k_{I\,max}$$

and

$$K_{II} = \frac{-2\sin\alpha/2}{1+\cos\alpha} k_{I\,max} \qquad \text{Eqn.(8-7)}$$

Since the coordinates of a point along a plane in which maximum k_{Imax} occurs are r and α, eqn(8-2) can be written as

$$\sigma_\theta = \frac{K_I}{\sqrt{2\pi r}}\left(\frac{3}{4}\cos(\alpha/2)+\frac{1}{4}\cos(1.5\alpha)\right)+\frac{K_{II}}{\sqrt{2\pi r}}\left(-\frac{3}{4}\sin(\alpha/2) - \frac{3}{4}\sin(1.5\alpha)\right)$$

Eqn.(8-8)

Substituting eqn.(8-7) into eqn.(8-8), one obtains

$$\sigma_\theta = \frac{k_{I\,max}}{\sqrt{2\pi r}}\left[\frac{3\cos\alpha -1}{\cos\alpha/2(1+\cos\alpha)}\left(\frac{3}{4}\cos\alpha/2 +\frac{1}{4}\cos 1.5\alpha\right) +\frac{2\sin\alpha/2}{1+\cos\alpha}\left(\frac{3}{4}\sin\alpha/2 + \frac{3}{4}\sin 1.5\alpha\right)\right]$$

Eqn.(8-9)

The trigonometric term in this equation is unity, simplifying the equation to:

$$\sigma_\theta = \frac{k_{I\,max}}{\sqrt{2\pi r}} \qquad \text{Eqn.(8-10)}$$

It is clear from this equation that under linear elastic mixed mode loading conditions, k_{Imax} can be used as a parameter to characterise the stress field ahead of the crack tip. Similarly, any mixed mode loading problem can be reduced to a simulated pure mode I problem in which k_{Imax} at the appropriate angle takes the same role as K_I. It may be noted that k_{Imax} indicates both the maximum magnification of k_I and the direction of crack growth.

However, in the plastic range, the material behaves in non-linear manner and superposition is not possible, so that this procedure is not valid.

In 1976, Shih (117) extended the pure mode non-linear analyses (HRR field) by combining mode I and mode II problems under small scale yielding. It was found that the near tip field was completely determined by two parameters $K_M{}^p$ and M^p

$$\sigma_{ij}=\sigma_y K_M{}^p r^{-1/(n+1)} \sigma_{ij}(\theta,M^p) \qquad \text{Eqn.(8-11)}$$

Here M^p is a parameter which gives the relative composition of mode I and mode II ahead of the crack tip, and is defined as (117)

$$M^p = \frac{2}{\pi} \tan^{-1}\left[\lim_{r\to 0} \left(\frac{\sigma_{\theta\theta(r,\theta)}}{\sigma_{r\theta(r,\theta)}}\right)\right] \qquad \text{Eqn.(8-12)}$$

$K_M{}^p$ is the plastic stress intensity factor which can be expressed in terms of the J integral and M^p, as

$$J=\alpha\sigma_y{}^2/E I_{n(}M^p)(K_M{}^p)^{n+1} \qquad \text{Eqn(8-13)}$$

In tubular joints under axial loading conditions, the stress fields on the ligament of the crack plane combine tensile, bending and shear stresses. However, detailed full field stress finite element analyses are prohibitively costly and time consuming. In the present work, edge cracked bars subject to asymmetric three point bending and slant edge cracked bars subjected to a remote tensile load have been introduced to simulate the stress field of cracks in tubular joints. These geometries were chosen to give different combinations of mode II to mode I bending stress ; and mode II to mode I tensile stress, with the object of examining the J dominance conditions. The full field solutions are compared with the singular field due to Shih (117) in the direction of crack extension, and also with boundary layer formulations of small scale yielding in mixed mode loading.

Section 8.2 Finite Element Approach

8.2.1 Off-axis Three Point Bending

In order to obtain a mixed mode loading in which the mode I component arises from bending, two single edge cracked bars shown in Fig.8.2 subject to asymmetric three point bending have been analysed. A mixed mode loading was produced since the crack was located at a distance X away from the central loading point. The ratio of K_{II}/K_I increases with X. In the present case, X/T was chosen to be 1 and 0.5, where T is the thickness of the bar. The meshes for the two configurations are given in Fig.8.2. Mesh generation was accomplished using a commercial code (PATRAN,118), allowing the crack tip to be modelled with a focussed mesh in which there were 17 sets of elements around the crack tip. The radial length of the inner ring elements was about 0.1% of the crack length. Each mesh consisted of 216 elements with 11147 nodes and 3294 degrees of freedom. By examining the difference in the displacement of quarter point node across the crack flanks

under elastic conditions, the ratio of K_I to K_{II} was determined to be 3.5 when X/T=1 and 7.5 when X/T=0.5. Both problems were analysed on Cyber 205 computer at U.M.R.C.C. Typically, full plasticity of the uncracked ligament was achieved in 120-150 increments, each of which used about 3 iterations using a Newton method to obtain equilibrium with a Jacobian formed from the elastic-plastic tangent stiffness and requiring a total cpu time of the order of 24000 seconds for each case. In all cases the uni-axial material behaviour was modelled by a Ramberg-Osgood relationship and the parameter α was set at 3/7, υ was 0.3 and n=13. The equivalent tolerance value was of the order 0.1% of the applied nodal forces. Local stress values were obtained both at Gauss points and by extrapolation to the nodes. For the case in which K_I/K_{II}=7.5 the tensile circumferential stress was maximum on a plane at an angle of 14^0. When K_I/K_{II} was 3.5 the corresponding angle was 26^0.

8.2.2 Stress Field in Mixed Mode Bending Geometries

In the present work the stress fields from full field finite element calculations have been compared with the mixed mode HRR field. The variation of the normalised maximum tensile stress σ/σ_y with distance along the plane of maximum circumferential tensile stress normalised by J/σ_y for n=13 is shown in Fig.8.3. Typically, the values obtained from the full field solutions are lower than the HRR field for K_I/K_{II}=7.5 and 3.5. The level of plasticity deformation is indicated by $C/(J/\sigma_y)$, here C is the length of uncracked ligament or the length of the crack, which ever is smaller. The full field solutions for the two cases are in good agreement with the HRR field. At a distance of $2J/\sigma_y$, the full field solutions were within 10% of the HRR field up to $C\sigma_y/J$=76 for K_I/K_{II}=7.5. While for K_I/K_{II}=3.5 at

$C\sigma_y/J=55$ when the calculation were terminated, the full field solutions were still within 6.5% to the HRR field. The shape of the plastic zone under increasing plastic deformation is given in Fig.8.4. As the mode II component increases, the plastic zone expands and rotates anti-clock-wise about the crack tip.

8.2.3 Stress Field in Tension Geometries

A bar with a single edge crack under a remote uniform tension was used as a pure mode I benchmark to compare with the mixed mode loading problems. The ratio of the crack depth to the thickness was 0.5. Due to the symmetry of the geometry and loading only a half of the configuration was modelled, as shown in Fig.8.5. The model involved 310 eight noded isoparametric elements and 1630 nodes, giving a system 3258 degrees of freedom. The crack tip was modelled with a focussed mesh with 17 rings of elements, the radial length of the inner element was approximately 0.1% of the crack length. The equilibrium tolerance was set between 0.1% and 0.5% of the applied forces, which was met in three or four iteration per increment. Typically full plasticity was obtained in 90-120 increments thus requiring 8.5 hours CPU time in Cyber 205 in U.M.R.C.C.

The full field solutions were compared with the HRR field. The tensile stress directly ahead of the crack tip normalised by the yield stress is plotted against the distance normalized by J/σ_y for n=13 in Fig.8.6. From this figure, it is clear that stresses in the full field solution are lower than the HRR field. By examining the stress at a distance $2J/\sigma_y$, with increasing deformation, the full field solution is shown to be within 10% of the HRR field until $C\sigma_y/J=350$, in agreement with the calculations of Shih and German (76).

8.2.4 Single Edge Slant Cracked Bars

Under pure mode I conditions, the size requirement for maintaining J dominance of bend specimens is not severe enough to maintain J dominance for specimens subject to pure tensile loading. To examine the size requirement for J dominance under mixed mode tensile condition, two bars with a single edge slant crack under tension were considered with a ratio of normal crack depth to thickness 0.5. The plane of the crack was inclined at 15 and 30 degrees to the normal to the plate edge. This produced mixed mode loadings with K_I/K_{II}=7.5 and 3.5 based on Wilson calculations (99). One of the meshes for these geometries is shown in Fig.8.7. Each model involved 310 eight noded isoparametric element and 1630 nodes, giving a system with 3258 degrees of freedom. The crack tip was modelled as a focussed mesh with 17 ring of elements, the radial length of the inner element is approximately 0.1% of the crack length. These problems were analysed on VAX11/750. The equilibrium tolerance value was of 0.1% of the applied nodal force. This tolerance was met in three or four iterations per increment. Typically the full plasticity was obtained in 90-120 increments thus requiring 80 hours CPU time on a VAX11/750.

Local stress values were sampled both at the Gauss points and by extrapolation to the nodes. For K_I/K_{II}=7.5 the tensile circumferential stress is maximum on a plane at 14^0 to the crack plane, for K_I/K_{II}=3.5 the corresponding angle is 26^0. The shapes of the plastic zone under increasing plastic deformation are also given in Fig.8.8, indicating that with increasing mode II component, the plastic zone expands but almost maintains symmetry about the normal to the plate edge.

8.2.5 Stress Field in Slant Edge Cracked Bars

The full field solutions have been compared with the mixed mode HRR field. The maximum tensile stress normalised by the yield stress is plotted against the distance along the plane of maximum tensile stress normalised by J/σ_y in Fig.8.9. It is clear that the stresses obtained from the full field solution are lower than the HRR field at a distance $2J/\sigma_y$. The extent of deformation is indicated by the value of $C\sigma_y/J$. For $K_I/K_{II}=7.5$ the full field solution is within 10% of the asymptotic HRR field at $C\sigma_y/J=310$, and for $K_I/K_{II}=3.5$ the full field solution is within 10% of the asymptotic field even when $C\sigma_y/J=125$ when the calculation was terminated.

Section 8.3 Discussion

From Figs. 8.3, 8.6 and 8.9, it is clearly that under large scale yielding conditions, the dominance of the HRR singularity is dependent on the specimen geometry and loading. The loss of dominance in mixed mode bending problems occurs more slowly than in the mixed mode tensile problems. In addition, the stresses ahead of the crack becomes closer to the HRR field as the ratio of K_{II}/K_I increases, which also favours J dominance. The maintenance of J dominance is most likely to be the effect of the shear stresses and the positive T stresses derived by Rice (119), which will be discussed later. Calculations by Betegon and Hancock (120) on pure mode I problems have indicated that positive T stresses stabilise the stress field, while geometries with negative T stresses are more easy to loose J dominance.

In order to examine mixed-mode problems in small scale yielding conditions, a plane strain two terms boundary layer formulation was considered. The finite element mesh is given in Fig.8.10. The remote

boundaries were subject to imposed displacement boundary conditions corresponding to combined linear elastic K_I, K_{II} and T fields defined as :

$$u_x=\left(\frac{r}{2\pi}\right)^{1/2}\frac{1}{2G}\left[K_I\cos(\theta/2)\,(\kappa-1+2\sin^2(\theta/2))+K_{II}\sin(\theta/2)(\kappa+1+2\cos^2(\theta/2))\right]$$

$$+\frac{(1-\upsilon^2)\,K_{eff}\,r}{E\sqrt{\pi a}}B\cos\theta$$

$$u_y=\left(\frac{r}{2\pi}\right)^{1/2}\frac{1}{2G}\left[K_I\sin(\theta/2)(\kappa+1-2\cos^2(\theta/2))-K_{II}\cos(\theta/2)(\kappa-1-2\sin^2(\theta/2))\right]$$

$$\frac{\upsilon(1-\upsilon)\,K_{eff}\,r}{E\sqrt{\pi a}}B\,\sin\theta \qquad \text{Eqn.(8-14)}$$

Here, $K_{eff}=\sqrt{(K_I^2+K_{II}^2)}$, B is defined as $T\sqrt{\pi a}/K_{eff}$. T is the asymptotic tensile or compressive stress parallel to the crack, corresponding to the second term in the asymptotic elastic crack tip expansion(119). That is

$$\begin{bmatrix}\sigma_{xx} & \sigma_{xy}\\ \sigma_{yx} & \sigma_{yy}\end{bmatrix}=\frac{K}{\sqrt{r}}\begin{bmatrix}f_{xx}(\theta) & f_{xy}(\theta)\\ f_{yx}(\theta) & f_{yy}(\theta)\end{bmatrix}+\begin{bmatrix}T & 0\\ 0 & 0\end{bmatrix} \qquad \text{Eqn.(8-15)}$$

In the current study T was varied from $-0.5\sigma_y$ to $0.5\sigma_y$ The crack tip was modelled with a focussed mesh comprising 14 sets of elements around the crack tip. The element adjacent to the crack tip had a radial length which was 0.4% of radial length of outer elements. The mesh consisted of 280 eight noded isoparametric hybrid elements with 1513 nodes giving a system 3026 degrees of freedom.

In the computation, J_2 flow theory plasticity based on the Ramberg-Osgood power law was used, α was set at 3/7, υ was 0.3 and n=13. The

computations were performed with small displacement theory implemented in the finite element code ABAQUS mounted on a VAX11/750. Problems with different ratios of K_I/K_{II} (0, 1.0, 3.5, 7.5 and ∞) were analysed. The corresponding angles at which the tensile circumferential stress was maximum were 76^0, 52^0, 26^0,14^0 and 0^0. The pure mode I boundary layer formulation was computed by Betegon et al (119). The solution time for each iteration was approximately 30 mins. In order to maintain small scale yielding conditions, the maximum plastic zone size was restricted to less than one half of the radius at which the boundary conditions were applied.

The local stresses were obtained at the Gauss points. The maximum circumferential stresses non-dimensionalised by the HRR asymptotic stresses given by Shih (117), at distances both $2J/\sigma_y$ and $5J/\sigma_y$ away from the crack tip were plotted as a function of the T stress normalised by the yield stress σ_y in Fig.8.11. This figure clearly demonstrates the effect of T stresses which are independent of the B values. In all case with different ratio of K_I/K_{II}, the data is close to the HRR field for positive T stresses but falls below the HRR field with negative T stresses. This is consistent with Betegon and Hancock calculations in pure mode I problems(120). In addition, Fig.8.11 also indicates that the bigger the shear stress, the smaller differences between the data and the HRR field.

The shapes of the plastic zone are also given in Fig.8.12 under various mixed mode conditions. These figures illustrate that as the mode II component increases the shape of the plastic zone expands and rotates. In addition, when B is non-zero, the plastic zone is asymmetric, although the minimum radial distance of plastic zone, which indicates the crack extension occurs at almost the same angle as that with B=0.

Insight into the complete bending and tension cracked geometries discussed in the previous sections, by performing a detail linear elastic

stress analysis ahead of the crack tip on these geometries, B values were determined to be -0.22 for K_I/K_{II}=7.5 and 0.22 with K_I/K_{II}=3.5 for the slant cracked geometries subject to tensile stress, and 0.68 with K_I/K_{II}=7.5 and 1.1 with K_I/K_{II}=3.5 for the cracked geometries subject to asymmetric three point bending. This indicates that positive T stresses, which favour J dominance occur in the geometries subject to bending.

For a tubular T joint under axial loading, deep cracks are subject to mixed mode loading conditions which combine mode I bending stress, mode I tensile stress, and mode II shear stress. For example at a/T=0.6, K_I/K_{II} =5.5 and M/Fb=0.608 while at a/T=0.9, K_I/K_{II} =1.3 and M/Fb=7.656 These results indicate that when crack grows deeper, the mode II component increases comparison to the mode I component, in addition, the contribution of the bending stress increases compared to the tensile stress in the mode I component. All these suggest that a tubular T joint is most likely to have positive T stresses under axial loading. By considering the J dominance criteria for combining tensile stress and bending stress derived by Shih (78). it is suggested that the size requirement for J dominance with $C\sigma_y/J \geq 60$ for a/T=0.6, while $C\sigma_y/J \geq$ 25 for a/T=0.9. are made more conservative by the addition of a mode II component.

Section 8.4 Conclusion

The size requirements for J dominance under mixed mode loading conditions decrease with increasing mode II component and the positive T stresses. The size requirements for problems combining mode I bending stress and mode II shear stress are less demanding than those for combined mode I tensile stress and mode II shear stress.

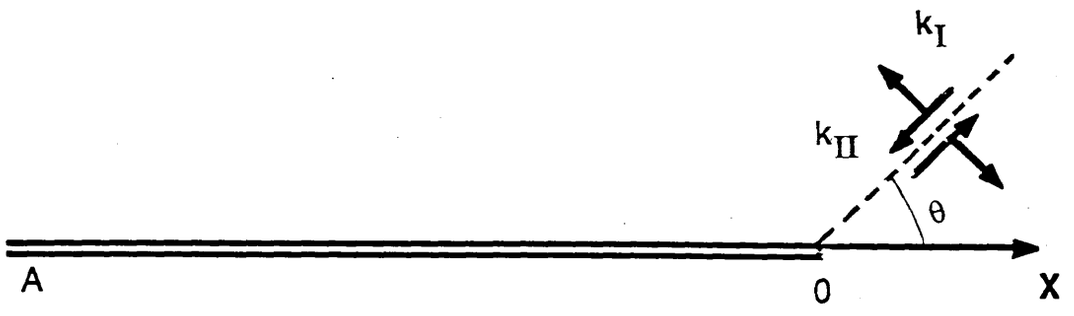

FIG.8.1 A schematic illustration of a straight crack extends in a non-planar fashion along a plane inclined to the original crack plane by an angle.

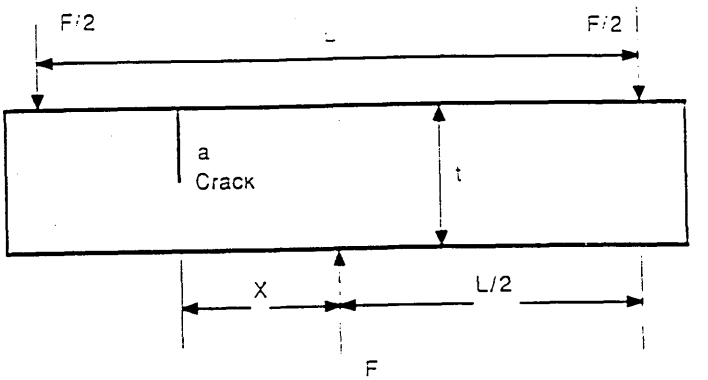

a)

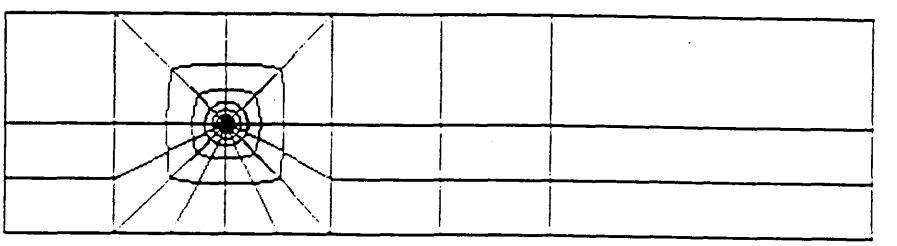

b)

FIG.8.2 a) A single edge bar subject to asymmetric three point bending

b) Mesh of a single edge bar subject to asymmetric three point bending

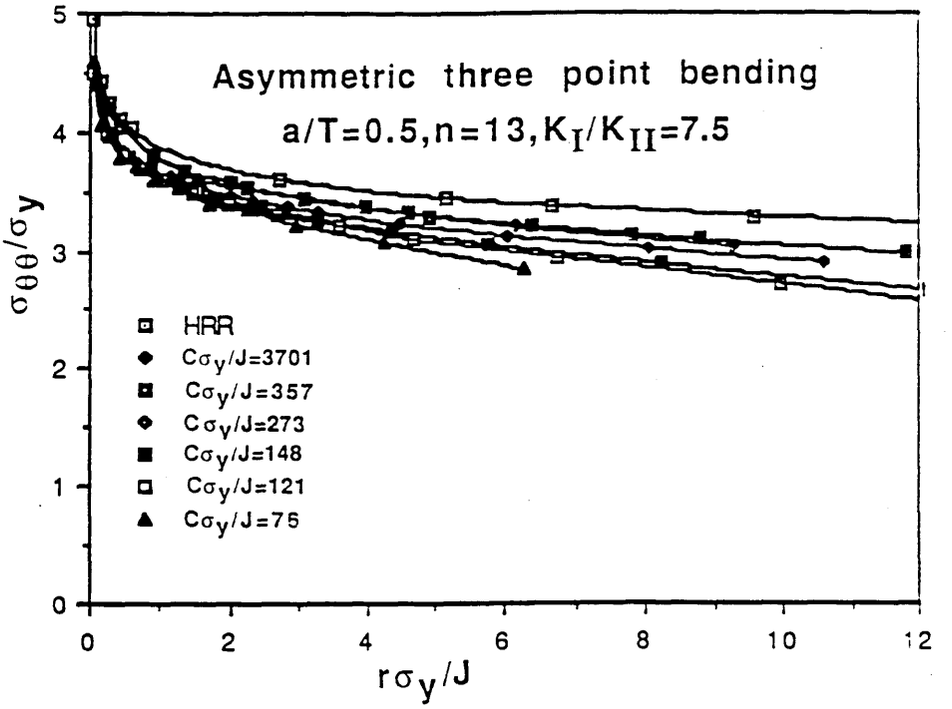

a)

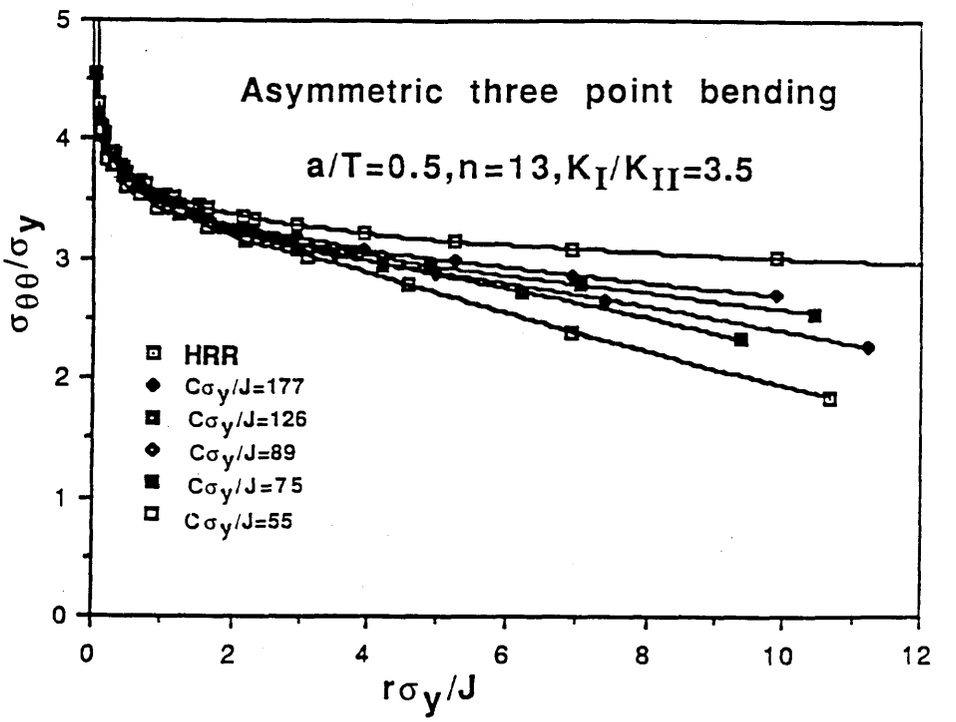

b)

FIG.8.3 Maximum circumferential tensile stress normalised by the yield stress as a function of distance from the crack tip normalised by J/σ_y for asymmetric three point bending

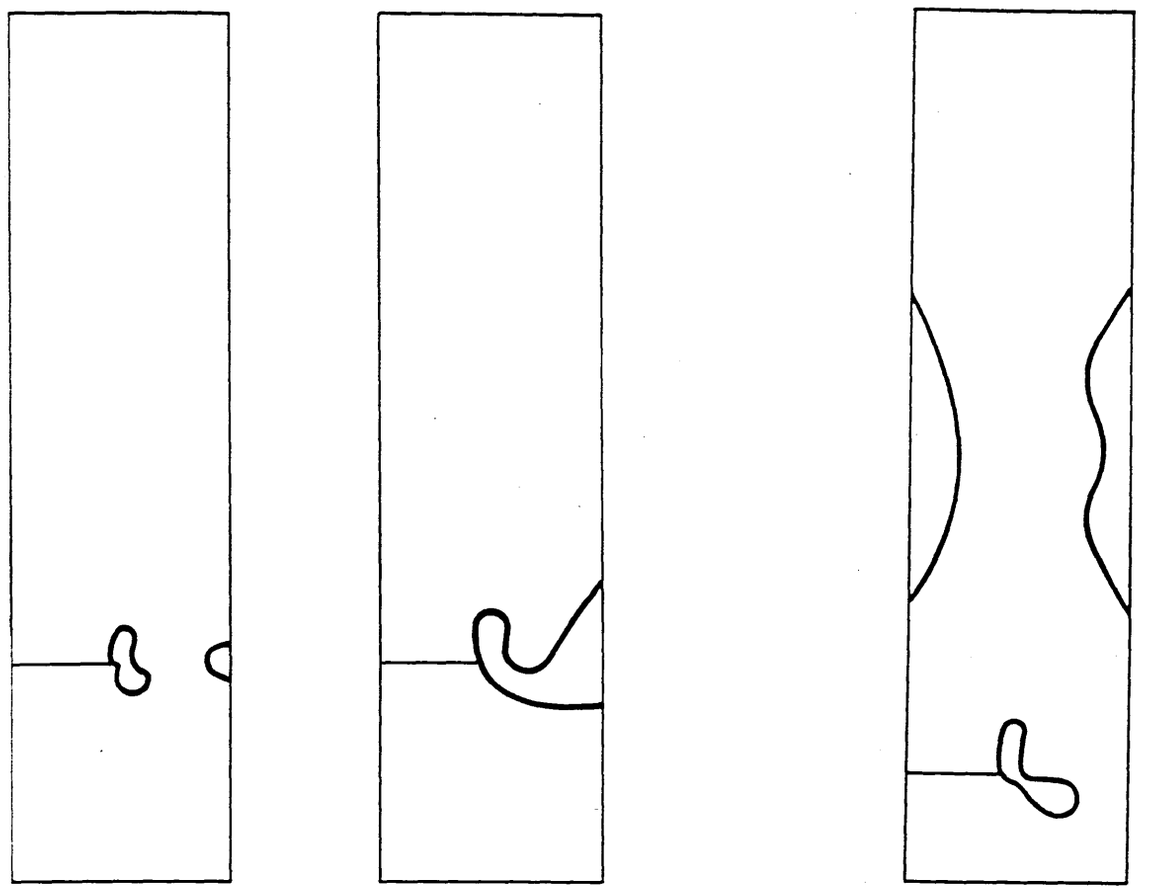

FIG.8.4 Illustration of plastic zone for asymmetric three point bending

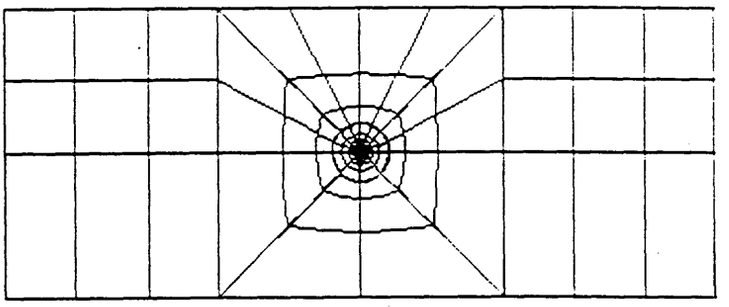

FIG.8.5 Mesh of a single edge cracked bar

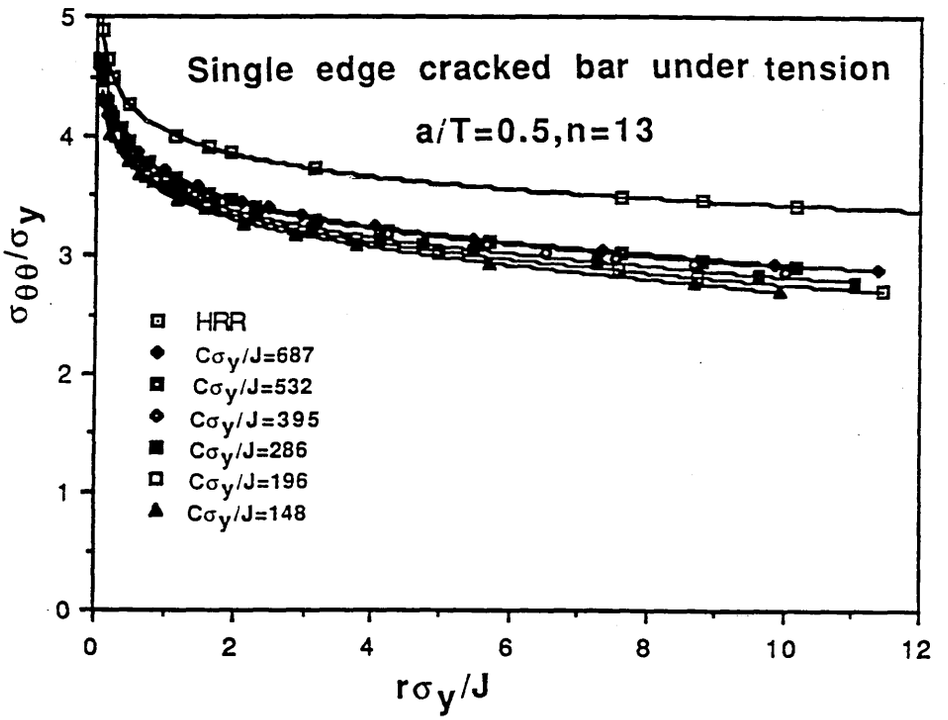

FIG.8.6 Maximum circumferential tensile stress normalised by the yield stress as a function of distance from the crack tip normalised by J/σ_y for single edge cracked bar

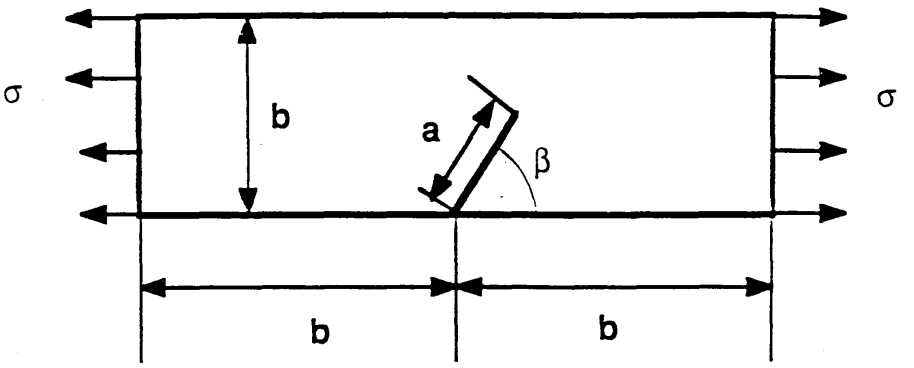

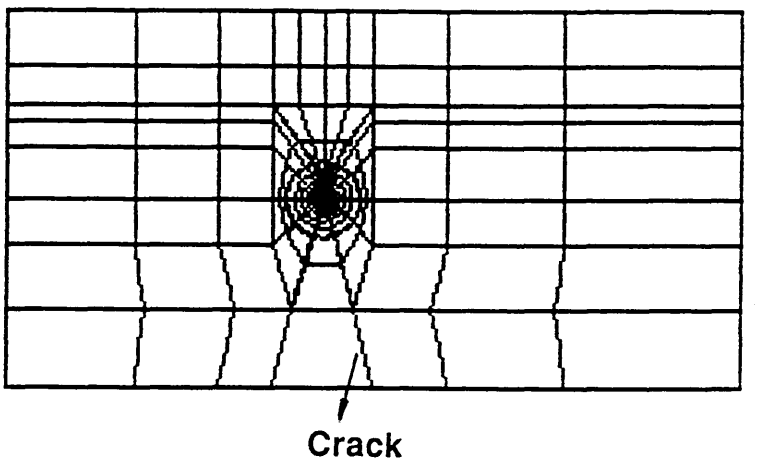

FIG.8.7 Mesh of a single edge slant cracked bar

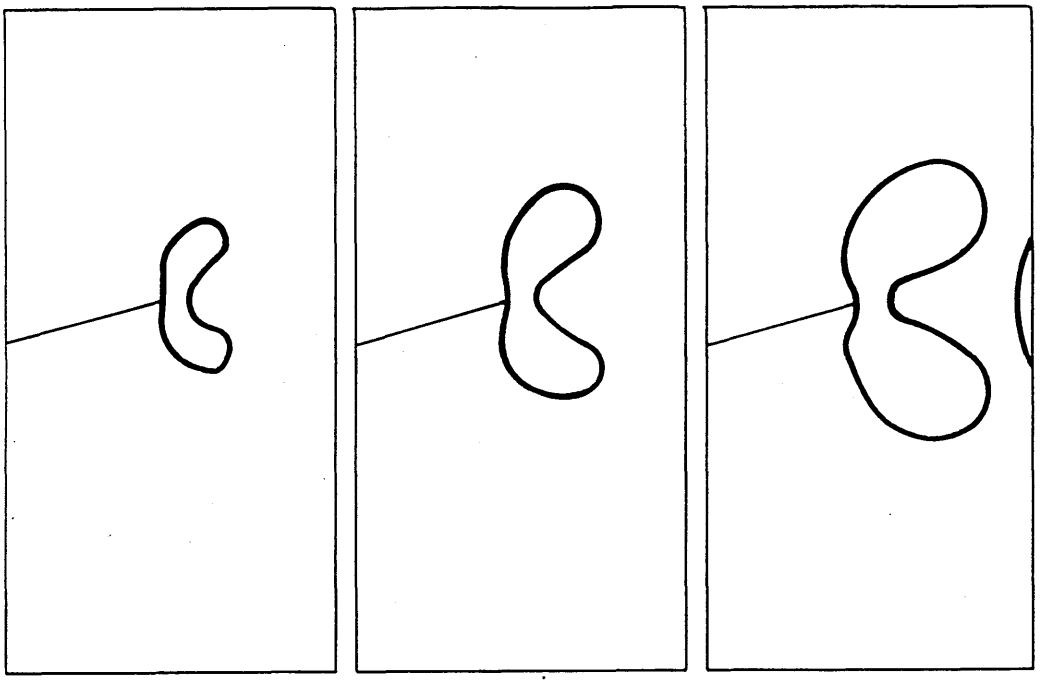

$C\sigma_y/J=243$ $C\sigma_y/J=417$ $C\sigma_y/J=155$

a) $K_I/K_{II}=7.5$

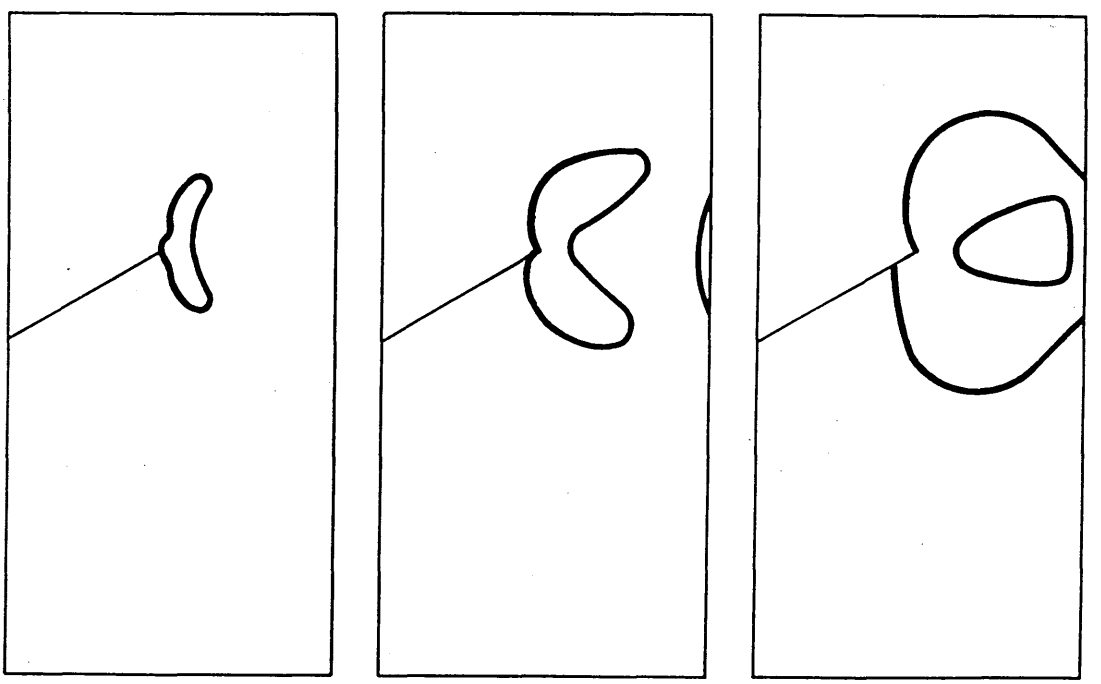

$C\sigma_y/J=740$ $C\sigma_y/J=331$ $C\sigma_y/J=129$

b) $K_I/K_{II}=3.5$

FIG.8.8 Illustration of plastic zone for single edge slant cracked bar

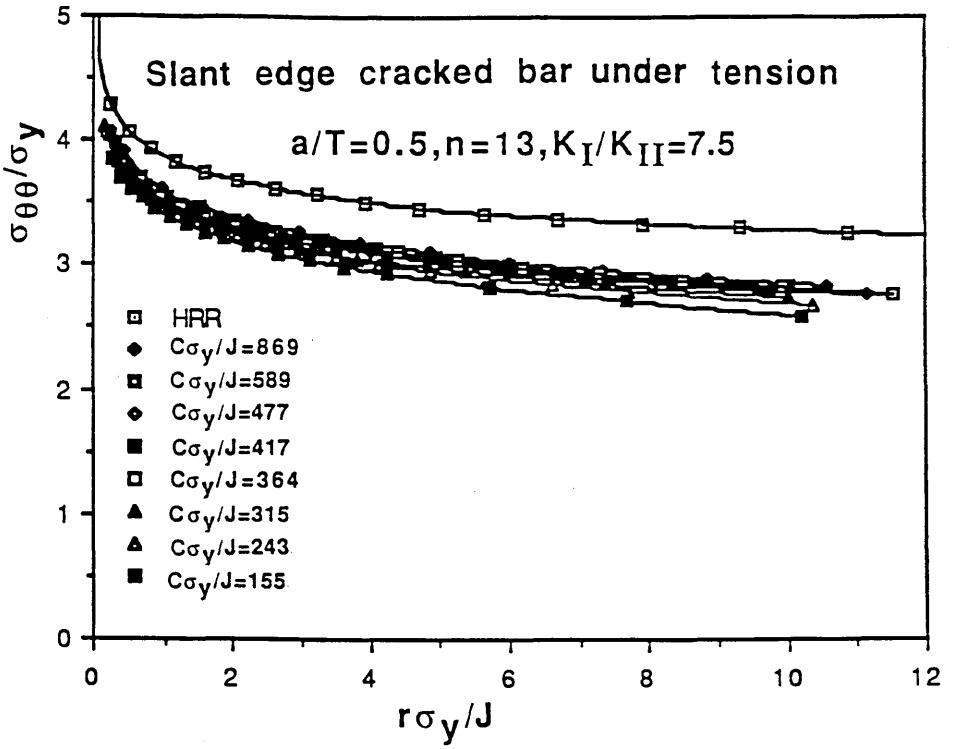

a)

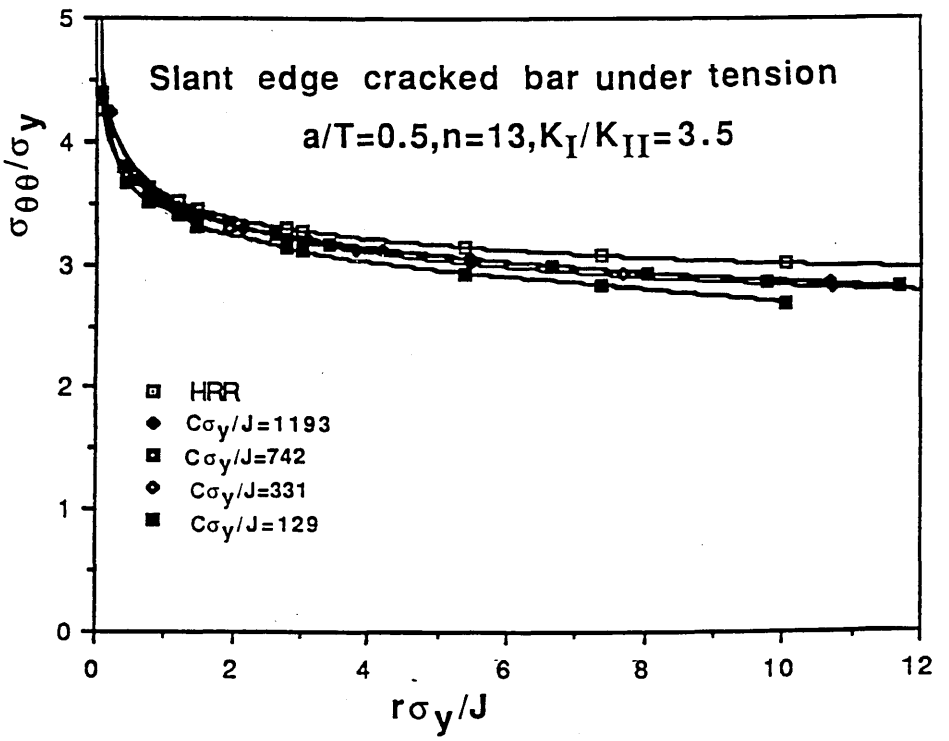

b)

FIG.8.9 Maximum circumferential tensile stress normalised by the yield stress as a function of distance from the crack tip normalised by J/σ_y for single edge Slant cracked bar

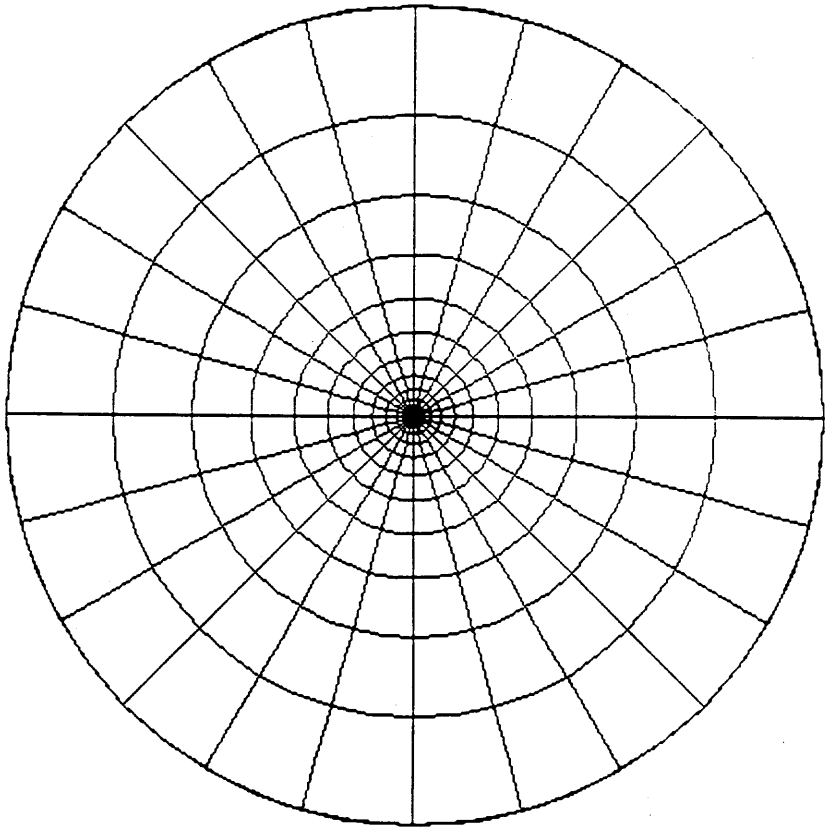

FIG.8.10 A finite element mesh for boundary layer formulation

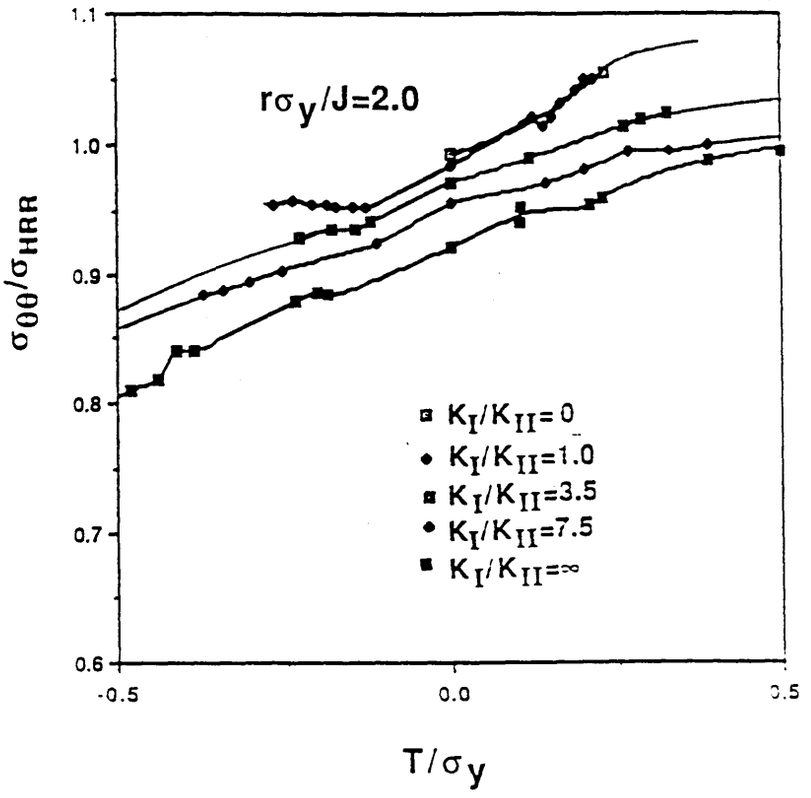

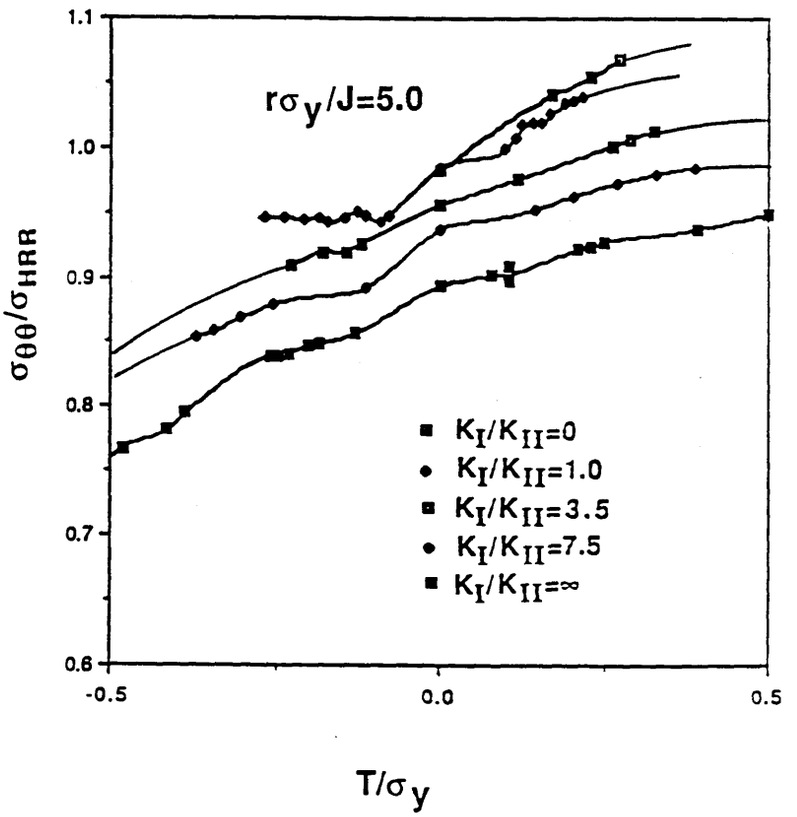

FIG.8.11 Maximum circumferential tensile stress normalised by the HRR as a function of T/σ_y at distance from the crack tip $r\sigma_y/J=2.0$, $r\sigma_y/J=5.0$ for boundary layer formulation

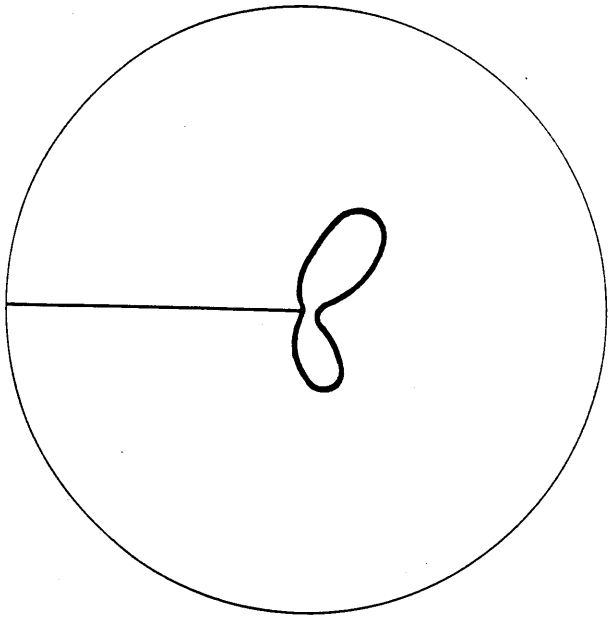

T/σ_y=-0.34

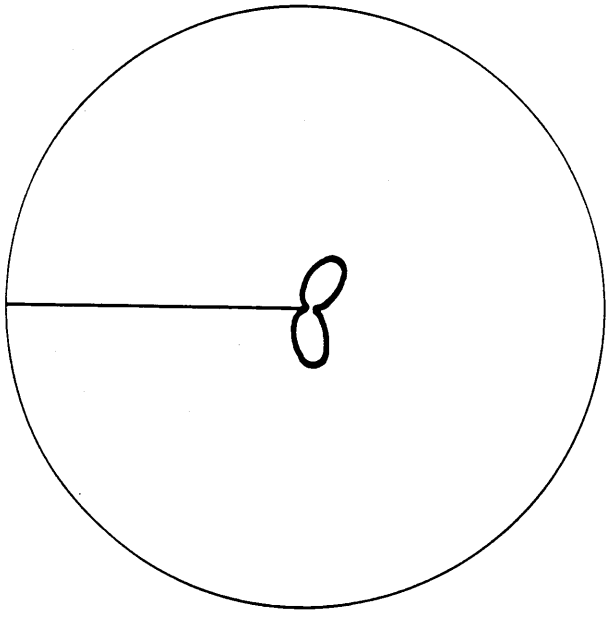

T/σ_y= 0

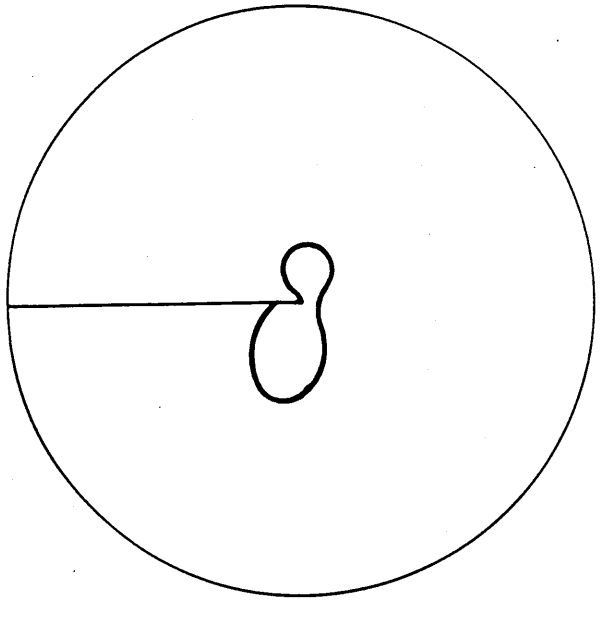

T/σ_y=0.38

a) K_I/K_{II}=7.5

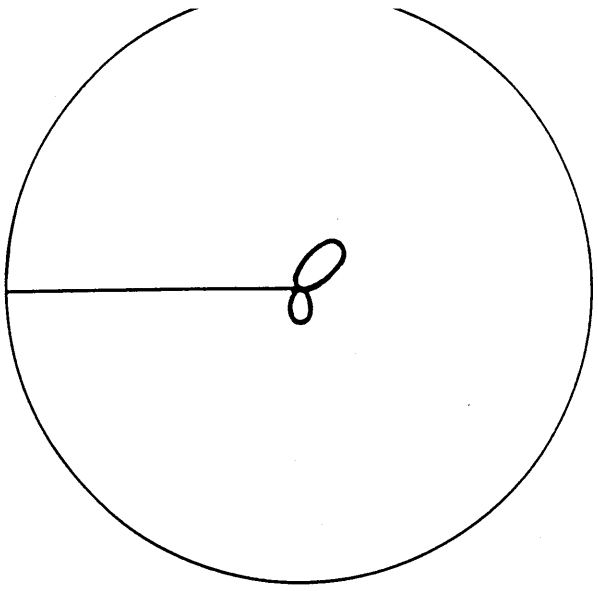

$T/\sigma_y=-0.23$

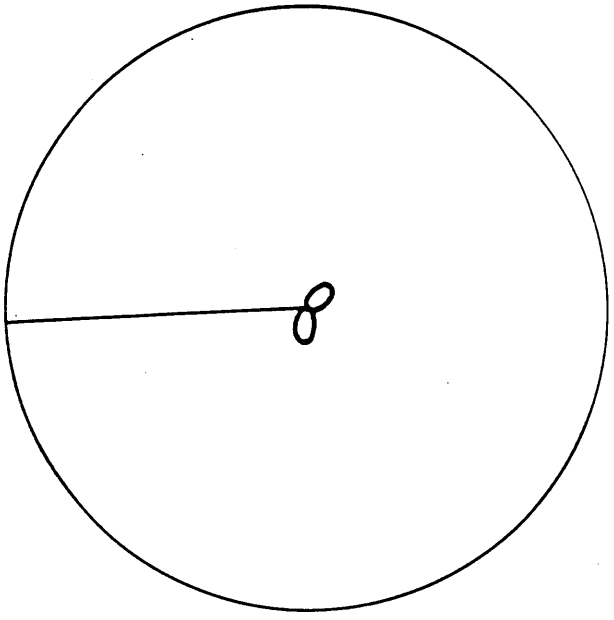

$T/\sigma_y=0$

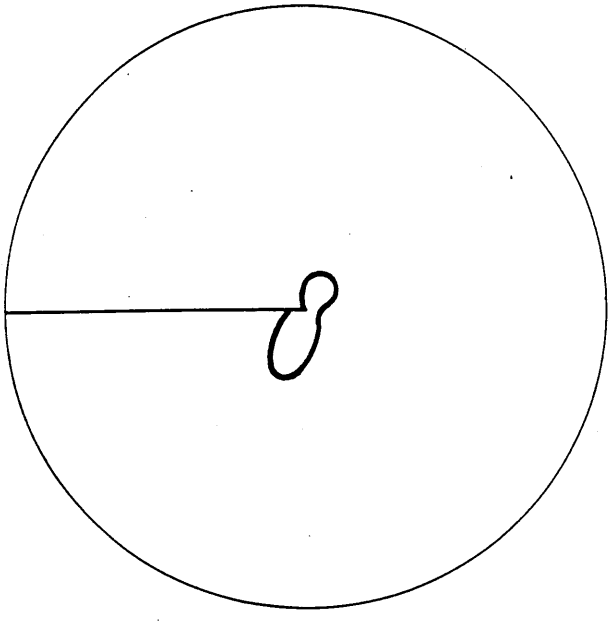

$T/\sigma_y=0.28$

b) $K_I/K_{II}=3.5$

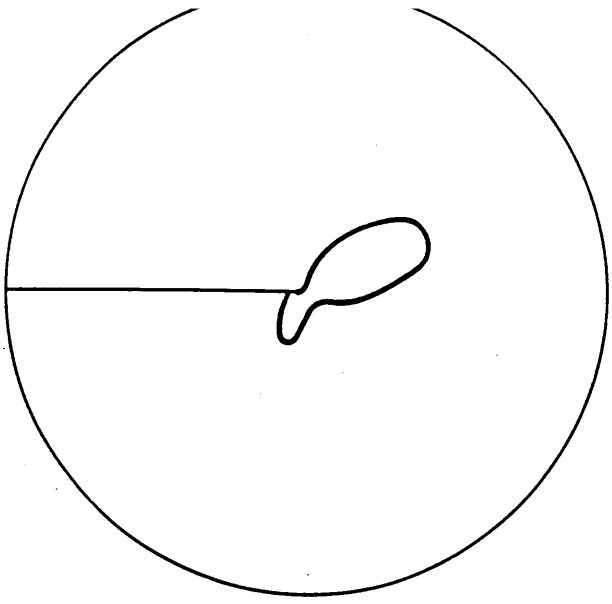

T/σ_y=-0.18

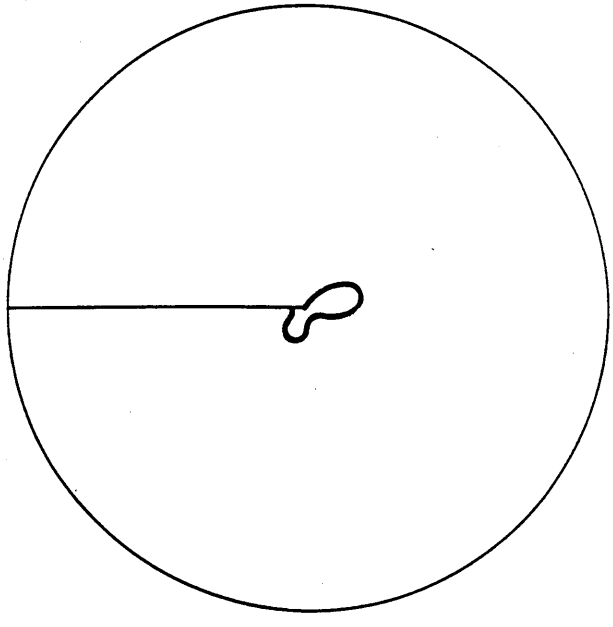

T/σ_y=0

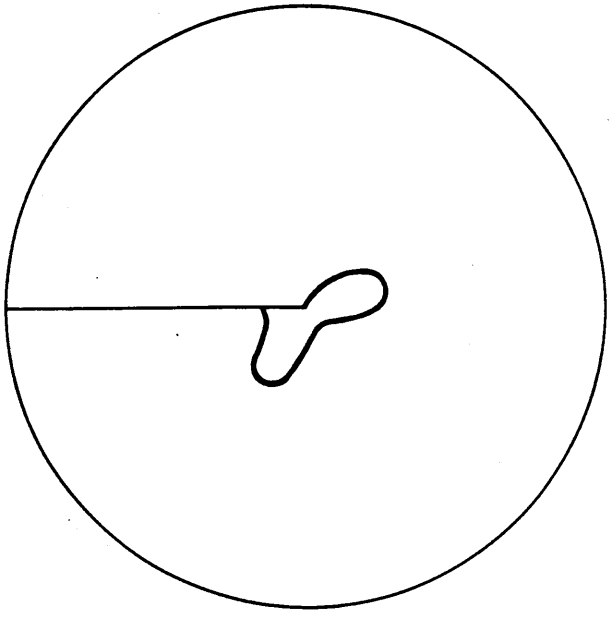

T/σ_y=0.16

c) K_I/K_{II}=1.0

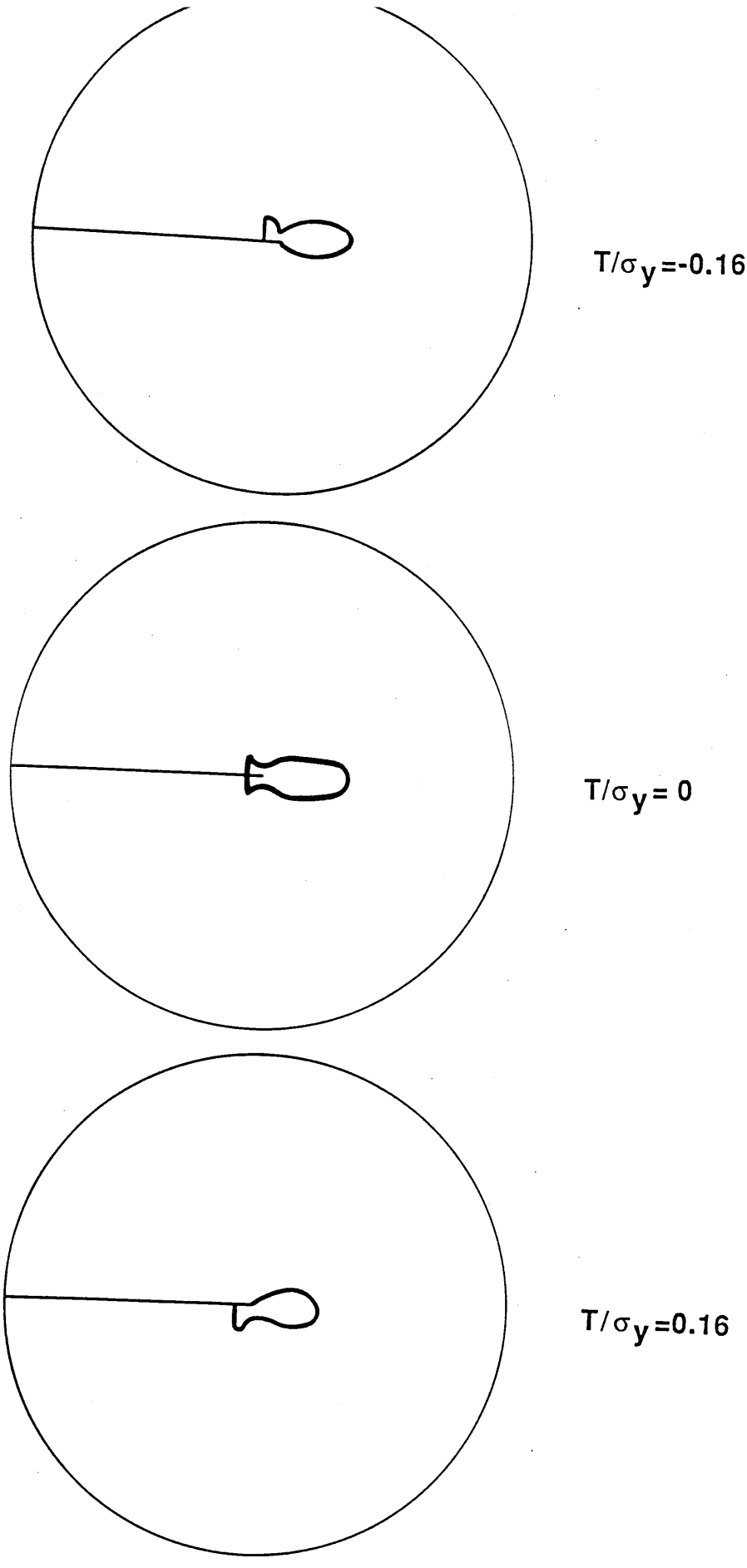

d) K_I/K_{II}=0

FIG.8.12 Illustration of plastic zone obtained from boundary layer formulation

References

1, Department of Energy Offshore Installations; Guidance on Design and Construction, HMSO, London, April,1984

2, Wordsworth, A.C. and Smedley, G.P., "Stress Concentration at Unstiffened Tubular joints", European Offshore Steels Research select Seminar,Paper 34, Cambridge,1978

3, Kuang, J.G., Potvin, A.B. and Leick, R.D., "Stress Concentration in Tubular Joints",Offshore Technology Conference,Paper number 2205,Houston,1975

4, Gibsten, M.B., "Parametric Stress Analysis of T Joints", Paper 26, Europcan Offshore Steel Research Seminar, Cambridge, 1978

5, Westergaard, H.M.,"Bearing Pressures and Cracks", Transactions of the ASME,61, pp. A49-A53 (1939)

6, Ewalds, H.L. and Wanhill, R. J. H., "Fracture Mechanics", 1984.

7, Irwin,G.R., "Fracture Mode Transition for a Crack Traversing a Plate", J. Basic Eng. ASME, Vol,82, pp417-425,1960.

8, Griffith,A.A. Phil,Trans. Roy. Soc. A221,163,1921.

9, Irwin, G.R., Fracture ,Encyclopedia of Physics, (ed., S. Fluge, Springer Verlag, pp.551-589, 1958)

10,A.S.T.M., "Standard E399-78A, Standard Test Method for Plane Strain Fracture Toughness of Metallic Materials", 1979 annual book of ASTM Standard, part 10, pp.540-561, (1979), Philadelphia.

11,Tada, H., Paris, P. and Irwin, G., "The Stress Analysis of Cracks Handbook ", ' Del Research Corporation', Helltown, Pa, 1973.

12,Rooke,D.P. and Cartwright,D.J.,"Compendium of Stress Intensity Factors The Hillington Press", Uxbridge,1976.

13,Irwin,G.R., "Crack Extension Force for a Part-Through Crack in a Plate",Paper No.62-WA-13, J. Appl. Mech. Trans. 1962.

14, Paris,P.C.and Sih,G.C., "Stress Analysis of Cracks, Fracture Toughness Testing and its Application" ,ASTM S.T.P. 381,1965.

15, Smith, F.W. and Alavi, M.J., "Stress Intensity Factor for Part-Circular Surface Flaws", Procs. Ist, Int. Pressure Vessel Conference, Delft,1969.

16, Smith,F.W., Kobayashi, A.S. and Emery, A.F., "Stress Intensity Factors for Penny Shaped Cracks", J. Appl. Mech. Trans ASME, Dec. 1967.

17, Hayes, D.J., "A practical Application of Buekner's Formulation for the Determination of Stress Intensity factors", Int. J. Fracture Mechanics, 8, pp. 157-165,1972.

18, Burdekin, F.M., "Engineering Design against Fracture at Stress Concentrators", Materials Science and Technology, 1,pp.487-493, 1985

19, Hibberd,R.D. and Dover, W.D., "The Analysis of Random Load Fatigue Crack Propagation", 4th Int. Conference on Fracture, Canada,1977

20,Dover,W.D.,Chaudhury,G.K. and Dharmavasan,S. "Experimental and Finite Element Comparisons of local Stress and Compliance in Tubular Welded T-joints",Int. Conf. on Steel in Marine Structures, Paris,1981

21, Brown, D.K., Hancock, J.W. and Green, D.R., "On the Finite Element Analysis of a Welded Tubular T-joint with a Throught Thickness Crack", Third Int. Conf. on Numerical methods in Fracture Mechanics, University College Swansea, 1984

22, Parks, D.M., "A Stiffness Derivative Finite Element Technique for Determination of Crack Tip Stress Intensity Factors", Int. J. of Frac.,10, No.4, pp. 487-502,1974.

23, Hellen,T.K., "On the Method of Virtual Crack Extension" , Int. J. Num. Meth. Eng. ,pp.187-207,1975.

24, Delorenzi,H.G., "On the Energy Release Rate and the J-Integral for 3D

Crack Configurations",. Int. J. of Fracture,19,pp.183-193, 1982.

25, Delorenzi,H.G. and Shih,C.F.,"3-D Elastic-Plastic Investigation of Fracture Parameters in Side Grooved Compact Specimen", Report, 80CRD211, General Electric company, Schementady, N.Y. 1980

26, Zienkiewicz, O.C., "The Finite Element Method in Engineering Science", McGraw Hill London,1971.

27, Parks, D.M., "The Virtual Crack Extension Method for Nonlinear Behavior", Comp. Meths. Appl. Mech. Eng.,12, pp.529-546,1970.

28, Bueckner,H.F., "A Novel Principal for the Computation of Stress Intensity". Zeitschrift fur Angewandte Mathematik and Mechanik,50 pp.529-546,1970.

29, Bueckner, H.F., "Field Singularities and related Integral representations", Chap5, In "Methods of Analysis and Solutions of Crack Problems", pp.239-314, Noordhoff Int. Publicating, ed. G.C. Sih, 1973.

30, Parks,D.M. and Kamentzky,Z.M., "Weight Function from Virtual Crack Extension", Int. J. Numerical Methods in Engineering, 14, pp.1693-1707,1979.

31, Rice, J.R. , "Some Remarks on Elastic Crack-Tip Stress Fields" , Int. J. Sol. Structure,. pp.751-758,1972

32, Petroski, H.J.,and Achenbach,J.D."Computation of the Weight Function from a Stress Intensity Factor",Eng. Fract Mechanics 10, pp.257 -266, 1978.

33, Rybicki,E.F.and Kanninen, M. F., "A Finite Element Calculation of Stress Intensity Factors by a Modified Crack Closure Integral", Eng. Fracture Mechanics,9,pp.931-938,1977

34, Oore,M. and Burns,D.J., "Estimation of Stress Intensity Factors for Embedded Irregular Cracks subjected to Arbitrary Stress Field", ASME, J. of Pressure Vessel Technology, pp25-29,1979.

35, Kassir, M.K. and Sih, G.C., "Three dimensional Crack Problems" Noodnoff,1975

36, Oore, M.and Burns,D.J.,"Estimation of Stress Intensity Factors for Irregular Cracks subjected to Arbitary Normal Stress Field", Proc. of 4th Int. Conf. on Pressure Vessel Technology, London, I. Mech. Eng.,1980

37, Burdekin, F.M. et. al."Fracture Mechanics Analysis of Fatigue Crack Propagation in Tubular Joints", Int. Conference on Fatigue and Crack Growth in Offshore Structures, I. Mech. E., London, 1986

38, Dover,W.D. and Connolly,M., "Fatigue Fracture Mechanics Assessment of Tubular Welded Y and K Joints", Int. Conference on Fatigue and Crack Growth in Offshore Structures, I. Mech. E. , London,1986

39, Desjardins, J.L, Lambert, S.B., Burns, D.J. and Thompson, J.C. "A Weight Function Technique for Surface Cracks with Application to Welded Joints", Proc. of Conf. on Fatigue of Offshore Structures, EIS, London, 1988

40, Niu, X. and and Glinka, G, "Stress Intensity Factors for Semi-Elliptical Surface Cracks in Welded Joints", Int. J. of Fracture, 1989 (To be published)

41, Niu, X,and Glinka, G, "The Weld Profile Effect on Stress Intensity Factors in Weldments", Int. J. of Fracture, Vol35,1987

42, Bell, R. "Determination of Stress Intensity Factors for Weld Toe Defects", Phase II, Final Report, DSS Contract OST 89-00125, Carleton University Canada,1985

43, Rice,J.R. and Levy, N., "The Part-Through Surface Crack in an Elastic Plate" , ASME J. App. Mech., 39, pp.185-194 ,1972,

44, Delale, F. and Erdogan, F.,"A Application of the Line Spring Model to a Cylindrical Shell containing a Circumferentical or Axial Part-Through Crack", Lehigh University Report for DOT contract No. Dot-Rc-

82007,1981.

45, Parks, D.M., "The Inelastic Line Spring estimates of Elastic-Plastic Fracture Mechanics Parameters for Surface-Cracked Plates and Shells", ASME, Journal of Pressure Vessel Technology,103, pp.246-254,1981.

46, Parks, D.M., Lockett,R.R. and Brockenbrough, J.R., "Stress Intensity Factors for Surface Cracked Plates and Cylindrical Shells using Line-Spring Finite Elements", in 1981 Advances in Aerospace Structures and Material AD-01, A.S.M.E. N.Y. ,pp.279-285,1981.

47, Parks,D.M. and White,E.S., "Elastic-Plastic Line Spring Finite Elements for Surface Cracked Plates and Shells" J. Pressure Vessels and Piping, ASME, 104, pp.287-292, 1982

48, Desvaux,G.J., "The Line Spring Model for Surface, An Extension to Mode 2 and Mode 3", Msc Thesis, Massachusetts Insitute of Technology,1985

49, Raju,J.S. and Newman,J.C., "Stress Intensity Factor for a Wide range of Semi-Elliptical Surface Cracks in Finite Thickness plates", Engineering Fracture Mechanics,11,pp.817-829,1979.

50, Kumar,V. and Lee,Y.J., "J-Integral and Compliance Analysis of a Single Edge Cracked Plate under Combined Tension and Bending for Elastic-Plastic Strain Hardening Materials",General Electric Company Report.

51, Huang, X. and Hancock, J.W.,"The Stress Factors of Semi-Elliptical Cracks in a Tubular Welded T-joint under Axial Loading", J. Eng. Fracture Mechanics, Vol.30, 1988 pp.25-36

52, Noordhoek, C. and Verheul, A. " Comparison of the ACPP Method of In-depth Fatigue Crack Growth Monitoring with the Crack Front Marking Technique, Delft University of Technology, Department of Civil Engineering, Report 6-84-13.

53, Delorenzi,H.Z., "Elastic-Plastic Analysis of the Maximum Postulated Flaw in the Beltline Region of a Reactor Vessel" ,J of Pressure Vessel

Technology, Vol.104,1982,pp.278-283

54, Wilkening,W.W., Delorenzi,H.G. and Barishpolsky,M.,"Elastic-Plastic Analysis of Surface Flaws in a Reactor Vessel",. J. of Pressure Vessel Technology,106,Aug. 1984

55, Hutchinson,J.W.,"Fundamentals of the Phenomenological Theory of Non-Linear Fracture Mechanics",. J. of Applied Mechanics, 50,Dec.1983

56, Hutchinson, J.W., "Nonlinear Fracture Mechanics Solid Mechanics",Tech. University of Denmark, 1979

57, Rice, J.R.,"A Path Independent Integral and the Approximate Analysis of Strain Concentration by Notches and Cracks", J. of Appl. Mechs.,35 pp.379-386,1968.

58, Derbalian,G., "J-Integral Estimation Procedures", J. of Pressure Vessel Tech.,105, pp.299-308,1983

59, Rice,J.R. "Mathematical Analysis in the Mechanics of Fracture, In Fracture", ed.H. Leibowitz,Academic Press, New York, 2, pp.191-311, 1968.Vol.2 Academic press New York,1969

60, Hutchinson,J.W.,"Singular Behavior at the end of a Tensile Crack in Hardening Material" J. of the Mechanics and Physis of Solids, 16, pp.13-31, 1968

61, Rice, J.R. and Rosengren,G.F. , "Plane Strain Deformation near Crack Tip in Power law Hardening Material", J. of the Mechanics and Physics of Solids, 16, pp1-12 ,1968

62, Shih, C.F, "Tables of Hutchinson-Rice-Rosengren Singular Field Quantities", Division of Engineering, Brown University, Providence, R.I., 1983

63, Wells,A.A.,"Unstable Crack Propagation in Metals: Damage and Fast Frac. "Proceeding of the Crack Propagation Symposium, Cranfield,The Coll. of Aeronauties,1 pp.210-230,1962,Cranfield, England.

64, Bilby,B.A.,Cottrell,A.H. and Swinden,K.H.,"The Spreead of Plastic Yield

from a Notch" ,Proc. Roy. Soc. series A, 272, pp.304-314, 1963.

65, Burdekin,F.M. and Stone, D.E.W.,"The Crack Opening Displacement Appro.to Fracture Mechanics in Yielding Materials", J. of Strain Analysis ,1, No.2,1966

66, Dugdale,D.S., "Yielding of Steel Sheets Containing Slits", J. Mech. Phys.Solids, 8,p100,1960

67, British Standard Institution BS5762,"Methods for Crack Opening Displacement (COD) Testing", BSI (1979), London

68, Wessel,E.T., "Linear Elastic Fracture Mechanics for Thick Wall Steel Pressure Vessels: Material Property Considerations", Practical Fracture Mechanics for Structural Steel,1969, Risley, Chapman and Hall.

69, Hayes,D.J., "Some Applications of Elastic Plastic Analysis to Fracture Mechanics", PhD. Thesis, 1970, London University

70, Shih,C.F., "Relationship between the J-Integral and the Crack Opening Displacement for Stationary and Extending Cracks", J. Mech. Phys. Sol. 29, pp305-326,1981

71, Tracey,D.M., " Finite Element Solutions for Crack Tip Behaviour in Small-Scale Yielding" J. Eng. Material and Technology,98,pp.146-151, 1976

72, Sailors, R.H., "Properties related to Fracture Tougness",ASTM-STP-605 p34, American Society for Testing and Materials Philadelphia, 1976

73, Robinson, J.N., Int. J. Fracture. 12, 723 ,1976

74, McMeeking, R.M.," Finite Deformation Analysis of Crack-Tip Opening in Elastic-Plastic Materials and Implications for Fracture" J. Mech. Phys. Solids, 25, pp.357-381, 1977

75, McMeeking, R.M. and Parks, D.M., " On Criteria for J-dominance of Crack-Tip Fields in Large-Scale Yielding" In Elastic-Plastic Fracture ASTM STP 668,pp.175-194, (1979)

76, Shih, C.F. and German, M.D. , "Requirements for a One Parameter Characterization of Crack Tip Field by the HRR Singularity", Int. J. of Frac.17, 1981

77, McClintock,F.A.,"Plasticity Aspects of Fracture, Fracture-An Advanced Treatise", Vol.3,H.Liebowitz (ed.),New York,pp.47-225, 1971

78, Shih,C.F.,"J Dominance Under Plane Strain fully Plastic Conditions: The Edge Crack Panel Subject to Combined Tension and Bending" Int. J. of Fracture,29,1985,pp.73-84

79, Kumar,V. , German,M.D. and Shih, C.F., "An Engineering Approach for Elastic-Plastic Fracture Analysis", Report No. EPRI, NP-1931,July, 1981, General Electric Co. Schenectady, NY

80, Kumar,V. and German, M.D.,"Studies of the Line-Spring Model for Non-Linear Crack Problems", J. of Press. Vessel Tech. ,107, 1985

81, Kumar,V.and Shih,C.F.,"Fully Plastic Crack Solution,Estimation Scheme and Stability Analyses for Compact Specimens in Fracture Mechanics",ASTM ,S.T.P. 700,pp.406-438 ,1980

82, Goldman, N.L. and Hutchinson, J.W.,"Fully Plastic Crack Problems: the Center Strip Under Plane strain",. Int. J. of Solids and Structures,11, pp75- 91,1975

83, Ezzat,H. and Erdogan,F.,"Elastic-PLastic Fracture of Cylindrical Shells containing a Part-Through circuferential Crack", J. of Pressure Vessel Technology,Vol.104,pp.323-328,1982

84, Rice,J.R.,"Models for Stable Crack Growth",In Mechanics and Mechanism of Crack Growth, ed.M.J. May, British Steel Corporation Physical Meta. Centre Publication, 1975.

85, Shawki, T.G., Nakamura, T. and Parks,D.M., "Line Spring Analysis of Surface Flawed Plates and Shell Using Deformations Theory",1988 (To be Published)

86, Rice,J.R., Paris,P.C.and Merkle,J.G. " Some Further Results of J-Integral Analysis and Estimates" ASTM,S.T.P.536,1973,pp.231-245.

87, ABAQUS User's Manual, Hibbitt, Karlsson and Sorensen, Inc. Providence Rhode Island (1982)

88, FEMGEN User's Manual,"A General Finite Element Mesh Generator" , FEGs. Ltd. Oakington, Cambridge CB4 5BA

89, SESAM usuer's Manual, PREFEM, "Preprocessor for General Finite Element Programs", A. S Veritec, P.O. Box 300, Norway.

90, SESAM User's Manual, PRETUBE "Finite Element Preprocessor for Tubular Joints", A. S Veritec, P.O. Box 300, Norway

91, Sloan,S.W. and Randolph, M.F., "Automatic Element Reordering for Finite Element Analysis with Frontal Solution Schemes", Int. J. for Numerical Methods in Engineering, 19, pp.1153-1181 (1983).

92, FEMVIEW Usuer's Manual, " A General Finite Element Mesh and Result Viewing Program" Version 3.5, Femview Ltd.,1983

93, Huang, X. , "A Fracture Mechanics Analysis of the Fatigue Reliability of Tubular Welded joints", PhD thesis University of Glasgow 1987.

94, Barsoum, N. S., "On the use of Isoparametric Finite Elements in LEFM", Int. J. Num. Meth. Engineering, 10, pp. 25-37, (1976)

95, Henshell, N.D.and Shaw, K.G,"CrackTip Finite Element are Unnecessary", Int. J. Num. Mech. Engineering , 9, pp. 495-509, (1975)

96, Shih, C.F., Delorenzi, H.G. and German, M.D. ,"Crack Extension Modelling with Singular Quadratic Isoparametric Elements", Int.J. Fracture 12, pp. 647-651 1976.

97, Tracey, D.M. , "Discussion of Reference (94)", Int. J. Num. Meth. Eng,11, pp.401-402,1977

98, Ingraffea,A.R. and Manu, C.,"Stress Intensity Factor Computation in Three Dimensions with quarter point Elements",Int. J. Num. Meth. Eng.15, pp.1427-1445, 1980

99, Wilson,W.K.,"Research Report 69-1E7-FMECH-R1", Westinghous Research Laboratories, Pittsburgh (1969)

100,Chu,W.H., Msc Thesis, UMIST, (1984)

101,Burdekin, F.M., "Engineering Design against Fracture at Stress Concentrations", Mat. Sci. and Tech. 1,pp487-493,(1985)

102,Maddox,S.J., "An Analysis of Fatigue Cracks in Fillet Welded Joints", Int.J. of Fracture, 11, pp.221-243,1978

103,Hodgson, C.W. Private communication,1988

104,Sih, G.C. and Liebowitz, H., " Mathematical Theories of Brittle Fracture", in Fracture Vol.II ed. Liebowtz, H. 1968, Academic Press.

105,Bilby, B. A. and Cardew, G.E.,"The Crack with a Kinked Tip",Int. J. Fract., 11,pp.708-712,(1975)

106,Hussain,M.A., Pu, S.L. and Underwood, J.,In Fracture analysis STP 560, American Society for Testing and Materials, Philadelphia, pp.2-28, 1974

107,Masahiro, I.and Sakae, T.,"A Critical Analysis of the Relationship between the Energy Release Rate and the Stress Intensity Factors for non-coplanar Crack Extension under Combined Mode Loading", Int. J. of Fracture,18,pp.19-28,(1982)

108,Kagayama, H. and Yuuki, K.,"Stress Intensity Factor for Branched Cracks and Consideration of Branching Phenomenon", Preprint of Jap. Sol. Mech, Eng. No. 750-11, p183 1975

109,Hua, G,Brown,M.W.and Miller,K.J., "Mixed mode Fatigue Thresholds", Fatigue of Engineering Materials and Structures,Vol.5,pp.1-17, 1981

110,Parks,D.M. Private communication,1988

111,Nagtegaal,J.C., Parks, D.M. and Rice, J.R., "On Numerically Accurate Finite Element Solution in the Fully Plastic Range", Computer Methods in

Applied Mechanics and Engineering, Vol.4 pp153-178,1974

112,Du,Z.Z. and Hancock,J.W., J Pressure Vessel Technology,1989 (In press)

113,Nakamura,T. and Shawki,T.G.," Accuracy of Deep-Crack Solutions in Fully-Plastic Edge Crack Panel Problems", Submitted to Int. J. Fracture, 1987

114,Shih, C.F. and Hutchinson,J.W.,"Combined Loading of a Fully Plastic Ligament ahead of an Edge Crack", J. of Applied Mechanics, Vol.53 pp.271-277,1986

115,Rhee, H.C. and Salama,M.M.,"On the Evaluation of Stress Intensity Factor for Tubular Joint Fatigue Study",Offshore Technology Conference, 1985,Houston,OTC4988

116,Rhee,H.C., "The Behavior of Stress Intensity Factor of Weld Toe Surface Flaw of Tubular X-Joint", Offshore Technology Conference, 1986, Houston,OTC5136

117,Shih, C. F. "Small Scale Yielding Analysis of Mixed Mode Plane-Strain Crack Problems", Fracture Analysis ASTM,STP560, pp187-210,1977

118,PATRAN Plus User Manual,PDA Engineering,2975 Redhill Avenue Costa Mesa,California 92626,U.S.A.

119,Rice, J.R. "Limitation to the Small Scale Yielding Approximation from Crack Tip Plasticity", J. of the Mechanics and Physics of Solids, Vol.22, pp.17-26,1974

120,Betegon, C. and Hancock J.W. " Two Parameter Charactersation of Elastic-Plastic Crack Tip Fields", To be published,1989

Appendix (Fortran Program)

```
C        PRO TO RENUM NODE AND ELENUM
C        S.W.SLOAN AND M.F. RANDOLPH
C        AUTOMATIC ELEMENT REORDERING FOR FINITE ELEMENT
C        ANALYSIS WITH FRONTAL SOLUTION SCHEMES
C        (INTERNATIONAL JOURNAL FOR NUMERICAL METHODS IN
C        ENGINEERING, VOL.19, 1153-1181 (1983))
C           ZHEN-ZHONG DU AND JOHN W. HANCOCK
C        THE DEPARTMENT OF MECHANICAL ENGINEERING
C        UNIVERSITY OF GLASGOW,G12,8QQ
C*****************************************************************
C ALL    LOGICAL VARIABLE WHICH IS USED TO ASCERTAIN WHETHER
C        ALL OF THE NODES IN THE FINITE ELEMENT MESH ARE TO BE
C        USED IN THE REORDERING PROCEDURE. FOR MESHES WITH ONE
C        TYPE OF HIGH ORDER ELEMENT, IT IS NECESSARY TO CONSIDER
C        OF NODE I IS EQUAL TO LEV(I). DIMENSION EQUAL TO NODES.
C MAXDEG CONTROL PARAMETER INDICATING THE MAXMUN ALLOWABLE
C        DEGREE OF ANY NODE IN THE GRAPH
C MAXNOD CONTROL PARAMETER INDICATING THE MAXIMUN ALLOWABLE
C        NUMBER OF NODES FOR ANY ELEMENT IN THE ME
C        MANNER, USING THE FULL LIST OF NODES FOR EACH ELEMENT
C        AND THE NEW ELEMENT NUMBERING STRATEGY (STORED IN
C        ARRAY NEN)
C NADJ   VECTOR CONTAINING THE ADJACENCY LISTS FOR ALL THE NODES
C
C        ADJACENT TO NODE I IS GIVEN BY (I-1)*MAXDEG+1,(I-1)*
C        MAXDEG+2,.....,(I-1)*MAXDEG+NDEG(I))
C NDEG   VECTOR CONTAINING THE DEGREE OF EACH NODE. DIMENSION
C        IS EQUAL TO NODES. THE DEGREE OF NODE I IS EQUAL TO
C        NDEG(I)
C NEN    VECTOR CONTAINING THE NEW ELEMENT NUMBERS. THE ADDRESS
C        IN THIS ARRAY INDICATES THE OLD ELEMENT NUMBER :E.G.
C        NEN(1)=6 MEANS THAT THE NEW NUMBER FOR OLD ELEMENT ONE
C        IS SIX. DIMENSION EQUAL TO NET
C NET    CONTROL PARAMETER INDICATING THE TOTAL NUMBER OF ELEMENTS
C        IN THE MESH
C NEWNN  VECTOR CONTAINING THE NEW NODE NUMBERS GENERATED FOR EACH
C        STARTING NODE IN SUBROUTINE RESEQ1. T
C        VECTOR GIVES THE OLD NODE NUMBER,E.G.NEWNN(1)=6 MEANS
C        THAT THE NEW NUMBER FOR OLD NODE ONE IS SIX. DIMENSION
C        EQUAL TO NODES
C NEWNUM VECTOR CONTAINING THE NEW NODE NUMBER WHICH GIVE THE
C        MEANS THAT THE NEW NUMBER FOR OLD NODE ONE IS SIX. DIMENSION
C        EQUAL TO NODES. AFTER THE NEW ELEMENT NUMBERS HAVE BEEN
C        COMPUTERED IN SUBROUTINE RESEQ2, THE CONTENTS OF THIS ARRAY
C        MAY BE IGNORED AGRID OF ONE TYPE OF HIGH ORDER ELEMNT,NODES
C        WOULD BE EQUAL TO THE NUMBER OF CORNER NODES, NOTE THAT
C        IF NODES IS NOT EQUAL TO THE TOTAL NUMBER OF NODES,THEN THE
C        LOGICAL VARIABLE ALL MUST BE SET TO FALSE
C NPE    VECTOR CONTAINING THE NUMBER O
C        ELEMENTS. THE ADDRESSES OF NODES WHICH DEFINE ELEMENT I ARE
C        GIVEN BY (I-1)*MAXNOD+1,(I-1)*MAXNOD+2,...,(I-1)*MAXNOD+NPE(I)
C        IN THIS ARRAY IT IS ASSUMED THAT THE CORNER NODES ARE LIST
C        FIRST. DIMENSION EQ
C NS     THE NUMBER OF PSEUDO-PERIPHERAL NODES WHICH ARE TO BE USED
C         AS STARTING POINTS FOR THE NODE RENUMBERING ALGORITHM
C NSTART VECTOR OF PSEUDO-PERIPHERAL NODES WHICH ARE TO BE USED AS
C        STARTING NODES FOR THE NODE RENUMBERING SUBROUTINE RESEQ1
C OLDELE OLD ELEMENT FILE ,IF THE NUMBER OF NODES IN ONE ELEMENT IS
C        LESS THAN 20, NODE NUMBER EQUALS ZERO SHOULD BE USED
```

```
     3  LA6(408),LA7(408),LA8(408),LA9(408),LA10(408),LA11(408),
     4  LA12(408),LA13(408),LA14(408),LA15(408),LA16(408),LA17(408),
     5  LA18(408),LA19(408),LA20(408),LA(408)
        OPEN(UNIT=2,FILE='NPE',STAT
        PRINT *,'S.W.SLOAN AND M.F. RANDOLPH'
        PRINT *,'AUTOMATIC ELEMENT REORDERING FOR FINITE ELEMENT'
        PRINT *,'ANALYSIS WITH FRONTAL SOLUTION SCHEMES'
        PRINT *,'(INTERNATIONAL JOURNAL FOR NUMERICAL METHODS IN
     1  ENGINEERING, VOL.19, 1153-1181 (1983))'
        PRINT *,'ZHEN-ZHONG DU AND JOHN W. HANCOCK'
        PRINT *,'THE DEPARTMENT OF MECHANICAL ENGINEERING'
        PRINT *,'UNIVERSITY OF GLASGOW,G12,8QQ'
        MAXDEG=81
        MAXNOD=20
        NET=408
        NODES=1858
        DO 400 I=1,NET
        READ(2,*) NPE(I)
 400    CONTINUE
        DO 500 II=1,8160
        READ(3,*) NPN(II)
 500    CONTINUE
        CALL SETUP(NPN,NADJ,NDEG,NPE,NODES,NET,MAXNOD,MAXDEG,
     1  .TRUE.)
        CALL DIAM(NDEG,NSTART,LEV,NADJ,NODES,MAXDEG,NS)
        MINMAX=1000000000
        CALL RESEQ1(NADJ,NDEG,NEWNN,NEWNUM,NSTART,NODES,MAXDEG,
     1  NS,MINMAX)
        DO 88 J=1,NODES
        WRITE(7,*) NEWNUM(J),J
 88     CONTINUE
        IF(NEN(J).EQ.0)THEN
        NEN(J)=J
        ENDIF
        WRITE(8,*) NEN(J),J
99      CONTINUE
       CALL ORDER(NET,NPN,NPE,NEN,LA,LA1,LA2,LA3,LA4,
     1  LA5,LA6,LA7,LA8,LA9,LA10,LA11,LA12,LA13,LA14,LA15,
     2  LA16,LA17,LA18,LA19,LA20)
        STOP
        END
        SUBROUTINE SETUP(NPN,NADJ,NDEG,NPE,NODES,NET,MAXNOD,MAXDEG,
     1  ALL)
C*****************************************************************
C       SUBPROGRAM SETUP -COMPUTER ADJA CENCY LIST AND FOR EACH
C                         NODE
C                        -MODIFIED VERSION OF COLLINS ROUTINE
C                        -USE ONLY CORNER NODES IF
C*****************************************************************
        DIMENSION NPN(8160),NADJ(150498),NDEG(1858),NPE(408)
        LOGICAL ALL
C
        DO 10, J=1,NODES
  10    NDEG(J)=0
C
        DO 60 J=1,NET
        NN=NPE(J)
C
        DO 50 I=1,NN
        JNTI=NPN((J-1)*MAXNOD+I)
```

```
      DO 40 II=1,NN
      IF(II.EQ.I) GOTO 40
      JJT=NPN((J-1)*MAXNOD+II)
      MEM1=NDEG(JNTI)
      IF(MEM1.EQ.0) GOTO 30
C
      DO 20 III=1,MEM1
      IF(NADJ(JSUB+III).EQ.JJT) GOTO 40
   20 CONTINUE
C
   30 NDEG(JNTI)=NDEG(JNTI)+1
      NADJ(JSUB+NDEG(JNTI))=JJT
   40 CONTINUE
C
   50 CONTINUE
C
   60 CONTINUE
C
      RETURN
      END

      SUBROUTINE DIAM(NDEG,NSTART,LEV,NADJ,NODES,MAXDEG,NS)
C*****************************************************************
C     SUBPROGRAM DIAM - COMPUTE SET OF PSUEDO-PERIPHERAL NODES
C*****************************************************************
      DIMENSION NDEG(1858),NADJ(150498),LEV(1858),NSTART(1858)
      LOGICAL BETTER
C
C     BEGIN ITERATION
C     SELECT INITIAL ROOT NODE ARBITRARILY AND GENERATE ITS LEVEL
C     STRUCTURE
C
      IROOT=1
      ITER=0
      CALL LEVEL(NDEG,LEV,IDEPTH,NADJ,IWIDTH,NODES,IROOT,MAXDEG)
C
C     CREATE LIST OF NODES WHICH ARE AT MAXIMUM DISTANCE FROM ROOT
C     NODE
C
      LHW=0
      DO 20 I=1,NODES
      IF(LEV(I).NE.IDEPTH) GOTO 20
      LHW=LHW+1
      NSTART(LHW)=I
   20 CONTINUE
C
C     STORE ROOT ON END OF LIST OF POSSIBLE STARTING NODES
C
      NS=LHW+1
      NSTART(NS)=IROOT
C
C     LOOP OVER NODES AT MAXIMUM DISTANCE FROM ROOT NODE
C     GENERATE LEVEL STRUCTURE FOR EACH NODE
C     SET SWICH IF A LEVEL STRUCTURE OF GREATER DEPTH OCCURS
C
      BETTER=.FALSE.
      DO 30 I=1,LHW
      NEND=NSTART(I)
      CALL LEVEL(NDEG,LEV,NDEPTH,NADJ,NWIDTH,NODES,NEND,MAXDEG)

   30 CONTINUE
      IF(BETTER)GOTO 10
```

```
C
      RETURN
      END

      SUBROUTINE LEVEL(NDEG,LEV,LSD,NADJ,MLW,NODES,NROOT,MAXDEG)
C*****************************************************
      DO 10 I=1,NODES
   10 LEV(I)=0
      LEV(NROOT)=1
      KOUNT=1
      MLW=1
C
C     ASSIGN LEVELS TO VERTICES
C
      DO 40 L=2,NODES
      LW=0
C
      DO 30 I=1,NODES
      IF(LEV(I).GT.0) GOTO 30
      NCS=NDEG(I)
      JSUB=(I-1)*MAXDEG
C
      DO 20 JJ=1,NCS
      NODE=NADJ(JSUB+JJ)
      IF(LEV(NODE).NE.L-1) GOTO 20
      LSD=L
      LW=LW+1
      LEV(I)=L
      KOUNT=KOUNT+1
   20 CONTINUE
C
   30 CONTINUE
      IF(LW.GT.MLW)MLW=LW
C
   40 CONTINUE
   50 IF(LW.GT.MLW)MLW=LW
C
      RETURN
C
      END

      SUBROUTINE RESEQ1(NADJ,NDEG,NEWNN,NEWNUM,NSTART,NODES,MAXDEG,
     1 NS,MINMAX)
C*************************************************************
     1 NSTART(1858)
C
C     LOOP OVER SET OF STARTING NODES
C
C
      DO 100 II=1,NS
      I=NSTART(II)
      DO 10 J=1,NODES
   10 NEWNN(J)=0
      NIF=NDEG(I)
      MAXFRT=NIF
      NEWNN(I)=1
C
      NDEG(N)=-NDEG(N)
   20 CONTINUE
      NDEG(I)=-NDEG(I)
C
C     LOOP OVER NODES TO BE RENUMBERED
C
```

```
      DO 60 K=2,NODES
      MINNEW=10**8
      LMIN=10**8
C
C     LOOP OVER UNNUMBERED NODES
C     SKIP TO NEXT NODE IF OLD NODE IS ALREADY RENUMBERED
C     RESTRICT SEARCH TO ACTIVE NODES FOR KING SCHEME
C
      DO 40 J=1,NODES
      IF((NEWNN(J).GT.0).OR.(NDEG(J).GT.0))GOTO 40
      NEW=0
      MIN=10**8
      NCN=IABS(NDEG(J))
      LSUB=(J-1)*MAXDEG
C
C     COMPUTE THE INCREMENT IN ACTIVE NODES FOR EACH NODE J
C     COMPUTE WHEN NODE WAS FIRST ACTIVATED BY CHECKING FOR RENUMBERI
C     NEIGHBOURS WITH LOWEST NUMBERS
C
      DO 30 L=1,NCN
      N=NADJ(LSUB+L)
      IF(NDEG(N).GT.0)NEW=NEW+1
      IF(NEWNN(N).EQ.0)GOTO 30
      IF(NEWNN(N).LT.MIN)MIN=NEWNN(N)
   30 CONTINUE
C
      MINNEW=NEW
      LMIN=MIN
      NEXT=J
   40 CONTINUE
C
C     RENUMBER NODE AND COMPUTE NUMBER OF ACTIVE NODES
C     ABANDON SCHEME IF NUMBER OF ACTIVE NODES EXCEEDS PREVIOUS
      IF(MAXFRT.GE.MINMAX)GOTO 80
C
C     NEGATE ALL NDEG ENTRIES FOR NODES WHICH ARE
C     ADJACENT TO NODE JUST RENUMBERED
C
      IF(MINNEW.EQ.-1)GOTO 60
      NCN=IABS(NDEG(NEXT))
      JSUB=(NEXT-1)*MAXDEG
      DO 50 J=1,NCN
      N=NADJ(JSUB+J)
      IF(NDEG(N).GT.0)NDEG(N)=-NDEG(N)
   50 CONTINUE
C
   60 CONTINUE
C
C     STORE NUMBERING SCHEME GENERATED
C     RESET NDEG TO POSITIVE VALUES
C
      DO 70 J=1,NODES
      NEWNUM(J)=NEWNN(J)
   70 CONTINUE
      MINMAX=MAXFRT
   80 DO 90 J=1,NODES
      NDEG(J)=IABS(NDEG(J))
   90 CONTINUE
  100 CONTINUE
      MINMAX=MINMAX+1
C
  200 FORMAT(I4,',')
      RETURN
```

```
      END

      SUBROUTINE RESEQ2(NEWNUM,NPN,NEN,IEN,NPE,MAXNOD,NET,NODES,ALL)
C
C*****************************************************************
      DIMENSION NEWNUM(1858),NPN(8160),NEN(408),NPE(408),IEN(408)
      LOGICAL ALL
C
      DO 10 I=1,NET
   10 NEN(I)=0
      KOUNT=0
C
C     LOOP OVER EACH NEW NODE NUMBER
C     LOOP ONLY OVER CORNER NODES IF ALL=.FALSE.
C
      DO 40 I=1,NODES
C
C     LOOP OVER EACH ELEMENT
C     SKIP TO NEXT ELEMENT IF ALREADY RENUMBERED
C
      DO 30 J=1,NET
      IF(NEN(J).GT.0)GOTO 30
      NN=NPE(J)
      I1=(J-1)*MAXNOD
C
C     LOOP OVER EACH NODE IN ELEMENT
C     USE ONLY CORNER NODES IF ALL=.FALSE.
C     ASSUMED THAT CORNER NODES ARE LISTED FIRST IN NODAL DEFINITION
C     VECTORS IF ALL=.FALSE.
C
      DO 20 K=1,NN
      N=NPN(I1+K)
      N=NEWNUM(N)
      IF(N.NE.I) GOTO 20
      KOUNT=KOUNT+1
      NEN(J)=KOUNT
      IEN(KOUNT)=J
      IF(KOUNT.EQ.NET) GOTO 50
      GOTO 30
   20 CONTINUE
C
   30 CONTINUE
C
   40 CONTINUE
  200 FORMAT(I4,',')
C
   50 RETURN
      END
      SUBROUTINE ORDER(NET,NPN,NPE,NEN,LA,LA1,LA2,LA3,LA4,
     1 LA5,LA6,LA7,LA8,LA9,LA10,LA11,LA12,LA13,LA14,LA15,
     2 LA16,LA17,LA18,LA19,LA20)
      DIMENSION LA1(408),LA2(408),LA3(408),LA4(408),LA5(408),
     1 LA6(408),LA7(408),LA8(408),LA9(408),LA10(408),LA11(408),
     2 LA12(408),LA13(408),LA14(408),LA15(408),LA16(408),LA17(408),
     3 LA18(408),LA19(408),LA20(408),LA(408),N
     1 LA6(L2),LA7(L2),LA8(L2),LA9(L2),LA10(L2),LA11(L2),LA12(L2),
     2 LA13(L2),LA14(L2),LA15(L2),LA16(L2),LA17(L2),LA18(L2),LA19(L2)
     3 LA20(L2)
      IF(LA4(L2).EQ.0)THEN
      WRITE(1,80) NEN(L2),LA1(L2),LA2(L2),LA3(L2)
      ELSE IF(LA5(L2).EQ.0)THEN
      WRITE(1,90) NEN(L2),LA1(L2),LA2(L2),LA3(L2),LA4(L2)
      ELSE IF(LA9(L2).EQ.0)THEN
```

```
      WRITE(1,100) NEN(L2),LA1(L2),LA2(L2),LA3(L2),LA4(L2),LA5(L2),
     1  LA6(L2),LA7(L2),LA8(L2)
      ELSE IF(LA13(L2).EQ.0)THEN
      WRITE(1,200) NEN(L2),LA1(L2),LA2(L2),LA3(L2),LA4(L2),LA5(L2),
     1  LA6(L2),LA7(L2),LA8(L2),LA9(L2),LA10(L2),LA11(L2),LA12(L2)
      ELSE IF(LA16(L2).EQ.0)THEN
      WRITE(1,300) NEN(L2),LA1(L2),LA2(L2),LA3(L2),LA4(L2),LA5(L2),
     1  LA6(L2),LA7(L2),LA8(L2),LA9(L2),LA10(L2),LA11(L2),LA12(L2),
     2  LA13(L2),LA14(L2),LA15(L2)
      ELSE IF(LA19(L2).EQ.0)THEN
      WRITE(1,400) NEN(L2),LA1(L2),LA2(L2),LA3(L2),LA4(L2),LA5(L2),
     1  LA6(L2),LA7(L2),LA8(L2),LA9(L2),LA10(L2),LA11(L2),LA12(L2),
     2  LA13(L2),LA14(L2),LA15(L2),LA16(L2),LA17(L2),LA18(L2)
      ELSE
      WRITE(1,500) NEN(L2),LA1(L2),LA2(L2),LA3(L2),LA4(L2),LA5(L2),
     1  LA6(L2),LA7(L2),LA8(L2),LA9(L2),LA10(L2),LA11(L2),LA12(L2),
     2  LA13(L2),LA14(L2),LA15(L2),LA16(L2),LA17(L2),LA18(L2),
     3  LA19(L2),LA20(L2)
      ENDIF
 20   CONTINUE
 30   FORMAT(3(I4,','),I4)
 90   FORMAT(4(I4,','),I4)
100   FORMAT(8(I4,','),I4)
200   FORMAT(12(I4,','),I4)
300   FORMAT(15(I4,','),I4)
400   FORMAT(16(I4,',')/,(2(I4,','),I4))
500   FORMAT(16(I4,',')/,(4(I4,','),I4))
      RETURN
      END
100   FORMAT(8(I4,','),I4)
200   FORMAT(12(I4,','),I4)
300   FORMAT(15(I4,','),I4)
400   FORMAT(16(I4,',')/,(2(I4,','),I4))
500   FORMAT(16(I4,',')/,(4(I4,','),I4))
      RETURN
```